

Numerical simulation of deformation of a droplet in a stationary electric field using DG

Vom Fachbereich Maschinenbau an der Technischen Universität
Darmstadt zur Erlangung des akademischen Grades eines
Doktor-Ingenieurs (Dr.-Ing) genehmigte

DISSERTATION

vorgelegt von

M.Sc. Nehzat Emamy

aus Shiraz / Iran

Berichterstatter: Prof. Dr.-Ing. habil. Martin Oberlack
Mitberichterstatter: Prof. Dr.-Ing. Thomas Weiland
Tag der Einreichung: 22.08.2012
Tag der mündl. Prüfung: 05.11.2014

Darmstadt, 2014

D17

Erklärung

Hiermit erkläre ich, dass ich die vorliegende Arbeit, abgesehen von den in ihr ausdrücklich genannten Hilfen, selbstständig verfasst habe.

Nehzat Emamy

Bitte zitieren Sie dieses Dokument als:

URN: : urn:nbn:de:tuda-tuprints-34712

URL: <http://tuprints.ulb.tu-darmstadt.de/id/eprint/3471>

Dieses Dokument wird bereitgestellt von tuprints, E-Publishing-Service der TU Darmstadt.

<http://tuprints.ulb.tu-darmstadt.de>

tuprints@ulb.tu-darmstadt.de

Die Veröffentlichung steht unter folgender Creative Commons Lizenz:

Namensnennung-Keine kommerzielle Nutzung-Keine Bearbeitung 2.0 Deutschland

<http://creativecommons.org/licenses/by-nc-nd/2.0/de/>



Abstract

English

Numerical simulation of deformation of a droplet in a stationary electric field is performed in the present research. The droplet is suspended in another immiscible fluid with the same density and viscosity but a different dielectric property (permittivity). By applying the electric field, the fluids are polarized that gives rise to mechanical forces and deformation. A two-way coupling occurs because of the forces exerted from the electric field on the droplet and the deformation of the droplet which changes the geometry for the electric field calculations. The droplet continues to deform until a force balance between the electric force, pressure and the surface tension is achieved and the droplet becomes a spheroid.

An electromechanical approach is adopted to solve the above mentioned problem, which includes solving the governing equations of both the electric and fluid fields, computing the coupling forces and capturing the movement of the interface of the droplet and the surrounding fluid. A one-fluid approach is followed, which enables us to solve one set of the governing equations for both the droplet and the surrounding fluid. The interface is represented as the zero iso-value of a level set function and an advection equation is solved to find the movement of the interface. A diffuse interface model is used to regularize the jump in the fluid and electric properties.

The governing equations of the electric and fluid fields and the level set advection equation are discretized using the Discontinuous Galerkin Finite Element method (DG) in the BoSSS code for solving conservation laws. The electric field is computed from the electric potential by considering the electrostatics equations. To find the electric potential, a Laplace equation is solved which has a jump in the permittivity at the interface. The Laplace equation is discretized using the interior penalty method (IP) which we modified for the case of high jumps in the permittivity. Assuming that the fluids are linear dielectric materials, the electric force is the dielectrophoretic force which is computed from the Kortweg-Helmholtz formula. This force is added as a body force to the incompressible Navier-Stokes equations, which are the governing equations for the fluid flow. Considering that there is no jump in the fluid properties, a single phase solver of the Navier-Stokes equations including the surface tension at the interface is developed. The surface tension force is added as a body force to the Navier-Stokes equations using the continuum surface force model (CSF). This model is known for producing a spurious velocity field. To decrease the spurious velocities, the surface tension term is calculated by using high degree polynomials for a precise calculation of the normal vector and curvature.

To solve the incompressible Navier-Stokes equations using the DG method, a projection scheme with a consistent Neumann pressure boundary condition is employed and the

same polynomial degree for the velocity and pressure (equal-order method) is applied. Using the above-mentioned pressure boundary condition leads to an optimal convergence rate of $k+1$ in the L^2 -norm for the pressure, which is not reported from other DG solvers. However, using the DG method, we have observed that discontinuities in the solutions at the cell boundaries can affect the solution accuracy and even cause a numerical instability. These accuracy and stability issues occur when the derivatives of the solution are computed. Therefore a flux-based method for calculation of the derivatives of the flow variables was adopted. As the results showed considerably improved accuracy and stability characteristics, we used the proposed method also in solving the above mentioned coupled problem.

German

In der aktuellen Arbeit wird eine numerische Simulation der Deformation eines Tröpfchens in einem stationären elektrischen Feld durchgeführt. Das Tröpfchen ist in einem nicht vermischbaren Fluid mit gleicher Dichte und Viskosität aber abweichender dielektrischer Eigenschaft (Dielektrizitätskonstante) eingebettet. Durch Anlegen eines elektrischen Feldes werden beide Fluide polarisiert, was zu einer mechanischen Kraft und Deformation führt. Wegen der Kraft, die das elektrische Feld auf das Tröpfchen ausübt, und der entstehenden Deformation des Tröpfchens, welche zu einer Veränderung der Geometrie in der Berechnung des elektrischen Feldes führt, tritt eine Zwei-Wege-Kopplung auf. Das Tröpfchen verformt sich, bis ein Gleichgewicht zwischen den Kräften aus elektrischem Feld, Druck und Oberflächenspannung auftritt und das Tröpfchen ein Sphäroid wird.

Es wird ein elektromechanischer Ansatz zur Lösung des oben genannten Problems, welches aus der Lösung der beschreibenden Gleichungen des elektrischen und des Strömungsfeldes, der Berechnung der Kopplungskräfte und der Bestimmung der Bewegung des Interface zwischen dem Tröpfchens und dem umgebenden Fluids besteht, verwendet. Ein Ein-Fluid-Ansatz wird betrachtet, welcher uns ermöglicht nur einen Satz an bestimmenden Gleichungen für das Tröpfchen und das umgebende Fluid zusammen lösen zu müssen. Das Interface wird durch die Null-Isolinie einer "level set" Funktion repräsentiert und eine Advektionsgleichung zur Bestimmung der Bewegung des Interface wird gelöst. Um den Sprung in den Eigenschaften des Fluids und des elektrischen Felds zu regularisieren wird ein Modell mit unscharfem Interface verwendet.

Die bestimmenden Gleichungen des elektrischen und des Strömungsfeldes und die "level set" Advektionsgleichung werden unter Verwendung der diskontinuierlichen Galerkin Finite Elemente Methode (DG) im BoSSS Code diskretisiert. Das elektrische Feld wird aus dem elektrischen Potential unter Verwendung der Gleichungen der Elektrostatik berechnet. Um das elektrische Potential zu bestimmen wird eine Poisson Gleichung gelöst, welche einen Sprung in der Dielektrizitätskonstanten am Interface aufweist. Die Poisson Gleichung wird mit der "interior penalty method" (IP), welche wir für den Fall hoher Sprünge in der Dielektrizitätskonstanten modifiziert haben, diskretisiert. Unter der Annahme, dass die Fluide linear dielektrische Materialien sind, ist die elektrische Kraft die dielektrophoretische Kraft, welche von aus der Kortweg-Helmholtz-Gleichung berechnet wird. Diese Kraft wird als Volumenkraft in die inkompressiblen Navier-Stokes-

Gleichungen eingefügt, welche die beschreibenden Gleichungen der Fluidströmung sind. Auf Grund der Tatsache, dass kein Sprung in den Fluideigenschaften auftritt, wird ein einphasiger Löser für die Navier-Stokes-Gleichungen mit Oberflächenspannung am Interface entwickelt. Die Kraft, welche aus der Oberflächenspannung resultiert, wird als Volumenkraft zu den Navier-Stokes-Gleichungen unter Verwendung des "continuum surface force"-Modell (CSF) hinzugefügt. Dieses Modell ist dafür bekannt Störungen im Geschwindigkeitsfeld zu produzieren. Um diese Störungen zu reduzieren wird der Oberflächenspannungsterm mit Polynomen hoher Ordnung berechnet, womit der Normalenvektor und die Krümmung präzise bestimmt werden können.

Um die inkompressiblen Navier-Stokes-Gleichungen mit der DG Methode zu lösen wird ein Projektionsschema mit einer konsistenten Neumann-Druck-Randbedingung eingesetzt und die gleiche polynomiale Ordnung für die Geschwindigkeit und den Druck ("equal-order method") angewendet. Die Anwendung der oben genannten Druck-Randbedingungen führen zu einer optimalen Konvergenzrate von $k + 1$ in der L^2 -Norm für den Druck, was für andere DG-Löser nicht berichtet wird. Allerdings haben wir bei der Anwendung der DG-Methode beobachtet, dass Diskontinuitäten in der Lösung an den Zellengrenzen die Lösungsgenauigkeit beeinträchtigen und sogar numerische Instabilitäten auslösen. Diese Genauigkeits- und Stabilitätsprobleme treten bei der Berechnung der Ableitungen der Lösung auf. Daher wurde eine Fluss-basierte Methode zur Berechnung der Ableitungen eingeführt. Da die Ergebnisse deutlich verbesserte Genauigkeits- und Stabilitätscharakteristiken aufwiesen, haben wir die vorgeschlagene Methode auch bei der Lösung des oben genannten Kopplungsproblems verwendet.

Acknowledgments

This work has been financially supported by the Excellence Initiative of the German Federal and State Governments through the Graduate School of Computational Engineering (GSC CE) at Technische Universität Darmstadt.

I would like to thank my supervisor Prof. Dr.-Ing. habil. Martin Oberlack for giving me the opportunity to accomplish this PhD thesis at the Chair of Fluid Dynamics and providing me the freedom to follow my own ideas while encouraging me along the way. I should thank Prof. Dr.-Ing. Thomas Weiland that accepted to be my second supervisor and co-referee. This gave me the chance to get into contact with PD Dr. rer. nat. Erion Gjonaj, Annette Fröhlcke and Harald Songoro at the Computational Electromagnetics Laboratory, who I am thankful for the fruitful discussions that we had.

I would like to acknowledge Florian Kummer for his great attitude in the development of the BoSSS code, which provided the basement for my PhD project. Furthermore, I should thank him for the discussions that we had during the time. I have to thank Roozbeh Mousavi for the common parts of our projects, which I benefited from his work and his suggestions. I am thankful to Björn Müller for his contributions in the BoSSS code and the technical support with the code that facilitated my work to a large extent. I had useful discussions with Benedikt Klein.

For writing the dissertation, I should thank Prof. Dr.-Ing. habil. Yongqi Wang who provided me useful guidelines and comments. For the proof reading, I would like to thank Andreas Nold, Björn Müller, Florian Kummer, Olga Kelbin and Andreas Zieleniewicz (also for the German translation of the abstract).

Furthermore, I would like to thank all my colleagues at the FDY and the GSC CE for the friendly environment which I enjoyed during the time. I should thank the staff at the GSC CE, specially Heike Hoffmann and Carina Schuster for their help in many aspects that allowed me to focus and concentrate on my project.

I would like to express my special thanks again to Roozbeh Mousavi as my husband because of his great support, understanding and patience. I am deeply grateful to the continuous support of my lovely parents in all aspects of my life specially their attitude for my education. And finally, I owe to the sweet smiles of my little Mana, who brings me hope and delight.

Contents

Nomenclature	xiii
1 Introduction	1
1.1 State of the art	2
1.2 Research goals	2
1.3 Problem definition and assumptions	3
2 Governing equations	5
2.1 The Maxwell's equations	5
2.1.1 Slowly varying electric fields	6
2.2 The incompressible Navier-Stokes equations	8
2.3 Forces exerted from the electric field to the fluid	8
3 Governing equations of the multi-phase problem	11
3.1 Multiphase equations with the two-fluid approach	11
3.2 Multiphase equations with the one-fluid approach	12
3.3 Non-dimensional equations with the one-fluid approach	13
3.3.1 Special cases	16
4 The discontinuous Galerkin Finite Element method	17
4.1 Basics of DG	17
4.2 Solving a scalar conservation law in BoSSS	19
4.2.1 Physical and numerical flux functions	19
4.2.2 Time discretization	21
5 The single-phase incompressible Navier-Stokes equations	23
5.1 Introduction	23
5.2 Methodology	24
5.3 Spatial discretization	26
5.4 Computational options for the derivatives	27
5.5 Numerical results	29
5.5.1 Laminar boundary layer on a flat plate	29
5.5.2 Fully developed channel flow	32
5.5.3 Fully developed channel flow with periodic boundaries	36
5.5.4 Unsteady Taylor vortex flow	38
5.5.5 Stokes channel flow	47
5.5.6 Channel flow with transpiration	53
5.6 Conclusion	55
6 Numerical modeling of the surface tension force	57

6.1	The diffuse interface model	57
6.2	Test case: Stationary flow with pressure jump	59
6.2.1	h-convergence study	59
6.2.2	p-convergence study	65
6.2.3	Approximating the regularized delta function	69
6.3	The Computation of the normal vector and curvature	73
6.3.1	p-enrichment of the normal vector	73
6.3.2	The signed-distance level set function	80
6.3.3	The Narrow band technique	83
6.4	Test case: Moving interface	83
7	Solving the electrostatics equations	87
7.1	Electric potential	88
7.2	Electric field	91
7.3	Convergence study	98
7.4	Stabilization method	101
7.4.1	Average coefficient for the penalty term	101
7.4.2	Maximum coefficient for the penalty term	108
7.5	High jumps in the dielectric property	120
8	Coupling the electric and fluid fields	129
8.1	Numerical modeling of the electric force	129
8.2	The creeping flow	130
8.3	Deformation of a droplet in a stationary electric field	130
8.4	Spurious currents	149
8.5	Equilibrium shape of a droplet in a stationary electric field	153
8.5.1	The steady state deformation	153
8.5.2	Numerical test case	154
9	Summary, discussions and outlook	157
10	Bibliography	161
11	Curriculum Vitae	165

Nomenclature

\mathbf{f}_Ω	External body force
χ	Dielectric susceptibility
δ	Dirac delta function
ϵ	Half-thickness of the diffuse interface
η	Electrowetting number
γ	Surface tension
\hat{u}_{jn}	n th DG coordinate for cell K_j in modal representation
$\hat{\mathbf{E}}$	Electromotive intensity
\hat{n}	Normal vector to an edge of a cell
κ	Curvature
μ	Dynamic viscosity
μ_0	Magnetic permeability of vacuum
μ_P	Penalty parameter
μ_r	Relative permeability
Ω	Physical domain
$\partial\Omega$	Boundary of physical domain
Φ	Electric potential
ϕ	Level set function
ρ	Fluid density
ρ_f	Free charge volume density
σ	Conductivity
τ_E	Characteristic time for electric phenomena
τ_P	Time scale of transport processes
τ_{EM}	Electromagnetic wave transmit time
\mathbf{d}	Rate of deformation tensor
\mathbf{T}^M	Maxwell stress tensor
θ	Contact angle
θ_Y	The Young (static) contact angle

ε	Permittivity
ε_0	Permittivity of vacuum
ε_d	Relative permittivity of a dielectric layer
ε_r	Relative permittivity
B	Magnetic field
D	Electric displacement vector
E	Electric field
f	Flux function
f*	Numerical flux function
\mathbf{f}_Ω^H	Kortweg-Helmholtz body force
\mathbf{f}_Ω^K	Kelvin body force
g	Gravitational body force
H	Magnetic field intensity (magnetising field)
J	Total electric current
J_c	Electric conduction current
J_f	Free current density
M	Magnetization (density)
n	Normal vector to an interface
P	Polarization vector (Polarization density)
u	Fluid velocity
w^s	Speed of a moving interface
X	Spatial position
<i>a</i>	Equatorial radius of a spheroid
<i>b</i>	Polar semi-axis of a spheroid
<i>c</i>	Index for characteristic variables
<i>D</i>	Spatial dimension
<i>d</i>	Thickness of the dielectric layer
d_∞	Steady state deformation of a droplet
D_n	Electric displacement vector in the normal direction to an interface
E_∞	Electric field at infinity
E_n	Electric field in the normal direction to an interface
E_t	Electric field in the tangential direction to an interface
<i>Eu</i>	The Euler number

Fr	The Froude number
g	Gravitational acceleration
H	Heaviside function
h	Element size
J	Number of computational cells
j	Index for computational cells
k	Polynomial degree
K_j	Cell j
l_c	Characteristic length
m	index for test functions
n	Index for basis polynomials
N_p	Number of polynomials
p	Pressure
p_0	Pressure of the unpolarized fluid
q	Source term
Re	The Reynolds number
T	Temperature
t	Time
$u(\mathbf{x}, t)$	Global solution
$u^h(\mathbf{x}, t)$	Polynomial approximation of the global solution
$u_j^h(\mathbf{x}, t)$	Local polynomial solution in cell K_j
w	Water
$w - a$	Water-Air
We	The Weber number

1 Introduction

The motivating application background of the current research, concerns rain or dew droplets which accumulate on the surface of high voltage insulators. Due to the strong electric field, droplets have the tendency to change their shapes, to form structures, to split or to merge. This may lead to electric discharges on the surface, which are the cause of long-term deteriorations. Therefore, studying water droplets in presence of an electric field is the key to understand the aging mechanism of the insulators.

Besides studying water droplets on surface of high voltage insulators, there are many other technological applications like liquid lenses, displays, Lab-on-a-chip and so on that make use of electric fields as a tool to manipulate liquids on small scales. Electric fields are used to generate drops, control their shape and their movement. These applications are related to the *electrowetting* field of study. The basic idea of the electrowetting is to spread liquid drops on solid surfaces by applying a voltage. As it is shown in figure 1.1, when a voltage is applied to a drop, its contact angle (the angle formed between the liquid-gas interface and the solid surface) decreases. A dielectric (insulating layer) is usually used between the drop and the electrode to make use of higher voltages possible and this is called electrowetting on dielectrics (EWOD).

In other research areas, the deformation of a fluid drop suspended in another immiscible

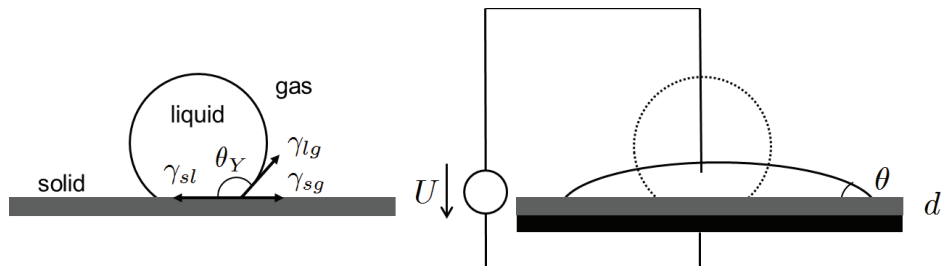


Figure 1.1: Electrowetting on dielectrics (EWOD). (left) The drop makes the contact angle θ_Y with the surface, which is the Young contact angle. (right) As a result of the application a voltage U , the apparent contact angle θ is smaller than θ_Y (wetting).

fluid under the influence of an imposed electric field has been extensively studied. A classification of these studies is done in (Supeene, Koch & Bhattacharjee 2008). The underlying applications of these studies include sprays, aerosols and ink jet printing, to name a few.

1.1 State of the art

In the conventional electrowetting applications, drops are considered conductive and the macroscopic (apparent) contact angle θ is computed from the Lippmann-Young equation,

$$\begin{aligned}\cos(\theta) &= \cos(\theta_Y) + \eta, \\ \cos(\theta_Y) &= \frac{\gamma_{sg} - \gamma_{sl}}{\gamma_{lg}}, \\ \eta &= \frac{\varepsilon_0 \varepsilon_d U^2}{2d\gamma_{lg}},\end{aligned}$$

where θ_Y is the Young (static) contact angle and η is the electrowetting number. γ_{sg} , γ_{sl} and γ_{lg} are the surface tensions at interfaces between the solid, liquid and gas mutually. ε_d is the relative permittivity of the dielectric layer with respect to the permittivity of vacuum, ε_0 , and d is the thickness of the dielectric layer, which is considered to be much smaller than the size of the drop.

Experimental measurements show that in the vicinity of the contact line, the contact angle is the static contact angle (Tsori & Steiner 2009). Recent research is focused on the microscopic details of the electric field distribution and the surface curvature near the contact line of the liquid-gas and liquid-solid interfaces. In a study done by Mugele and Buehrle (Mugele & Buehrle 2007), a domain near the contact line is considered and the curvature of the interface is calculated by balancing the electric force and the surface tension at the interface. In their study, the fluid flow is not computed and the pressure is not considered in the force balance at the interface.

Considering the applications concerning drops suspending in another immiscible liquid, Supeene et al. (Supeene et al. 2008) have chosen an electromechanical approach. They have simulated the transient response of a drop to an imposed stationary electric field. In their study, the perfect dielectric and leaky dielectric models (see sections 2.1.1.1 and 2.1.1.2) are used. They have solved the Navier-Stokes equations to compute the flow field and for the interface between the two fluids, they have adopted a moving mesh approach.

1.2 Research goals

Besides the above mentioned shortcomings of the conventional electrowetting, there are some phenomena like the saturation or instability of the contact line that are not yet understood and the Lippmann-Young equation is not able to predict them (Quilliet & Berge 2001) and (Mugele & Baret 2005). It seems that applying an electromechanical approach can overcome the limitations of the conventional electrowetting. The electromechanical approach concerns solving the governing equations of the electric and fluid problems and making a coupling between them. The aim of the current research is to apply an electromechanical approach to provide a framework for solving the electrofluid-dynamic (EFD) problems. We expect to achieve accurate simulations which enable us to understand some underlying physics of the EFD problems.

1.3 Problem definition and assumptions

For the first step and as an example application, we have considered a liquid droplet suspended in another immiscible fluid. The numerical simulation of the deformation of a droplet in an existing electric field needs solving of the governing equations for both the electric and fluid fields which are coupled. The coupling occurs through the forces exerted from the electric field on the droplet and the deformation of the droplet which changes the geometry for the electric field calculations. The following algorithm is applicable for the case of an applied stationary electric field that we consider in the present research.

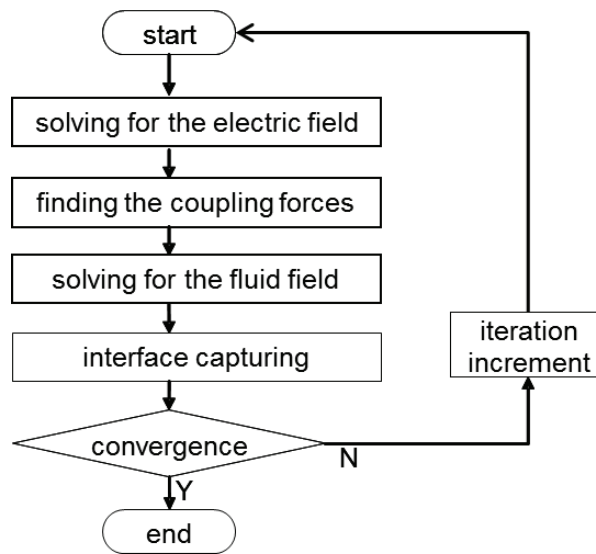


Figure 1.2: The solution algorithm for a typical EFD problem with a stationary electric field.

In chapter 2, the governing equations of the electric and fluid problems are introduced, which are the Maxwell's and Navier-Stokes equations. The Maxwell's equations are simplified using the electrostatic assumption. This assumption is discussed in the following section 2.1.1. The electric forces exerted on the fluid flow are introduced in section 2.3. In chapter 3 the governing equations are extended for the case of multiphase flows and are non-dimensionalized.

In chapter 4, the discontinuous Galerkin Finite Element method (DG) is introduced, which is used for the spatial discretization of the governing equations. Solving the single phase Navier-Stokes equations using the DG method is described in chapter 5. Numerical modeling of the surface tension force, which is present in the multiphase flows and is quite important for the current problem of droplet deformation, is described in chapter 6.

The electrostatics equations are solved in chapter 7 to find the electric field. In chapter 8, the computed electric field is used to compute the electric forces and insert them to the Navier-Stokes equations and finally, the coupled problem is solved.

2 Governing equations

2.1 The Maxwell's equations

Governing equations of the classical electrodynamics are the Maxwell's equations. Assuming that materials consist of some dipoles and free charges (electrons and/or ions), the Maxwell's equations are written below in a macroscopic differential form. These equations are called the Maxwell's equation for matter.

$$\nabla \cdot \mathbf{D} = \rho_f, \quad (2.1a)$$

$$\nabla \times \mathbf{H} = \mathbf{J}_f + \partial_t \mathbf{D}, \quad (2.1b)$$

$$\nabla \cdot \mathbf{B} = 0, \quad (2.1c)$$

$$\nabla \times \mathbf{E} = -\partial_t \mathbf{B} \quad (2.1d)$$

The first equation (2.1a) is the Gauss's law and the second one (2.1b) is the Ampere's law. \mathbf{D} is called the electric displacement vector and ρ_f is the free charge volume density. The total electric current \mathbf{J} is sum of the free current density \mathbf{J}_f and the displacement current $\partial_t \mathbf{D}$. Equation (2.1c) is the Gauss's law for magnetism and equation (2.1d) is the Faraday's law of induction. \mathbf{H} is the magnetic field intensity (magnetising field). \mathbf{E} and \mathbf{B} are the electric and magnetic fields, respectively. For polarizable and magnetizable medium, the displacement vector and magnetic field intensity are defined as

$$\mathbf{D} = \varepsilon_0 \mathbf{E} + \mathbf{P}, \quad (2.2)$$

$$\mathbf{H} = \frac{\mathbf{B}}{\mu_0} - \mathbf{M}, \quad (2.3)$$

where \mathbf{P} is the polarization vector (polarization density), μ_0 is the magnetic permeability of vacuum and \mathbf{M} is the magnetization (density). The free current density is defined as

$$\mathbf{J}_f = \rho_f \mathbf{u} + \mathbf{J}_c, \quad (2.4)$$

where \mathbf{u} is the fluid velocity and \mathbf{J}_c is the electric conduction current. Additional information are required about the polarization, magnetization and electric conduction current which are provided by the constitutive relations for material properties. Fluid flows under the influence of the externally applied and internally generated electric and magnetic fields, electro-magneto-hydrodynamics (EMHD) (or electro-magneto-fluid-dynamics (EMFD)) are considered. For simple rate-dependent, memory-independent and isotropic fluids, any field variable Ψ , which must be defined by a constitutive relation, can be defined (Ko & Dulikravich 2000) as

$$\Psi = \Psi(\mathbf{d}, \hat{\mathbf{E}}, \mathbf{B}, \nabla T, T, \rho), \quad (2.5)$$

where $\mathbf{d} = \frac{1}{2}[\nabla\mathbf{u} + (\nabla\mathbf{u})^T]$ is the rate of deformation tensor, $\hat{\mathbf{E}} = \mathbf{E} + \mathbf{u} \times \mathbf{B}$ is the electromotive intensity, T is the temperature and ρ is the fluid density. For the above relation, the assumption of a material with purely instantaneous response has been also made. The constitutive equations for the polarization and electric conduction current are required in the following sections. For linear dielectric materials, the displacement vector is

$$\mathbf{D} = \varepsilon_0\mathbf{E} + \mathbf{P} = \varepsilon_0\mathbf{E} + \varepsilon_0\chi\mathbf{E} = \varepsilon\mathbf{E},$$

where χ is the dielectric susceptibility and ε is the permittivity of the material. For the electric conduction current, the following equation is used.

$$\mathbf{J}_c = \sigma\mathbf{E},$$

where σ is the conductivity of the material.

2.1.1 Slowly varying electric fields

The Maxwell's equations can be simplified for slowly varying fields. For such cases, the electromagnetic wave effects can be neglected because they propagate in a short time which is much smaller than the time of interest. This is called the quasistatic assumption. For the quasistatic assumption,

$$\tau \gg \tau_{EM}, \quad (2.6)$$

where τ is the time scale of interest. $\tau_{EM} = l_c\sqrt{\varepsilon_0\varepsilon_r\mu_0\mu_r} = \frac{l_c}{c}\sqrt{\varepsilon_r\mu_r}$ is the electromagnetic wave transmit time, where l_c is a characteristic length and c is the speed of light in free space. Also,

$$\begin{aligned} \tau_{EM} &= \sqrt{\tau_E\tau_M}, \\ \tau_E &= \frac{\varepsilon_0\varepsilon_r}{\sigma}, \\ \tau_M &= \mu_0\mu_r\sigma l_c^2, \end{aligned}$$

where τ_E is the characteristic time for electric phenomena, which is the ratio of the displacement current to the ohmic current. ε_r is the relative permittivity of the material. τ_M is the characteristic time for the magnetic phenomena, where μ_r is the relative permeability of the material.

We assume the slow processes

$$\tau_P \geq \tau_E \gg \tau_M, \quad (2.7)$$

for which the electro-quasistatic assumption is valid and the magnetic field can be ignored, see for example (Fröhliche 2013). τ_P is the time scale of transport processes such as the viscous relaxation, diffusion, oscillation of an imposed field or motion of a boundary. On the millimeter scale, the above assumption (2.7) applies if $\tau_E > 10^{-12}s$ (Saville 1997). For typical cases of $\sigma = 4 \times 10^{-6} \frac{S}{m}$ for demineralized water and $\sigma = 0.1 \frac{S}{m}$ for aqueous salt (NaCl) solution, see (Mugele & Baret 2005) and (Keim 2004), $\tau_E \sim 10^{-4}s$ and $\tau_M \sim 10^{-8}s$, respectively. Thus, for the case of water droplets, the assumption (2.7) is

fulfilled. In case of stationary or slowly moving electric charges or absence of a time varying magnetic field, the electric field is irrotational, $\nabla \times \mathbf{E} = 0$. Therefore, an electric potential Φ can be defined as $\mathbf{E} = -\nabla\Phi$ and the electric field equations are derived from the Maxwell's equations, by taking a divergence of equation (2.1b) as the following:

$$\nabla \cdot \mathbf{D} = \rho_f, \quad (2.8a)$$

$$\nabla \cdot \mathbf{J}_f + \nabla \cdot \partial_t \mathbf{D} = 0, \quad (\text{or } \nabla \cdot \mathbf{J} = 0) \quad (2.8b)$$

$$\mathbf{E} = -\nabla\Phi \quad (2.8c)$$

For linear dielectric materials, the dielectric displacement is equal to $\mathbf{D} = \varepsilon\mathbf{E}$. So the equations are further simplified to the so called electro-quasistatics equations,

$$\nabla \cdot (\varepsilon\mathbf{E}) = \rho_f, \quad (2.9a)$$

$$\nabla \cdot \mathbf{J}_f + \nabla \cdot \partial_t(\varepsilon\mathbf{E}) = 0, \quad (2.9b)$$

$$\mathbf{E} = -\nabla\Phi \quad (2.9c)$$

2.1.1.1 Equations for perfect dielectric materials

In general, dielectric materials have both the dielectric and conductive properties. If the conductive property of a material is negligible compared to its dielectric property, it can be modeled as a perfect dielectric. For a perfect dielectric material, both the free current density \mathbf{J}_f and the free charge volume density ρ_f are zero. Therefore, in the stationary limit, equations (2.9a) and (2.9b) reduce to $\nabla \cdot (\varepsilon\mathbf{E}) = 0$. Using equation (2.9c), we obtain the well-known electrostatics equation for the electric potential.

$$\nabla \cdot (\varepsilon\nabla\Phi) = 0 \quad (2.10)$$

2.1.1.2 Equations for the Leaky dielectric model

The Leaky dielectric model is proposed by Taylor in mid 1960s for poorly conducting liquids, (Taylor 1966) and (Melcher & Taylor 1969). Under the assumptions of this model, see (Saville 1997) and (Supeene et al. 2008), the free charge volume density ρ_f is ignored. Therefore, in the stationary limit, the electro-quasistatics equations (2.9a) and (2.9b) reduce to $\nabla \cdot \mathbf{J}_f = 0$. For leaky dielectric materials, the free current density \mathbf{J}_f is considered as $\mathbf{J}_c = \sigma\mathbf{E}$. Using equation (2.9c), we have the following equation to solve for the electric potential.

$$\nabla \cdot (\sigma\nabla\Phi) = 0 \quad (2.11)$$

2.2 The incompressible Navier-Stokes equations

The governing equations of the fluid flow are the Navier-Stokes equations for conservation of momentum and the continuity equation for conservation of mass. The Navier-Stokes and continuity equations are written here in the incompressible form as,

$$\nabla \cdot \mathbf{u} = 0, \quad (2.12)$$

$$\rho \left(\frac{\partial \mathbf{u}}{\partial t} + \mathbf{u} \cdot \nabla \mathbf{u} \right) = -\nabla p + \nabla \cdot (\mu \nabla \mathbf{u}) + \rho \mathbf{g} + \mathbf{f}_\Omega, \quad (2.13)$$

where p is the pressure and μ is the dynamic viscosity. \mathbf{g} is the gravitational body force and \mathbf{f}_Ω is an external body force exerted to the bulk of the fluid.

2.3 Forces exerted from the electric field to the fluid

Polarization occurs if an electric field penetrates into the bulk of a dielectric material. The polarization process gives rise to some dipoles (polarization or bound charges), shown in figure 2.1. The polarization process is accompanied by deformations and exchange

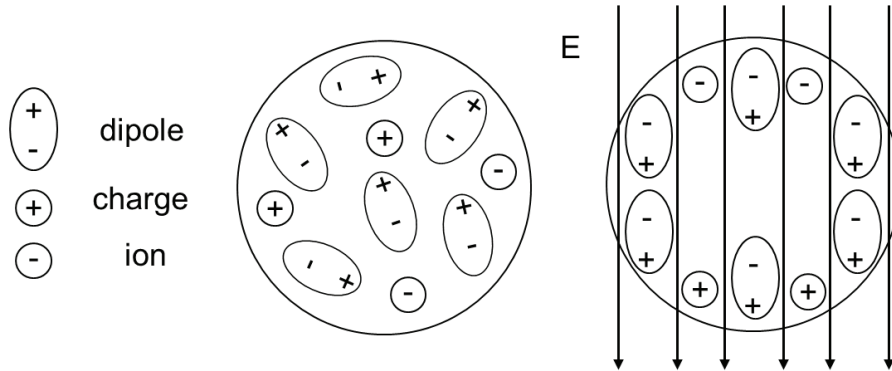


Figure 2.1: The Polarization process

of heat which are not generally negligible. The behavior of a fluid dielectric material is rather sensitive to temperature variations. If free charges (electrons and/or ions) exist in a dielectric material, it also has the conductive property. Otherwise it would be a perfect dielectric. The influence of an applied electric field on the bound and/or free charges results in mechanical forces. These forces (per unit volume), are the Kelvin body force and are instances of the body force f_Ω in the Navier-Stokes equations (2.13).

$$\mathbf{f}_\Omega^K = \rho_f \mathbf{E} + \mathbf{P} \cdot \nabla \mathbf{E} \quad (2.14)$$

The above formulation is general, irrespective of the constitutive relations linking the electric field and the polarization. One should note that, in the Navier-Stokes equations for a polarized fluid, the pressure p also depends on the polarization $p(\rho, T, \mathbf{P})$ (Bobbio 2000),

$$p = p_0 + \frac{1}{2} \mathbf{P} \cdot \mathbf{E} - \frac{1}{2} |\mathbf{E}|^2 \rho \frac{\partial \varepsilon}{\partial \rho}, \quad (2.15)$$

where $p_0(\rho, T)$ is the pressure of the unpolarized fluid. We prefer that the pressure p_0 appears in our formulations; therefore, we use the body force below instead of the Kelvin body force and from now on, by using p we mean p_0 , the pressure in the absence of the electric field.

$$\mathbf{f}_\Omega = \rho_f \mathbf{E} + \mathbf{P} \cdot \nabla \mathbf{E} - \frac{1}{2} \nabla (\mathbf{P} \cdot \mathbf{E}) + \frac{1}{2} \nabla \left(|\mathbf{E}|^2 \rho \frac{\partial \varepsilon}{\partial \rho} \right) \quad (2.16)$$

For a linear dielectric material, for which $\mathbf{D} = \varepsilon(\rho, T) \mathbf{E}$, the above body force simplifies to the Kortweg-Helmholtz body force (see (Bobbio 2000) and (Dulikravich & Lynn 1997))

$$\mathbf{f}_\Omega^H = \rho_f \mathbf{E} - \frac{1}{2} |\mathbf{E}|^2 \nabla \varepsilon + \frac{1}{2} \nabla \left[|\mathbf{E}|^2 \rho \frac{\partial \varepsilon}{\partial \rho} \right] \quad (2.17)$$

The first term in the Kortweg-Helmholtz body force is the electrophoretic or the Coulomb force acting on the free charges in an electric field. The second and third terms originate from the dielectric property of the material and are called dielectrophoretic and electrostriction forces, respectively. The dielectrophoretic or pondermotive force is present where there are high gradients of the permittivity. This is the case in high temperature gradient flows, multi-constituent flows, particulate flows or any time the electric field must pass through contacting media with different permittivities (Dulikravich & Lynn 1997). The third term, which is the electrostriction force, accounts for the deformations because of the polarization process. This term is usually smaller than the electrophoretic and dielectrophoretic forces but is present in flows with non-uniform electric field, high pressure gradient or compressible flows.

The Kortweg-Helmholtz body force can also be written as the divergence of Maxwell stress tensor (for linear dielectric materials),

$$\mathbf{T}^M = \varepsilon \mathbf{E} \mathbf{E} - \frac{1}{2} \varepsilon |\mathbf{E}|^2 \left[1 - \frac{\rho}{\varepsilon} \left(\frac{\partial \varepsilon}{\partial \rho} \right) \right] \mathbf{I}, \quad (2.18)$$

$$\mathbf{f}_\Omega^H = \nabla \cdot \mathbf{T}^M = \rho_f \mathbf{E} - \frac{1}{2} |\mathbf{E}|^2 \nabla \varepsilon + \frac{1}{2} \nabla \left[|\mathbf{E}|^2 \rho \frac{\partial \varepsilon}{\partial \rho} \right] \quad (2.19)$$

To derive the above relation, $\nabla \cdot (\varepsilon \mathbf{E}) = \rho_f$, equation (2.9a), is used.

3 Governing equations of the multiphase problem

In multiphase problems, two or more fluids are mutually separated from each other by common interfaces. There are basically two approaches for the numerical modeling of multiphase problems, which are the one-fluid and two-fluid approaches. In the one-fluid approach, there is one set of governing equations that is solved for the whole computational domain. In the two-fluid approach, a set of governing equations is solved for each fluid and there are some boundary conditions to be satisfied at the common interfaces. Considering our problem, we have adopted the one-fluid approach for two immiscible fluids, where there is no mass transfer across the interface.

3.1 Multiphase equations with the two-fluid approach

In this approach, two sets of the continuity, incompressible Navier-Stokes (2.13) and electric field equations for a perfect dielectric, equation (2.10), or a leaky dielectric material, equation (2.11), must be solved. At the interface between the two fluids, the following boundary conditions must be satisfied. In the following, $||g|| = g^2 - g^1$ is the jump of quantity g over the interface (Wang & Oberlack 2011).

Conservation of mass Mass must be conserved across the interface. This requires that $||\rho(\mathbf{w}^s - \mathbf{u}) \cdot \mathbf{n}|| = 0$, where \mathbf{w}^s is the speed of the moving interface. For material interfaces, where there is no mass transfer across the interface, this condition requires that the velocity component in the normal direction is continuous.

Conservation of momentum Momentum must be conserved across the interface. This condition leads to a force balance in the normal and tangential directions to the interface. Considering the momentum equation (2.13), pressure, surface tension and a component of the electric body force balance each other in the normal direction. The viscous shear stress is balanced with the component of the electric body force in the tangential direction.

$$|| -p\mathbf{n} + \mathbf{T}^D \cdot \mathbf{n} + \mathbf{T}^M \cdot \mathbf{n} || - \gamma\kappa\mathbf{n} = 0, \quad (3.1)$$

where $\mathbf{T}^D = \mu\nabla\mathbf{u}$ is the dynamic stress tensor and \mathbf{T}^M is the Maxwell stress tensor, which its divergence is the electric body force (see section 2.3). γ is the surface tension and κ is the curvature and \mathbf{n} is the normal vector to the interface.

Continuity of the tangential component of the velocity The condition $||u_t|| = 0$ is a widely accepted assumption according to the physical observations but cannot be proved from the conservation laws.

Continuity of the electric potential According to physical observations, the electric potential is continuous across the interface, $||\Phi|| = 0$.

Continuity of the tangential component of the electric field This condition $||E_t|| = 0$ can be found from the fourth equation of the Maxwell's equation (2.1d). The derivation is beyond the scope of this text.

Jump in the normal component of the displacement vector From the first equation in the Maxwell's equations (2.1a), one can find the jump in the normal component of the displacement vector that is equal to the free charge surface density $||D_n|| = \rho_f^s$. The above condition obviously shows that the normal component of the electric field E_n is discontinuous across the interface even in the case of an interface between two perfect dielectrics (where $\rho_f^s = 0$) $||\varepsilon E_n|| = 0$. If the free charge surface density is not zero and it is changing on the interface, one needs to solve an additional surface equation along the interface to find its distribution (Supeene et al. 2008). This is the case, if the convection/diffusion of the ions are taken into account or the time scale of the charge migration is important.

Continuity of the electric current Conservation of the electric current, equation (2.9b), results in its continuity in the normal direction across the interface $||J_n|| = 0$. In the case of an interface between two perfect dielectrics, this condition simplifies to $||\varepsilon E_n|| = 0$. In the case of an interface between two leaky dielectric liquids, $J = J_f$, therefore $||\sigma E_n|| = 0$. Considering both the perfect and dielectric materials, there is a jump in the normal component of the electric field.

One should choose an appropriate set of boundary conditions from the above conditions according to the model that is used for a specific problem.

3.2 Multiphase equations with the one-fluid approach

In the one fluid approach, one set of the governing equations is solved for the whole domain and the interface is represented implicitly as the zero iso-surface of a level set function ϕ .

$$\nabla \cdot \mathbf{u} = 0, \tag{3.2}$$

$$\rho(\phi)(\partial_t \mathbf{u} + \mathbf{u} \cdot \nabla \mathbf{u}) = -\nabla p + \nabla \cdot (\mu(\phi) \nabla \mathbf{u}) - \gamma \delta(\phi) \kappa \mathbf{n} + \rho \mathbf{g} - \frac{1}{2} |\mathbf{E}|^2 \nabla \varepsilon(\phi), \tag{3.3}$$

$$\nabla \cdot (\sigma(\phi) \nabla \Phi) + \nabla \cdot \partial_t (\varepsilon(\phi) \nabla \Phi) = 0, \tag{3.4}$$

$$\mathbf{E} = -\nabla \Phi, \tag{3.5}$$

$$\partial_t \phi + \mathbf{u} \cdot \nabla \phi = 0 \tag{3.6}$$

The advantage of the one-fluid approach is that no boundary conditions need to be satisfied at the interface.

In the one-fluid approach, the material properties are defined in the whole domain using a Heaviside function of the level set,

$$\begin{aligned} \rho(\phi) &= \rho_1 H(\phi) + \rho_2(1 - H(\phi)), \\ \mu(\phi) &= \mu_1 H(\phi) + \mu_2(1 - H(\phi)), \\ \sigma(\phi) &= \sigma_1 H(\phi) + \sigma_2(1 - H(\phi)), \\ \varepsilon(\phi) &= \varepsilon_1 H(\phi) + \varepsilon_2(1 - H(\phi)), \\ H(\phi) &= \begin{cases} 1 & \phi \geq 0 \\ 0 & \phi < 0 \end{cases}, \end{aligned}$$

and $\delta(\phi)$ is the Dirac delta function defined as the following,

$$\delta(\phi) = \begin{cases} +\infty & \phi = 0 \\ 0 & \phi \neq 0 \end{cases} \quad \text{and} \quad \int_{-\infty}^{+\infty} \delta(\phi) d\phi = 1$$

The gradients of the material properties are found using the gradient of the Heaviside function, $\nabla H = \delta(\phi)\nabla\phi$.

In the above Navier-Stokes equation (3.3), the surface tension force is included as a body force $-\gamma\delta(\phi)\kappa\mathbf{n}$ (see chapter 6). The body force exerted from the electric field is the dielectrophoretic force (see section 2.3). The electrophoretic force $\rho_f\mathbf{E}$ is not included because in both of the perfect dielectric and leaky dielectric models, the free charge volume density ρ_f is considered to be zero. The electrorstriction force is also ignored because it is usually small with respect to the electrophoretic and dielectrophoretic forces. The last equation above, equation (3.6), is a transport equation for the level set function.

3.3 Non-dimensional equations with the one-fluid approach

The characteristic variables, that are used to make the equations non-dimensional, are given in table 3.1. The characteristic pressure is derived by balancing gradient of the pressure and the electric force in the normal direction to the interface. Material properties of water in table 3.2 are used to find the characteristic variables.

Table 3.1: The characteristic variables for non-dimensionalizing the governing equations.

Symbol	Property	Value
l_c	Length	$\sqrt[3]{Vol}$
p_c	Pressure	$\varepsilon_c E_c^2$
u_c	Velocity	Problem dependent
τ_c	Time	$\frac{l_c}{u_c}$
ρ_c	Density	ρ_w
μ_c	Viscosity	μ_w
γ_c	Surface tension	Problem dependent
g	Gravitational acceleration	$9.806 \frac{m}{s^2}$
E_c	Electric field	E_∞
Φ_c	Electric potential	$l_c E_c$
ε_c	Permittivity	ε_0
σ_c	Conductivity	σ_w

Below there is a list of the non-dimensional variables to be substituted in the equations.

$$\begin{aligned}
 \mathbf{x}' &= \frac{\mathbf{x}}{l_c}, & \rho' &= \frac{\rho}{\rho_c}, & \mathbf{E}' &= \frac{\mathbf{E}}{E_c}, \\
 t' &= t \frac{u_c}{l_c}, & \mu' &= \frac{\mu}{\mu_c}, & \Phi' &= \frac{\Phi}{l_c E_c}, \\
 \mathbf{u}' &= \frac{\mathbf{u}}{u_c}, & \gamma' &= \frac{\gamma}{\gamma_c}, & \varepsilon' &= \frac{\varepsilon}{\varepsilon_c}, \\
 p' &= \frac{p}{p_c}, & \mathbf{g}' &= \frac{\mathbf{g}}{g}, & \sigma' &= \frac{\sigma}{\sigma_c}
 \end{aligned}$$

Table 3.2: Material properties of water at 25°C, (Keim 2004).

Symbol	Property	Unit (SI)	Value
ρ_w	Density	$\frac{Kg}{m^3}$	1000
μ_w	Dynamic viscosity	$\frac{Kg}{ms}$	0.001
γ_{w-a}	Surface tension	$\frac{N}{m} \left(\frac{Kg}{s^2} \right)$	0.072
ε_w	Permittivity	$\frac{C^2}{Nm^2} \left(\frac{A^2s^4}{Kgm^3} \right)$	$80\varepsilon_0$
σ_w	Conductivity	$\frac{S}{m} \left(\frac{A^2s^3}{Kgm^3} \right)$	6.0×10^{-6}
ε_0	Permittivity of vacuum	$\frac{C^2}{Nm^2} \left(\frac{A^2s^4}{Kgm^3} \right)$	$8.85418782 \times 10^{-12}$

The non-dimensional form of the governing equations is the following (note that ' is omitted).

$$\nabla \cdot \mathbf{u} = 0, \quad (3.7)$$

$$\begin{aligned} \rho(\phi)(\partial_t \mathbf{u} + \mathbf{u} \cdot \nabla \mathbf{u}) = & -Eu \nabla p + \frac{1}{Re} \nabla \cdot (\mu(\phi) \nabla \mathbf{u}) - \frac{1}{We} \gamma \delta(\phi) \kappa \mathbf{n} \\ & + \frac{1}{Fr^2} \rho(\phi) \mathbf{g} \\ & - Eu \left(\frac{1}{2} |\mathbf{E}|^2 \nabla \varepsilon(\phi) \right), \end{aligned} \quad (3.8)$$

$$\nabla \cdot (\sigma(\phi) \nabla \Phi) + \tau \nabla \cdot \partial_t (\varepsilon(\phi) \nabla \Phi) = 0, \quad (3.9)$$

$$\mathbf{E} = -\nabla \Phi, \quad (3.10)$$

$$\partial_t \phi + \mathbf{u} \cdot \nabla \phi = 0 \quad (3.11)$$

Followings are definitions of the non-dimensional Euler, Reynolds, Weber and Froude numbers that appear in the Navier-Stokes equations. A non-dimensional time scale τ appears in the electro-quasistatics equation which is the ratio of the electric time scale $\tau_E = \frac{\varepsilon_c}{\sigma_c}$ to the fluid time scale $\tau_c = \frac{u_c}{l_c}$.

$$\begin{aligned} Eu &= \frac{\varepsilon_c E_c^2}{\rho_c u_c^2}, \\ Re &= \frac{\rho_c u_c l_c}{\mu_c}, \\ We &= \frac{\rho_c u_c^2 l_c}{\gamma_c}, \\ Fr &= \frac{u_c}{\sqrt{g l_c}}, \\ \tau &= \frac{\varepsilon_c u_c}{\sigma_c l_c} \end{aligned}$$

The material properties are defined as in section 3.2 but using the non-dimensional variables.

$$\begin{aligned}
 \rho(\phi) &= \rho_1 H(\phi) + \rho_2 (1 - H(\phi)), \\
 \mu(\phi) &= \mu_1 H(\phi) + \mu_2 (1 - H(\phi)), \\
 \sigma(\phi) &= \sigma_1 H(\phi) + \sigma_2 (1 - H(\phi)), \\
 \varepsilon(\phi) &= \varepsilon_1 H(\phi) + \varepsilon_2 (1 - H(\phi)), \\
 H(\phi) &= \begin{cases} 1 & \phi \geq 0 \\ 0 & \phi < 0 \end{cases}
 \end{aligned}$$

3.3.1 Special cases

Considering equation (3.9) and remembering the governing equations of the electric problem that were simplified for perfect dielectric materials, the non-dimensional multiphase version of equation (2.10) is the following,

$$\nabla \cdot (\varepsilon(\phi) \nabla \Phi) = 0 \tag{3.12}$$

Referring to equation (2.11) for the leaky dielectric model, the multiphase version of the equation is the following,

$$\nabla \cdot (\sigma(\phi) \nabla \Phi) = 0 \tag{3.13}$$

The rest of the equations in the set of the governing equations (3.7) to (3.11), remain the same.

4 The discontinuous Galerkin Finite Element method

The discontinuous Galerkin Finite Element method (DG), like the Finite Element method (FEM), is based on a polynomial representation for the solution of the partial differential equations (PDEs). The DG method is higher order and the solution is defined locally in the computational cells. Higher order methods for solving the PDEs are known for achieving more accurate results with reduced computational costs. The locality of the solution in the DG method, makes this method ideal for an hp-adaption and parallel computing. Comparing to other numerical methods, the DG method has the local statement of the finite volume method (FVM), which makes the upwinding natural for the problems with shocks. In contrast, the finite difference method (FD), the Finite Integration Techniques (FIT) (Weiland 1977) and FEM are not well-suited for upwinding. The DG method has the geometric flexibility of FVM and FEM, considering the problems with curved boundaries, while FD and FI are not suitable for such problems. However, the DG method is not well-suited for the elliptic problems which is the same as with the FVM.

4.1 Basics of DG

For the spatial discretization using the DG method, the computational domain Ω with boundary $\partial\Omega$ is divided into J non overlapping cells, K_j . The global solution $u(\mathbf{x}, t)$ is approximated by the piecewise polynomial approximation $u^h(\mathbf{x}, t)$ of degree k , which is a direct collection of the J local polynomial solutions $u_j^h(\mathbf{x}, t)$,

$$u(\mathbf{x}, t) \simeq u^h(\mathbf{x}, t) = \bigoplus_{j=0}^{J-1} u_j^h(\mathbf{x}, t) \quad (4.1)$$

The local polynomial solution in cell K_j is represented by

$$u_j^h(\mathbf{x}, t) = \sum_{n=0}^{N_p-1} \hat{u}_{jn}(t) \phi_{jn}(\mathbf{x}) = \sum_{n=0}^{N_p-1} u_j^h(\mathbf{x}_{jn}, t) l_{jn}(\mathbf{x}), \quad (4.2)$$

where N_p is the number of basis polynomials per cell,

$$N_p = \frac{1}{D!} \prod_{1 \leq l \leq D} (k + l)$$

D is the spatial dimension. The first representation in equation (4.2) is called *modal* and the second one *nodal*. $\hat{u}_{jn}(t)$ in the modal representation and $u_j^h(\mathbf{x}_{jn}, t)$ in the nodal

representation are the *DG coordinates* for each cell K_j which change with time. In the nodal representation, the *lagrange* interpolating polynomials are used which have the cardinal property $l_n(\mathbf{x}_m) = \delta_{nm}$. In that case, the coefficients are in fact the solution at the interpolating points \mathbf{x}_{jn} . In the modal representation, the polynomials need to be orthogonal; here we use the orthonormal ones,

$$\int_{K_j} \phi_{jm}(\mathbf{x})\phi_{jn}(\mathbf{x})d\mathbf{x} = \delta_{mn},$$

where δ_{mn} is the Kronecker's delta,

$$\delta_{mn} = \begin{cases} 0 & m \neq n \\ 1 & m = n \end{cases}$$

To show how conservation laws are discretized using the DG method, a scalar instationary transport equation with flux \mathbf{f} and source term q is considered here as an example,

$$\partial_t u(\mathbf{x}, t) + \nabla \cdot \mathbf{f}(u(\mathbf{x}, t), \mathbf{x}, t) + q(u(\mathbf{x}, t), \mathbf{x}, t) = 0 \quad \mathbf{x} \in \Omega, \quad (4.3a)$$

$$u(\mathbf{x}, t) = g(\mathbf{x}, t) \quad \mathbf{x} \in \partial\Omega, \quad (4.3b)$$

$$u(\mathbf{x}, 0) = f(\mathbf{x}) \quad (4.3c)$$

In the first step, we form the local residual on each cell K_j and require this to vanish locally in a Galerkin sense by choosing the space of the test functions to be the same as the solution space. In this way, the residual is orthogonal to the test functions ψ ,

$$\begin{aligned} R_j^h(\mathbf{x}, t) &= \partial_t u_j^h + \nabla \cdot \mathbf{f}_j^h + q_j^h \quad \mathbf{x} \in K_j, \\ \int_{K_j} R_j^h(\mathbf{x}, t)\psi_{jm}(\mathbf{x})d\mathbf{x} &= 0 \quad 0 \leq m \leq N_p - 1 \end{aligned}$$

Then, we consider the above equation and use integration by parts to arrive at the following equation

$$\int_{K_j} [\partial_t u_j^h \psi_{jm} - \mathbf{f}_j^h \cdot \nabla \psi_{jm} + q_j^h \psi_{jm}]d\mathbf{x} + \oint_{\partial K_j} \hat{n} \cdot \mathbf{f}_j^h \psi_{jm} d\mathbf{x} = 0 \quad 0 \leq m \leq N_p - 1$$

The polynomial representation of the solution in domain Ω is piecewise continuous. Therefore, the solution is not unique at the boundaries of the cells. To calculate the above integral on ∂K_j , one should note that the physical flux function \mathbf{f}_j^h depends on the values of the variable u_j^h on both sides of the boundary. Therefore, the physical flux function \mathbf{f}_j^h is approximated by introducing a numerical flux function \mathbf{f}_j^* . This gives us the weak form of the DG method,

$$\int_{K_j} [\partial_t u_j^h \psi_{jm} - \mathbf{f}_j^h \cdot \nabla \psi_{jm} + q_j^h \psi_{jm}]d\mathbf{x} + \oint_{\partial K_j} \hat{n} \cdot \mathbf{f}_j^* \psi_{jm} d\mathbf{x} = 0 \quad 0 \leq m \leq N_p - 1, \quad (4.4)$$

where \hat{n} is the normal vector to each edge of cell K_j which points outward.

4.2 Solving a scalar conservation law in BoSSS

BoSSS code (Kummer 2012) uses the weak formulation of the DG method and a modal representation. Therefore, equation (4.4) is written here again as

$$\int_{K_j} \partial_t u_j^h \phi_{jm} d\mathbf{x} - \int_{K_j} [\mathbf{f}_j^h \cdot \nabla \phi_{jm} - q_j^h \phi_{jm}] d\mathbf{x} + \oint_{\partial K_j} \hat{n} \cdot \mathbf{f}_j^* \phi_{jm} d\mathbf{x} = 0 \quad (4.5)$$

$$0 \leq m \leq N_p - 1$$

The components of the above equation can be linear or nonlinear functions with respect to the variable u . This leads to different discretizations of the equation. Nonlinear terms should be linearized first. To accomplish this, the DG-coordinates of the variable u from the initial or previous time steps are used. The linear terms can be handled with both explicit or implicit time discretizations. If an implicit scheme is chosen, we arrive at a matrix formulation. For more detailed information on the BoSSS code, see also (Emamy 2010) and (Kummer 2012).

4.2.1 Physical and numerical flux functions

Referring to the weak formulation of a scalar conservation law, equation (4.5), \mathbf{f} and \mathbf{f}^* are the physical and numerical flux functions which both depend on the variable $u(\mathbf{x}, t)$, the spatial coordinates \mathbf{x} and time t . The choice of the numerical flux function $f^*(u_-^h, u_+^h)$ is very important. First of all, it should be consistent $f^*(u^h, u^h) = f(u^h)$. Another guideline is to require that the chosen flux reduces to a monotone scheme in the low order/finite volume limit. This is insured by requiring that $f^*(a, b)$ is nondecreasing in the first argument and non-increasing in the second one. There are verified fluxes with the above property defined in the classic finite volume literature. The Lax-Friedrich flux is perhaps the simplest numerical flux and often the most efficient flux, but generally not leading to the most accurate scheme. It includes, as special cases, the central and upwind fluxes. For a scalar linear problem, the Lax-Friedrich flux

$$f^{LF}(a, b) = \frac{a + b}{2} + \frac{C}{2} \hat{n}(a - b),$$

provides the central and upwind fluxes with $C = 0$ and $C = 1$, respectively.

4.2.1.1 Linear second order derivative terms

The linear 2nd order derivative term $\nabla^2 u$ can be written as $\nabla \cdot \boldsymbol{\sigma}$, where $\boldsymbol{\sigma} = \nabla u$ is an auxiliary variable. The following weak formulation is used for the discretization; see (Arnold, Brezzi, Cockburn & Marini 2002) and (Hartmann 2008).

$$\begin{aligned} \int_{K_j} \nabla \cdot \boldsymbol{\sigma}_j^h \phi_{jm} d\mathbf{x} &= - \int_{K_j} \nabla u_j^h \cdot \nabla \phi_{jm} d\mathbf{x} \\ &+ \int_{\partial K_j} \hat{n} \cdot \boldsymbol{\sigma}^* \phi_{jm} d\mathbf{x} - \int_{\partial K_j} (u^* - u_j^h) \hat{n} \cdot \nabla \phi_{jm} d\mathbf{x} \end{aligned} \quad (4.6)$$

$$0 \leq m \leq N_p - 1$$

The numerical fluxes for $\boldsymbol{\sigma}^* = \boldsymbol{\sigma}^*(u, \nabla u, \hat{n})$ and $u^* = u^*(u, \hat{n})$ for the symmetric interior penalty method (SIPG) are

$$\begin{aligned} u^* &= \{u\}, \\ \boldsymbol{\sigma}^* &= \{\nabla u\} - \mu_P [[u]], \end{aligned}$$

where $\{\cdot\}$ and $[[\cdot]]$ are the average and jump operators defined as

$$\{u\} = \frac{1}{2}(u^+ + u^-), \quad (4.7)$$

$$[[u]] = u^+ \hat{n}^+ + u^- \hat{n}^- = (u^- - u^+) \hat{n} \quad (4.8)$$

μ_P is a penalty parameter, which is necessary for stabilization. The penalty parameter is a positive constant and is used from (Shahbazi 2005) for the interior penalty method (IP),

$$\mu_P = \alpha_P c_i, \quad (4.9)$$

$$c_i = c_{K^-} \quad e_i \in \partial\Omega, \quad (4.10)$$

$$c_i = \max(c_{K^-}, c_{K^+}) \quad e_i \in \Gamma_I, \quad (4.11)$$

$$c_{K_j} = \frac{(k+1)(k+D)}{D} \frac{A(\partial K_j \setminus \partial\Omega)/2 + A(\partial K_j \cap \partial\Omega)}{V(K_j)}, \quad (4.12)$$

where α_P is a coefficient adjusted to a value equal or greater than 1 to assure the stability. ∂K_j is the boundary of cell K_j , and e_i specifies the edge i , which may be on the boundary of the computational domain $\partial\Omega$ or belong to the internal edges Γ_I . For each cell, the area is shown by A and the volume by V .

4.2.2 Time discretization

For the time discretization of the scalar conservation law (4.5), we choose the first order backward Euler scheme to discretize the temporal term $\int_{K_j} \partial_t u_j^h \phi_{jm} d\mathbf{x}$. We assume that the test functions and basis polynomials don't change with time.

$$\begin{aligned} \int_{K_j} \partial_t u_j^h \phi_{jm} d\mathbf{x} &\approx \int_{K_j} \frac{u_j^{h,(n+1)} - u_j^{h,(n)}}{\Delta t} \phi_{jm} d\mathbf{x} \quad 0 \leq m \leq N_p - 1 \\ &= \frac{1}{\Delta t} \int_{K_j} u_j^{h,(n+1)} \phi_{jm} d\mathbf{x} - \frac{1}{\Delta t} \int_{K_j} u_j^{h,(n)} \phi_{jm} d\mathbf{x} \\ &= \frac{1}{\Delta t} \int_{K_j} \hat{u}_{jn}^{h,(n+1)} \phi_{jn} \phi_{jm} d\mathbf{x} - \frac{1}{\Delta t} \int_{K_j} \hat{u}_{jn}^{h,(n)} \phi_{jn} \phi_{jm} d\mathbf{x} \end{aligned}$$

Considering a general case and demonstrating the result of the spatial discretization with matrix \mathbf{W} and the matrix of DG coordinates with \mathbf{U} , we can write the discretized equation as

$$\text{diag}\left(\frac{1}{\Delta t}, \dots, \frac{1}{\Delta t}\right) \mathbf{U}^{(n+1)} + \mathbf{W} = \text{diag}\left(\frac{1}{\Delta t}, \dots, \frac{1}{\Delta t}\right) \mathbf{U}^n \quad (4.13)$$

Using the explicit Euler scheme and multiplying equation (4.13) by Δt , we can find the DG coordinates for the next time step,

$$\mathbf{U}^{(n+1)} = \mathbf{U}^n - \mathbf{W}^{(n)} \Delta t \quad (4.14)$$

For an implicit scheme, the spatial discretization results in

$$\mathbf{W}^{(n+1)} = A \mathbf{U}^{(n+1)} + B$$

Therefore, using the implicit Euler scheme, the following system of equations must be solved,

$$\left(\text{diag}\left(\frac{1}{\Delta t}, \dots, \frac{1}{\Delta t}\right) + A\right) \mathbf{U}^{(n+1)} = \text{diag}\left(\frac{1}{\Delta t}, \dots, \frac{1}{\Delta t}\right) \mathbf{U}^n - B \quad (4.15)$$

The matrix A in equation (4.15) is a sparse matrix. For solving the above system of equations of the form $Mx = b$, we need linear solvers. For solving this system of equations, direct or iterative solvers may be used. There are some available solvers integrated and some programmed in BoSSS (Kummer 2012). We have used PARDISO, which is a direct solver, and the iterative CG solver from the HYPRE libraries.

5 The single-phase incompressible Navier-Stokes equations

5.1 Introduction

The incompressible Navier-Stokes equations are solved using the DG method. As mentioned before in chapter 4, the DG method is based on a polynomial representation for the solution and the solution is defined locally in the computational cells. The locality of the polynomials makes the DG method ideal for an hp-adaption and parallel computing; however, this locality makes the solution discontinuous at the cell boundaries.

Precautions must be taken when dealing with this discontinuity because it may cause a numerical instability or affect the solution accuracy. Our study shows that these instability or accuracy issues can be severe when coarse grids or low polynomial degrees are used because the discontinuity may be large. Of course, as the grid is refined or higher polynomial degrees are used, the inter-cell discontinuity becomes negligible at the cell boundaries. We have shown that the origin of the above mentioned problem lies in the calculation of the flow variables' derivatives from their local representation. One should note that, although the flow variables may be continuous, their local DG polynomial representations, which we call here *DG-fields*, are discontinuous. In this case, the analytical approach to calculate the derivatives inside each cell does not provide enough accuracy on the cell boundaries. Moreover, in the extreme case of using a zero order DG representation, derivatives are zero for the field variables and hence the analytical approach completely fails. We have adopted numerical fluxes in our computations to deal with the discontinuities at the cell boundaries, which we call the *flux/enhanced* computational option. More details are provided in section 5.4, which describes the computational options.

To solve the incompressible Navier-Stokes equations, the **Projection Consistent Pressure (NSE2-PCP)** solver is developed based on the *BoSSS* libraries ((Kummer, Emamy, Mousavi B. T. & Oberlack 2009)), which are a general framework for solving conservation laws using the DG method. The solver mentioned above, uses the projection scheme for time discretization. The projection scheme is a strategy to decouple the velocity and pressure to avoid solving a large system of equations (see, e.g., (Deville, Fischer & Mund 2002)). For a detailed comparison of the different types of projection schemes, see (E & Liu 1995) and (Guermond, Minev & Shen 2006). The projection scheme is known to produce a splitting error by splitting the equations into several steps. When both the Dirichlet boundary condition for the velocity in the intermediate steps and the homogeneous Neumann boundary condition for the pressure are used, the splitting error may be large in $O(\Delta t)$ for the velocity. To reduce the splitting error for the velocity, we have used the consistent Neumann pressure boundary condition that is derived from the Navier-Stokes equations and proposed by (Orszag, Israeli & Deville 1986) and

(Karniadakis, Israeli & Orszag 1991). Details of the projection scheme and the time integration of the equations with the stiffly stable scheme are described in section 5.2. We have noticed that, in addition to reducing the splitting error, applying the above-mentioned pressure boundary condition results in an optimal convergence rate $k + 1$ for the pressure in the L^2 -norm. Recently (Nguyen, Peraire & Cockburn 2011) proposed a hybridizable DG method for the incompressible Navier-Stokes equations that shows this optimal convergence rate. Within the DG methods, (Cockburn, Kanschat & Schötzau 2007) have used the LDG, and (Karakashian & Katsaounis 2006) and (Shahbazi, Fischer & Ethier 2007) have used the interior penalty (IP) method and have reported a k convergence rate for the pressure. The above results confirm that the theoretical convergence rate is k , which is derived for the Stokes equations in (Karakashian & Jureidini 1998) and (Cockburn, Kanschat, Schötzau & Schwab 2002) and for the Navier-Stokes equations in (Karakashian & Katsaounis 2000) and (Cockburn, Kanschat & Schötzau 2005). It is noted that, in these theoretical studies, no boundary condition is considered for the pressure. The mixed-order method is used in (Cockburn et al. 2007) and (Shahbazi et al. 2007), but in (Karakashian & Katsaounis 2006), the results for both the mixed-order and equal-order methods are provided. We have used the IP and the equal-order method (using the same polynomial degrees for the pressure and velocity), which is known to be more accurate than the mixed-order method (which uses one polynomial degree less for the pressure). The details of the spatial discretization with the DG method are presented in section 5.3.

Nearly the same approach, as is presently adopted, has recently been used by (Ferrer & Willden 2011) to solve the incompressible Navier-Stokes equations using the DG method. They have also observed similar stability problems but have related these stability problems to the time step size, which is the stabilizing factor in the projection scheme. Although we did not prove it, throughout our test cases we got the impression that the time step size is just an amplifying factor for the errors. The main reason, as discussed before, traces back to the discontinuity of the solution at the cell boundaries in the DG method; however, the projection scheme has previously been applied successfully within other frameworks, such as spectral element method (Karniadakis et al. 1991). We have shown enough evidence concerning this idea in section 5.5, the numerical results, by studying different types of flow and by considering the effect of other probable sources of error that may be specific to our methodology.

5.2 Methodology

The governing equations for the fluid flow are the conservation of mass and momentum, which are the continuity and Navier-Stokes equations written here in the incompressible and non-dimensional form

$$\nabla \cdot \mathbf{u} = 0, \tag{5.1}$$

$$\frac{\partial \mathbf{u}}{\partial t} + \mathbf{N}(\mathbf{u}) = -\nabla p + \frac{1}{Re} \mathbf{L}(\mathbf{u}), \tag{5.2}$$

where \mathbf{u} is the velocity vector, p is the pressure and Re is the Reynolds number. The nonlinear terms of the equations are the convective terms, and the linear terms are the diffusive viscous terms that take the form

$$\mathbf{L}(\mathbf{u}) = \nabla^2 \mathbf{u} = \left[\nabla(\nabla \cdot \mathbf{u}) - \nabla \times (\nabla \times \mathbf{u}) \right], \quad (5.3)$$

$$\mathbf{N}(\mathbf{u}) = \mathbf{u} \cdot \nabla \mathbf{u} = \nabla \cdot (\mathbf{u}\mathbf{u}) - \mathbf{u} \nabla \cdot \mathbf{u} \quad (5.4)$$

Using the incompressibility assumption, $\nabla \cdot \mathbf{u} = 0$, we will use the conservative form of the convective terms, $\mathbf{N}(\mathbf{u}) = \nabla \cdot (\mathbf{u}\mathbf{u})$, for the spatial discretization. Time integration of equations (5.2) is performed using the mixed (implicit/explicit) stiffly stable scheme used by (Karniadakis et al. 1991) for the incompressible Navier-Stokes equations. In this approach, which is applicable to multi-step methods, such as the projection scheme, each part can be integrated independently in an implicit or explicit manner to obtain

$$\frac{\gamma_0 \mathbf{u}^{n+1} - \sum_{k=0}^{J_i-1} \alpha_k \mathbf{u}^{n-k}}{\Delta t} = - \sum_{k=0}^{J_e-1} \beta_k \mathbf{N}(\mathbf{u}^{n-k}) - \nabla \bar{p}^{n+1} + \frac{1}{Re} \mathbf{L}(\mathbf{u}^{n+1}), \quad (5.5)$$

where $\nabla \bar{p}^{n+1}$ is an average pressure gradient when integrating from time step n to $n+1$ that is $\int_{t_n}^{t_{n+1}} \nabla p dt = \Delta t \nabla \bar{p}^{n+1}$. Coefficients α_k ($k = 0, \dots, J_i - 1$) are the standard coefficients of the implicit stiffly stable schemes (Gear 1971) corresponding to order J_i and $\gamma_0 = \sum_{k=0}^{J_i-1} \alpha_k$. The coefficients β_k ($k = 0, \dots, J_e - 1$) correspond to the explicit contributions of order J_e . The values of the α and the β coefficients for $J_e = J_i$ are $\{\alpha_0 = 1, \beta_0 = 1\}$ for the first order scheme and $\{\alpha_0 = 2, \alpha_1 = -\frac{1}{2}, \beta_0 = 2, \beta_1 = -1\}$ for the second order scheme. The stability of the implicit/explicit stiffly stable scheme is further studied by Hulsen, (Hulsen 1996). Applying the projection scheme, we perform the following three steps for the time integration of the Navier-Stokes equations instead of integrating equation (5.5) at once,

$$\frac{\gamma_0 \hat{\mathbf{u}} - \sum_{k=0}^{J_i-1} \alpha_k \mathbf{u}^{n-k}}{\Delta t} = - \sum_{k=0}^{J_e-1} \beta_k \mathbf{N}(\mathbf{u}^{n-k}), \quad (5.6a)$$

$$\gamma_0 \frac{\hat{\mathbf{u}} - \hat{\mathbf{u}}}{\Delta t} = - \nabla \bar{p}^{n+1}, \quad (5.6b)$$

$$\gamma_0 \frac{\mathbf{u}^{n+1} - \hat{\mathbf{u}}}{\Delta t} = \frac{1}{Re} \nabla^2 \mathbf{u}^{n+1} \quad (5.6c)$$

The projection scheme is performed by the time integration of the velocity field \mathbf{u} to find an intermediate velocity $\hat{\mathbf{u}}$ that does not necessarily fulfill the divergence-free constraint. Then, by solving the Poisson equation for the pressure, this intermediate velocity is projected to a divergence free field $\hat{\hat{\mathbf{u}}}$ in the second step. To accomplish this step, which

is found by integrating the pressure terms, we first take the divergence of equation (5.6b) and assume that $\nabla \cdot \hat{\mathbf{u}} = 0$. This gives us the Poisson equation (5.7a)

$$-\nabla^2 \bar{p}^{n+1} = -\frac{\gamma_0}{\Delta t} \nabla \cdot \hat{\mathbf{u}}, \quad (5.7a)$$

$$\frac{\partial \bar{p}^{n+1}}{\partial n} = \hat{n} \cdot \left[-\sum_{k=0}^{J_e-1} \beta_k \mathbf{N}(\mathbf{u}^{n-k}) - \frac{1}{Re} \sum_{k=0}^{J_e-1} \beta_k (\nabla \times \nabla \times \mathbf{u}^{n-k}) \right] \text{ at } \partial\Omega, \quad (5.7b)$$

$$\hat{\mathbf{u}} = \hat{\mathbf{u}} - \frac{\Delta t}{\gamma_0} \nabla \bar{p}^{n+1}, \quad (5.7c)$$

to be solved for the pressure. To solve this equation, we use the consistent Neumann pressure boundary condition, relation (5.7b), which is derived from the Navier-Stokes equations using the incompressibility assumption. This boundary condition, which is consistent with the Poisson equation (E & Liu 1995), is used at the inlet and wall boundaries where there are Dirichlet boundary conditions for the velocity (which do not vary with time). After solving the Poisson equation for the pressure and finding its gradient, we use relation (5.7c) to update the intermediate velocity $\hat{\mathbf{u}}$ to $\hat{\mathbf{u}}$, which is now divergence free. After making the velocity field divergence free, we can still superpose an additional pressure gradient that corresponds to a divergence-free flow field. This technique is used to impose a known pressure gradient to produce periodic flows. In this case, we use the following relation instead of relation (5.7c).

$$\hat{\mathbf{u}} = \hat{\mathbf{u}} - \frac{\Delta t}{\gamma_0} (\nabla \bar{p}^{n+1} + \nabla p_{\text{Periodic}}) \quad (5.8)$$

The third step of the projection scheme, equation (5.6c), is performed by solving the Helmholtz equation for the viscous terms using the implicit Euler scheme.

5.3 Spatial discretization

To discretize the convective part $\mathbf{N}(\mathbf{u}) = \nabla \cdot (\mathbf{u}\mathbf{u})$, we define its component in the d direction as $\nabla \cdot \mathbf{f} = \nabla \cdot (u_d \mathbf{u})$ and define the velocity as u_d in this direction. Then, we use integration by parts and Gauss's theorem to arrive at the following DG weak formulation,

$$\int_{K_j} \nabla \cdot \mathbf{f}_j^h \phi_{jm} d\mathbf{x} = \int_{\partial K_j} (\hat{n} \cdot \mathbf{f})^* \phi_{jm} d\mathbf{x} - \int_{K_j} \mathbf{f}_j^h \cdot \nabla \phi_{jm} d\mathbf{x} \quad 0 \leq m \leq N_p - 1$$

For the numerical flux (shown as $*$) we use the local Lax-Friedrich flux. The local Lax-Friedrich flux was employed before for the DG discretization of the nonlinear terms of the hyperbolic conservation laws (Cockburn & Shu 2001) and the Navier-Stokes equations (Shahbazi et al. 2007) as,

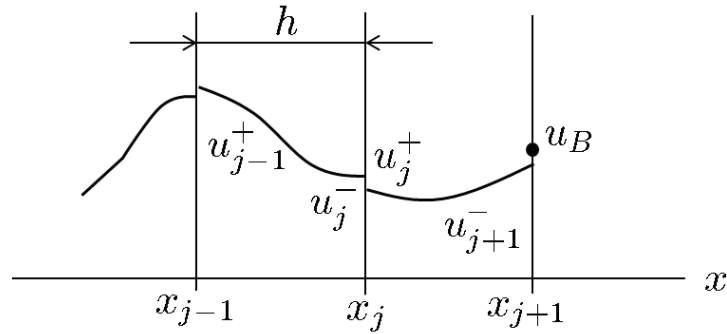
$$(\hat{n} \cdot \mathbf{f})^* = \hat{n} \cdot \mathbf{f}^* = \hat{n} \cdot \{\mathbf{f}\} + \hat{n} \cdot \frac{1}{2} \Lambda[[u_d]], \quad (5.9)$$

where $\{\cdot\}$ and $[[\cdot]]$ are the average and jump operators defined as

$$\{\mathbf{f}\} = \frac{1}{2}(\mathbf{f}^+ + \mathbf{f}^-),$$

$$[[u_d]] = u_d^+ \hat{n}^+ + u_d^- \hat{n}^- = (u_d^- - u_d^+) \hat{n},$$

$\Lambda = \max(\lambda^+, \lambda^-)$ and $\lambda^\pm = |\bar{\mathbf{u}}^\pm \cdot \hat{n}|$. $\bar{\mathbf{u}}$ is the cell-averaged velocity and λ^\pm are, in fact, the largest eigenvalues (in absolute values) of the Jacobian matrices $\frac{\partial}{\partial \mathbf{u}}(\mathbf{u}\mathbf{u} \cdot \hat{n}^+)|_{\bar{\mathbf{u}}^+}$ and $\frac{\partial}{\partial \mathbf{u}}(\mathbf{u}\mathbf{u} \cdot \hat{n}^-)|_{\bar{\mathbf{u}}^-}$. The boundary conditions are implemented using the direct method (figure 5.1), which is compatible with the hyperbolic nature of the convective terms. The



Direct method	$u_{j+1}^+ = u_B$
Mirror method	$\frac{u_{j+1}^- + u_{j+1}^+}{2} = u_B$

Figure 5.1: Implementation of the boundary conditions using the direct and mirror methods. u_B (shown by the point) is the specified value for the variable u at the boundary.

spatial discretization of both the diffusive viscous part, equation (5.6c), and the Poisson equation, (5.7a), involve linear 2nd order derivative terms. We use the weak formulation from (Arnold et al. 2002) that is described in section 4.2.1.1. The boundary conditions at the boundary edges are implemented using a mirror method (figure 5.1), which is compatible with the central type of discretization of the equations (5.6c) and (5.7a).

5.4 Computational options for the derivatives

In the second step of the projection scheme, we need to do computations to find the divergence of the velocity in equation (5.7a), the Neumann pressure boundary condition from the relation (5.7b) and the gradient of the pressure used in relation (5.7c). All of these computations involve the calculation of derivatives of the velocity or pressure. A usual analytical approach in the DG method, see, e.g., (Hesthaven 2008), is to calculate

derivatives of the basis polynomials ϕ used for representing a desired DG-field u^h . We call this approach the field-derivative option (FDO), which takes the form

$$\begin{aligned} \frac{\partial u_j^h(\mathbf{x}, t)}{\partial x_d} &= \sum_{n=0}^{N_p-1} \tilde{u}_{jn}(t) \frac{\partial \phi_{jn}(\mathbf{x})}{\partial x_d} = \sum_{m=0}^{N_{p-1}-1} \tilde{u}_{jm}(t) \phi_{jm}(\mathbf{x}), \\ \tilde{u}_{jm}(t) &= \sum_{n=0}^{N_p-1} \tilde{u}_{jn}(t) \int_{K_j} \frac{\partial \phi_{jn}(\mathbf{x})}{\partial x_d} \phi_{jm} d\mathbf{x} \quad 0 \leq m \leq N_{p-1} - 1 \end{aligned}$$

We use two other options: the flux and enhanced options. The flux option (FO) computes the derivative f of the DG-field u in the direction d globally by evaluating it directly from the equation $f - \frac{\partial u}{\partial x_d} = 0$. First, we rewrite the derivative in the divergence form to derive the DG weak formulation,

$$\begin{aligned} f &= \frac{\partial u}{\partial x_d}, \\ \int_{K_j} f_j^h \phi_{jm} d\mathbf{x} &= \int_{K_j} \frac{\partial u_j^h}{\partial x_d} \phi_{jm} d\mathbf{x} \\ &= \int_{K_j} \nabla \cdot (u_j^h \mathbf{e}_d) \phi_{jm} d\mathbf{x} \\ &= \int_{\partial K_j} \hat{n} \cdot (u_j^h \mathbf{e}_d)^* \phi_{jm} d\mathbf{x} - \int_{K_j} (u_j^h \mathbf{e}_d) \cdot \nabla \phi_{jm} d\mathbf{x} \\ & \quad 0 \leq m \leq N_{p-1} - 1 \end{aligned}$$

A central scheme is used to obtain the numerical flux. For the edges on the boundaries of the computational domain, we used values from inside the domain to compute the numerical flux. The third option, which is called the enhanced option (EO) is applicable when some Dirichlet boundary conditions exist in the computational domain. The difference between the EO and the FO is that, in the EO, the specified Dirichlet boundary conditions for the field u^h are used in the numerical flux at the boundary edges.

Subsequently, we compare the three options. The first option, FDO, calculates the derivatives locally. Therefore, because of the inter-cell discontinuities, we present that this option is not as accurate as the FO and EO. The second option, the FO, calculates the derivatives using flux functions that relate neighboring cells and hence reduces the error globally. Therefore, we may expect that this flux option is more accurate than the first option. The third option, EO, uses boundary conditions in addition to the FO. This creates a strong link to the known boundary values. The numerical results obtained by these three options are compared for stability, time and hp-convergence rates in the next section.

5.5 Numerical results

A total of six different flow fields are investigated. The first case is the laminar boundary layer flow on a flat plate, for which the velocity profile is compared with the Blasius data. The second test case is a fully developed channel flow, for which the splitting error of the projection scheme and the effect of the consistent Neumann pressure boundary condition in reducing this error are shown. Moreover, for this test case, the three computational options, FDO, FO and EO are compared with each other with respect to their stability characteristics. The third test case is the same fully developed channel flow but with periodic boundaries. Again, the stability characteristics are studied. As an instance of an unsteady problem, a Taylor vortex flow is simulated. For this test case, the time and hp-convergence studies are performed using the two computational options, FDO and FO. The possible effect of the penalty parameter is investigated. As an instance of the Stokes equations, an unsteady Stokes flow in a channel is considered and the time and h-convergence studies are performed. Here, the FDO and EO are selected. The effect of possible initial divergence in the velocity field is considered. The last test case is a steady channel flow with transpiration. For this test case, the effect of the computational options in a steady flow is studied with respect to the stability, accuracy and computational time. It should be mentioned that, in some of the above test cases, we had no Dirichlet pressure boundary conditions; therefore, it was necessary to set a reference pressure point in the computational domain.

5.5.1 Laminar boundary layer on a flat plate

As an instance of external flows, a laminar boundary layer flow on a flat plate is considered. The flat plate, which has a length of $L = 1$, is shown in figure 5.2. The flow is considered to have a Blasius velocity profile, see for example (Schlichting 1950), at the inlet, $x = 0$, where it enters the computational domain with a Reynolds number of 10000. A no-slip boundary condition is considered on the flat plate (considered as a wall). At the inlet and wall boundaries, the consistent Neumann boundary condition (5.7b) is considered for the pressure. Other boundaries of the domain are treated as outflow, except the upper right corner. For the outflow boundaries, homogenous Neumann boundary conditions are considered for the velocity and pressure. The upper right corner of domain is marked as pressure-outlet instead of setting a reference pressure point in the domain. At the pressure-outlet, a Dirichlet boundary condition, $p = 0$, is considered for the pressure and a homogenous Neumann boundary condition is considered for the velocity. The results of the simulation are compared to the Blasius data in figures 5.3 and 5.4. Figure 5.3 implies that the boundary layer grows in accordance to the boundary layer theory for the flat plate, $\delta \sim \sqrt{x}$, where δ is the thickness of the boundary layer. In figure 5.4, the velocity profile in x -direction is compared with the Blasius data at $x = 0.5$.

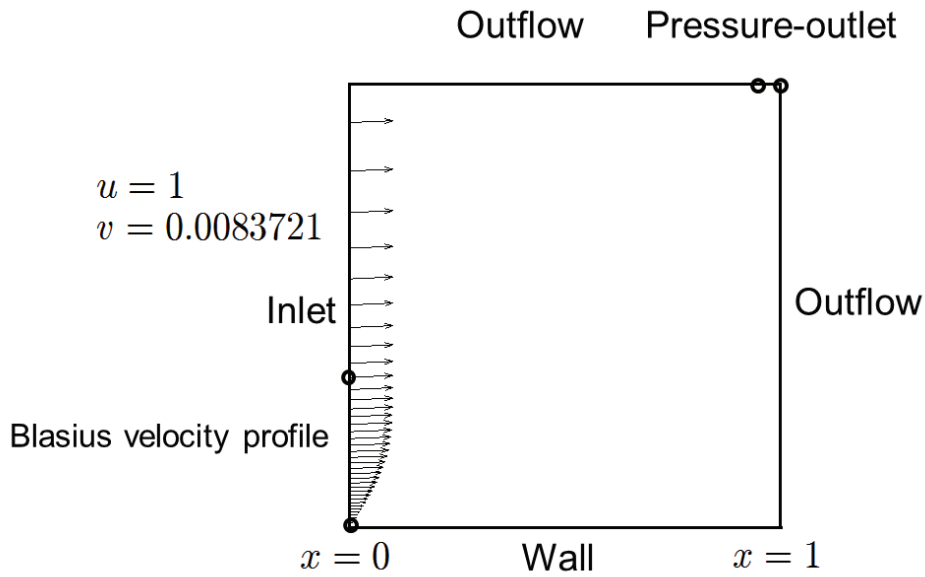


Figure 5.2: Computational domain and boundary conditions for the case of the laminar boundary layer flow on a flat plate. The flow enters the computational domain at $x = 0$ with a Blasius velocity profile corresponding to $Re = 10000$.

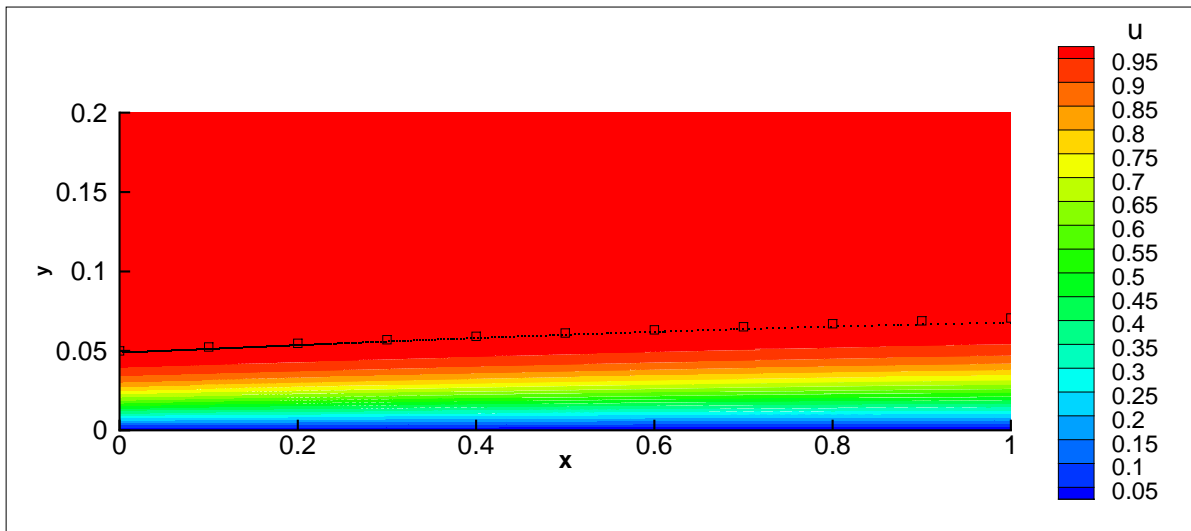


Figure 5.3: Growth of the laminar boundary layer thickness along a flat plate of length $L = 1$. The flow enters the computational domain at $x = 0$ with a Blasius velocity profile corresponding to $Re = 10000$. The — represents the edge of the boundary layer and \square represents the boundary layer thickness, which is taken from the Blasius data.

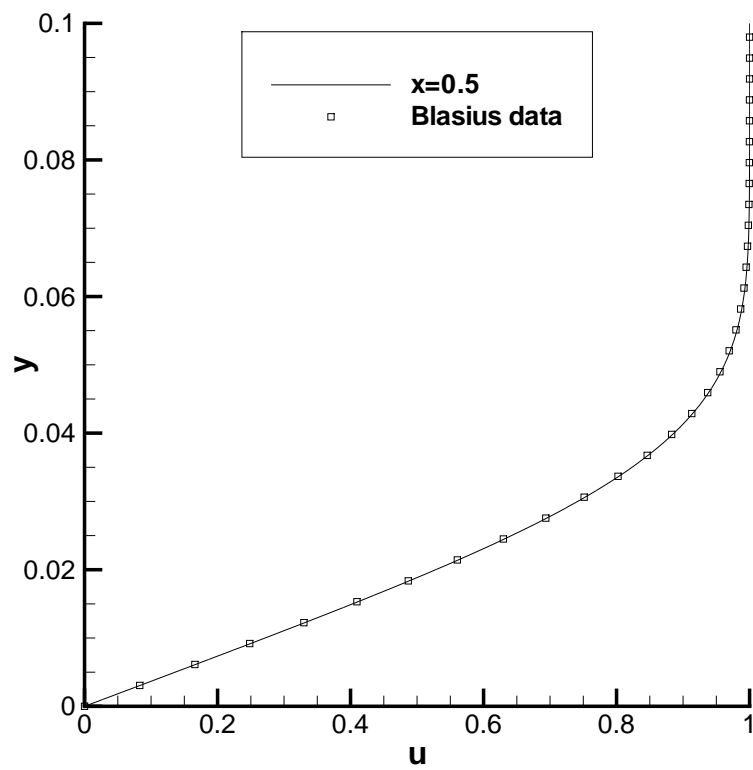
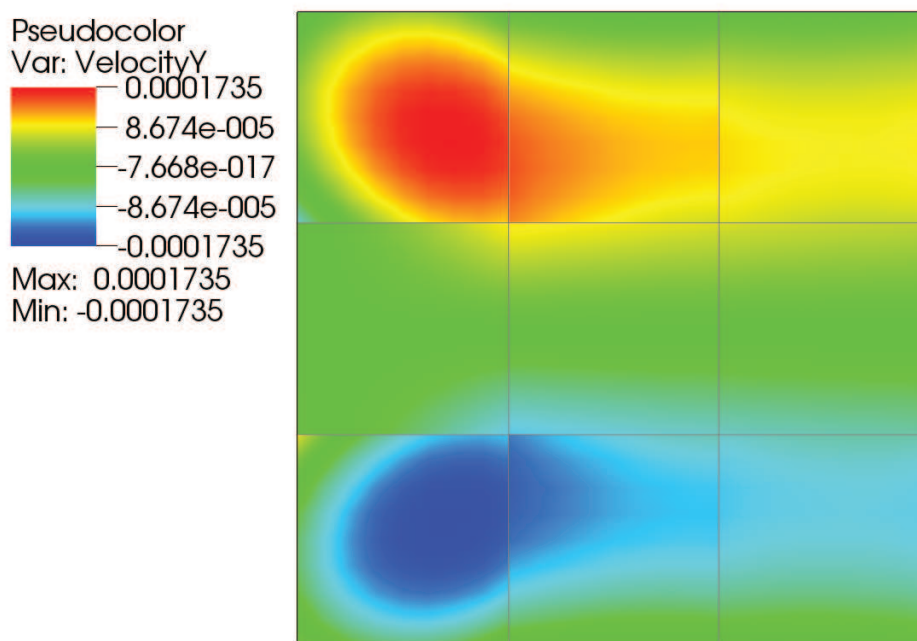


Figure 5.4: Velocity profile in x -direction at $x = 0.5$ for the case of the laminar boundary layer on a flat plate of length $L = 1$. The flow enters the computational domain at $x = 0$ with a Blasius velocity profile corresponding to $Re = 10000$.

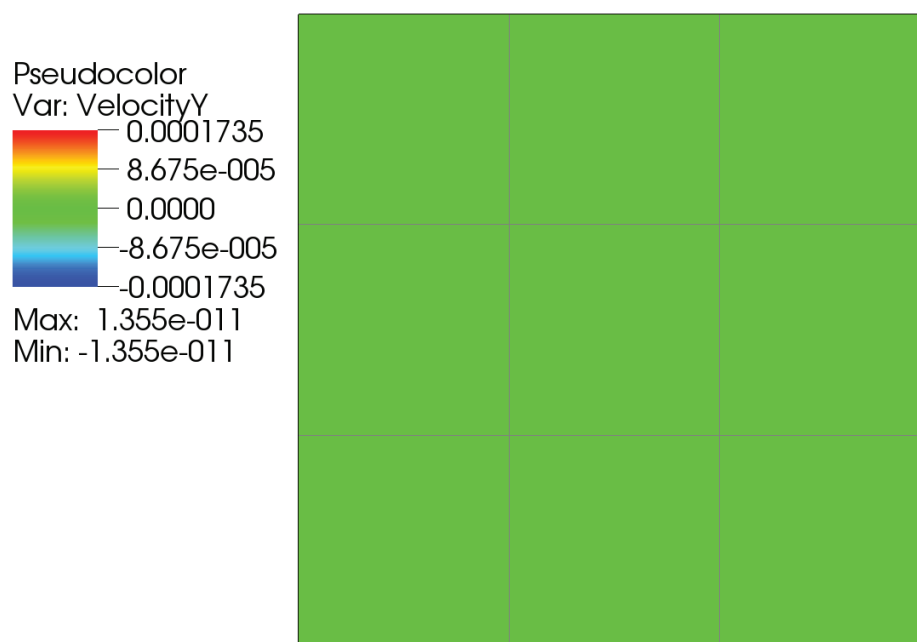
5.5.2 Fully developed channel flow

A 2D fully developed flow in a channel with a Reynolds number of 100 is considered. The computational domain is a $[-1, 1] \times [-1, 1]$ square. A parabolic velocity profile of $u = 1 - y^2$ is set at the inlet, $x = -1$. At the walls, $y = \pm 1$, a no-slip boundary condition is used for the velocity. At the outlet, $x = 1$, a Dirichlet pressure boundary condition of $p = 0$ and a homogenous Neumann boundary condition for the velocity, $\frac{\partial \mathbf{v}}{\partial n} = 0$, are applied. To show the splitting error related to the projection scheme, we have tested the homogenous Neumann boundary condition, $\frac{\partial p}{\partial n} = 0$, and the consistent Neumann boundary condition (5.7b) for the pressure at inlet and wall boundaries. For computing these boundary conditions, the FDO is used. The contours of the velocity in y -direction are shown in figure 5.5. A non-physically induced velocity in y -direction (known as the splitting error) is present in figure 5.5a by using the homogeneous Neumann boundary condition. This error is considerably reduced in figure 5.5b by using the consistent boundary condition. Therefore, from this point, all of the following numerical simulations are performed with the consistent Neumann pressure boundary condition (5.7b) at inlet and wall boundaries.

The long term stability characteristics of the solution using the three computational options, FDO, FO and EO are examined. The relative L^2 -norm residuals of the velocity in x -direction, $\frac{\|u^n - u^{n-1}\|_2}{\|u^2 - u^1\|_2}$, are shown in figure 5.6, where n is the number of pseudo-time steps. A Cartesian grid of 3×3 cells and four pseudo-time step sizes of 0.01, 0.005, 0.001, 0.0001 are used. Using the FDO, only the largest pseudo-time step size of 0.01 was stable. Using the FO, with the first two large pseudo-time step sizes, the solutions were long-term stable but the solutions were not stable with the smaller pseudo-time steps sizes of 0.001 and 0.0001. The EO provides stable solutions for all of the pseudo-time step sizes and does not show an evidence of error accumulation related to the time step size. This study shows the effect of the computational options in calculating the derivatives of the flow variables.

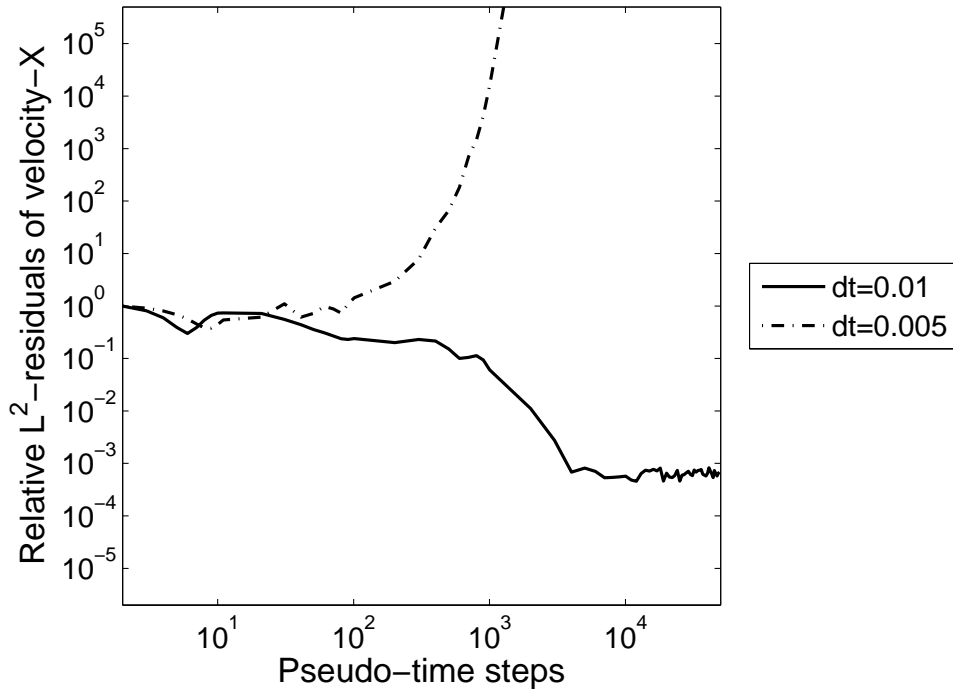


(a) Splitting error

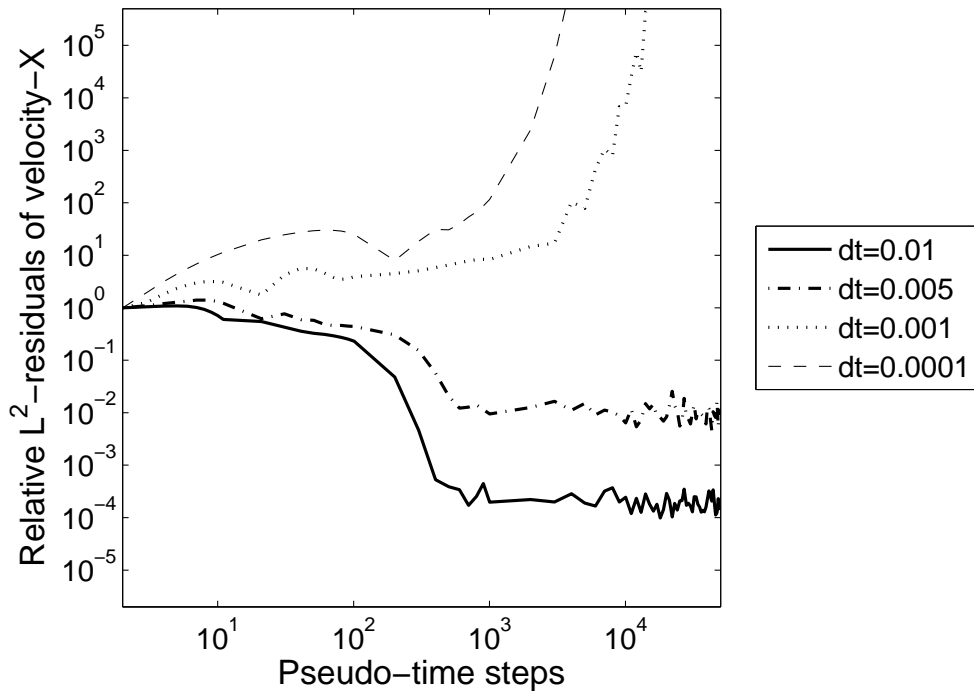


(b) Reduced splitting error

Figure 5.5: Contours of the velocity in y -direction for the case of the fully developed channel flow with $Re = 100$. The computational domain is a $[-1, 1] \times [-1, 1]$ square. (a) Non-physically induced velocity which is a result of the splitting error of the projection scheme. The homogenous Neumann pressure boundary condition is used at the inlet and walls. (b) Reduction of the non-physical velocity because of the reduction in the splitting error of the projection scheme by using a consistent Neumann pressure boundary condition at inlet and walls.

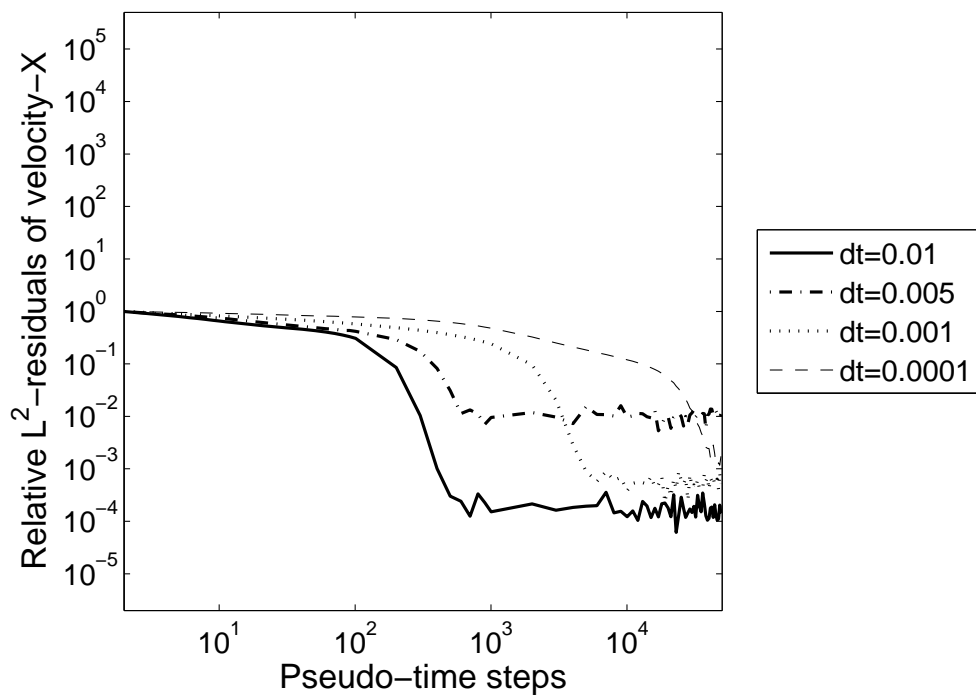


(a) Field-derivative



(b) Flux

Figure 5.6: Long term stability study for the case of the fully developed channel flow with $Re = 100$ using the field-derivative, flux and enhanced computational options. A grid of 3×3 cells is used (to be continued on the next page).

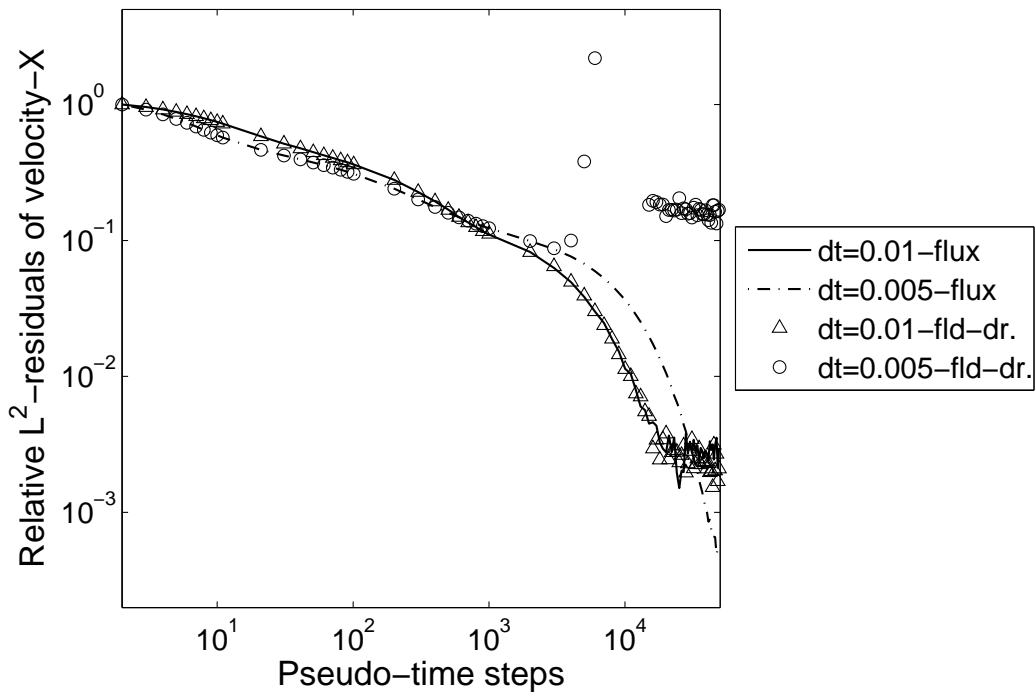


(c) Enhanced

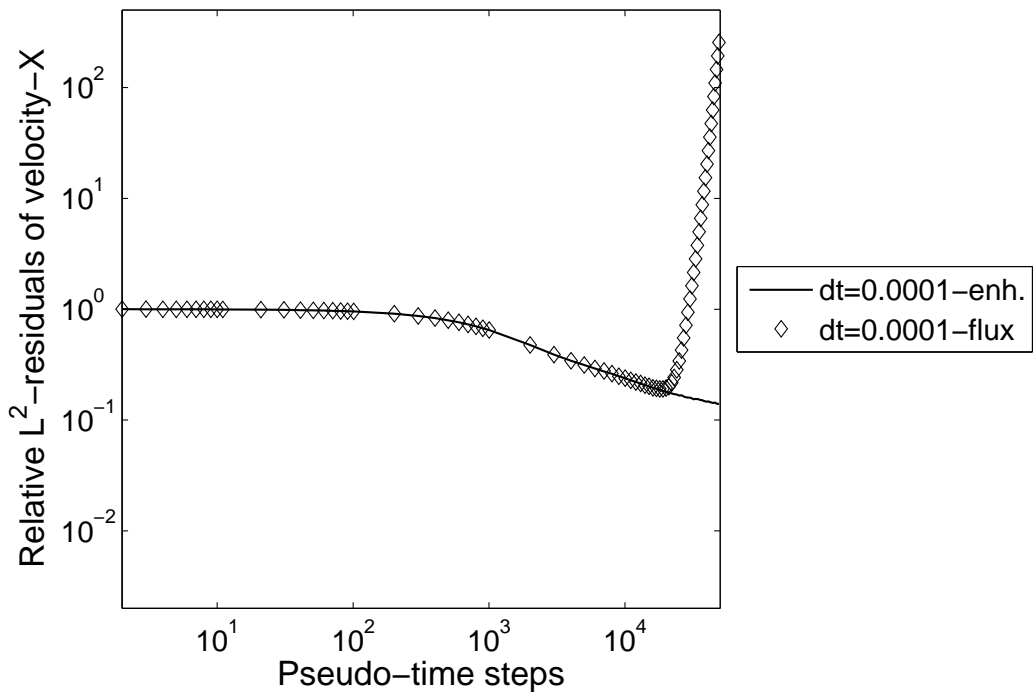
Figure 5.6: Continued.

5.5.3 Fully developed channel flow with periodic boundaries

A 2D fully developed flow in a channel with a Reynolds number of 100 is considered. The computational domain is a $[-1, 1] \times [-1, 1]$ square. The flow is periodic in the streamwise (x -) direction. A parabolic velocity profile, $u = 1 - y^2$, is set as the initial data. A periodic pressure gradient of $(-0.02, 0)$ is imposed on the flow field, see section 5.2. At the walls, $y = \pm 1$, a no-slip boundary condition is used for the velocity and the consistent Neumann pressure boundary condition, relation (5.7b), is applied for the pressure. Figure 5.7 shows the relative L^2 -norm residuals of the velocity in x -direction, $\frac{\|u^n - u^{n-1}\|_2}{\|u^2 - u^1\|_2}$, where n is the number of pseudo-time steps. The FDO and FO with two different pseudo-time step sizes of 0.01 and 0.005 are used. The grid is Cartesian and the number of cells in each direction is $N = 8$. Although both cases are stable for the larger pseudo-time step size of 0.01, for the smaller pseudo-time step size of 0.005, the FDO is not stable in the long term. Referring to the projection scheme, when computing the divergence of the intermediate velocity $\nabla \cdot \hat{\mathbf{u}}$ in equation (5.7a), it is obvious that $\frac{1}{\Delta t}$ is an amplifying factor for the corresponding errors. The same approach is selected to compare the FO and EO. Here we could use a much coarser grid with $N = 3$ and a very small pseudo-time step size of 0.0001. The EO is stable in the long term and shows the effect of using the existing Dirichlet boundary values of the velocity in calculating the above-mentioned divergence and the boundary condition (5.7b), which involve the derivatives of the velocity.



(a)



(b)

Figure 5.7: Long term stability study for the case of the periodic channel flow with $Re = 100$. (a) The field-derivative and flux computational options are compared with each other with respect to the size of the pseudo-time step. A grid of 8×8 cells is used. (b) The flux and enhanced computational options are compared with each other. A small pseudo-time step size of $dt = 0.0001$ and a coarse grid of 3×3 cells are used.

5.5.4 Unsteady Taylor vortex flow

The unsteady Taylor vortex is a $2D$ decaying flow, which is periodic in both x - and y -directions. The initial conditions for the velocity and pressure at $t = 0$ are found from the analytical solution below,

$$\mathbf{u} = (-\cos(\pi x) \sin(\pi y)\mathbf{i} + \sin(\pi x) \cos(\pi y)\mathbf{j}) \exp\left(\frac{-2\pi^2 t}{Re}\right),$$

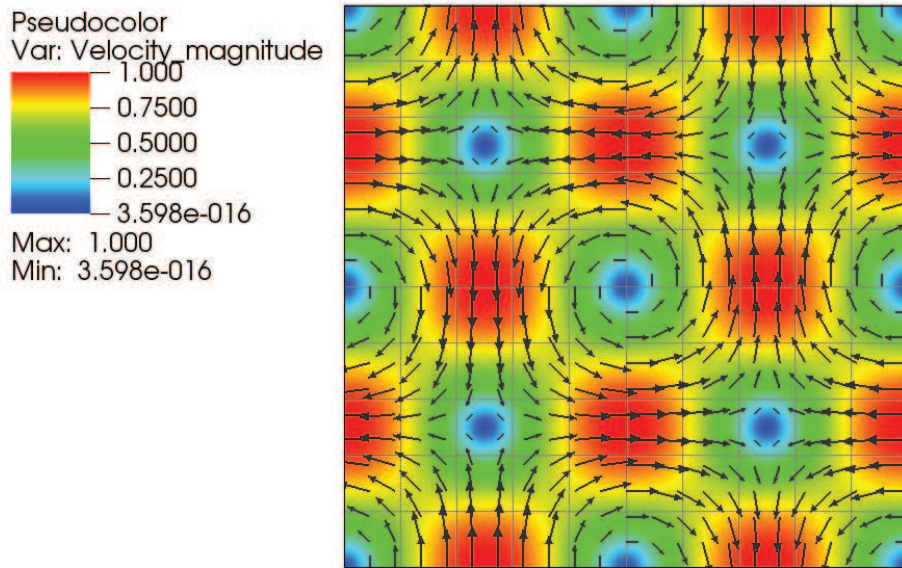
$$p = -\frac{\cos(2\pi x) + \cos(2\pi y)}{4} \exp\left(\frac{-4\pi^2 t}{Re}\right),$$

where $\mathbf{i} = (1, 0)$ and $\mathbf{j} = (0, 1)$. The computational domain is a $[-1, 1] \times [-1, 1]$ square. The Reynolds number is $Re = 100$. The simulations are performed until time $t = 5$ when the velocity field has decayed to approximately one-third of its initial amplitude, see figure 5.8. For the numerical simulation, a grid of 10×10 cells and a polynomial degree of 8 are employed.

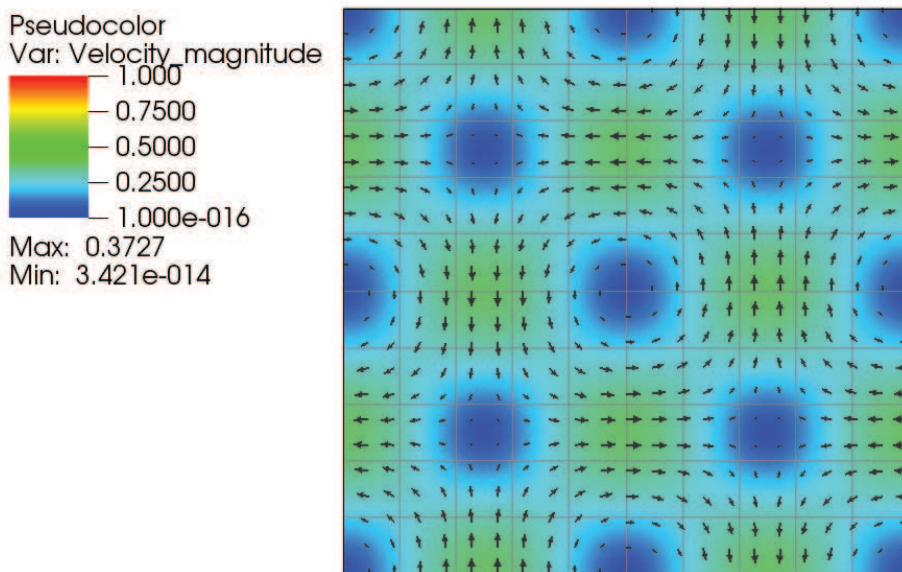
5.5.4.1 Time convergence study

To show the time convergence rate of the solution, the polynomial degree of $k = 8$ and a 10×10 Cartesian equidistant grid are selected. The applied time integration scheme is the second order (implicit/explicit) stiffly stable scheme (see 5.2). The temporal convergence rates are computed from figure 5.9 to give a fitted value of 1.98 for the velocity and 1.95 for the pressure, which are close to the analytical values. In this figure, the relative L^2 -norm errors of the velocity and pressure for other polynomial degrees are also shown. The errors are computed with respect to the analytical solution and are defined as $\frac{\|\mathbf{u}^h(t^n) - \mathbf{u}^h(n\Delta t)\|_2}{\|\mathbf{u}^h(n\Delta t)\|_2}$ for the velocity and computed in the same manner for the pressure. At certain points, the time discretization errors are dominated by the spatial errors; therefore, the (total) errors cannot be reduced further by decreasing the time step size. As an estimate, one can find the points, where the spatial errors become dominant, from the relation $err \sim O(\Delta t^2) \sim O(h^{k+1})$, where h is the element size and k is the polynomial degree. By further decreasing the size of the time step, small growths in the pressure error are observed. These growths in the errors are due to the effect of the time step size in the projection scheme, which has been discussed before. These error growths in the pressure, does not seem to affect the velocity field and figure 5.9 does not show that the projection scheme is becoming unstable due to the reduced time step size. However, we have studied the effect of the penalty parameter and our computational options on this error growth. The results mentioned above were achieved with a penalty parameter coefficient $\alpha_P = 1.0$ and with the FO. To study the effect of the penalty parameter on the solution accuracy and stability, three cases from figure 5.9 with polynomial degrees 2, 3 and 5 are repeated by changing the penalty parameter coefficient α_P . The results are shown in figure 5.10, which do not show any significant effect of α_P on the solution. Therefore, having $\alpha_P = 1.0$ appears to be appropriate for problems with equidistant Cartesian grids. In the following test cases, where not mentioned explicitly, the $\alpha_P = 1$ is used. The comparison between the FO and FDO for the solution accuracy

and stability is performed by choosing two cases with polynomial degrees 5 and 8. The relative L^2 -norm errors for the velocity and pressure are shown in figure 5.11. The computational option demonstrates an impact on both the solution accuracy as well as the stability. The FDO is not stable for some large time steps nor for very small ones; and for the intermediate time step sizes, the solution is not accurate enough. Impact of the computational option is less obvious for a polynomial degree of 8 rather than 5 because the solution discontinuity becomes negligible on the cell boundaries, when a higher polynomial degree is used and the error accumulation does not become severe. Referring to (Ferrer & Willden 2011), who reported that the projection scheme becomes unstable by reducing the time step size, it is not the projecting scheme that becomes unstable, but of course, it is the error accumulation. Therefore, one should be aware that the discontinuity of the polynomials and, accordingly, the solution at the cell boundaries can be a source of additional numerical errors.

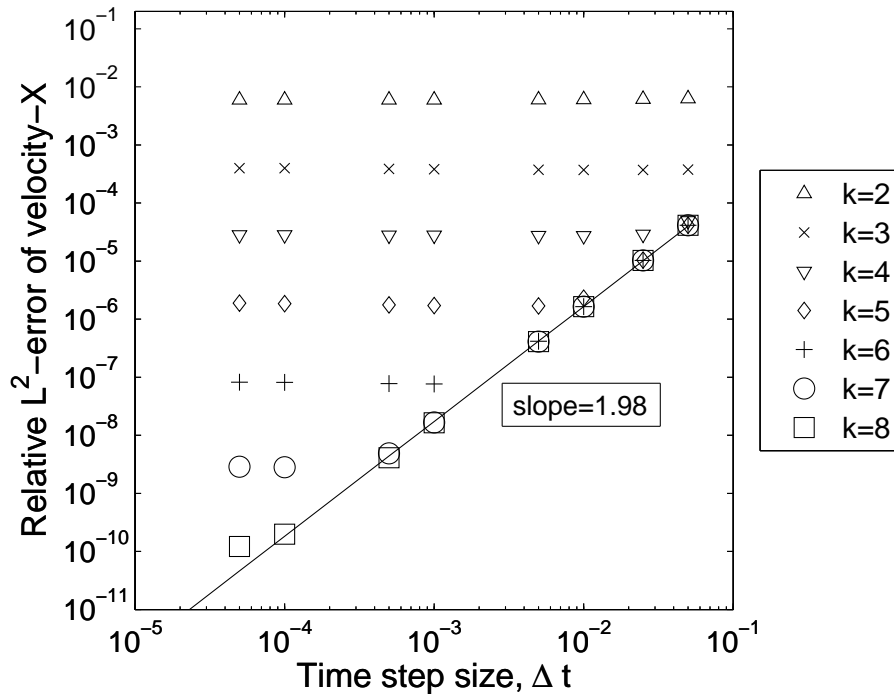


(a) $t = 0$

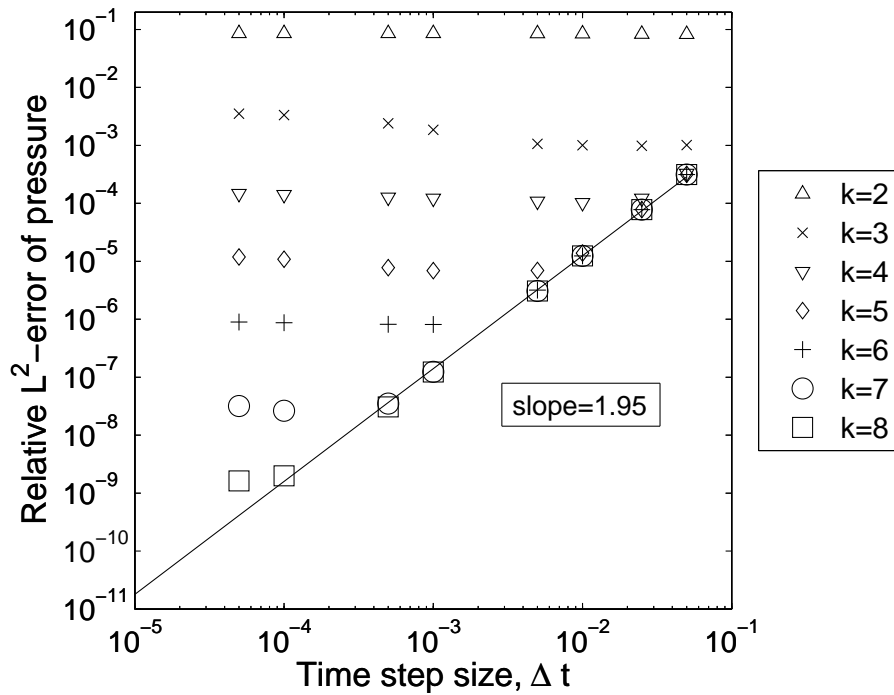


(b) $t = 5$

Figure 5.8: Contours of the velocity magnitude and vectors of the velocity for the case of the unsteady Taylor vortex flow with $Re = 100$. The computational domain is a $[-1, 1] \times [-1, 1]$ square. A grid of 10×10 cells and a polynomial degree of 8 are employed. (a) The initial velocity magnitude. (b) Reduction of the velocity magnitude three-fold from its initial value.



(a)



(b)

Figure 5.9: Time convergence study for the case of the unsteady Taylor vortex flow with $Re = 100$. The flux computational option and a penalty parameter coefficient of $\alpha_P = 1$ are used. A grid of 10×10 cells is employed. Relative L^2 -norm errors of the velocity in x -direction (a) and pressure (b) are shown.

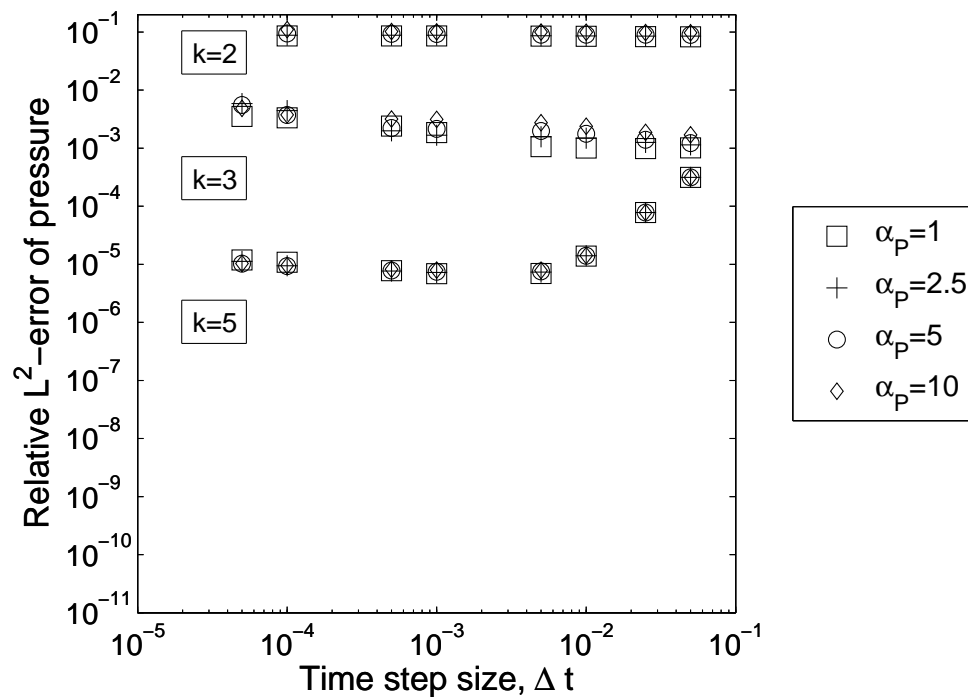
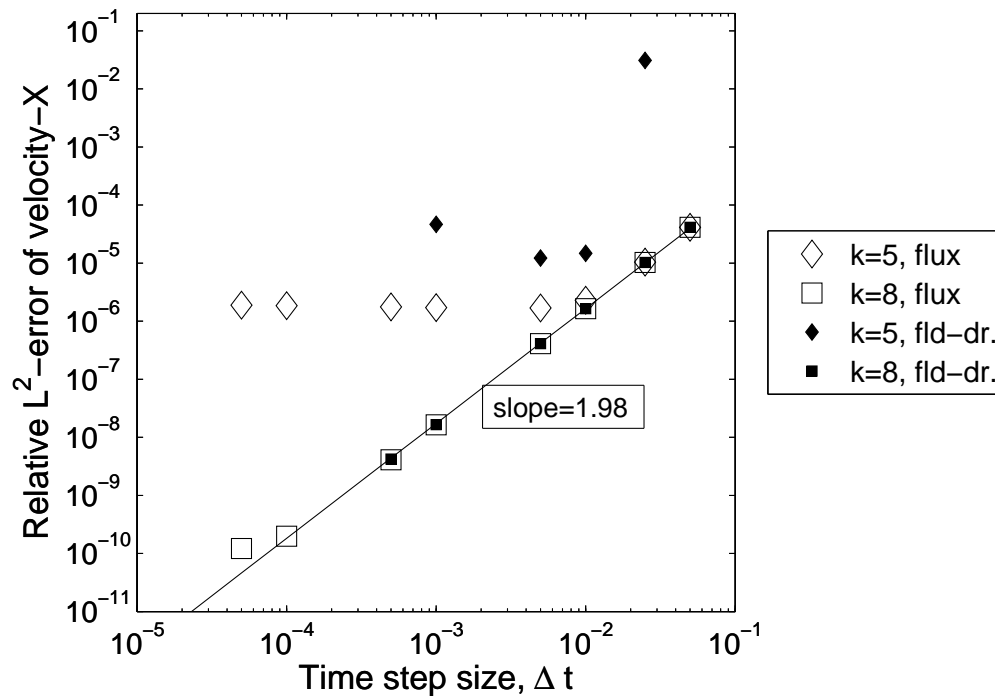
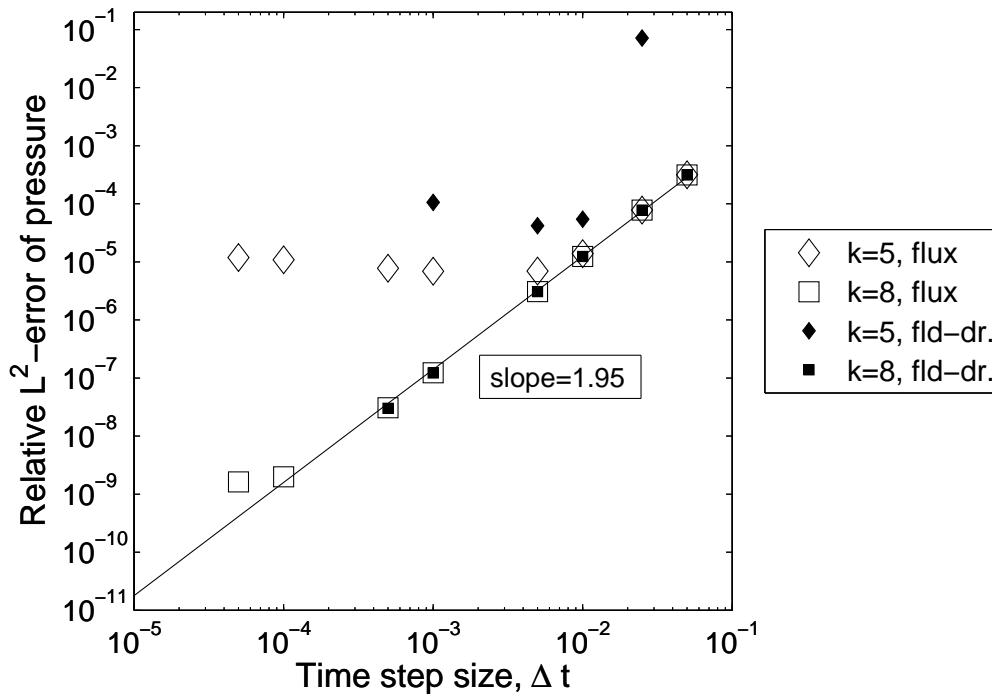


Figure 5.10: Effect of the penalty parameter coefficient, α_P , on the relative L^2 -norm errors of the pressure for the case of the unsteady Taylor vortex flow with $Re = 100$. A grid of 10×10 cells and polynomial degrees of 2, 3 and 5 are employed. Data for $\alpha_P = 1$ are taken from figure 5.9.



(a)



(b)

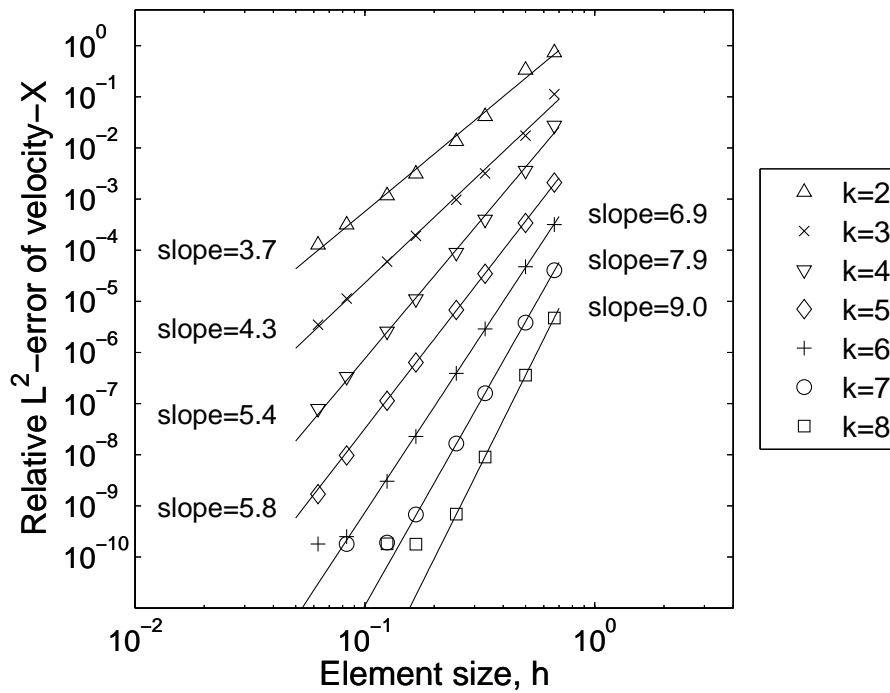
Figure 5.11: Effect of the flux and field-derivative computational options on the time convergence of the solution for the case of the unsteady Taylor vortex flow with $Re = 100$. A grid of 10×10 cells and polynomial degrees of 5 and 8 are employed. Data for the flux computational option are taken from figure 5.9. Relative L^2 -norm errors of the velocity in x -direction (a) and pressure (b) are shown.

5.5.4.2 hp-convergence study

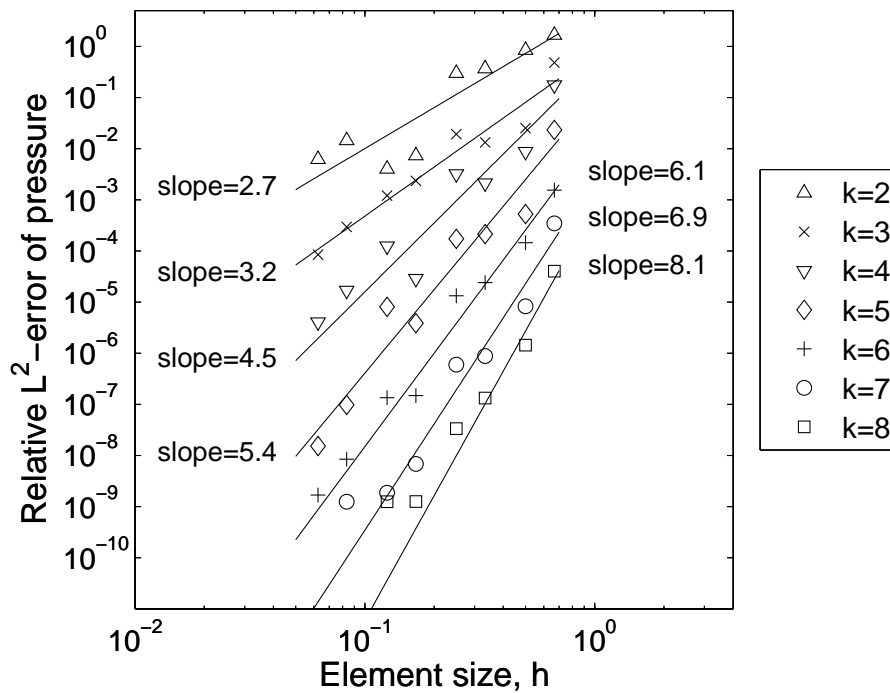
For polynomial degrees of 2 to 8, the grid refinement is performed by increasing the number of cells ($N \times N$), choosing $N = 3, 4, 6, 8, 12, 16, 24$ and 32. The time step size is chosen to be $\Delta t = 0.0001$. The penalty parameter coefficient is 1.0 and the FO is chosen. The relative L^2 -norm errors of the velocity and pressure are shown in figure 5.12. The optimal error of $O(h^{k+1})$ is achieved for the velocity. The convergence rate for the polynomial degree $k = 5$ is 5.8, which is a bit less than expected. This convergence rate is because of the slight error growth (discussed in figure 5.9) when using $\Delta t = 0.0001$, which is much smaller than what is required. We tested this by choosing another time step size, $\Delta t = 0.002$, which resulted in a convergence rate of 5.9 (not shown).

The error for the pressure is on the order of $O(h^k)$, which is not optimal. In this test case, we did not have any boundary conditions for the pressure because the flow is periodic in both directions. Regarding the discussions in section 5.1, we observe that this convergence rate is close to the theoretical values. Also, inserting a reference pressure point in the computational domain produced some error in the pressure field, which is not the same for different grids. This is why all of the points do not lie on the error curve fit line. We will show that this discrepancy can be corrected in the next test case, the Stokes flow, by having the consistent Neumann pressure boundary condition at the walls.

The same test case, the unsteady Taylor vortex flow, was studied by (Shahbazi et al. 2007), but they used Dirichlet boundary conditions for the velocity and pressure that were derived from the analytical solution. Their results show that an error of $O(h^k)$ for the pressure is only achieved when they used the mixed-order method. Here, we obtained the same convergence rate without the need to use the mixed-order method. For the p-convergence study we chose a grid of 6×6 cells and a time step size of 0.0001, which is the same as in the h-convergence study. The maximum errors (L_∞ -norms) and the L^2 -norm errors of the velocity and pressure are shown in figure 5.13. The plot shows the expected exponential decrease in the errors based on the polynomial degree.



(a)



(b)

Figure 5.12: h -convergence study for the case of the unsteady Taylor vortex flow with $Re = 100$. Relative L^2 -norm errors of the velocity in x -direction (a) and pressure (b) are shown.

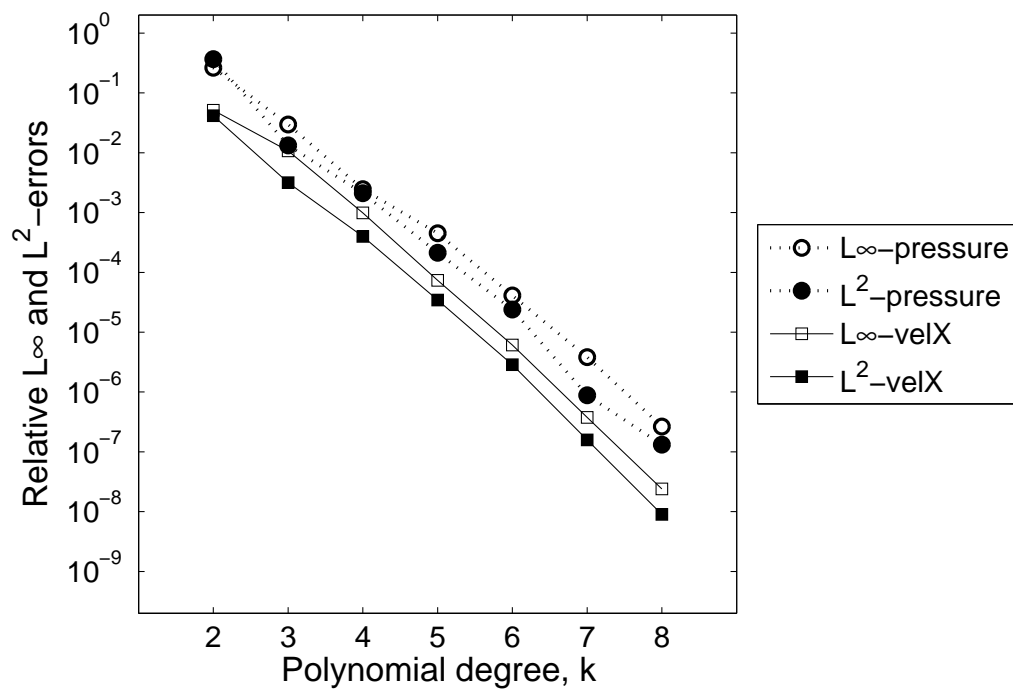


Figure 5.13: p-convergence study for the case of the unsteady Taylor vortex flow with $Re = 100$. A grid of 6×6 cells is used.

5.5.5 Stokes channel flow

The Stokes channel flow is periodic in the streamwise (x -) direction and there are walls in y -direction. It is an unsteady flow which decays with time. The computational domain is a $[-\pi, \pi] \times [-1, 1]$ rectangle, for which the analytical solution is as follows, see (Karniadakis et al. 1991), (Maday, Patera & Rønquist 1990) and (Deville & Montigny-Rannou 1984),

$$\begin{aligned} u &= [k \cos(\lambda) \sinh(ky) + \lambda \cosh(k) \sin(\lambda y)] \sin(kx) \exp(-\sigma t), \\ v &= k [-\cos(\lambda) \cosh(ky) + \cosh(k) \cos(\lambda y)] \cos(kx) \exp(-\sigma t), \\ p &= -\frac{\sigma}{Re} \cos(\lambda) \sinh(ky) \cos(kx) \exp(-\sigma t), \end{aligned}$$

where the streamwise wave number k is 1, which corresponds to a periodic length of $L = 2\pi$. The Reynolds number is also equal to 1. The decay rate σ is 9.3137399 and $\lambda = (\sigma Re - k^2)^{0.5} = 2.883356$. The boundary conditions are $u = v = 0$ at $y = \pm 1$. The initial data are found from the analytical solution above. This flow is studied until time $t = 0.1$ (for which it decays approximately three-fold), see figure 5.14. For the numerical simulation, a grid of 10×10 cells and a polynomial degree of 8 are employed.

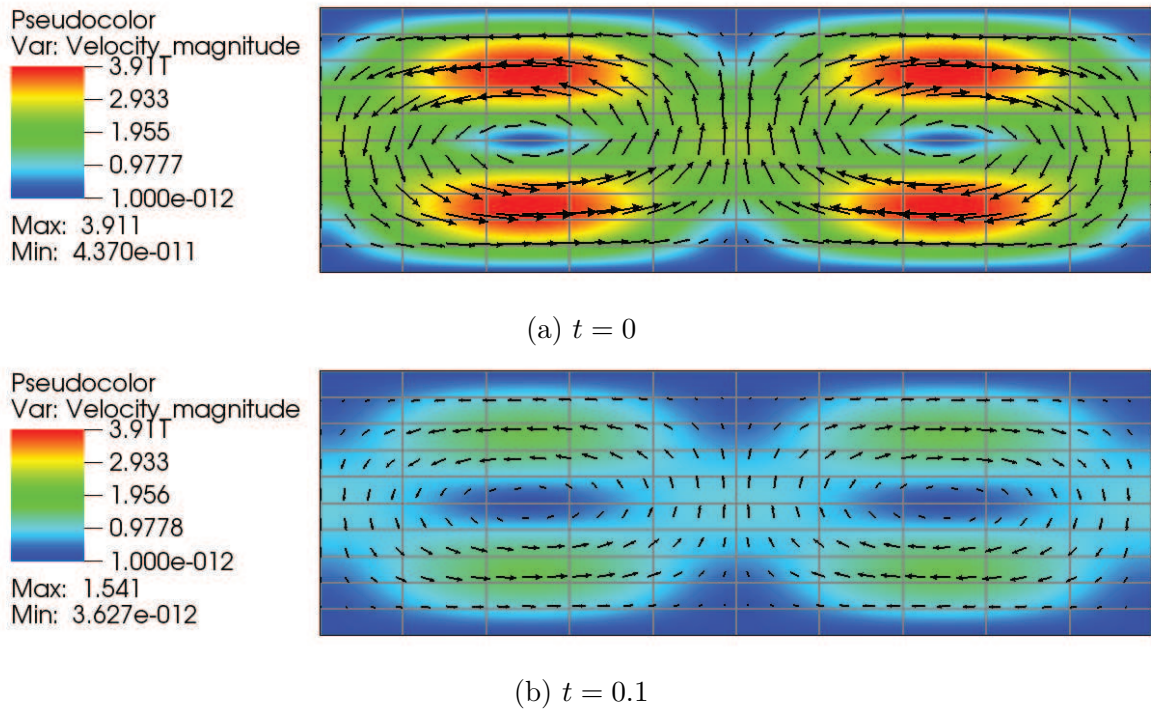


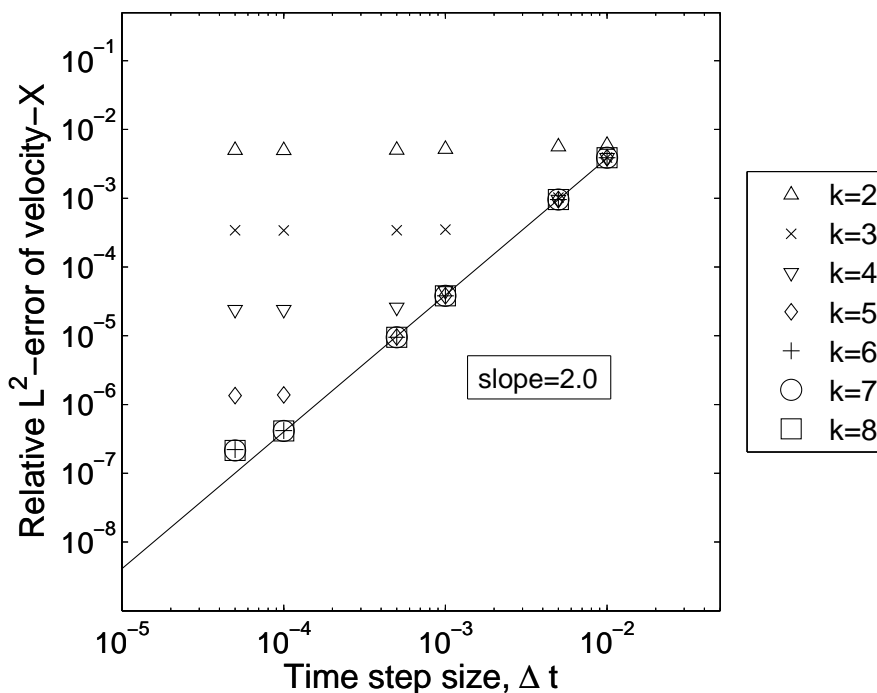
Figure 5.14: Contours of the velocity magnitude and vectors of the velocity for the case of the Stokes channel flow with $Re = 1$. The computational domain is a $[-\pi, \pi] \times [-1, 1]$ rectangle. A grid of 10×10 cells and a polynomial degree of 8 are employed. (a) The initial velocity magnitude. (b) Reduction in the velocity magnitude three-fold from its initial value.

5.5.5.1 Time convergence study

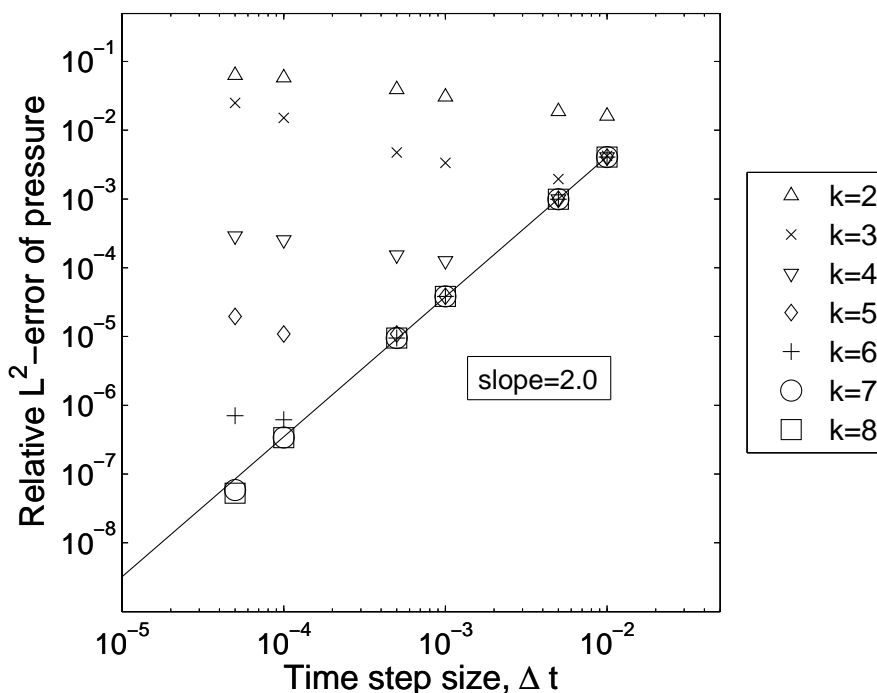
To show the time convergence rate of the solution, a Cartesian equidistant grid of 10×10 cells is selected. The applied time integration scheme is the second order (implicit/explicit) stiffly stable scheme (see 5.2). The time convergence study is performed using the EO and FDO, and the results are shown in figure 5.15 and 5.16, respectively. The relative L^2 -norm errors are computed with respect to the analytical solution as it was described in section 5.5.4.1 for the Taylor vortex flow. The expected time convergence rate of 2.00 is achieved for both the velocity and pressure with both options. This convergence rate is an interesting effect of using the consistent Neumann pressure boundary condition because (Shahbazi et al. 2007) had a lower time convergence rate for the pressure using the Dirichlet boundary conditions. Again, the same phenomena in the error growth, which was discussed before in the case of the Taylor vortex flow, is observed here. This error growth is also reported by (Ferrer & Willden 2011). One issue that should be noted is that if the initial velocity field is not divergence free, there is a possibility of error accumulation by increasing the number of time steps while reducing the time-step size to reach a certain time t . To study this effect, we have repeated the above time convergence study for the time $t = 0.3$ to increase the number of time steps to three times as many as for the time $t = 0.1$. The results (not shown) were the same as for the time $t = 0.1$, which show that the initial divergence produced by projecting the analytical solution to the computational domain (even with the low polynomial degrees) has not affected the solution and could not be a reason for the error growth.

5.5.5.2 h-convergence study

For the h-convergence study, the same strategy for the grid refinement is used as in the case of the unsteady Taylor vortex flow, section 5.5.4.2. The results are shown in figures 5.17 and 5.18. Again, with the FDO, it is obvious that the results are not accurate for very coarse grids with low polynomial degrees. In this case, inserting the pressure reference point does not affect the pressure field like in the case of the Taylor vortex flow. This is because of the solid boundaries and the consistent Neumann pressure boundary condition, which, as a constraint, controls the pressure field and suppresses this error. Also, by having this pressure boundary condition, the optimal error of $O(h^{k+1})$ is achieved for the pressure, which was $O(h^k)$ in the case of the Taylor vortex flow.

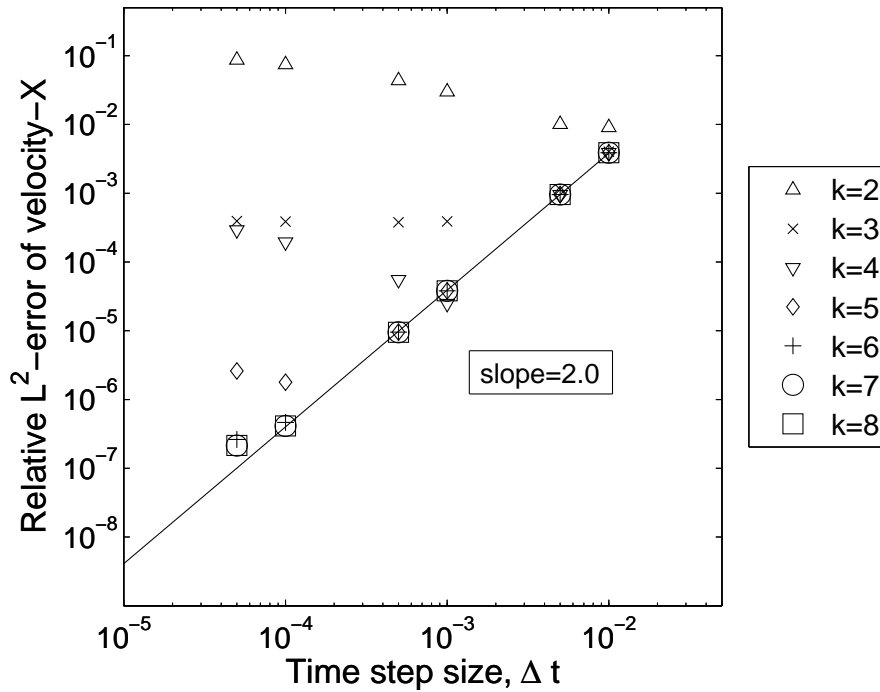


(a)

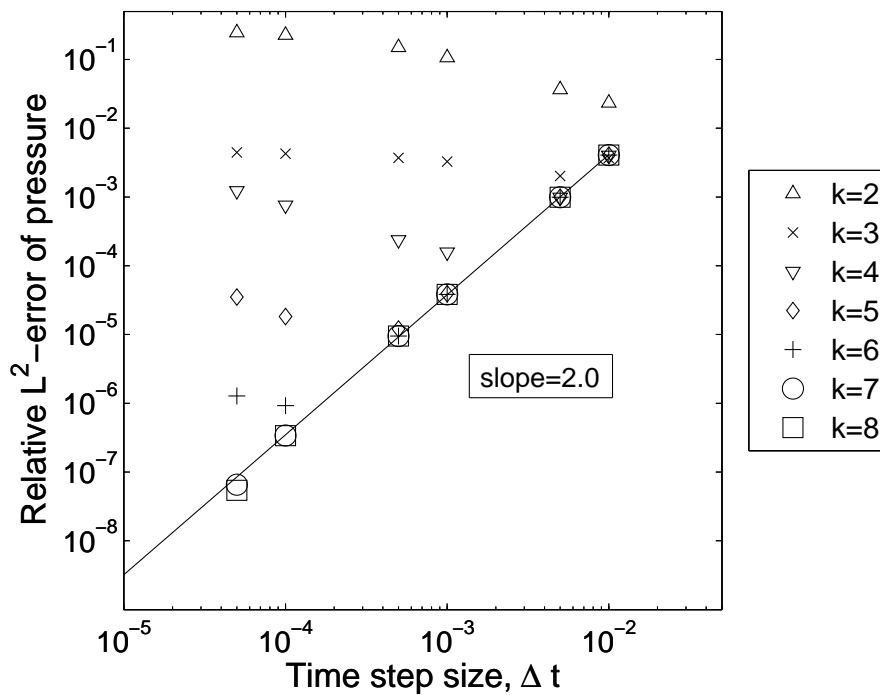


(b)

Figure 5.15: Time convergence study for the case of the Stokes channel flow with $Re = 1$. The enhanced computational option is used. A Cartesian equidistant grid of 10×10 cells is employed. Relative L^2 -norm errors of the velocity in x -direction (a) and pressure (b) are shown.

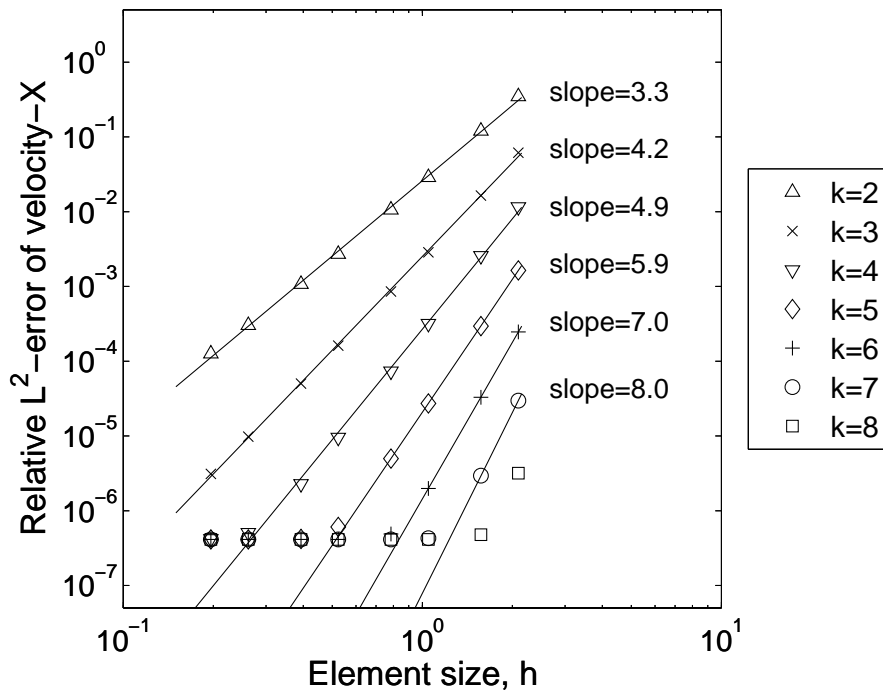


(a)

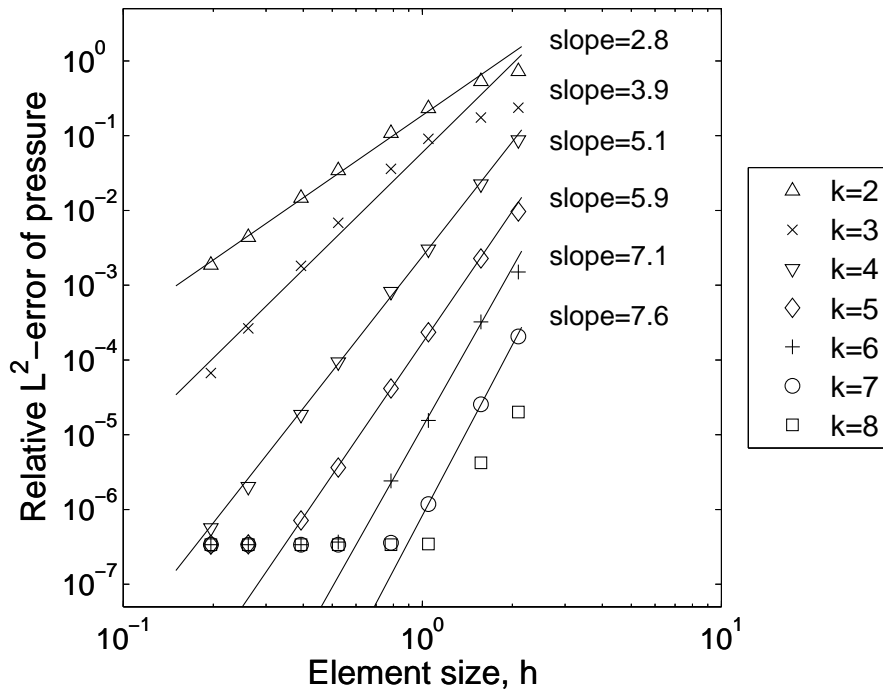


(b)

Figure 5.16: Time convergence study for the case of the Stokes channel flow with $Re = 1$. The field-derivative computational option is used. A Cartesian equidistant grid of 10×10 cells is employed. Relative L^2 -norm errors of the velocity in x -direction (a) and pressure (b) are shown.

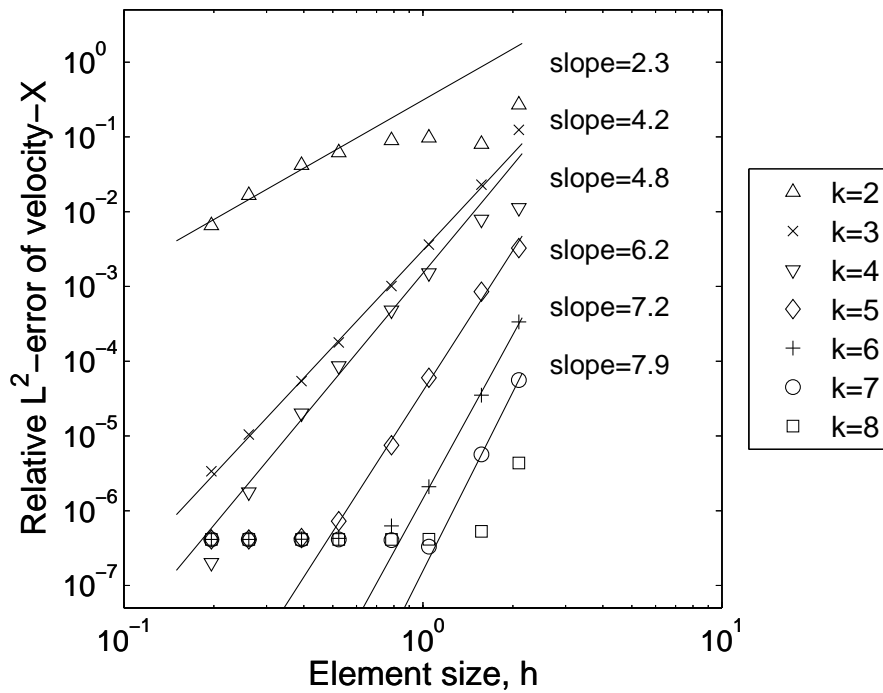


(a)

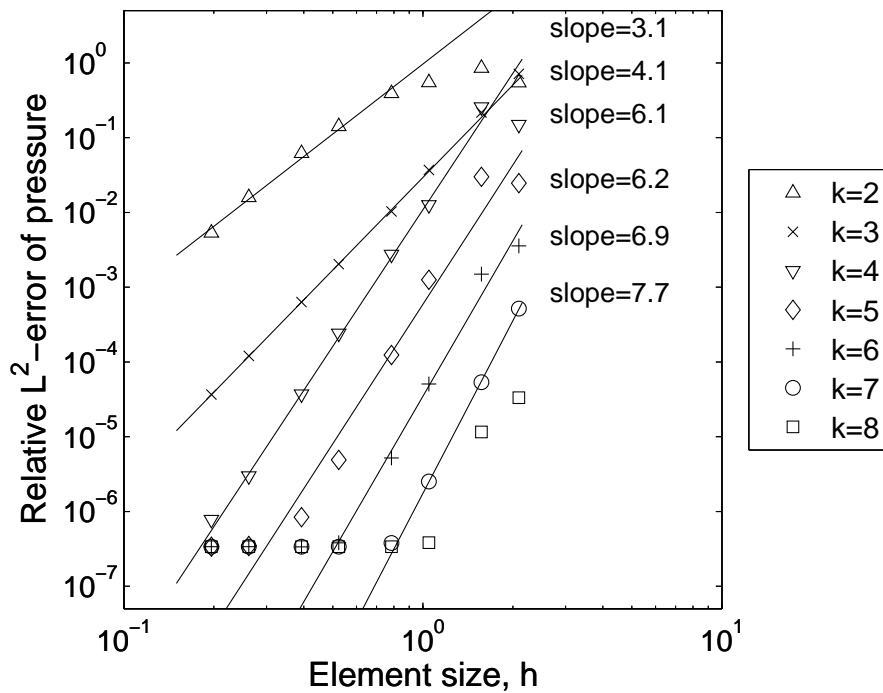


(b)

Figure 5.17: h -convergence study for the case of the Stokes channel flow with $Re = 1$. The enhanced computational option is used. Relative L^2 -norm errors of the velocity in x -direction (a) and pressure (b) are shown.



(a)



(b)

Figure 5.18: h -convergence study for the case of the Stokes channel flow with $Re = 1$. The field-derivative computational option is used. Relative L^2 -norm errors of the velocity in x -direction (a) and pressure (b) are shown.

5.5.6 Channel flow with transpiration

This is a test case of a 2D channel flow, which is periodic in x -direction and there are walls with transpiration in y -direction. The computational domain is a $[-1, 1] \times [-1, 1]$ square. The flow is steady and the analytical solution is shown below,

$$\begin{aligned} u &= \frac{y+1}{v_w} - \frac{2(1 - e^{v_w(y+1)Re})}{v_w(1 - e^{2v_w Re})}, \\ v &= v_w, \\ p &= -x + 1, \end{aligned}$$

where the Reynolds number is 10 and v_w is the velocity at the walls. The boundary conditions are $u = 0$ and $v = v_w = 0.3$ at $y = \pm 1$. A periodic pressure gradient of $\frac{\partial p}{\partial x} = -1$ is applied in x -direction. For this test case, the maximum possible pseudo-time step size that could be used is $dt_{max} = 0.02$ for the EO and $dt_{max} = 0.01$ for the FDO. These maximum pseudo-time step sizes are a small fraction of $dt_{CFL} = \frac{h}{V k^2}$ when the grid is coarse or the polynomial degree is low, but these pseudo-time steps are several times higher than dt_{CFL} for fine grids and high polynomial degrees.

For the h-convergence study, the grid refinement strategy is the same strategy that was used for the previous test cases, see section 5.5.4.2. The relative L^2 -norm errors are computed with respect to the analytical solution as it was described in section 5.5.4.1. The results are shown in figure 5.19. For some coarse grids with a polynomial degree of 1, the solution was not stable with the FDO. With both options, the results are the same when a very high accuracy is not acquired. The case with the EO provides the most accurate results and converges in a fewer number of pseudo-time steps than the FDO (figure 5.20). The computational time for the EO is higher in each pseudo-time step but can still be competitive because of less number of steps. This is what we see in table 5.1. In this table, two cases are shown: a polynomial degree of 6 with a 16×16 grid and a polynomial degree of 8 with a 6×6 grid. These cases, which are the same with respect to the accuracy, are chosen from figure 5.19. The fewer number of pseudo-time steps in the EO compensates for the higher computational time for each step in the case with a degree of 6. The reported time belongs to the total simulation time and includes some general operations or saving the results to the database. This is why the EO demonstrates a higher computational time when the total simulation time was small for the case of a degree 8.

Table 5.1: Comparing the computational time to reach the steady state solution for the case of the channel flow with a transpiration velocity of $v_w = 0.3$ and $Re = 10$. The two computational options field-derivative and enhanced are compared with each other. *DOF* is the degrees of freedom.

polynomial degree	Number of cells	DOF	Field-derivative	Enhanced
6	16×16	7168	23 min.	18 min.
8	6×6	1620	4 min.	7 min.

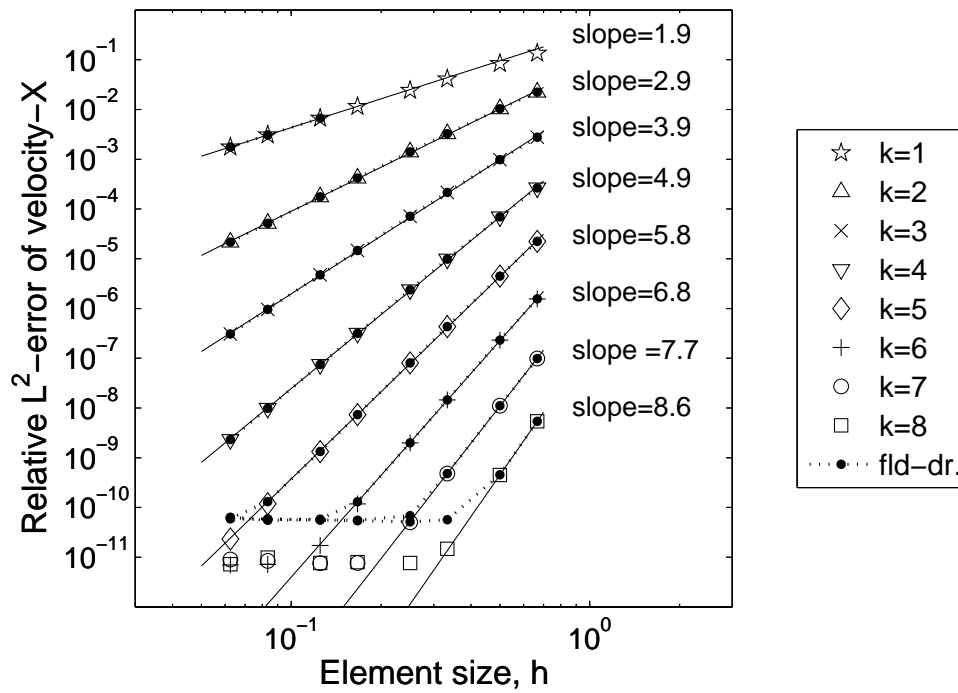


Figure 5.19: h -convergence study for the case of the channel flow with a transpiration velocity of $v_w = 0.3$ and $Re = 10$. Relative L^2 -norm errors of the velocity in x -direction are shown.

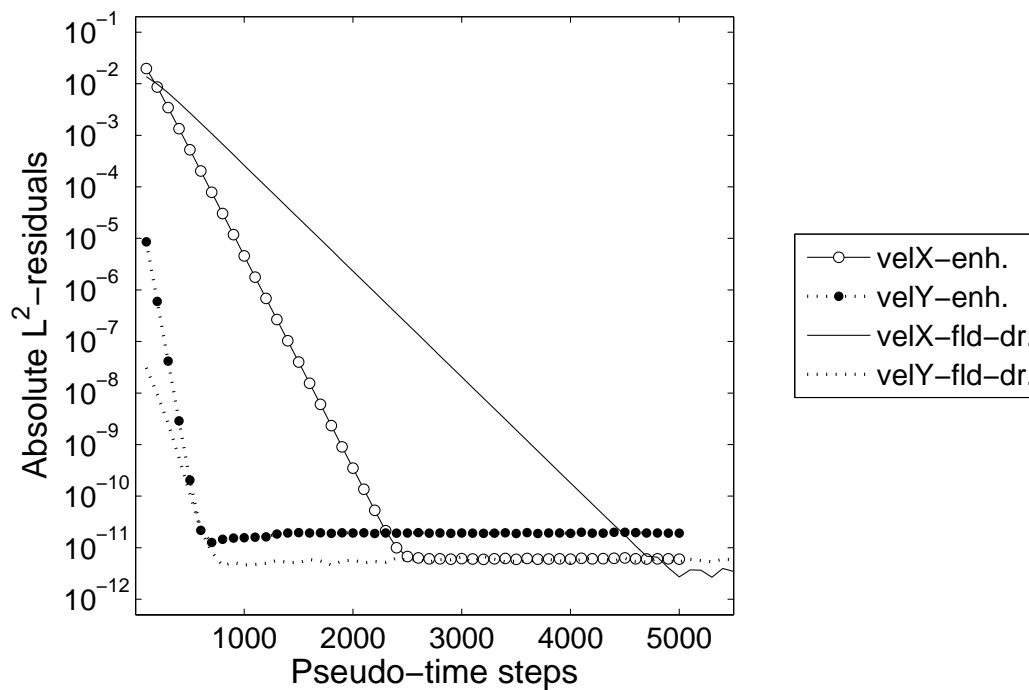


Figure 5.20: The absolute L^2 -norm residuals, $\|u^{n+1} - u^n\|_2$, are shown for the case of the channel flow with a transpiration velocity of $v_w = 0.3$ and $Re = 10$. n is the number of pseudo-time steps.

5.6 Conclusion

The Projection Consistent Pressure solver was developed and validated to solve the incompressible Navier-Stokes equations. The projection scheme for the velocity-pressure decoupling was employed with a consistent Neumann pressure boundary condition. The scheme resulted in an optimal convergence rate of $k + 1$ in L^2 -norm for the pressure. Using the DG method, the projection scheme was successfully applied without stability problems. The approach is based on the DG weak formulation and using numerical fluxes to compute the required derivatives of the flow variables (the flux approach) instead of using the derivatives of the local basis polynomials (field-derivative approach). The flux approach was quite effective in minimizing the errors originating from the discontinuity of the solution at the cell boundaries. Accordingly, a remarkable improvement in the accuracy of the results was achieved. More accurate results were obtained for the unsteady problems even when coarse grids and low polynomial degrees were used. Moreover, for steady problems, higher pseudo-time step sizes were applicable. The improved accuracy and stability characteristics makes the flux approach superior to the field-derivative approach.

6 Numerical modeling of the surface tension force

The surface tension force is modeled as a body force, $-\gamma\delta(\phi)\kappa\mathbf{n}$, in the Navier-Stokes equations (3.3) using the continuum surface force model (CSF) (Brackbill, Kothe & Zemach 1992). In the CSF model, the surface tension force is not a concentrated force but distributed around the interface (the diffuse interface model). A known problem of this approach is introducing spurious velocity fields. In the following sections, we study and try to reduce and control the resultant errors.

6.1 The diffuse interface model

The interface is represented by the zero iso-surface of the level set function ϕ . An example is shown in figure 6.1 for a square domain of $[-2, 2] \times [-2, 2]$. To be able to integrate the terms which involve the discontinuous Heaviside and delta functions, the diffuse interface model is used. In this model the interface is considered to have a finite thickness and the regularized Heaviside and delta functions are used instead of the discontinuous ones (figure 6.2). Here, the regularized Heaviside and delta functions

$$H(\phi) = \begin{cases} 0 & \phi < -\epsilon \\ \frac{1}{2}(1 + \frac{\phi}{\epsilon} + \frac{1}{\pi}\sin(\frac{\phi\pi}{\epsilon})) & -\epsilon \leq \phi \leq \epsilon \\ 1 & \phi > \epsilon \end{cases}, \quad (6.1)$$

$$\delta(\phi) = \begin{cases} 0 & \phi < -\epsilon \\ \frac{1}{2\epsilon}(1 + \cos(\frac{\phi\pi}{\epsilon})) & -\epsilon \leq \phi \leq \epsilon \\ 0 & \phi > \epsilon \end{cases} \quad (6.2)$$

have been used, where ϵ is the half-thickness of the diffuse interface. A signed-distance level set function (figure 6.3), which has the property $|\nabla\phi| = 1$, is required for the above definition to ensure the same thickness of the interface everywhere.

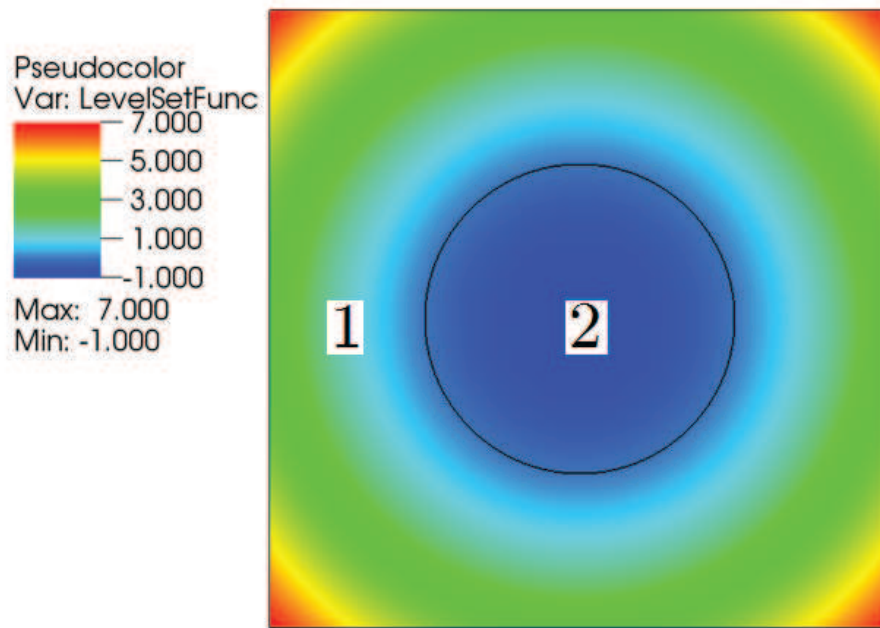


Figure 6.1: Representation of an interface between two immiscible fluids 1 and 2 as the zero iso-value of a level set function, $\phi = \sqrt{x^2 + y^2} - 1$. A square domain of $[-2, 2] \times [-2, 2]$ is considered. A grid of 24×24 cells is employed. A polynomial degree of 5 is used for the level set function.

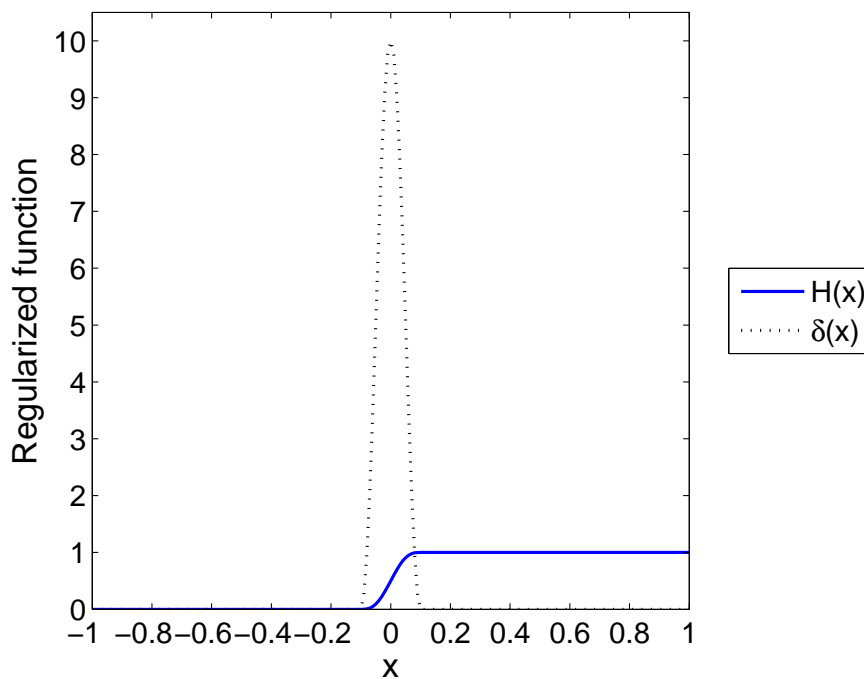


Figure 6.2: The regularized Heaviside and Dirac delta functions which are used for the diffuse interface model.

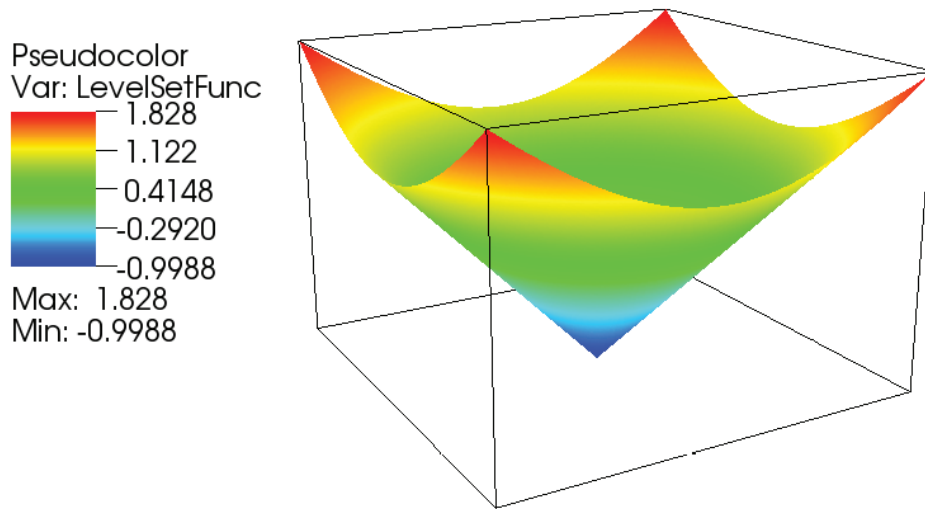


Figure 6.3: The signed-distance level set function $\phi = \sqrt{x^2 + y^2} - 1$ that is required for the regularization of the Heaviside and delta functions. A square domain of $[-2, 2] \times [-2, 2]$ is considered. A grid of 24×24 cells is employed. A polynomial degree of 5 is used for the level set function.

6.2 Test case: Stationary flow with pressure jump

As a test case, a stationary flow with a pressure jump at the interface (as a result of the surface tension) is considered. There are no jumps in the fluid properties of density and viscosity. The Reynolds and Weber numbers of 1 are considered. The computational domain is a $[-2, 2] \times [-2, 2]$ square. The interface is represented by the zero iso-value of a signed-distance level set function $\phi = \sqrt{x^2 + y^2} - 1$. The analytical solution consists of a pressure jump, $\nabla p = \frac{1}{We} = 1$ at the interface and a zero velocity field (figure 6.4). For the numerical simulation, $\epsilon = \frac{1}{8}$ is considered and the level set function is not advected. A polynomial degree of 5 is used for the velocity, pressure and level set function. A Cartesian computational grid, which consists of 24×24 cells, is employed. The computed flow fields using the FO and FDO computational options are shown in figure 6.5. There is a reduction of one order of magnitude in the produced spurious velocity with the FO option. The elevated contours of pressure are shown in figure 6.6.

6.2.1 h-convergence study

An h-convergence study for the test case of section 6.2 is shown in figure 6.7. The FO and FDO are considered. The grid refinement is performed by decreasing the element size, h , choosing $h = \frac{1}{3}, \frac{1}{4}, \frac{1}{5}, \frac{1}{6}, \frac{1}{7}$ and $\frac{1}{8}$. The FO is more accurate and it results in an error reduction of one order of magnitude compared to the FDO. Therefore, only the FO will be used for the following simulations. The same h-convergence study is repeated using the FO and polynomial degrees of 2 to 8. The results are shown in figure 6.8. The

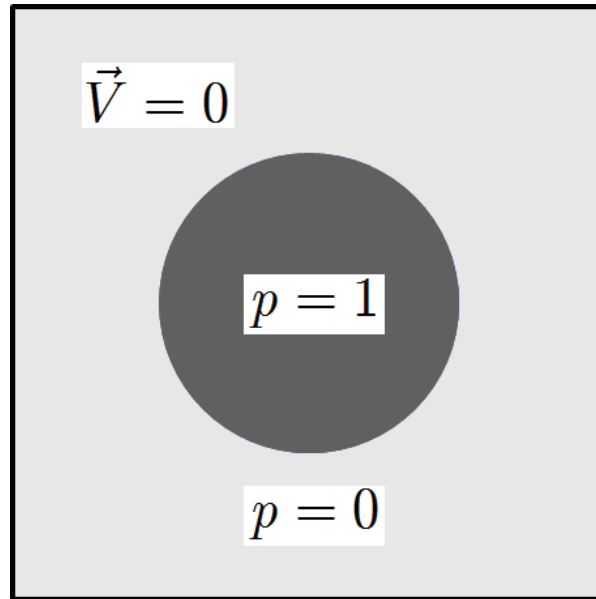
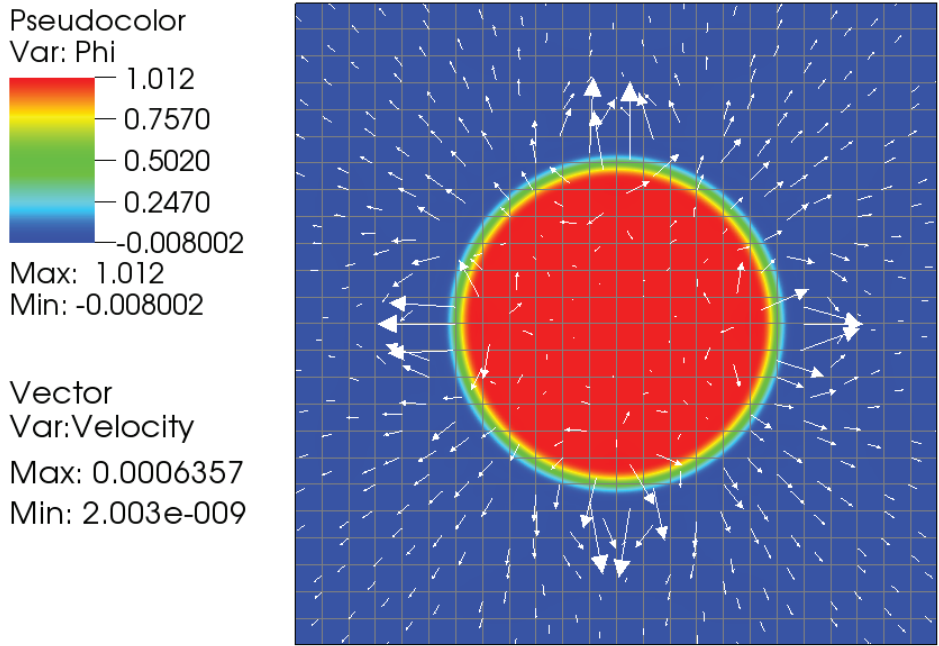
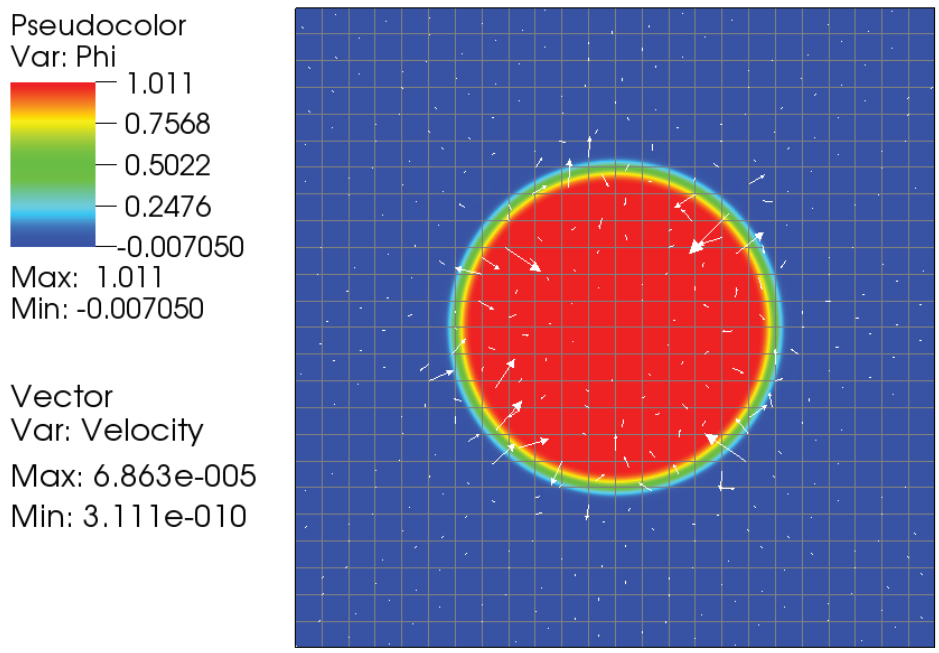


Figure 6.4: Analytical solution for the case of a stationary flow with pressure jump of 1 at the interface. The velocity field is zero.

errors, using degrees of 6 to 8, grow by marching in time and are not much different from that of degree 5. To find out the reason for this error growth, a polynomial degree of 8 is used for the level set function to minimize the errors related to the computation of the normal vector and curvature. The results for the converged solution are shown in figure 6.9, which are almost the same as the results shown in figure 6.8b. This implies that, in the case of a stationary flow with pressure jump, the dominant error is related to the integration of the delta function, rather than the computations of the normal vector and curvature. The errors that are related to the use of the regularized delta function are studied in the section 6.2.3.



(a)



(b)

Figure 6.5: Flow field for the case of a stationary flow with pressure jump of 1 at the interface. Contours of the pressure and vectors of the velocity are shown. The computational domain is a $[-2, 2] \times [-2, 2]$ square. A half-thickness of $\epsilon = \frac{1}{8}$ is considered for the diffuse interface. A Cartesian grid of 24×24 cells is employed. Polynomial degrees of 5 are used for the velocity, pressure and level set function. (a) The field-derivative computational option is used. (b) The flux computational option is used.

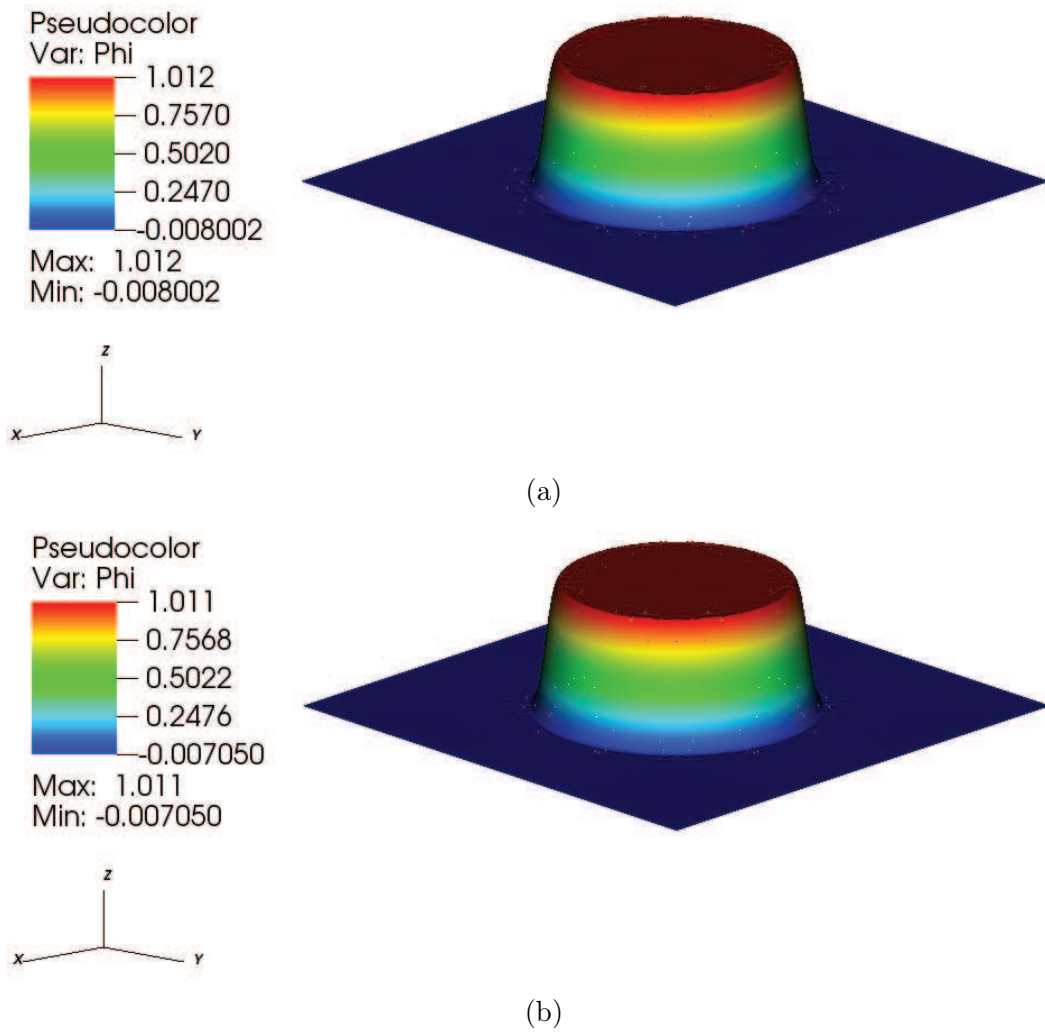


Figure 6.6: Elevated contours of the pressure for the case of a stationary flow with pressure jump of 1 at the interface. The computational domain is a $[-2, 2] \times [-2, 2]$ square. A half-thickness of $\epsilon = \frac{1}{8}$ is considered for the diffuse interface. A Cartesian grid of 24×24 cells is employed. Polynomial degrees of 5 are used for the velocity, pressure and level set function. (a) The field-derivative computational option is used. (b) The flux computational option is used.

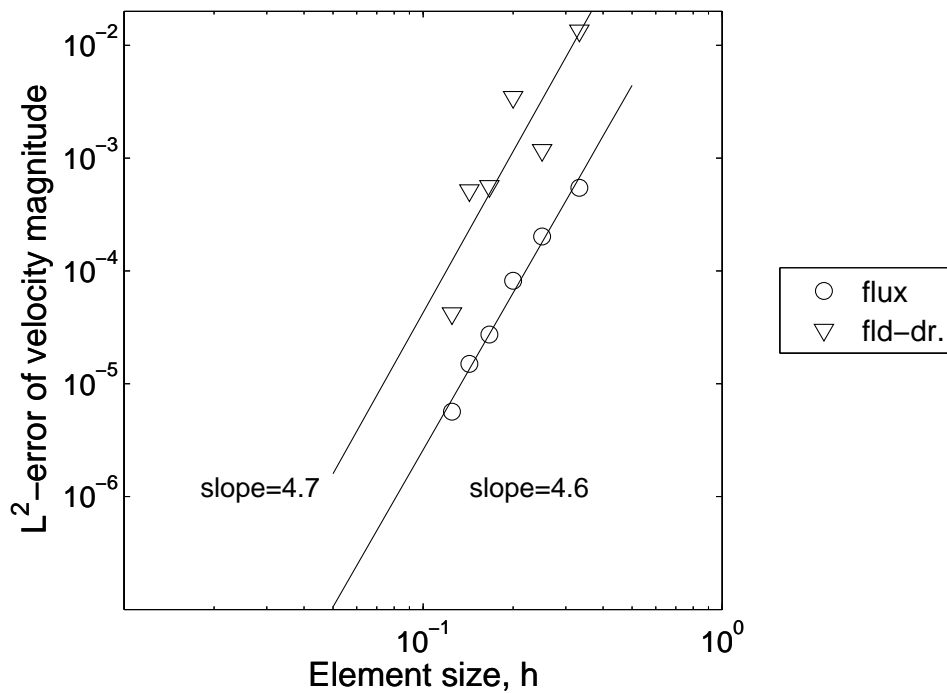
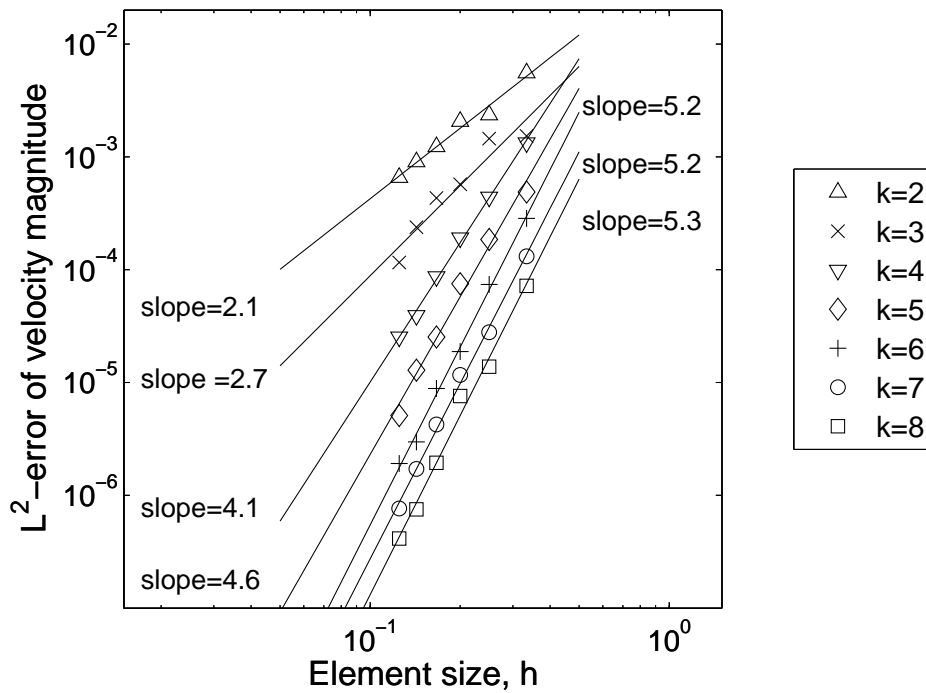
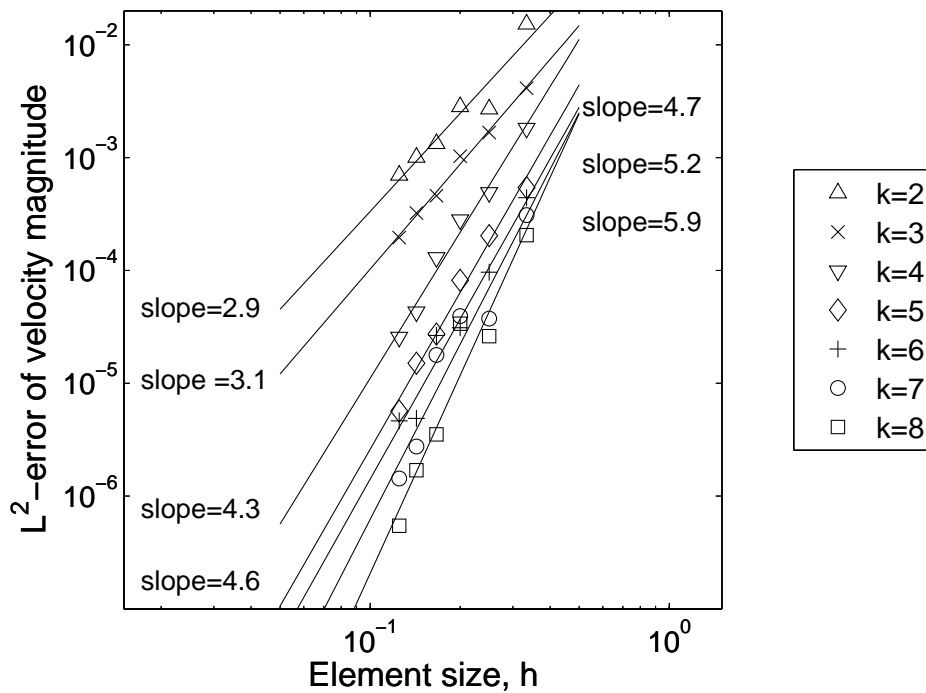


Figure 6.7: h -convergence study for the case of a stationary flow with pressure jump of 1 at the interface. Flux and field-derivative computational options are used. L^2 -norm errors of the velocity magnitude are shown. A half-thickness of $\epsilon = \frac{1}{8}$ is considered for the diffuse interface. Polynomial degrees of 5 are used for the velocity, pressure and level set function.



(a) First pseudo-time step



(b) Converged solution

Figure 6.8: h -convergence study for the case of a stationary flow with pressure jump of 1 at the interface. L^2 -norm errors of the velocity magnitude are shown. The flux computational option is used. A half-thickness of $\epsilon = \frac{1}{8}$ is considered for the diffuse interface. Polynomial degrees of the velocity, pressure and level set function are the same. (a) First pseudo-time step. (b) Converged solution, which shows an increment of the errors with respect to the first pseudo-time step for the polynomial degrees of 6, 7 and 8.

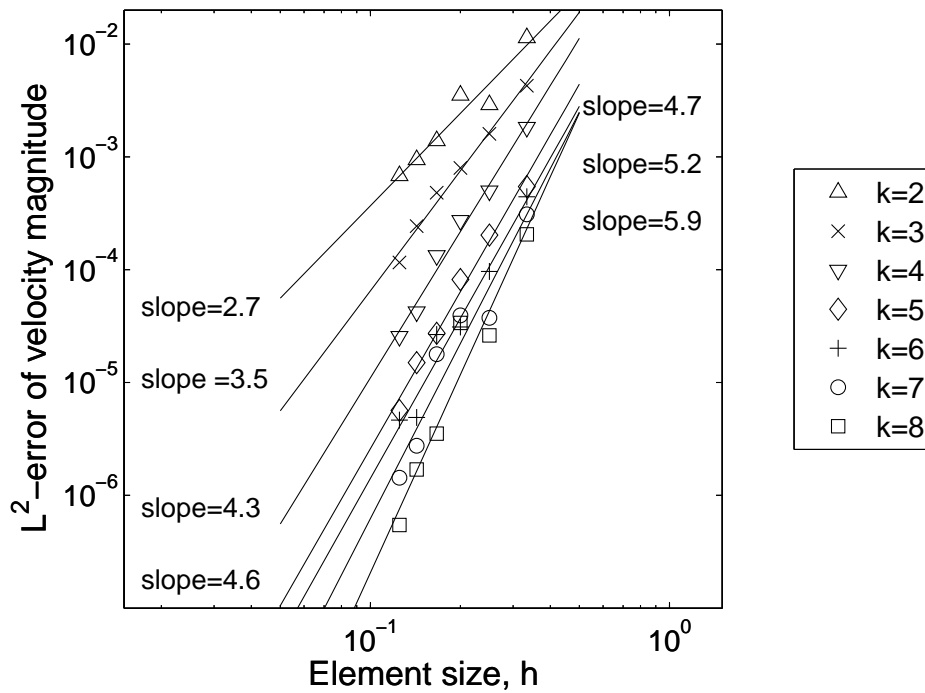


Figure 6.9: h-convergence study for the case of a stationary flow with pressure jump of 1 at the interface. L^2 -norm errors of the velocity magnitude are shown. The h-convergence study in figure 6.8b is repeated with a fixed polynomial degree of 8 for the level set function.

6.2.2 p-convergence study

The results of the p-convergence study for the case of a stationary flow with pressure jump are shown in figure 6.10. The p-convergence study confirms the results of the h-convergence study for this test case, namely that the errors are increasing whilst time stepping. The only exception is the degree of 5 for which the error increase is negligible. This finding suggests the use of a degree of 5 for the simulations, when the regularized delta function of equation 6.2 is used.

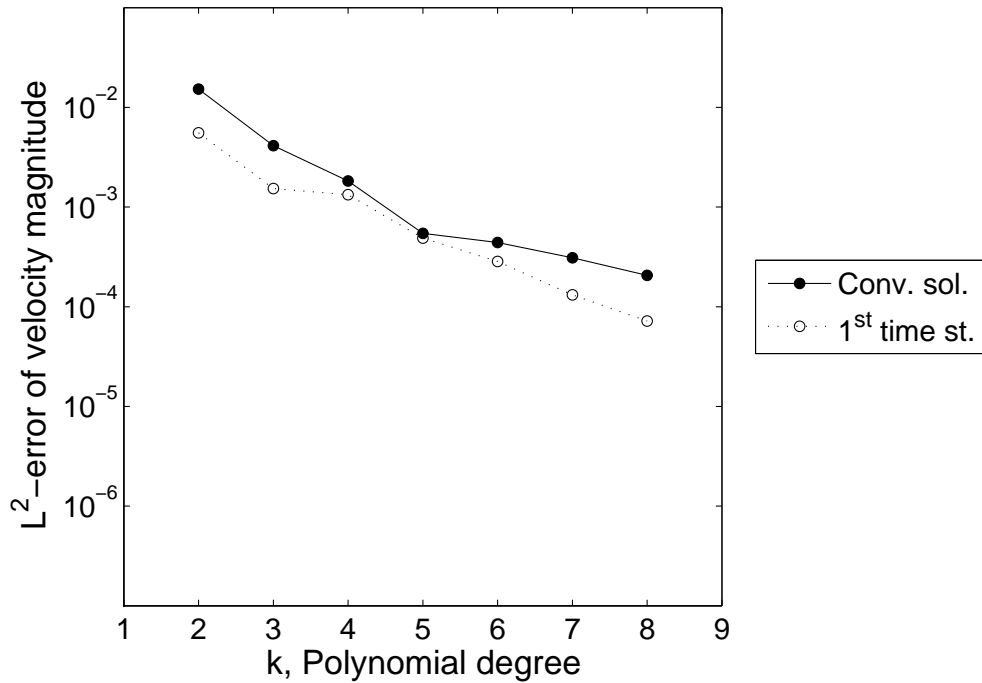
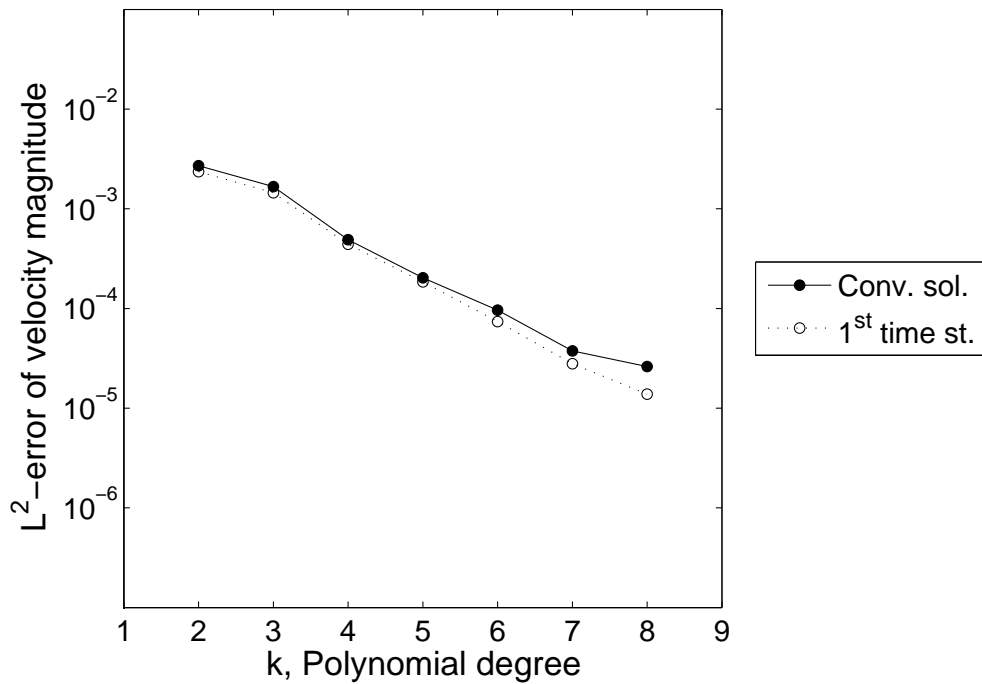
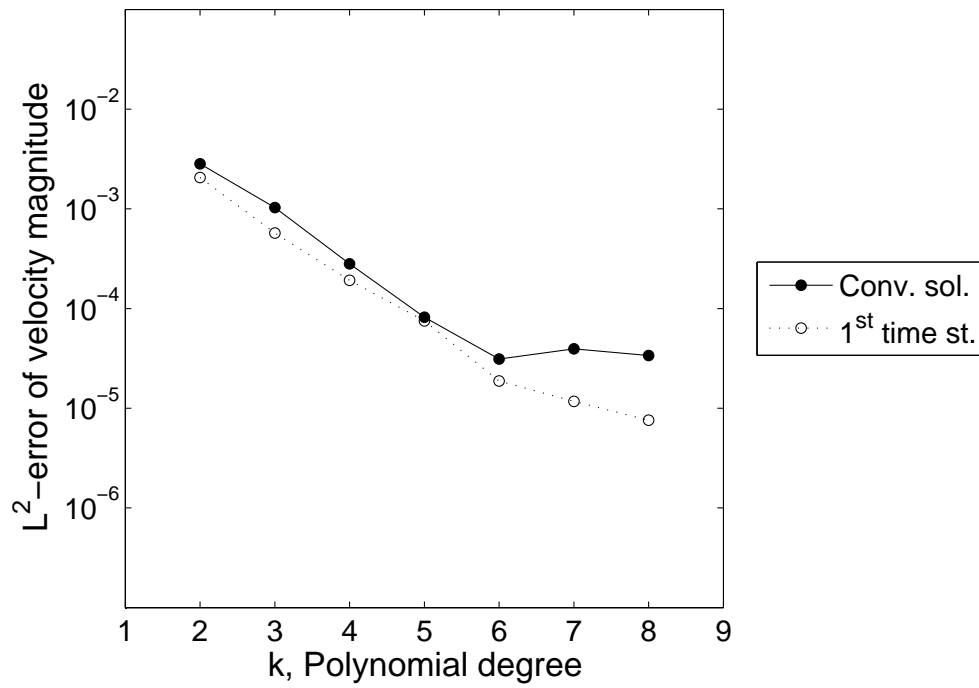
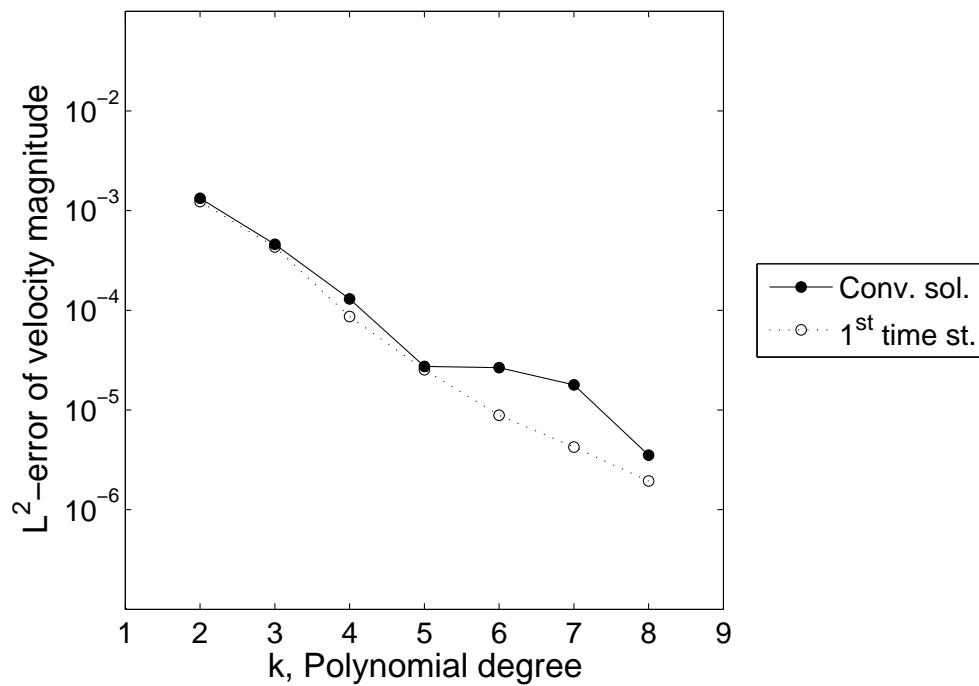
(a) $h = \frac{1}{3}$ (b) $h = \frac{1}{4}$

Figure 6.10: p-convergence study for the case of a stationary flow with pressure jump of 1 at the interface. L^2 -norm errors of the velocity magnitude are shown. A half-thickness of $\epsilon = \frac{1}{8}$ is considered for the diffuse interface. h is the element size (to be continued on the next pages).



(c) $h = \frac{1}{5}$



(d) $h = \frac{1}{6}$

Figure 6.10: To be continued on the next page.

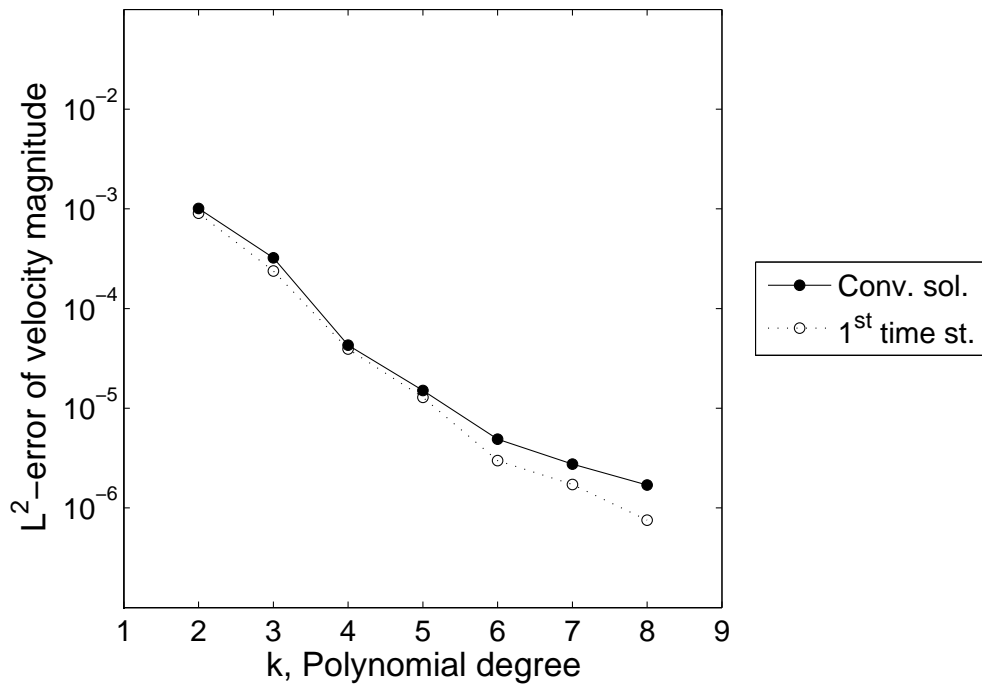
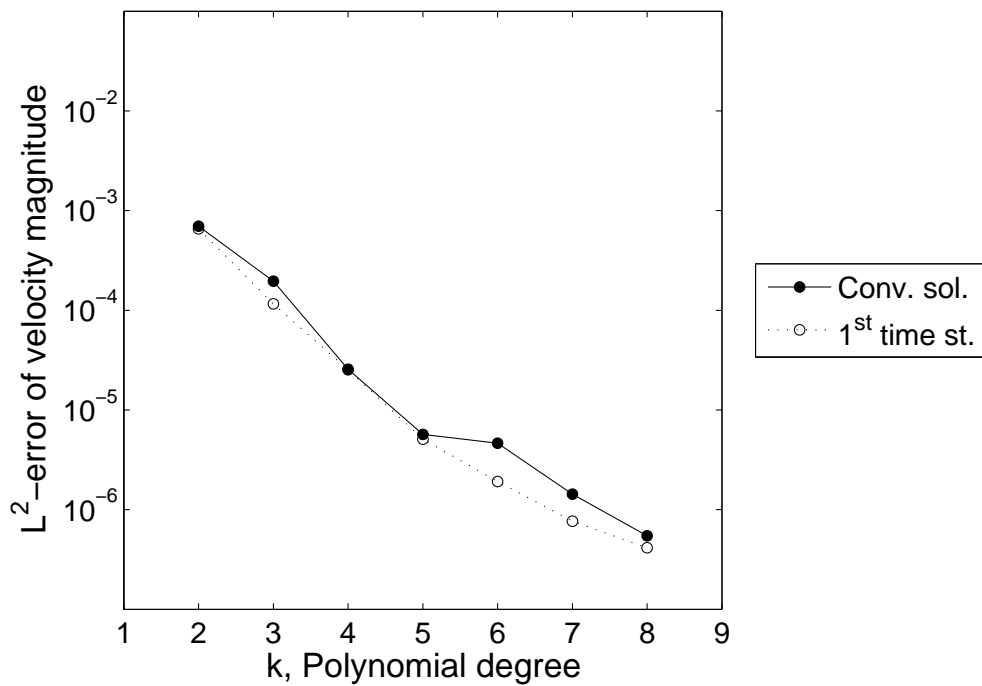
(e) $h = \frac{1}{7}$ (f) $h = \frac{1}{8}$

Figure 6.10: Continued.

6.2.3 Approximating the regularized delta function

A curve fit to the regularized delta function is performed using polynomial degrees of 2 up to 8. The result is shown in figure 6.11. The half-thickness ϵ is varied from $\frac{1}{3}$ down to $\frac{1}{8}$ to decrease the thickness of the interface. According to this figure, the regularized delta function is well approximated by the polynomial degree of 4 and there is not a great difference by increasing the polynomial degree further.

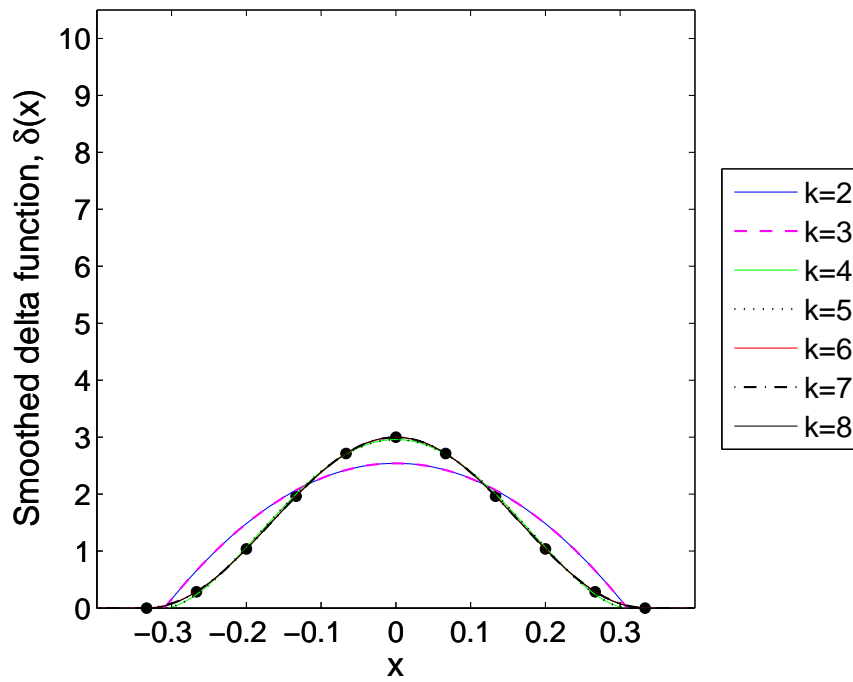
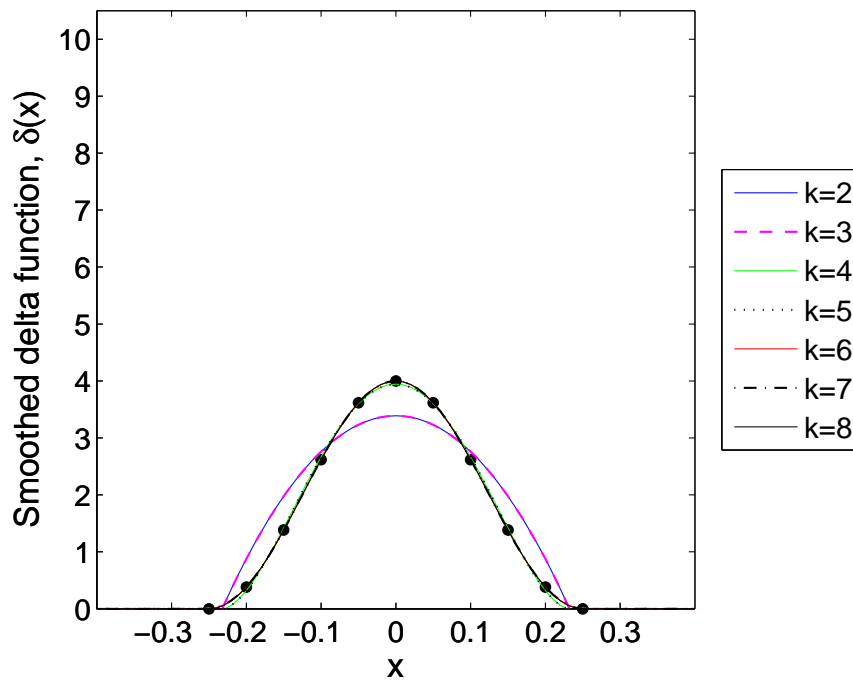
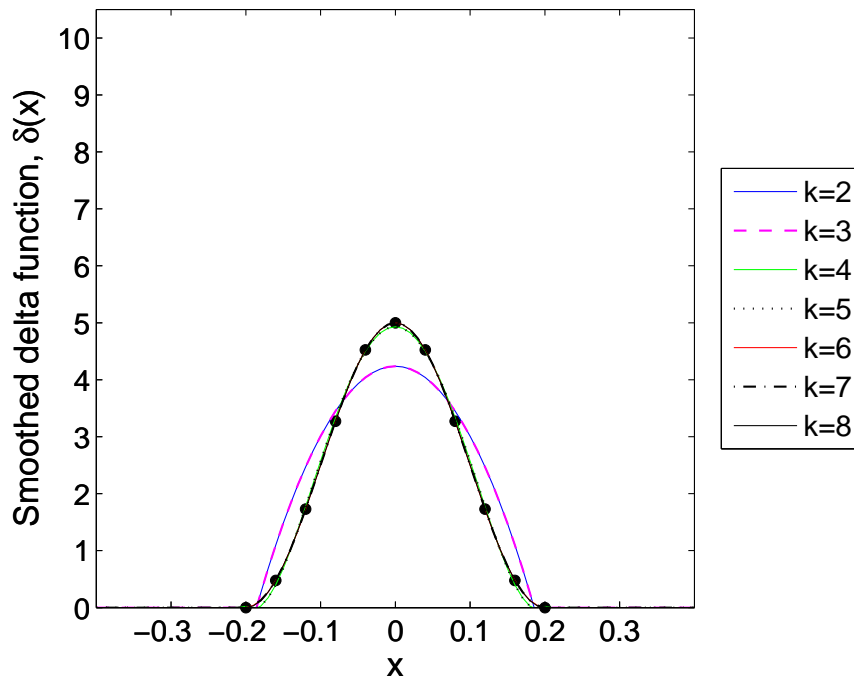
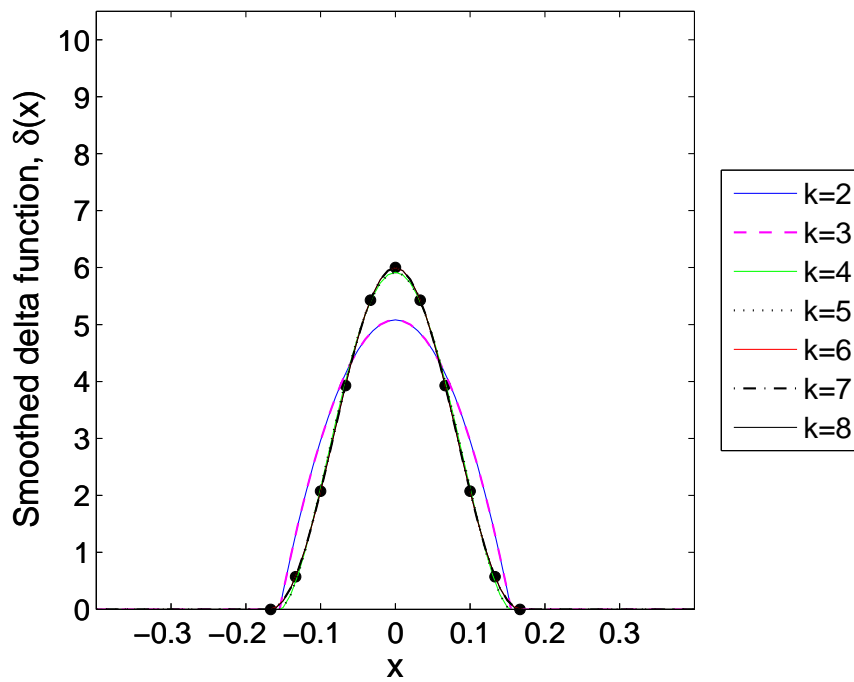
(a) $\epsilon = \frac{1}{3}$ (b) $\epsilon = \frac{1}{4}$

Figure 6.11: Polynomial interpolation of the regularized delta function. ϵ is the half-thickness of the diffuse interface that is used for the regularization (to be continued on the next pages).



(c) $\epsilon = \frac{1}{5}$



(d) $\epsilon = \frac{1}{6}$

Figure 6.11: To be continued on the next page.

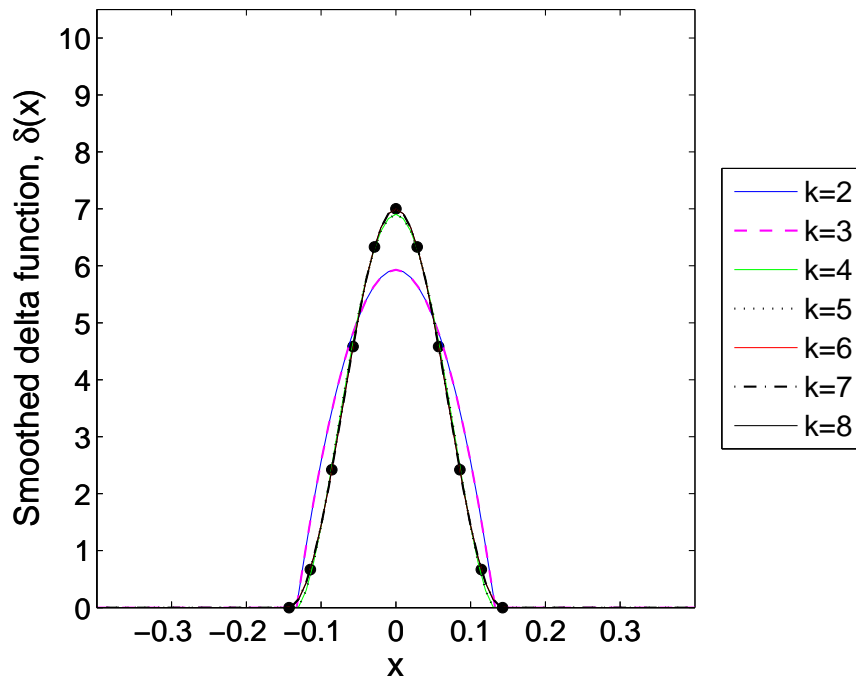
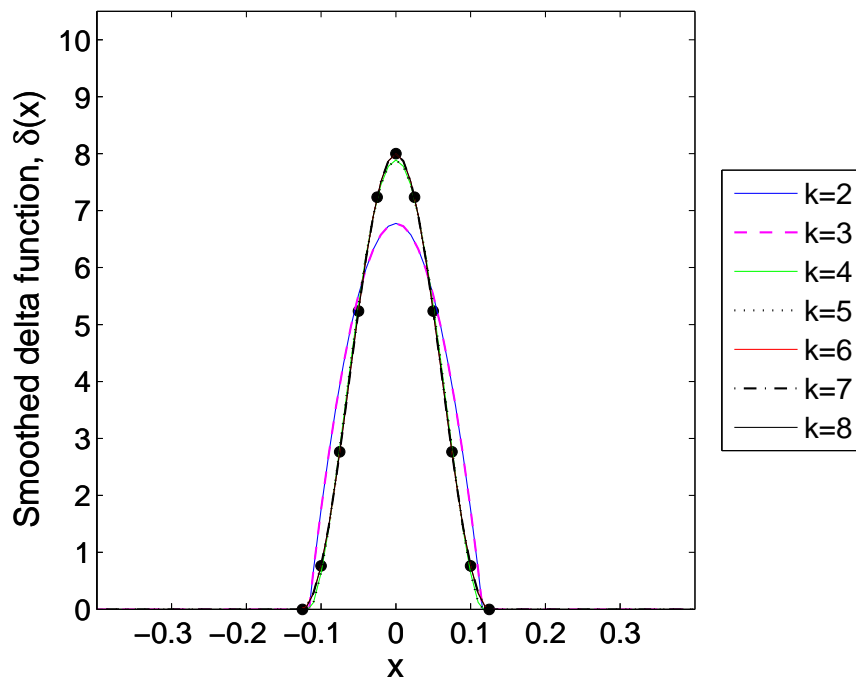
(e) $\epsilon = \frac{1}{7}$ (f) $\epsilon = \frac{1}{8}$

Figure 6.11: Continued.

6.3 The Computation of the normal vector and curvature

In the level set method, the normal vector and the mean curvature are found easily from the level set function from the following relations.

$$\mathbf{n} = \frac{\nabla\phi}{|\nabla\phi|},$$

$$\kappa = -\nabla \cdot \mathbf{n}$$

6.3.1 p-enrichment of the normal vector

Computing the normal vector accurately is very important, using any numerical scheme. On the other hand, operations for finding the magnitude of the level set function and the division are not defined in the polynomial space of the DG method. Therefore, to have a relatively accurate approximation of the normal vector, a high polynomial degree is used for the normal vector irrespective of the degree of the level set function. We call this modification as the *p-enrichment* of the normal vector. To show the effect of the p-enrichment of the normal vector, a test case for a level set function of $x^2 + y^2 - 1$ is considered. The analytical value for the curvature is $\kappa = -\frac{1}{\sqrt{x^2+y^2}}$. The computational domain is a $[-2, 2] \times [-2, 2]$ square. The level set function and its zero iso-surface, which represents the interface, are shown in figure 6.12. Contours of the curvature are shown in figure 6.13. In figure 6.13a, polynomial degrees of 2, 1 and 0 are used for the level set function, normal vector and curvature, respectively. Therefore, a constant value of the curvature in each cell is expected. In figure 6.13b the polynomial degree of the level set function is 2 but the p-enrichment with polynomial degrees of 10 and 9 is done for the normal vector and curvature, respectively. The iso-surface of -1 of the curvature, which is shown in figure 6.13b, coincides with the zero iso-surface of the level set, which represents the interface. Therefore, with the p-enrichment, the analytical value of -1 for the curvature is achieved at the interface. Despite the low number of degrees of freedom, the p-enrichment of the normal vector does not introduce any significant additional computational cost. Still, the computation of the normal vector and the curvature can be limited to a *narrow band* around the interface if necessary (figures 6.14 and 6.15).

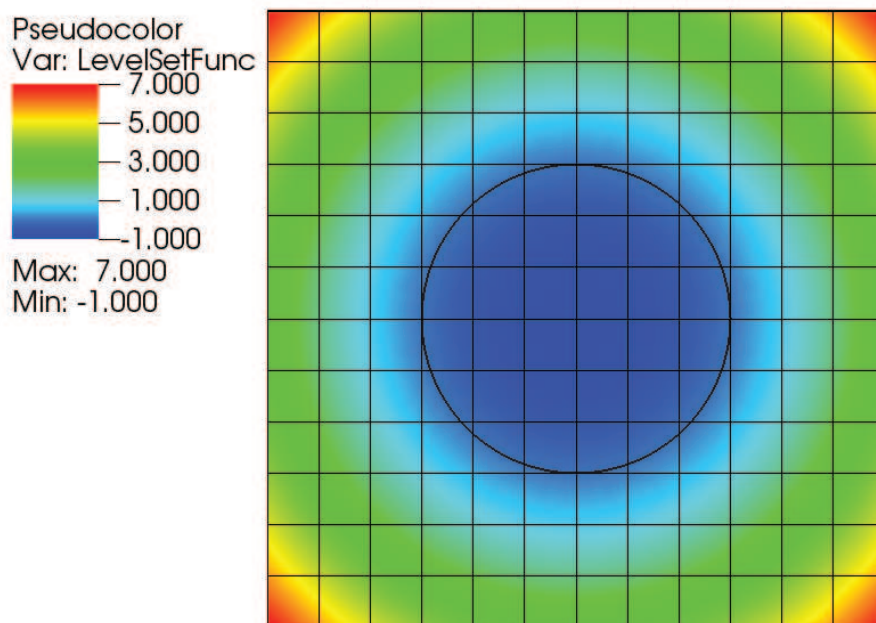


Figure 6.12: The level set function $\phi = x^2 + y^2 - 1$ and its zero iso-surface which represents the interface. The computational domain is a $[-2, 2] \times [-2, 2]$ square. A grid of 12×12 cells and a polynomial degree of 2 are used.

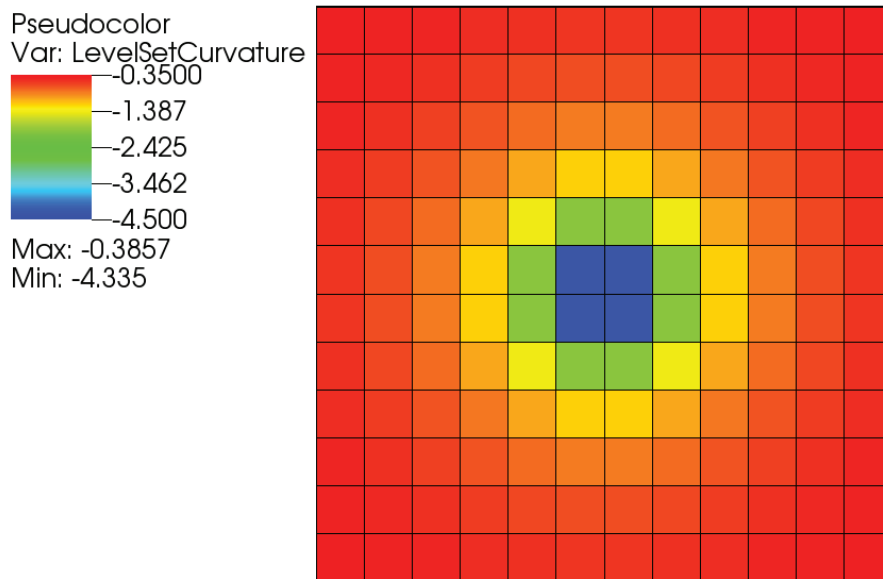
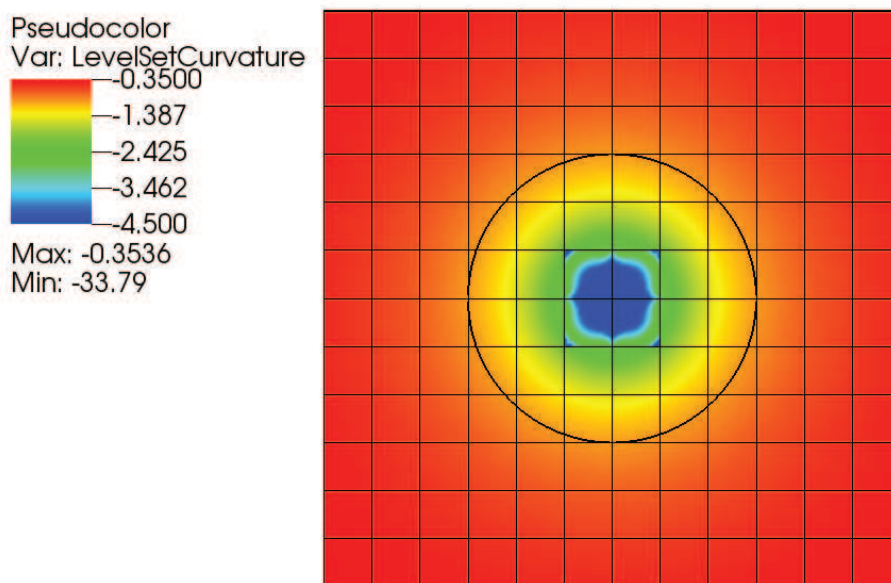
(a) $k_\phi = 2$, $k_{\mathbf{n}} = 1$, $k_\kappa = 0$ (b) $k_\phi = 2$, $k_{\mathbf{n}} = 10$, $k_\kappa = 9$

Figure 6.13: Contours of the curvature corresponding to the level set function $\phi = x^2 + y^2 - 1$ shown in figure 6.12. A polynomial degree of $k_\phi = 2$ is used for the level set function. $k_{\mathbf{n}}$ and k_κ are the polynomial degrees for the normal vector and curvature, respectively. p-enrichment of the normal vector is applied in (b) which provides the analytical iso-value of -1 for the curvature at the interface.

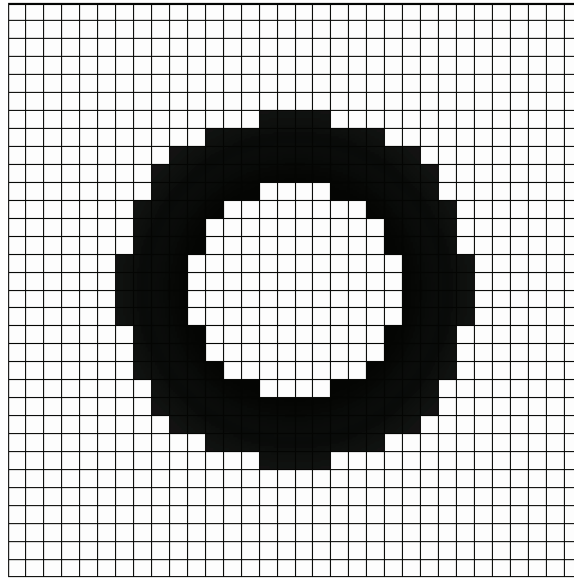


Figure 6.14: A narrow band of two cells on each side of the interface.

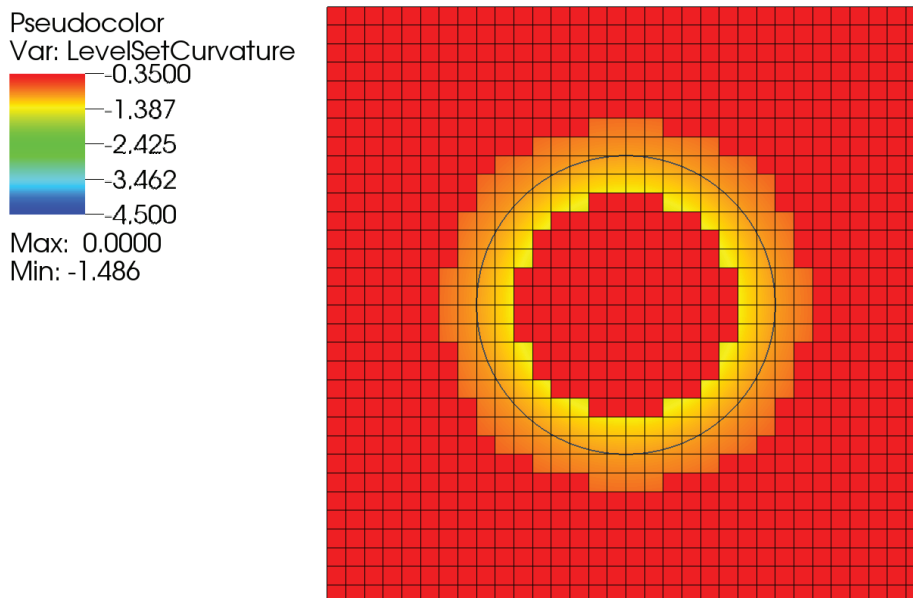


Figure 6.15: Contours of the curvature corresponding to the level set function $\phi = x^2 + y^2 - 1$. The iso-surface of -1 of the curvature represents the interface. The curvature is computed on a narrow band around the interface. p-enrichment of the normal vector is applied in the same way as in figure 6.13b. A grid of 32×32 cells is employed.

To study the p-enrichment of the normal vector, the case of a stationary flow with pressure jump in section 6.2 is considered again. As it was shown in section 6.2.1, the dominant errors are related to the integration of the delta function, rather than the computation of the normal vector and curvature. Therefore, we have considered the polynomial degree of 8 for the velocity and pressure to minimize the errors related to the integration of the delta function. The results, which are shown in figure 6.16, correspond to the first pseudo-time step to make sure that the errors will not increase by time stepping. As the interface is not moving, showing the results of the first pseudo-time step, is appropriate for demonstrating the errors related to the computation of the normal vector and curvature.

In figure 6.16a, there is not much error reduction by applying the p-enrichment of the normal vector. This is related to the projection of the signed-distance level set function with the polynomial degree of 2 which appears to produce larger errors than the computation of the normal vector and the curvature. The errors related to the projection of the level set function are studied in section 6.3.2. By increasing the polynomial degree of the level set function to 3 (see figure 6.16b), the p-enrichment of the normal vector shows a considerable error reduction and an increased convergence rate. By increasing the polynomial degree of the level set function to 4 and 5 (see figures 6.16c and 6.16d, respectively), a convergence rate of 5.3 is achieved which is the same as in figure 6.8a with the polynomial degree of 8 for the level set.

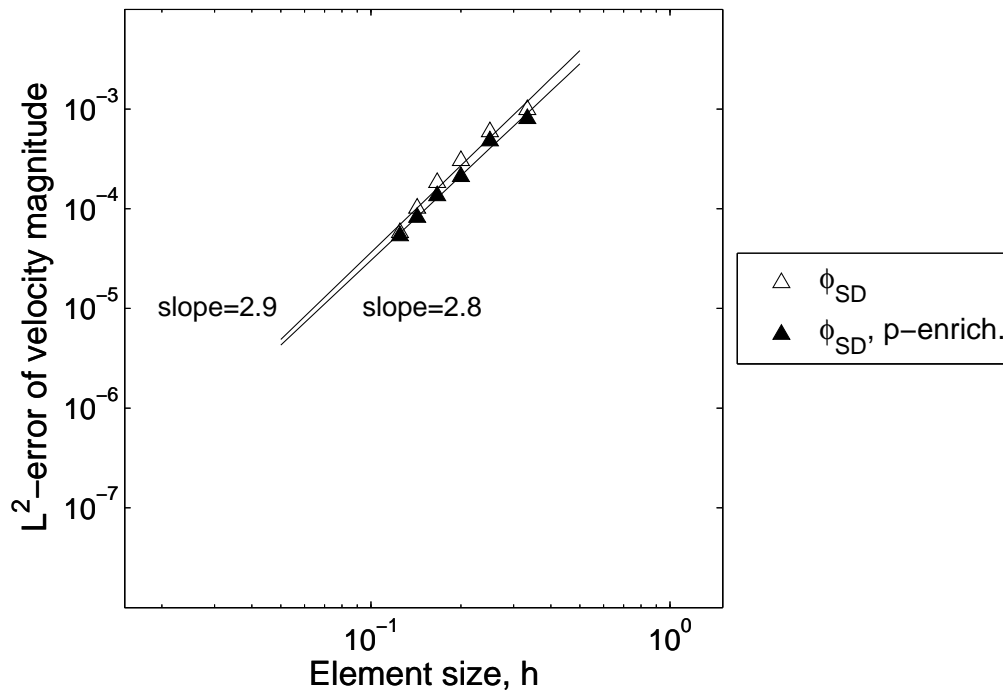
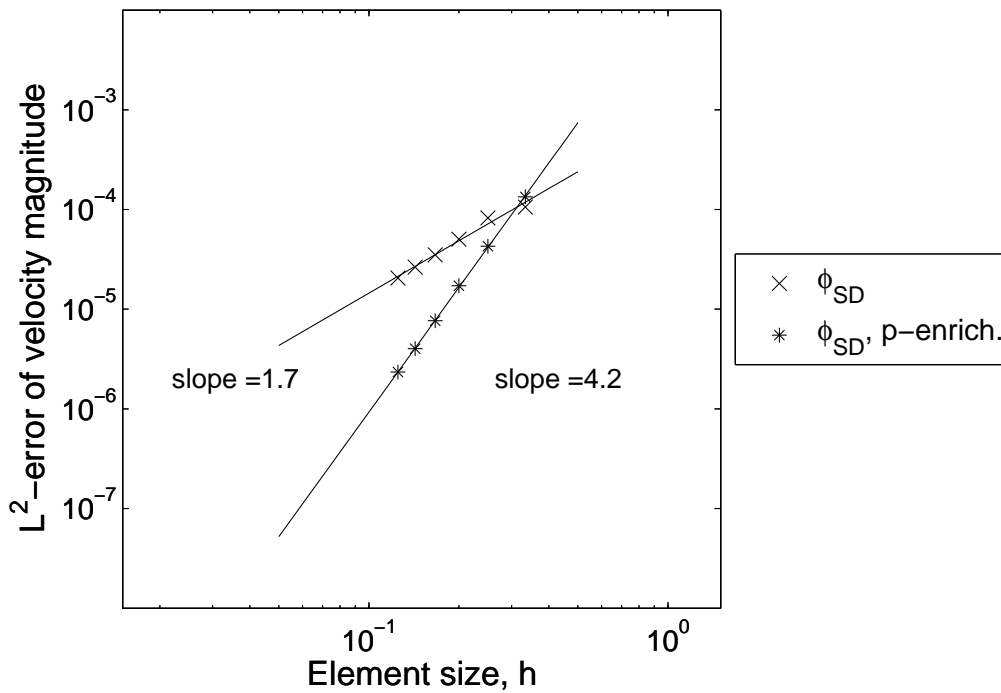
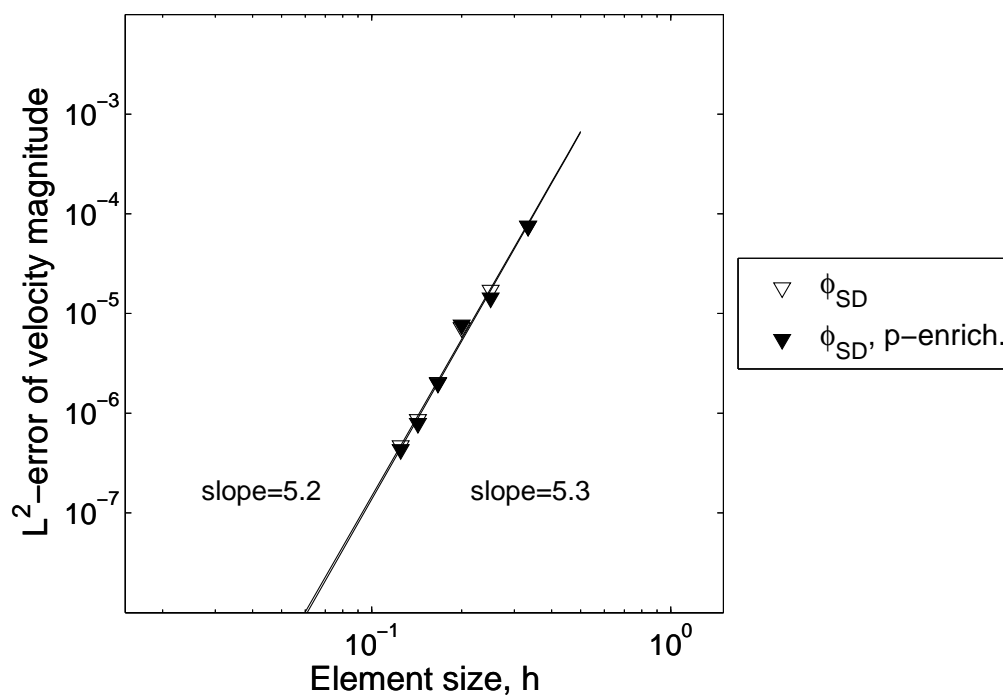
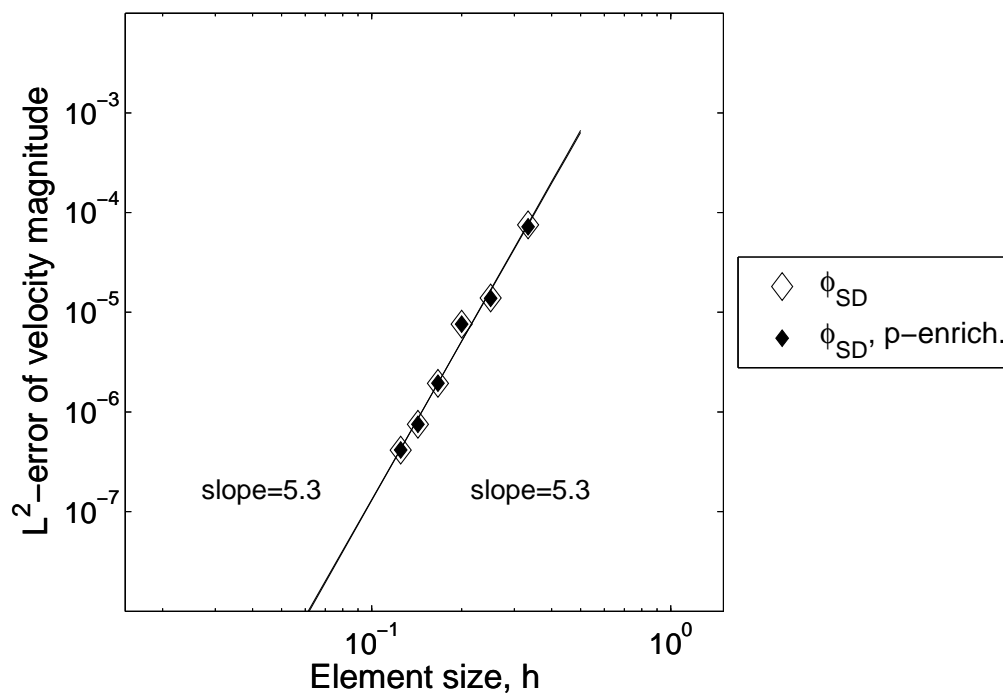
(a) $k_\phi = 2$ (b) $k_\phi = 3$

Figure 6.16: Effect of the p-enrichment of the normal vector on the h-convergence for the case of a stationary flow with pressure jump of 1 at the interface. L^2 -norm errors of the velocity magnitude are shown. Polynomial degrees of 8 are considered for the velocity and pressure. Polynomial degrees of 2 to 5 are considered for the level set function. The results correspond to the first pseudo-time step (to be continued on the next page).



(c) $k_\phi = 4$



(d) $k_\phi = 5$

Figure 6.16: Continued.

6.3.2 The signed-distance level set function

As mentioned before in section 6.1, a signed-distance level set function must be used due to the use of the regularized Heaviside and delta functions. On the other hand, a signed-distance function is not required for the computation of the normal vector and the curvature. As an example, consider the level set functions $\phi_1 = x^2 + y^2 - 1$ and $\phi_2 = \sqrt{x^2 + y^2} - 1$. Both define the same interface and have the same normal vector $\mathbf{n} = \frac{x\mathbf{i} + y\mathbf{j}}{\sqrt{x^2 + y^2}}$ and the same curvature field $\kappa = -\frac{1}{\sqrt{x^2 + y^2}}$. However, the projection of the signed-distance level set function, ϕ_2 , onto a DG-field produces additional errors because the square-root function is not contained in the polynomial space. These errors are also present in the computed normal vector and curvature. We call ϕ_1 the non signed-distance level set function in the following. The signed-distance, ϕ_{SD} , and non signed-distance, ϕ_{NS} , level set functions are shown in figure 6.17.

To eliminate the errors inherited from using a signed-distance level set function in computation of the normal vector and curvature, we use the ϕ_{NS} for the computation of the normal vector and curvature and the ϕ_{SD} for the regularized delta function. Although a non signed-distance formulation of the level set function does not exist in general, this approach covers a broad range of applications such as the formulation of a circle or a sphere that represents the surface of a droplet in $2D$ or $3D$. In practical cases, the interface will move as the level set function ϕ_{NS} is advected in the computational domain by solving an advection equation. The level set function ϕ_{SD} would then be a copy of the level set function ϕ_{NS} that is made signed-distance around the interface by solving a reinitialization equation in a narrow band.

To show how the combined $SD - NS$ level set functions can be effective, we perform a similar h-convergence study for the case of a stationary flow with pressure jump in section 6.2.1, figure 6.8a. A polynomial degree of 8 is considered for the velocity and pressure to minimize the error of integrating the regularized delta function. The results for the first pseudo-time step are shown in figure 6.18. Using a non signed-distance level set function, ϕ_{NS} , together with using the p-enrichment of the normal vector results in the convergence rates of 5.1 and 5.3 with polynomial degrees of 2 and 3 for the level set function, respectively. The convergence rate of 5.3 was achieved before (in figure 6.8a) with a polynomial degree of 8 for the level set function. This shows that applying the two ideas of the non signed-distance level set function and the p-enrichment of the normal vector could almost eliminate the errors related to the computation of the normal vector and curvature.

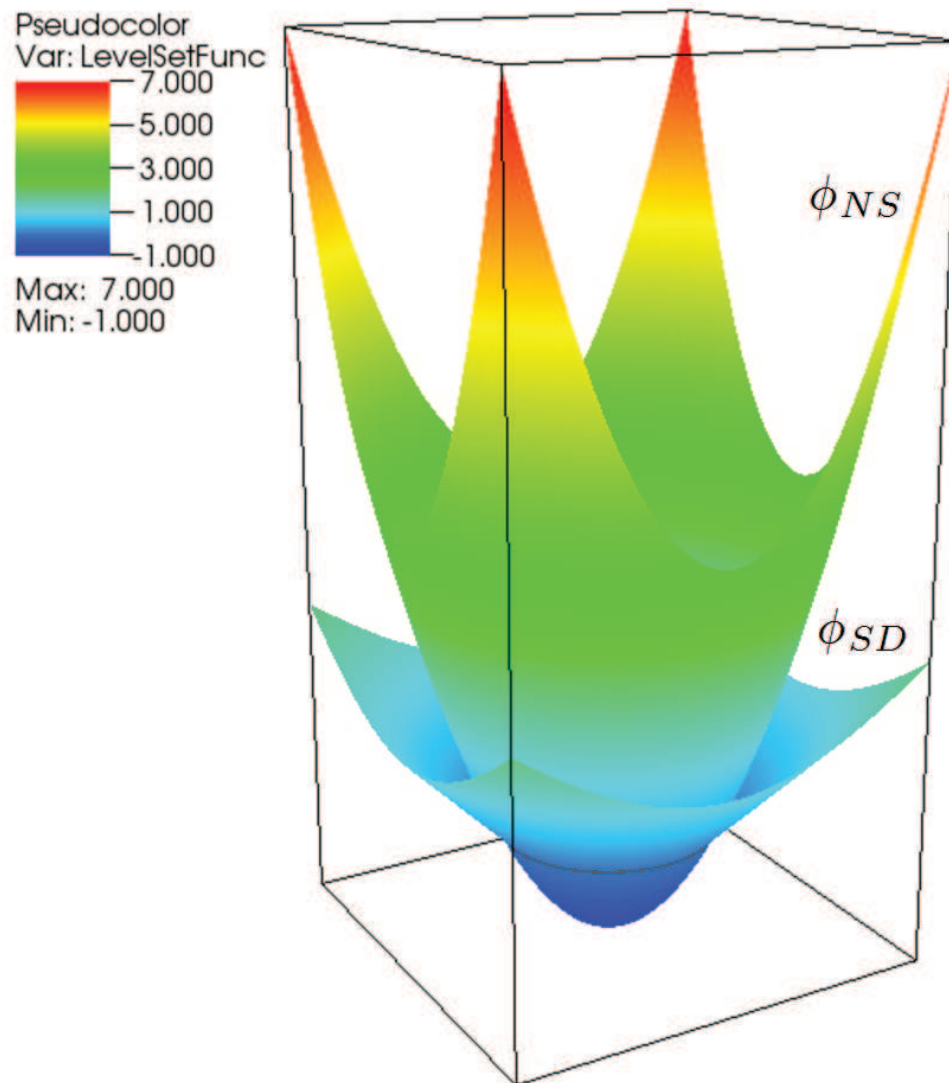


Figure 6.17: Representation of the interface by the zero iso-surface of the non signed-distance, $\phi_{NS} = x^2 + y^2 - 1$, and signed-distance, $\phi_{SD} = \sqrt{x^2 + y^2} - 1$, level set functions. The computational domain is a $[-2, 2] \times [-2, 2]$ square. A grid of 24×24 cells is employed. A polynomial degree of 5 is used for the level set function.

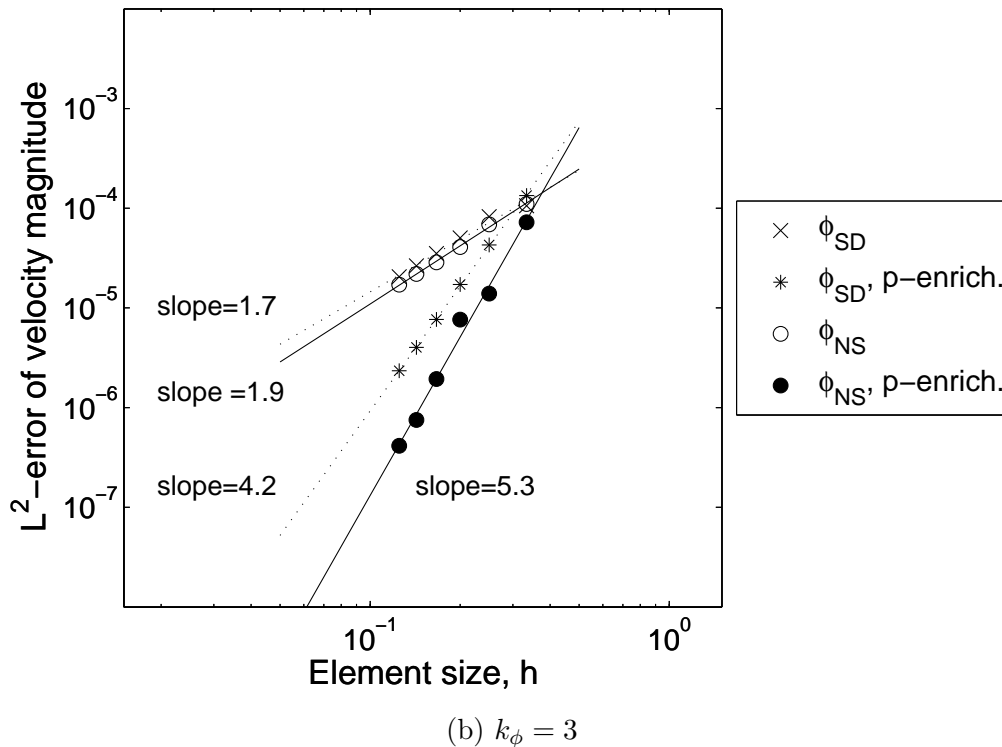
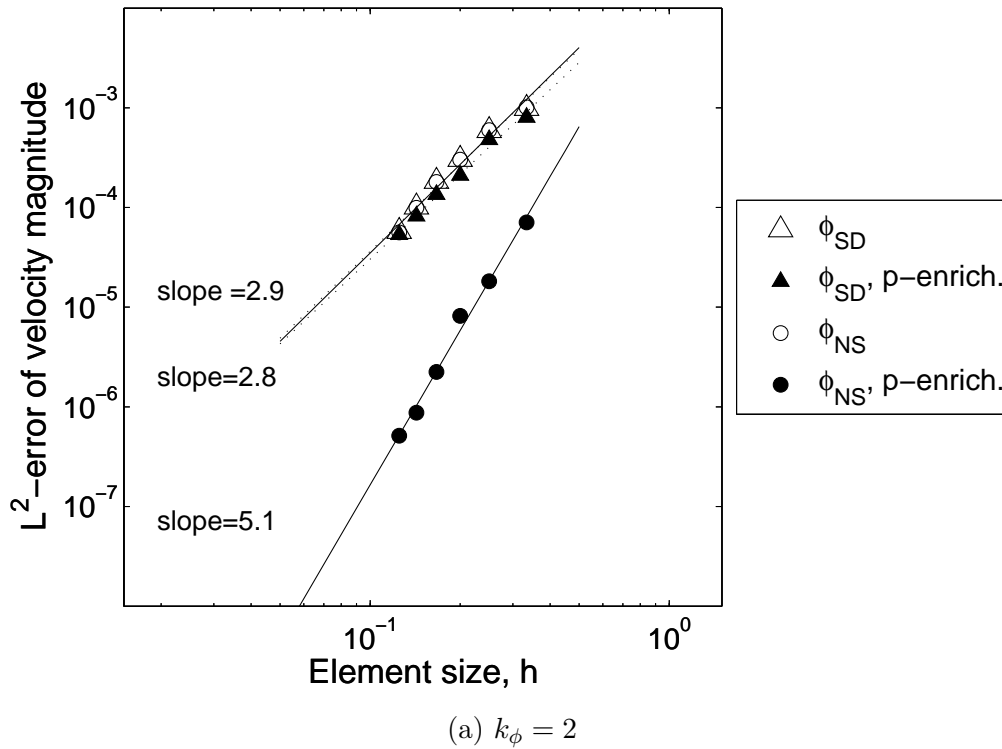


Figure 6.18: Effect of using a non signed-distance level set function for computing the normal vector and curvature and the p-enrichment of the normal vector on the h-convergence study for the case of a stationary flow with pressure jump of 1 at the interface. L^2 -norm errors of the velocity magnitude are shown. Polynomial degrees of 8 are considered for the velocity and pressure. Polynomial degrees of 2 and 3 are considered for the level set function. The results correspond to the first pseudo-time step.

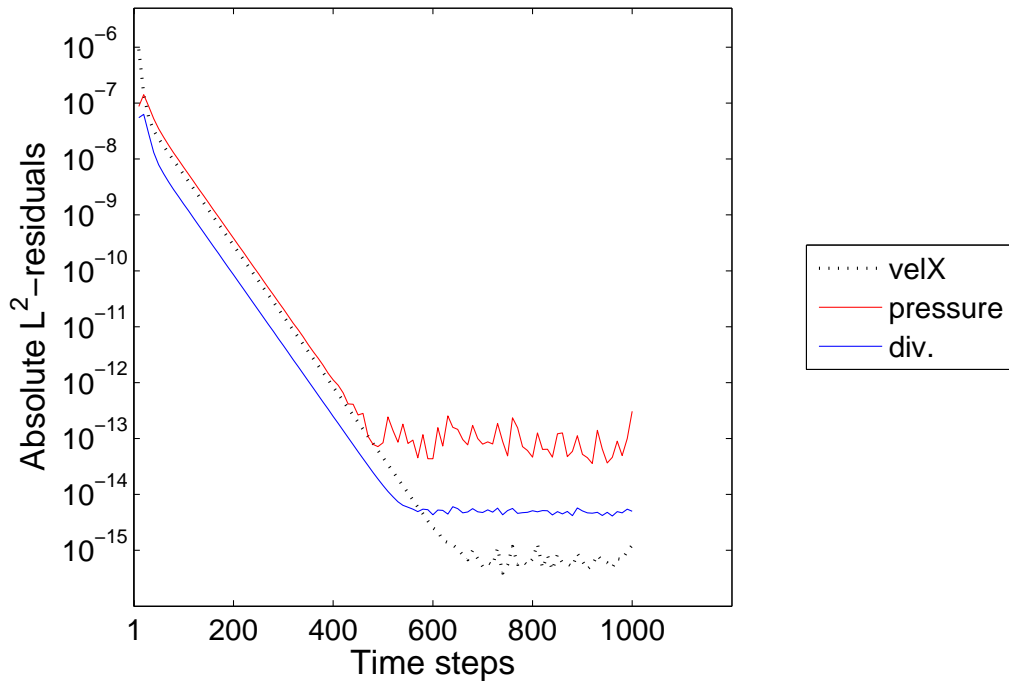
6.3.3 The Narrow band technique

As mentioned before in section 6.3.1, the normal vector and the curvature can be computed in a narrow band around the interface to reduce the computational costs. To show that performing computations on the narrow band does not influence the accuracy of the solution, we have repeated on the narrow band (as an example) the h-convergence study of figure 6.18b, which was performed for the whole domain, using the ϕ_{NS} and the p-enrichment of the normal vector. The results were the same. That is why they are not shown here.

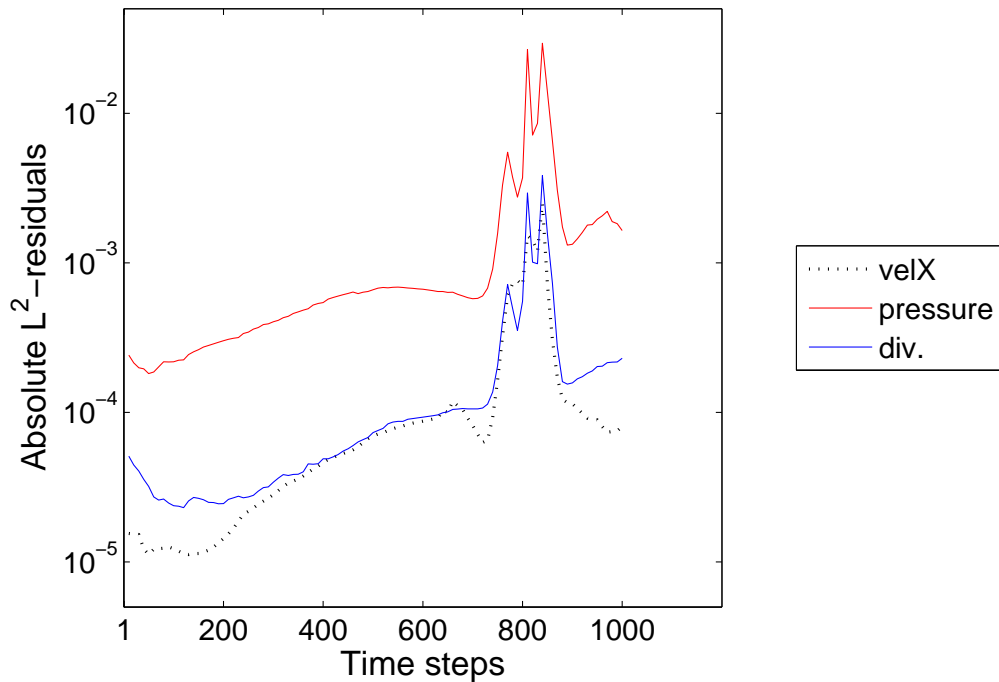
6.4 Test case: Moving interface

The test case of section 6.2 is repeated here with a moving interface model. According to the analytical solution, the interface does not move. The reason for performing this test is to study the stability of our numerical method in case of a moving interface. For the moving interface model, a level set advection equation is solved in each pseudo-time step. The residuals of the flow variables using the fixed interface and moving interface models are shown in figure 6.19. The numerical solution of this test case with the moving interface model did not show to be long term stable. Comparing to the fixed interface, it seems that there is an error accumulation which is related to the solution of the level set advection equation in each pseudo-time step.

As a method of error control, we performed a sub-cycling for the solution of the flow variables. That is, the level set has not been advected before the residuals at a single pseudo-time step of the flow solver have converged to a certain limit. For simplicity in referring to the results, we call this technique *frozen-interface* model. Comparing this technique to an implicit solver, one can say that the flow field is solved implicitly and the interface is advected explicitly although our flow solver as such is explicit. Using the frozen-interface model, a stable solution is achieved. The convergence history is shown in figure 6.19c. In figure 6.20, residuals of the pressure field using the fixed, moving and frozen interface models are compared. The flow field using the fixed interface and frozen interface models are almost the same, which are shown in figure 6.21.

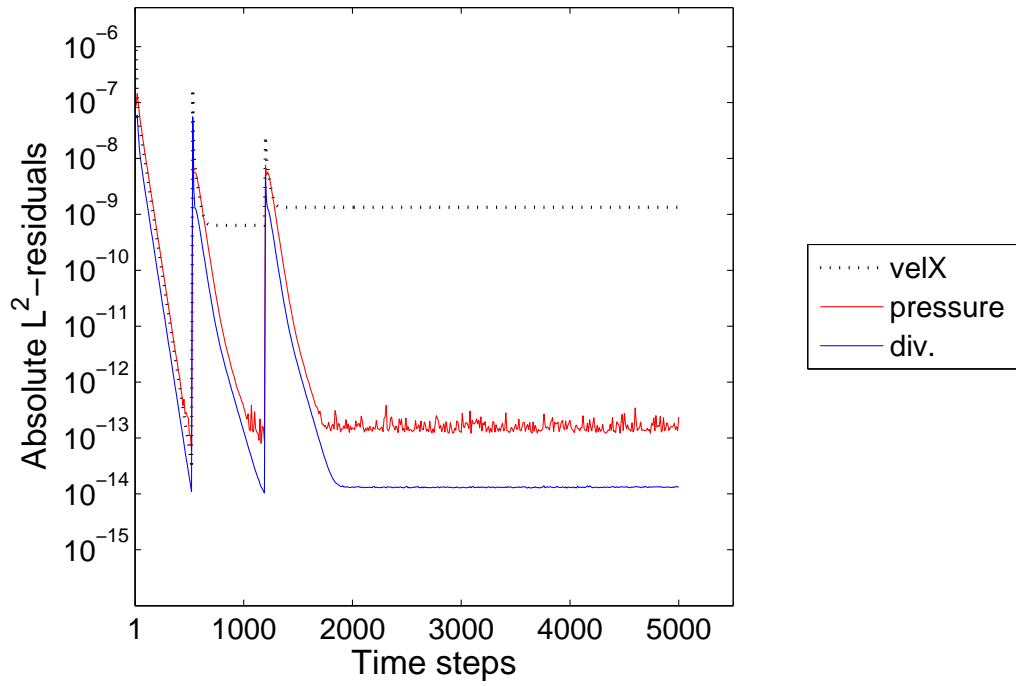


(a) The fixed interface



(b) The moving interface

Figure 6.19: Convergence history for the case of a stationary flow with pressure jump of 1 at the interface. L^2 -norm of the absolute residuals for the pressure, velocity in x -direction and divergence of the velocity are shown. (a) The fixed interface model; no level set advection is solved. (b) The moving interface model; the level set advection equation is solved in each time step. (c) The frozen interface model; the level set advection equation is solved only if the divergence of the velocity is reduced to a certain threshold.



(c) The frozen interface

Figure 6.19: Continued.

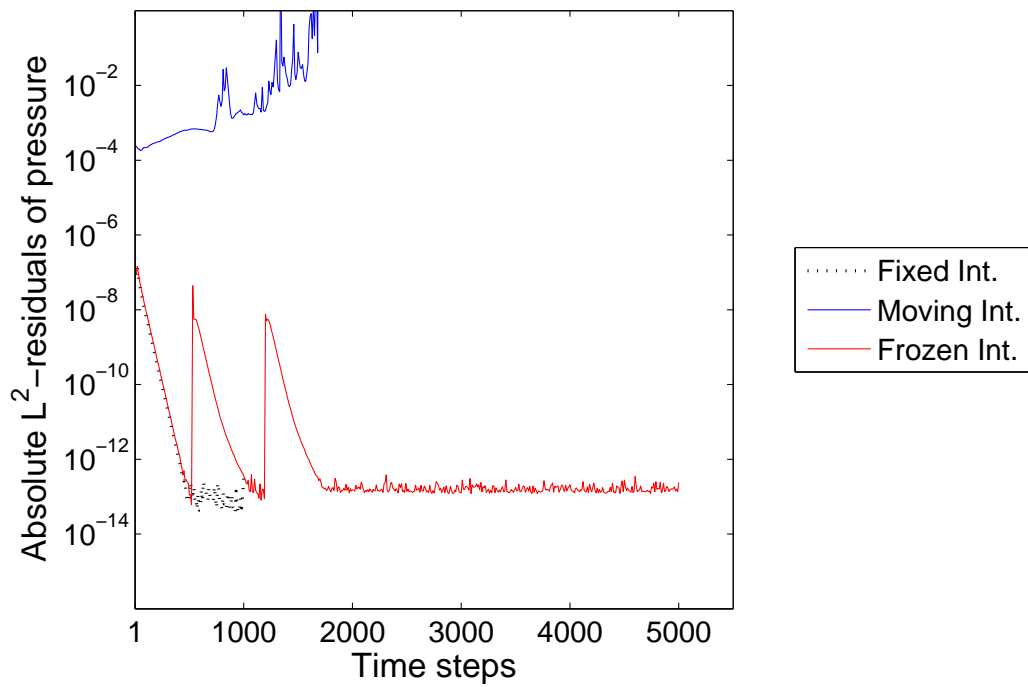
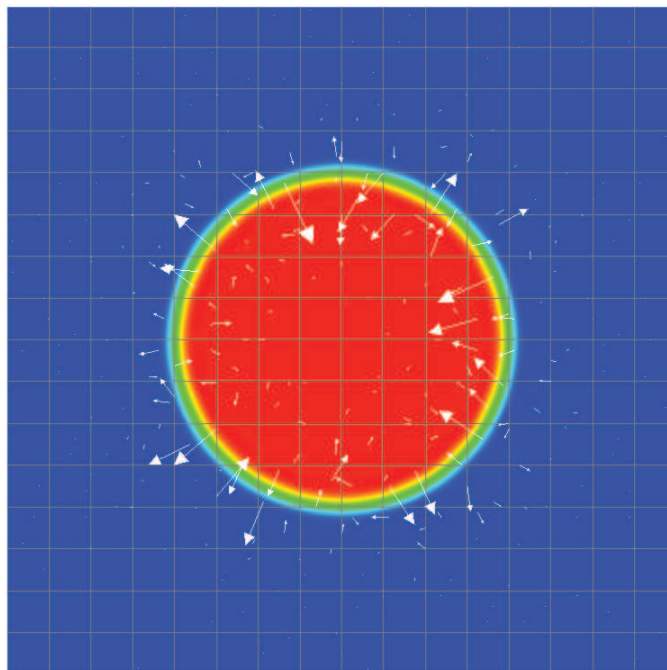


Figure 6.20: Comparison of the fixed, moving and frozen interface models. The absolute residuals of the pressure are shown, which are taken from figure 6.19.

Pseudocolor
 Var: Phi
 1.032
 0.7706
 0.5087
 0.2469
 -0.01493
 Max: 1.032
 Min: -0.01493

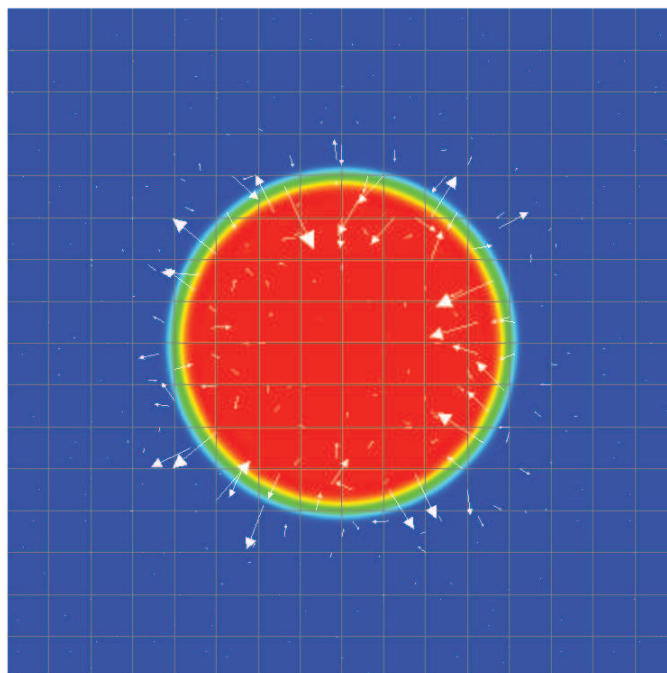
Vector
 Var: Velocity
 Max: 0.0003940
 Min: 5.381e-008



(a) The fixed interface

Pseudocolor
 Var: Phi
 1.033
 0.7707
 0.5088
 0.2469
 -0.01501
 Max: 1.033
 Min: -0.01501

Vector
 Var: Velocity
 Max: 0.0003959
 Min: 2.514e-008



(b) The frozen interface

Figure 6.21: The flow field for the case of a stationary flow with pressure jump of 1 at the interface. Contours of the pressure and vectors of the velocity are shown. (a) The fixed interface model (repeated from figure 6.5b); no level set advection is solved. (b) The frozen interface model; the level set advection equation is solved only if the divergence of the velocity is reduced to a certain threshold.

7 Solving the electrostatics equations

The content of this chapter concerns solving the appropriate form of the governing equations of the electric problem to find the electric potential and the electric field.

We have considered a perfect dielectric droplet suspended in another perfect dielectric medium. There is a jump in the dielectric properties at the interface with the permittivity ratio $\frac{\varepsilon_2}{\varepsilon_1}$, where indices 1 and 2 refer to the surrounding medium and the droplet, respectively. As both fluids are considered as perfect dielectrics, we should solve equation (3.12) to find the electric potential,

$$\nabla \cdot (\varepsilon(\phi)\nabla\Phi) = 0$$

The boundary conditions are shown in figure (figure 7.1). There is a potential difference of U applied in y -direction but there is no potential applied in x -direction. The spatial

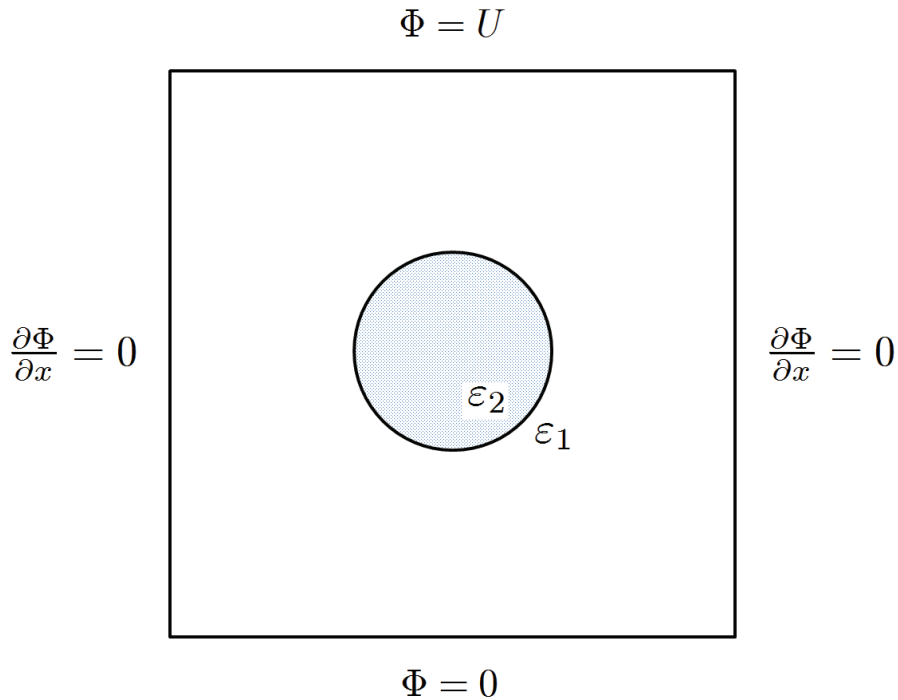


Figure 7.1: Boundary conditions for the case of a droplet suspended in another immiscible fluid with a jump in the dielectric property at the interface.

discretization of the above equation involves discretizing the linear 2nd order derivative terms of the variable Φ . The DG discretization of the second order linear terms of the form $\nabla^2 u$ is introduced in section 4.2.1.1. Here, we consider the form $\nabla \cdot (a(\mathbf{x})\nabla u)$,

where a is a coefficient. The auxiliary variable $\boldsymbol{\sigma}$ is defined as $a\nabla u$. Therefore, in case of a continuous coefficient, the discretized form would be

$$\begin{aligned} \int_{K_j} \nabla \cdot \boldsymbol{\sigma}_j^h \phi_{jm} d\mathbf{x} &= - \int_{K_j} a_j^h \nabla u_j^h \cdot \nabla \phi_{jm} d\mathbf{x} \\ &+ \int_{\partial K_j} \hat{\mathbf{n}} \cdot \boldsymbol{\sigma}^* \phi_{jm} d\mathbf{x} - \int_{\partial K_j} a_j^h (u^* - u_j^h) \hat{\mathbf{n}} \cdot \nabla \phi_{jm} d\mathbf{x} \end{aligned} \quad (7.1)$$

$$0 \leq m \leq N_p - 1$$

Using the SIPG method, the following numerical fluxes are applicable,

$$u^* = \{u\}, \quad (7.2a)$$

$$\boldsymbol{\sigma}^* = \{a\nabla u\} - \mu_P [[au]], \quad (7.2b)$$

where μ_P is the penalty parameter, which is found from equation (4.9). The penalty parameter is necessary for the stabilization and it compensates for the inter-cell discontinuities in DG. The penalty parameter is adjusted through the coefficient α_P (see equation 4.9).

In our case, the variable u is Φ , the variable $\boldsymbol{\sigma}$ is $\varepsilon\nabla\Phi$ and the coefficient a is the permittivity ε , which is not constant and has a jump at the interface. For solving the elliptic problems with discontinuous coefficients using DG, Dryja (Dryja 2003) has suggested a harmonic average with diffusion-dependent weights to formulate the interior penalty discretization. In this formulation, he has penalized the interface and boundary jumps using a diffusion-dependent penalty parameter. Taking the notation from (Di Pietro & Ern 2012),

$$u^* = \{u\}, \quad (7.3a)$$

$$\boldsymbol{\sigma}^* = \{a\nabla u\}_w - \mu_P \gamma_P [[u]], \quad (7.3b)$$

$$\{a\nabla u\}_w = \frac{2a_1 a_2}{a_1 + a_2} \{\nabla u\},$$

$$\gamma_P = \frac{2a_1 a_2}{a_1 + a_2}.$$

The above formulation from Dryja has the restriction that the jump in the coefficient (at the interface) must lie on the cell boundaries. This method is not applicable to our problem, where the interface crosses the computational cells. Therefore, we regularize the jump in the coefficient at the interface (see section 6.1) and use the SIPG method, equation 7.2. The discretized system of equations is solved using the PARDISO direct solver (see section 4.2.2).

7.1 Electric potential

The computational domain is considered as a $[-2, 2] \times [-2, 2]$ square. The droplet has a non-dimensional radius of 1. A Cartesian grid of 32×32 cells and a polynomial degree

of 8 are adopted. A half-thickness of $\epsilon = h = \frac{1}{8}$ is considered for the diffuse interface. Contours of the computed electric potential for three permittivity ratios of 2, 5 and 10 are shown in figure 7.2. For the higher ratio of 10, the solution is not smooth enough and the discontinuity of the solution at the cell boundaries is visible in figure 7.2c.

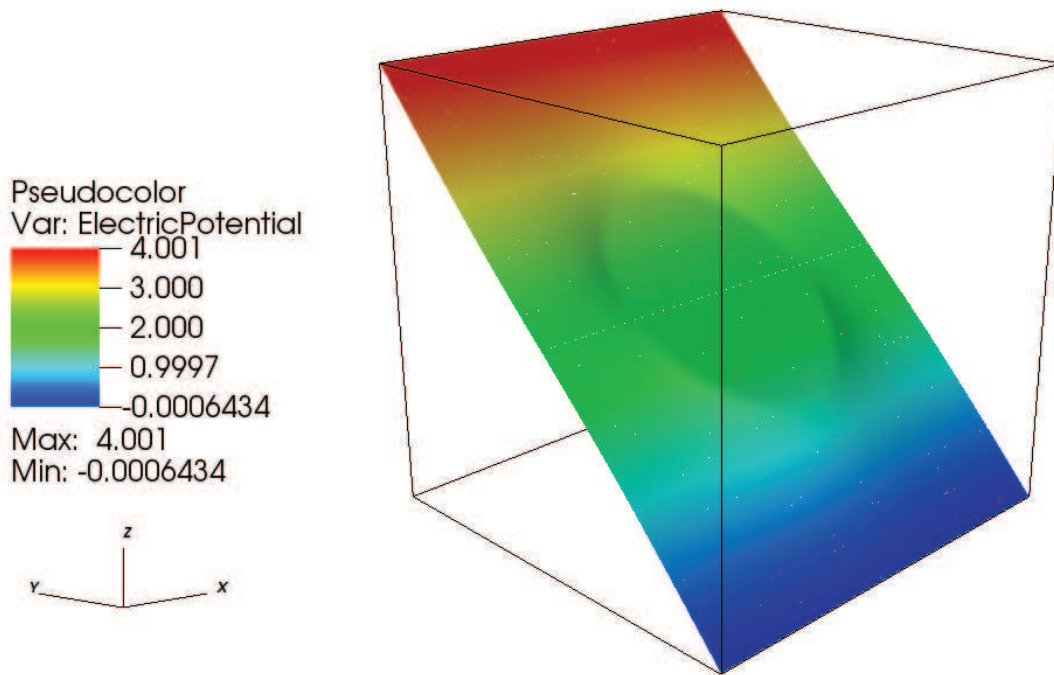
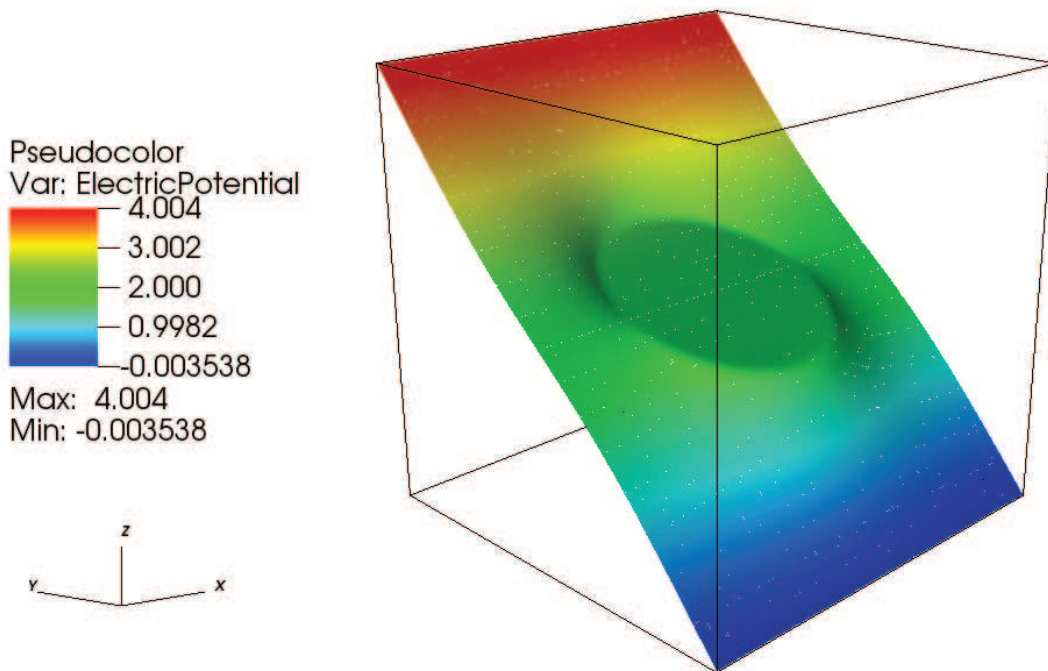
(a) $\frac{\epsilon_2}{\epsilon_1} = 2$ (b) $\frac{\epsilon_2}{\epsilon_1} = 5$

Figure 7.2: Effect of increasing the ratio of the jump in the dielectric property at the interface. Contours of the electric potential are shown for different permittivity ratios. The SIPG method with a penalty parameter coefficient of $\alpha_P = 1$ is used. The computational domain is a $[-2, 2] \times [-2, 2]$ square. A grid of 32×32 cells and a polynomial degree of 8 are employed.

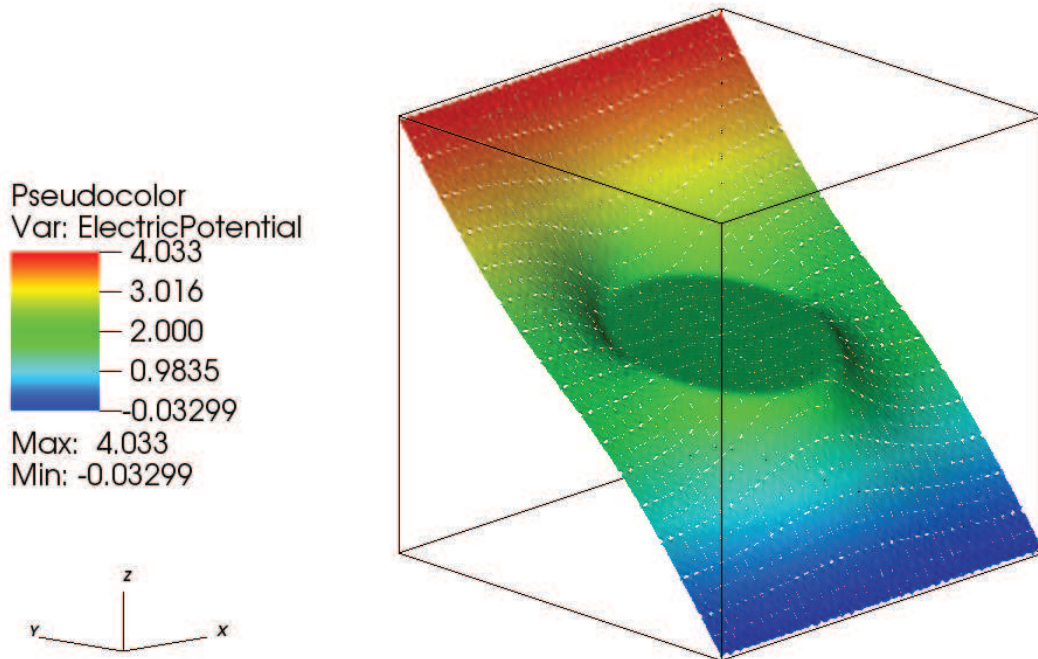
(c) $\frac{\epsilon_2}{\epsilon_1} = 10$

Figure 7.2: Continued.

7.2 Electric field

The electric field is computed from the definition of the electric potential, $\mathbf{E} = -\nabla\Phi$, see section 2.1.1. In order to reduce the effect of the discontinuity of the computed electric potential at the cell boundaries, the gradient operator is computed using numerical flux functions. We have applied this method to solve the single phase Navier-Stokes equations (see section 5.4). Contours of the computed electric field for three permittivity ratios of 2, 5 and 10 are shown in figures 7.3, 7.4 and 7.5, respectively. For the higher ratio of 10, the computed electric field is not acceptable. There are high non-physical jumps at the cell boundaries which are the result of applying the gradient operator on the electric potential that has discontinuities on the cell boundaries (figure 7.2c). To find a reasonable electric field, we have refined the grid to 64×64 cells. The computed electric potential and electric fields in x - and y - directions are compared with the results with the 32×32 grid in figures 7.6, 7.7 and 7.8, respectively. Using the fine grid, the computed electric potential and electric fields are reasonable. Suppression of the large oscillations by the grid refinement confirms that the inter-cell discontinuity of the solution of the electric potential is the reason for the oscillations in the computed electric field. This shows the requirement for modification of the SIPG method for additional stabilization, which will be discussed in the next sections.

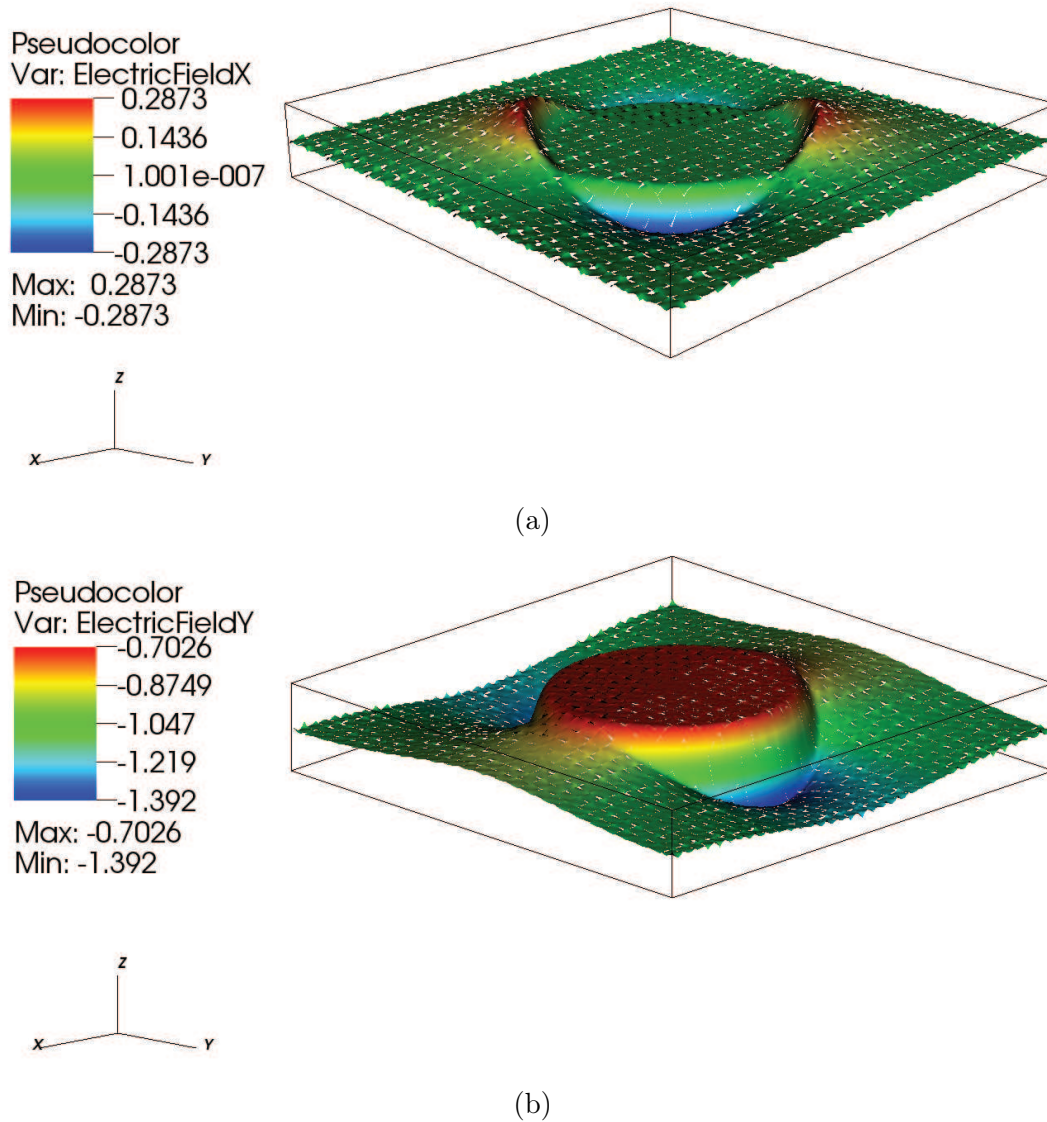


Figure 7.3: Contours of the electric field for the test case with a jump of ratio 2 in the dielectric property at the interface. The SIPG method with a penalty parameter coefficient of $\alpha_P = 1$ is used. The computational domain is a $[-2, 2] \times [-2, 2]$ square. A grid of 32×32 cells is employed. Polynomial degrees of 8 and 7 are used for the electric potential and electric field, respectively. (a) The electric field in x -direction. (b) The electric field in y -direction.

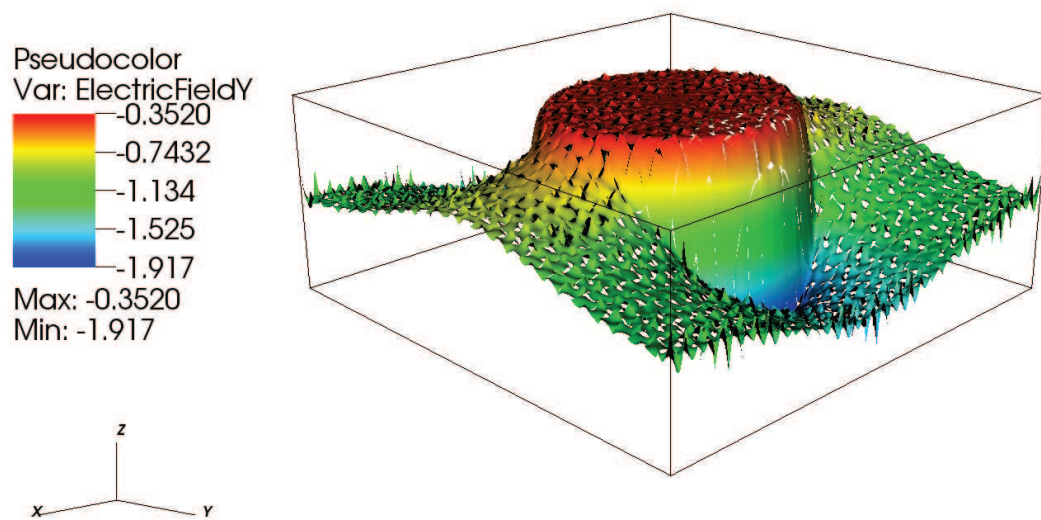
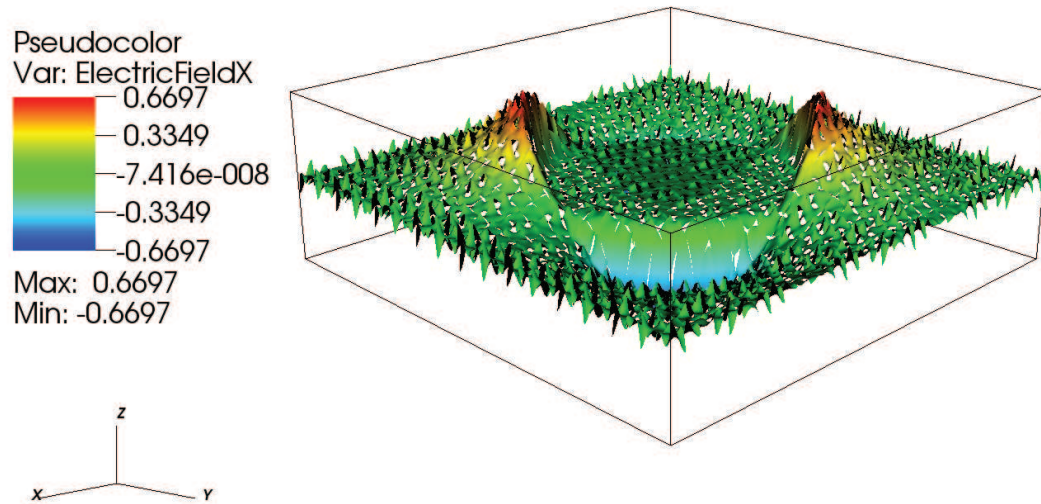


Figure 7.4: Contours of the electric field for the test case with a jump of ratio 5 in the dielectric property at the interface. The SIPG method with a penalty parameter coefficient of $\alpha_P = 1$ is used. The computational domain is a $[-2, 2] \times [-2, 2]$ square. A grid of 32×32 cells is employed. Polynomial degrees of 8 and 7 are used for the electric potential and electric field, respectively. (a) The electric field in x -direction. (b) The electric field in y -direction.

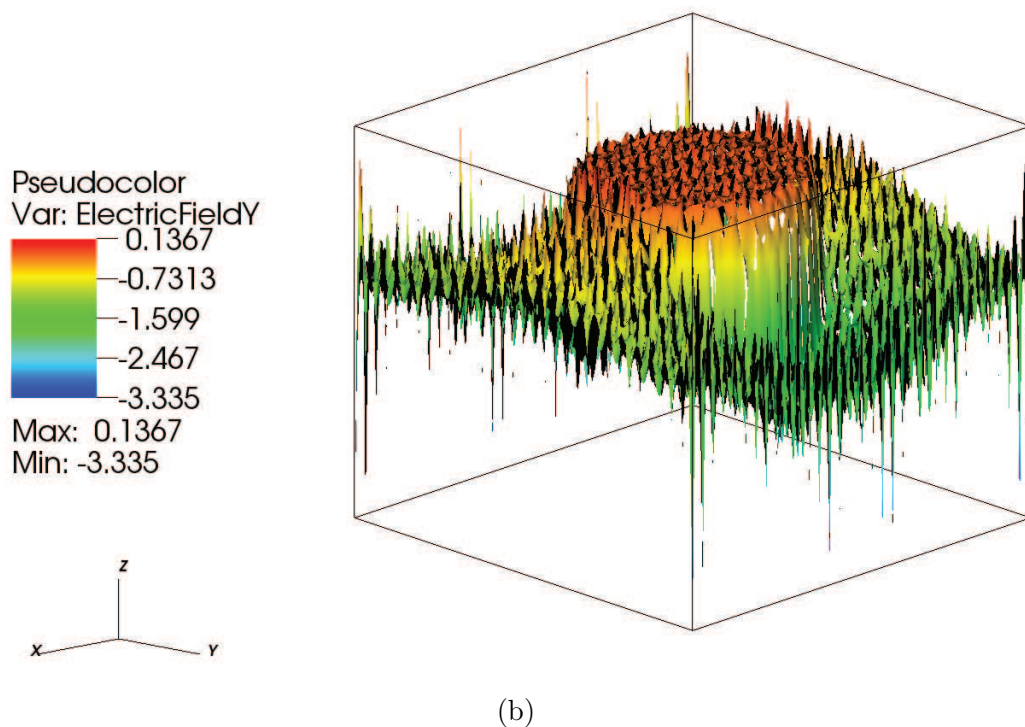
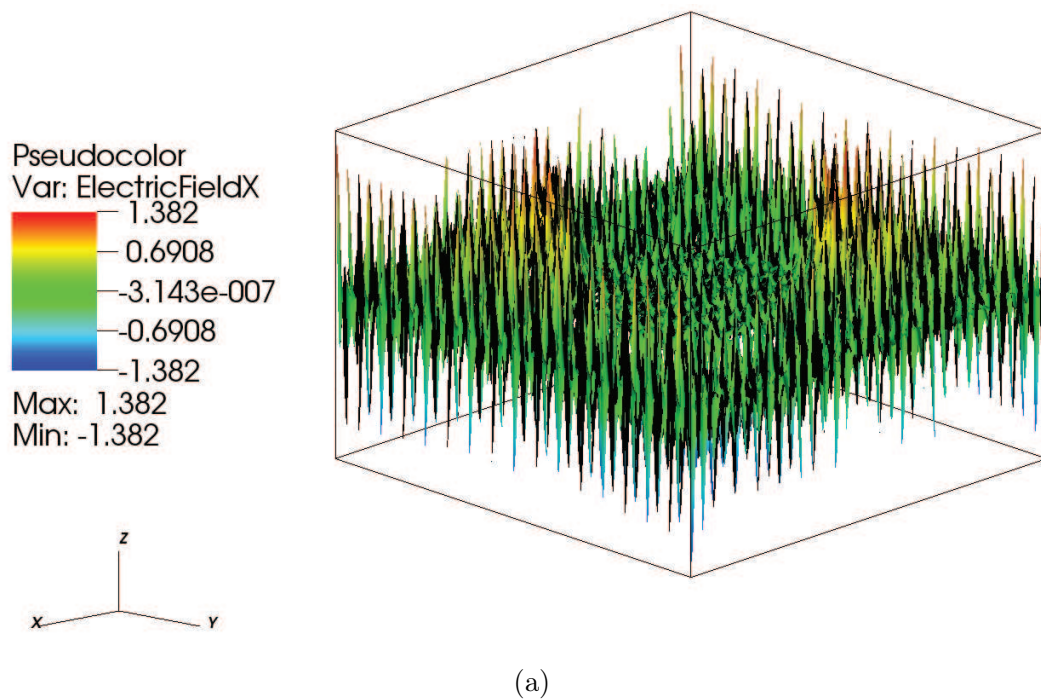


Figure 7.5: Contours of the electric field for the test case with a jump of ratio 10 in the dielectric property at the interface. The SIPG method with a penalty parameter coefficient of $\alpha_P = 1$ is used. The computational domain is a $[-2, 2] \times [-2, 2]$ square. A grid of 32×32 cells is employed. Polynomial degrees of 8 and 7 are used for the electric potential and electric field, respectively. (a) The electric field in x -direction. (b) The electric field in y -direction.

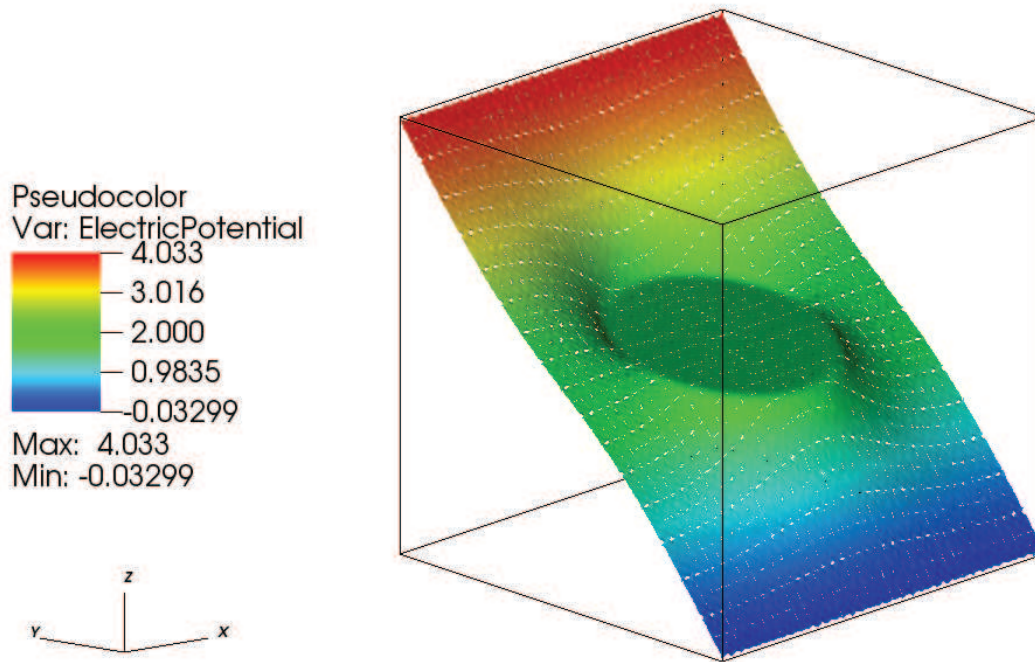
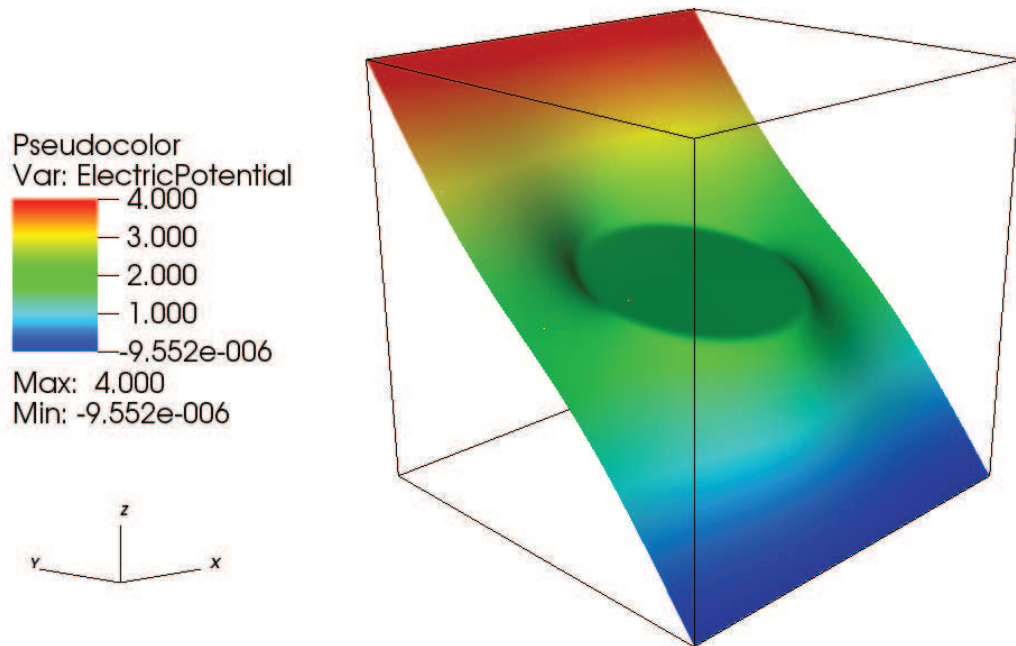
(a) $N = 32$ (b) $N = 64$

Figure 7.6: Effect of the grid refinement for the test case with a jump of ratio 10 in the dielectric property at the interface. Contours of the electric potential are shown. The SIPG method with a penalty parameter coefficient of $\alpha_P = 1$ is used. The computational domain is a $[-2, 2] \times [-2, 2]$ square. Grids of $N \times N$ cells and a polynomial degree of 8 are employed.

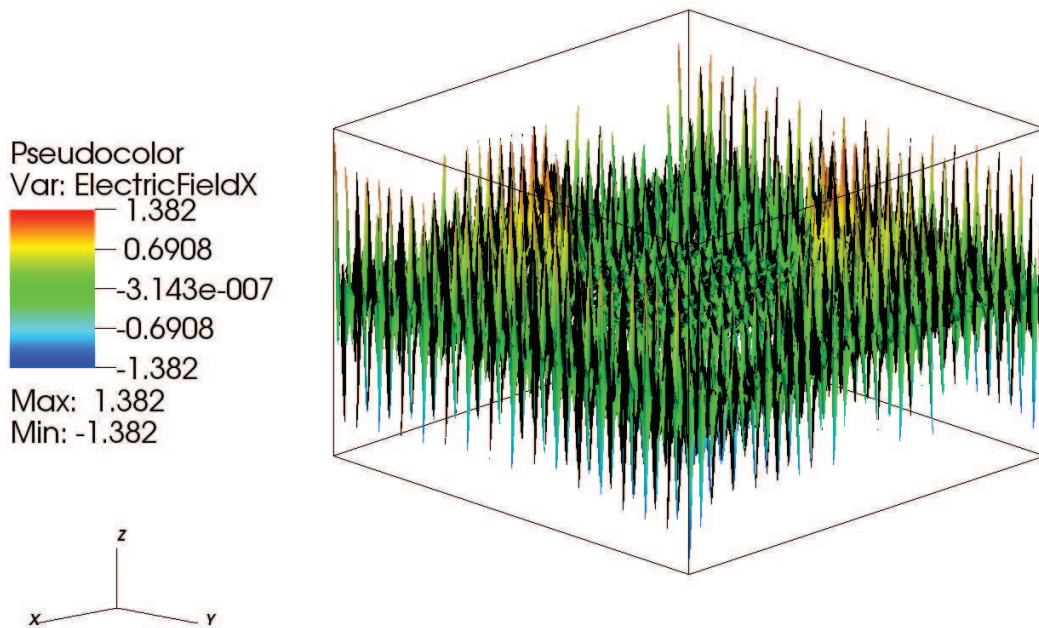
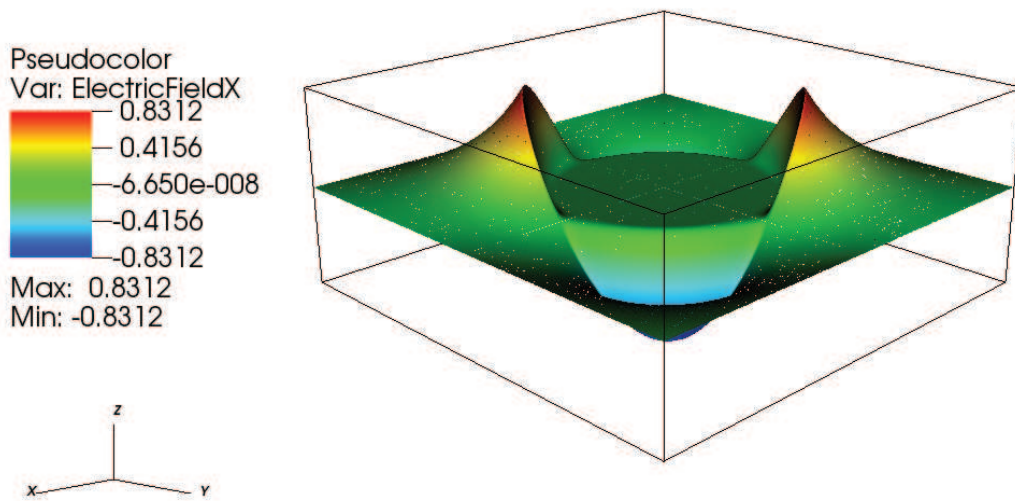
(a) $N = 32$ (b) $N = 64$

Figure 7.7: Effect of the grid refinement for the test case with a jump of ratio 10 in the dielectric property at the interface. Contours of the electric field in x -direction are shown. The SIPG method with a penalty parameter coefficient of $\alpha_P = 1$ is used. The computational domain is a $[-2, 2] \times [-2, 2]$ square. Grids of $N \times N$ cells are employed. Polynomial degrees of 8 and 7 are used for the electric potential and electric field, respectively.

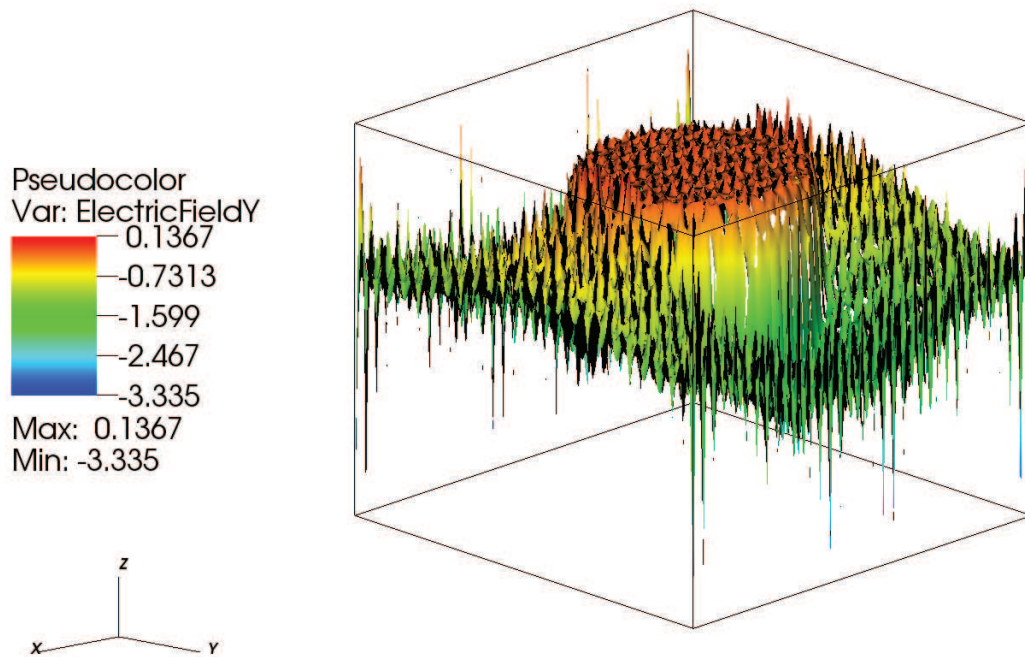
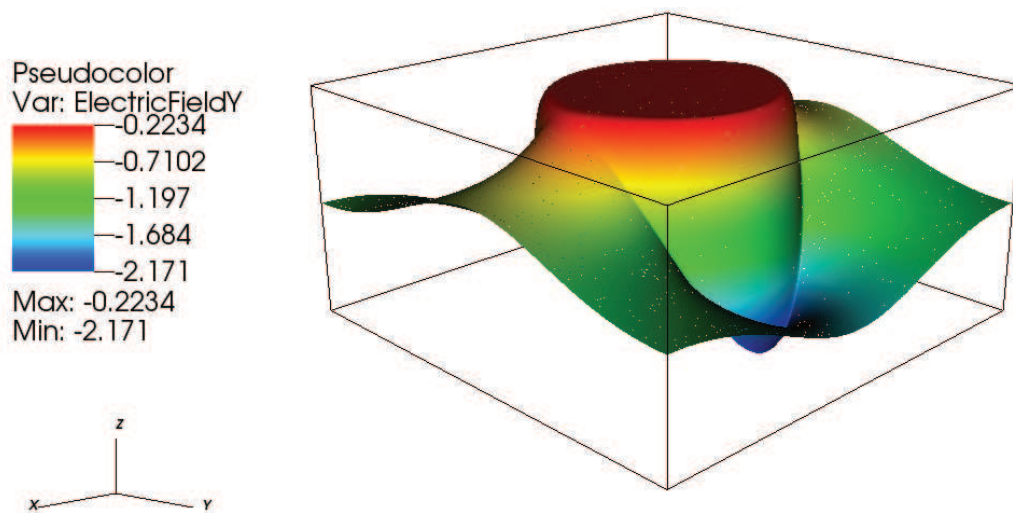
(a) $N = 32$ (b) $N = 64$

Figure 7.8: Effect of the grid refinement for the test case with a jump of ratio 10 in the dielectric property at the interface. Contours of the electric field in y -direction are shown. The SIPG method with a penalty parameter coefficient of $\alpha_P = 1$ is used. The computational domain is a $[-2, 2] \times [-2, 2]$ square. Grids of $N \times N$ cells are employed. Polynomial degrees of 8 and 7 are used for the electric potential and electric field, respectively.

7.3 Convergence study

A convergence study for the test case with a jump of ratio 10 in the dielectric property at the interface is performed using grids of $N \times N$ cells, $N = 32, 36, 40, 44, 48, 56$ and 64 . For the coarse grid ($N = 32$), $\epsilon = h$ and for the fine grid ($N = 64$), $\epsilon = 2h$, while $\epsilon = \frac{1}{8}$. Using each grid, polynomial degrees of 2 to 8 are applied. For each grid, the solution using the polynomial degree of 8 is considered as the reference solution. Relative L^2 -norm errors of the electric potential, $\frac{\|\Phi - \Phi_{ref}\|_2}{\|\Phi_{ref}\|_2}$, and the electric field, $\frac{\|\mathbf{E} - \mathbf{E}_{ref}\|_2}{\|\mathbf{E}_{ref}\|_2}$, on each grid are computed with respect to the corresponding reference solution and are shown in figures 7.9 and 7.10, respectively. These results are obtained using a penalty parameter coefficient of $\alpha_P = 10$ to reduce the inter-cell discontinuity and suppress the oscillations which were present in the contours of the electric potential and the electric field using $\alpha_P = 1$ (figures 7.2c and 7.5). The results in figures 7.9 and 7.10 show that the errors do not decrease exponentially as they should. Therefore, using only a high penalty parameter coefficient is not the appropriate way of dealing with jumps at the interface.

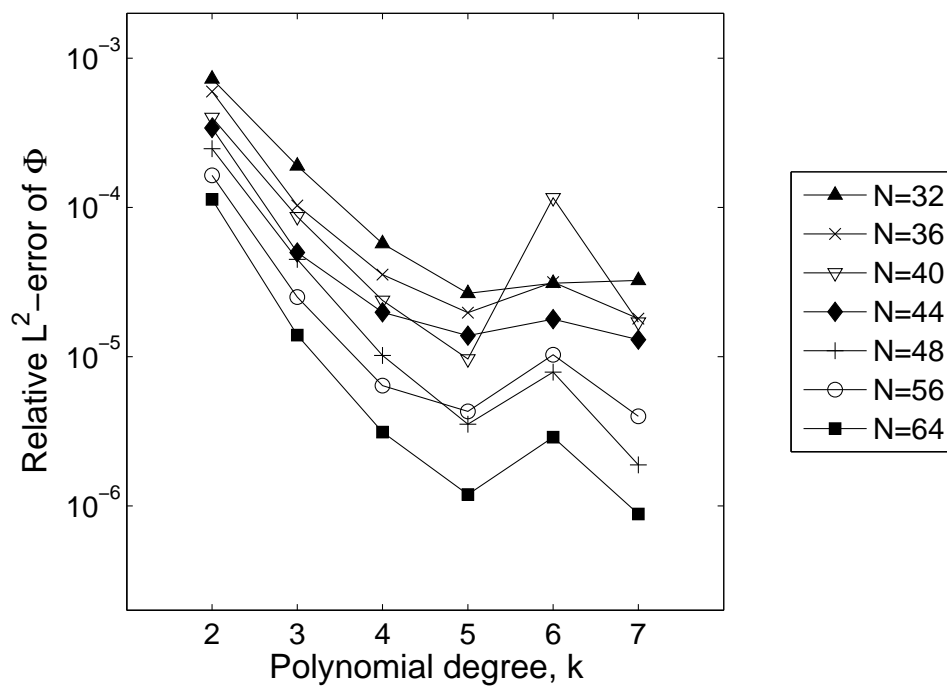
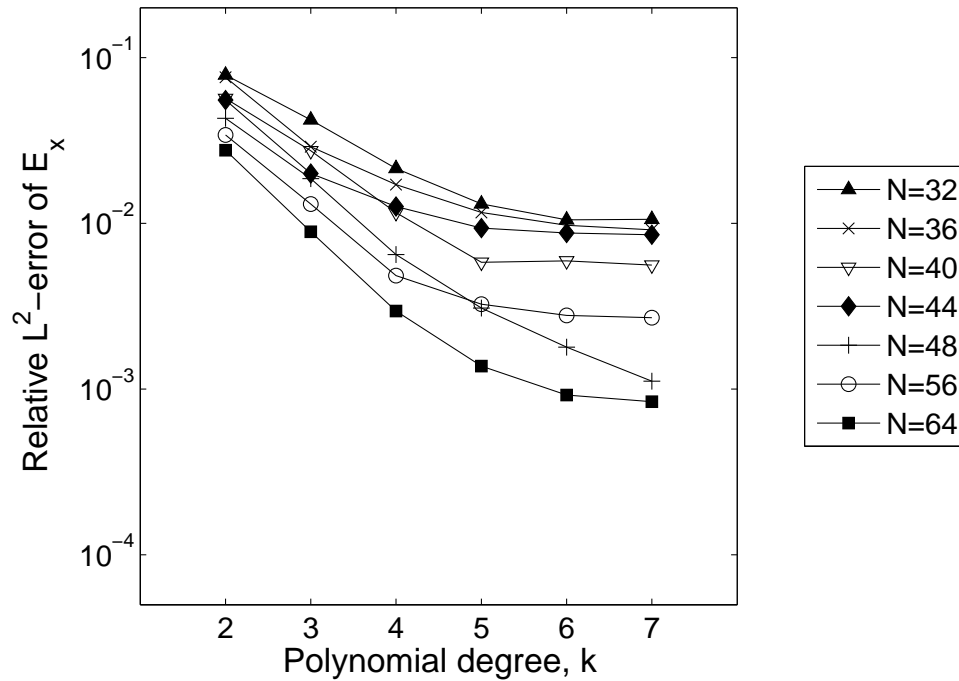
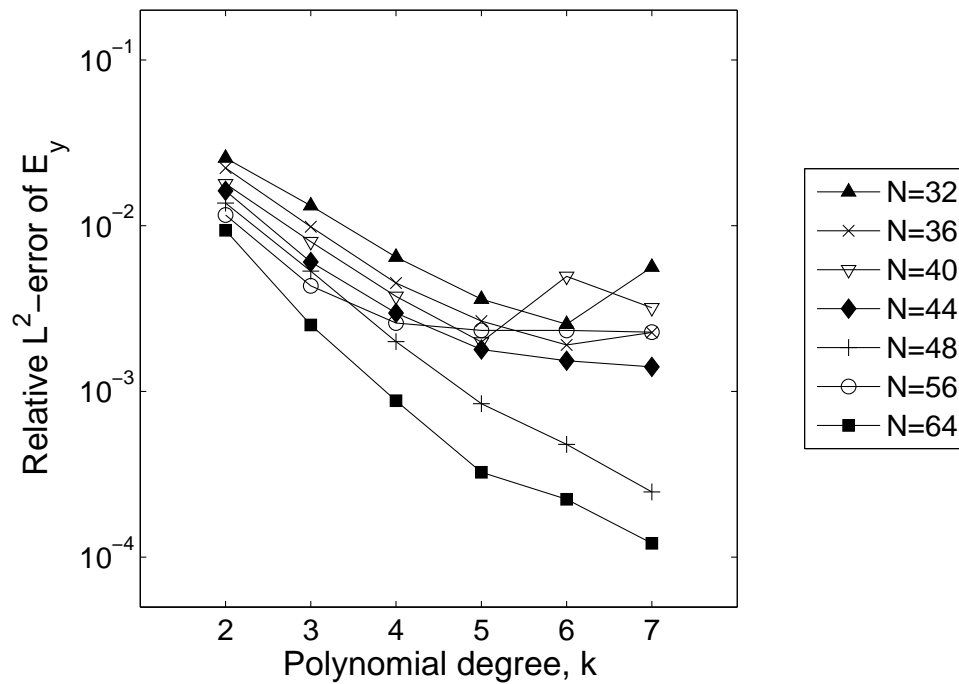


Figure 7.9: Convergence study for the test case with a jump of ratio 10 in the dielectric property at the interface. L^2 -norm errors of the electric potential are shown. The SIPG method with a penalty parameter coefficient of $\alpha_P = 10$ is used. The computational domain is a $[-2, 2] \times [-2, 2]$ square. Grids of $N \times N$ cells are employed.



(a)



(b)

Figure 7.10: Convergence study for the test case with a jump of ratio 10 in the dielectric property at the interface. L^2 -norm errors of the electric field are shown. The SIPG method with a penalty parameter coefficient of $\alpha_P = 10$ is used. The computational domain is a $[-2, 2] \times [-2, 2]$ square. Grids of $N \times N$ cells are employed. (a) Electric field in x -direction. (b) Electric field in y -direction.

7.4 Stabilization method

Considering the SIPG method, the numerical flux function for the variable, $\sigma^* = \{a\nabla u\} - \mu_P[[au]]$, consists of a penalty term which is proportional to the jump in the variable u . This term is added to stabilize the solution and approaches zero as the discontinuity of the solution becomes negligible. Concerning the numerical test case considered in the previous sections, the coefficient a has a jump at the interface which resulted in a considerable discontinuity of the solution at the cell boundaries. Therefore, it makes sense to modify the penalty term.

7.4.1 Average coefficient for the penalty term

A first idea is to use the average of the coefficient a in the penalty term. So we introduce a modified form of the SIPG method with the average coefficient in the penalty term (SIPG-ACP),

$$u^* = \{u\}, \quad (7.4)$$

$$\sigma^* = \{a\nabla u\} - \mu_P\{a\}[[u]] \quad (7.5)$$

The previous simulations are repeated for the permittivity ratio of 10. The results are shown in figure 7.11 for the electric potential. In figures 7.12 and 7.13 the electric fields in x and y -directions are shown. The computed electric field, using the coarse grid (32×32 cells) with a penalty parameter coefficient of $\alpha_P = 1$, shows a substantial improvement with respect to the results with the SIPG formulation with the same coefficient (figures 7.7a and 7.8a). The solution with the fine grid (64×64 cells) provides the same results that were achieved with the SIPG formulation.

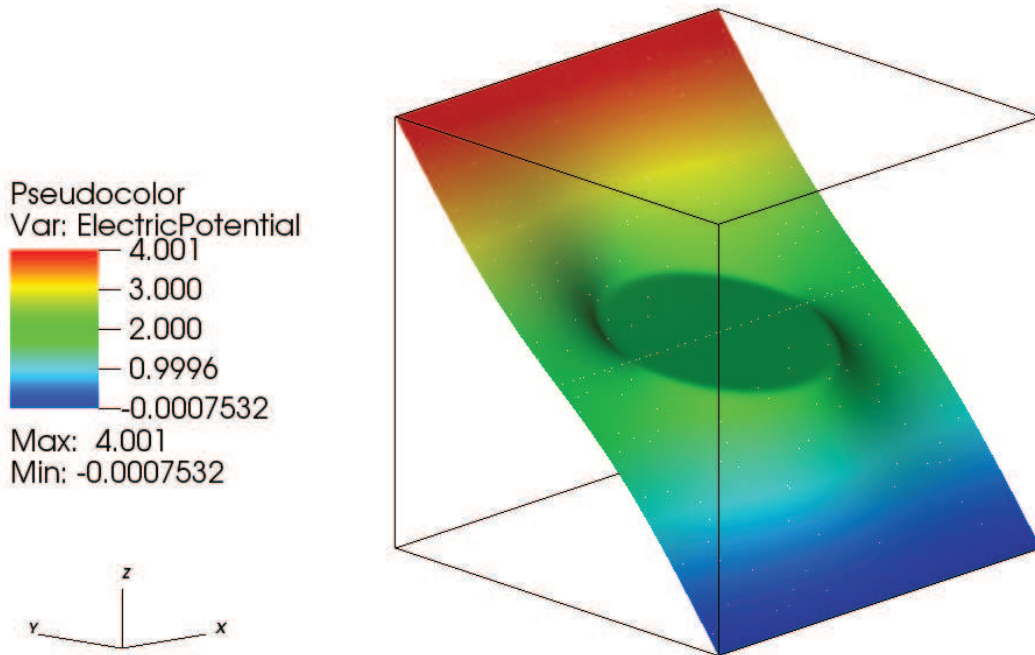
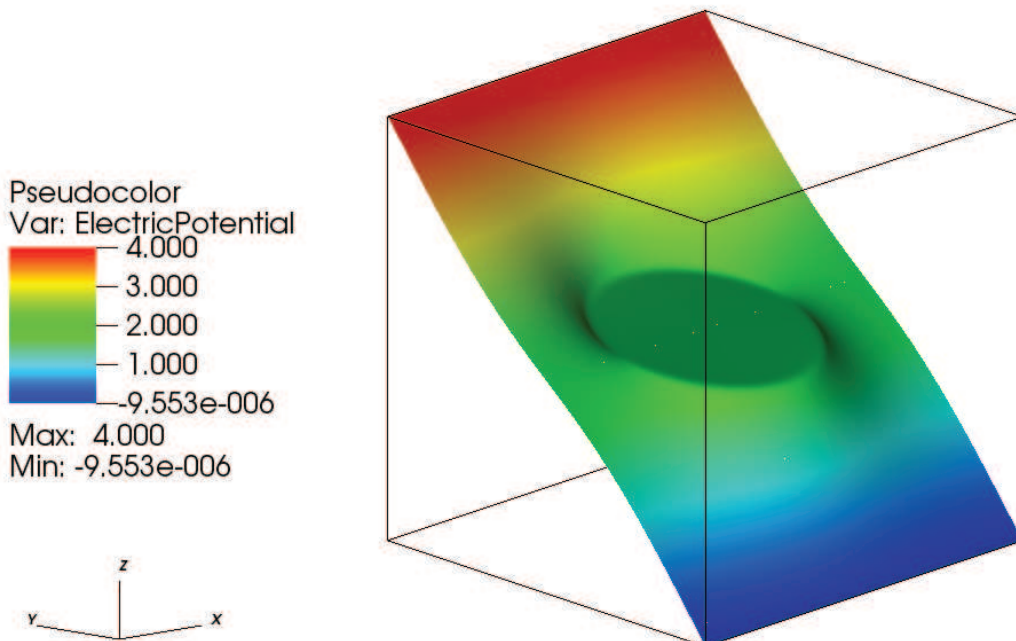
(a) $N = 32$ (b) $N = 64$

Figure 7.11: Effect of using the SIPG-ACP method for the test case with a jump of ratio 10 in the dielectric property at the interface. Contours of the electric potential are shown. A penalty parameter coefficient of $\alpha_P = 1$ is used. The computational domain is a $[-2, 2] \times [-2, 2]$ square. Grids of $N \times N$ cells and a polynomial degree of 8 are employed.

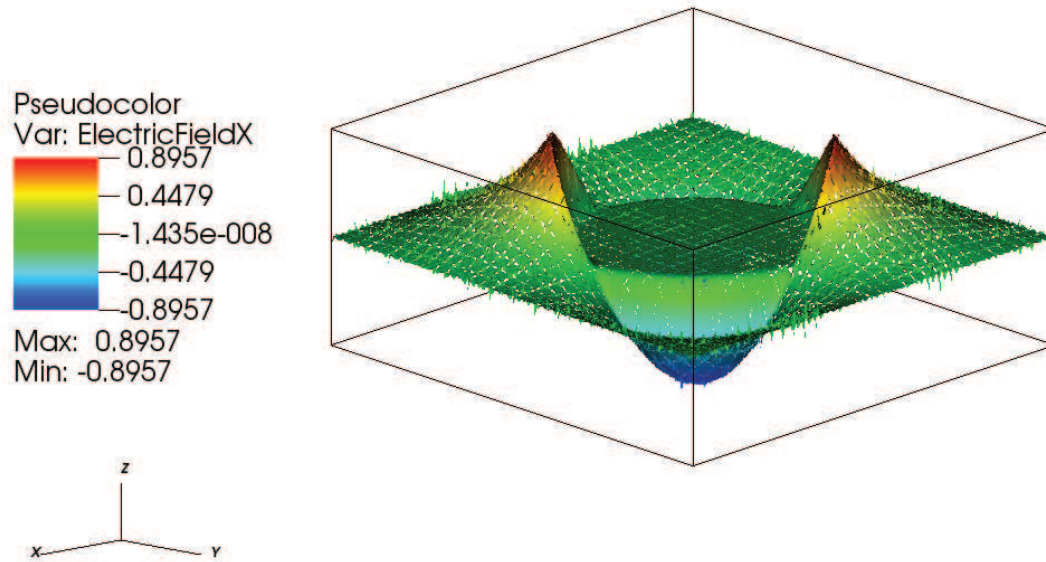
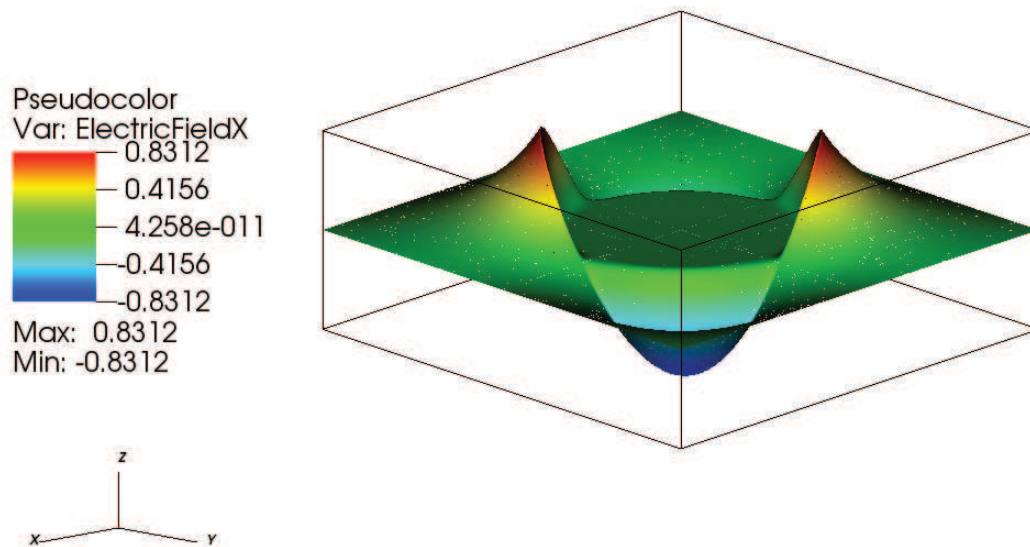
(a) $N = 32$ (b) $N = 64$

Figure 7.12: Effect of using the SIPG-ACP method for the test case with a jump of ratio 10 in the dielectric property at the interface. Contours of the electric field in x -direction are shown. A penalty parameter coefficient of $\alpha_P = 1$ is used. The computational domain is a $[-2, 2] \times [-2, 2]$ square. Grids of $N \times N$ cells are employed. Polynomial degrees of 8 and 7 are used for the electric potential and electric field, respectively.

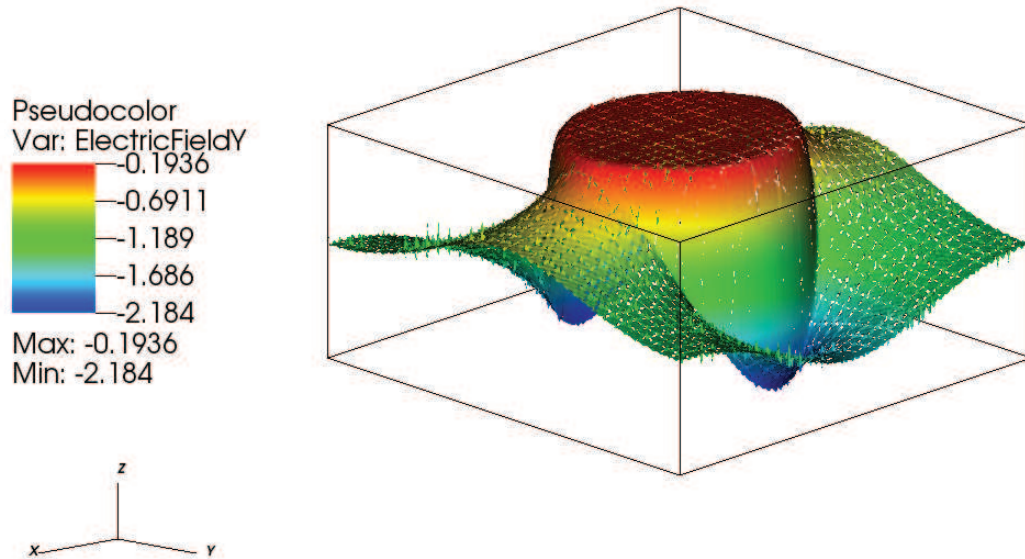
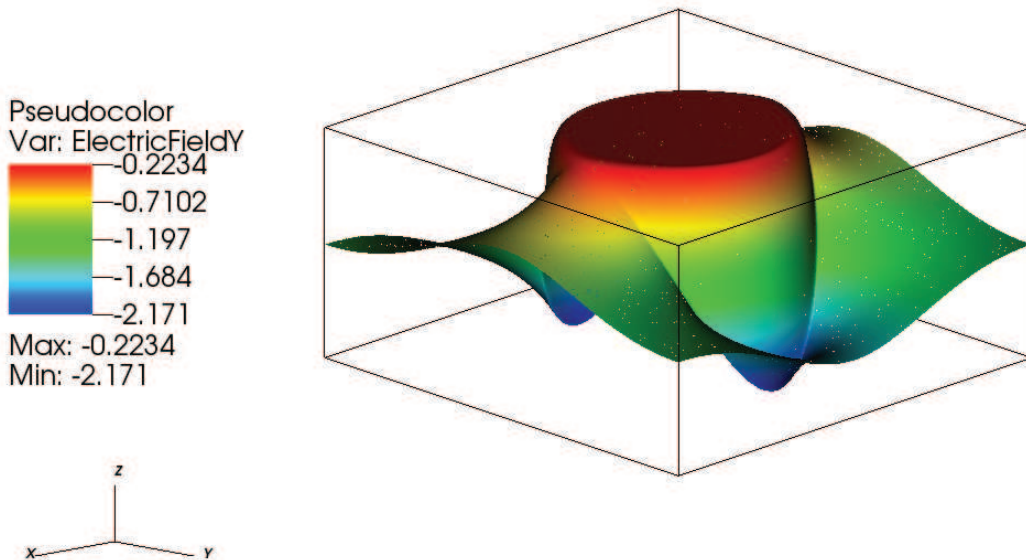
(a) $N = 32$ (b) $N = 64$

Figure 7.13: Effect of using the SIPG-ACP method for the test case with a jump of ratio 10 in the dielectric property at the interface. Contours of the electric field in y -direction are shown. A penalty parameter coefficient of $\alpha_P = 1$ is used. The computational domain is a $[-2, 2] \times [-2, 2]$ square. Grids of $N \times N$ cells are employed. Polynomial degrees of 8 and 7 are used for the electric potential and electric field, respectively.

The same convergence study of section 7.3 is repeated here with the SIPG-ACP method using a penalty parameter coefficient of $\alpha_P = 10$. The results are shown in figures 7.14 and 7.15 for the electric potential and electric field. The error reduction does not show the exponential convergence rate and the results are the same as the ones with the SIPG method (using the same α_P). This implies that although the SIPG-ACP method performs better than the SIPG for the low coefficient of $\alpha_P = 1$, for the higher ones, it would perform not different from the SIPG. The reason is that the jump in the permittivity coefficient is regularized at the interface and a high penalty parameter coefficient suppresses the inter-cell discontinuities. Concerning the convergence rate, this modification is not enough to achieve the exponential convergence rate.

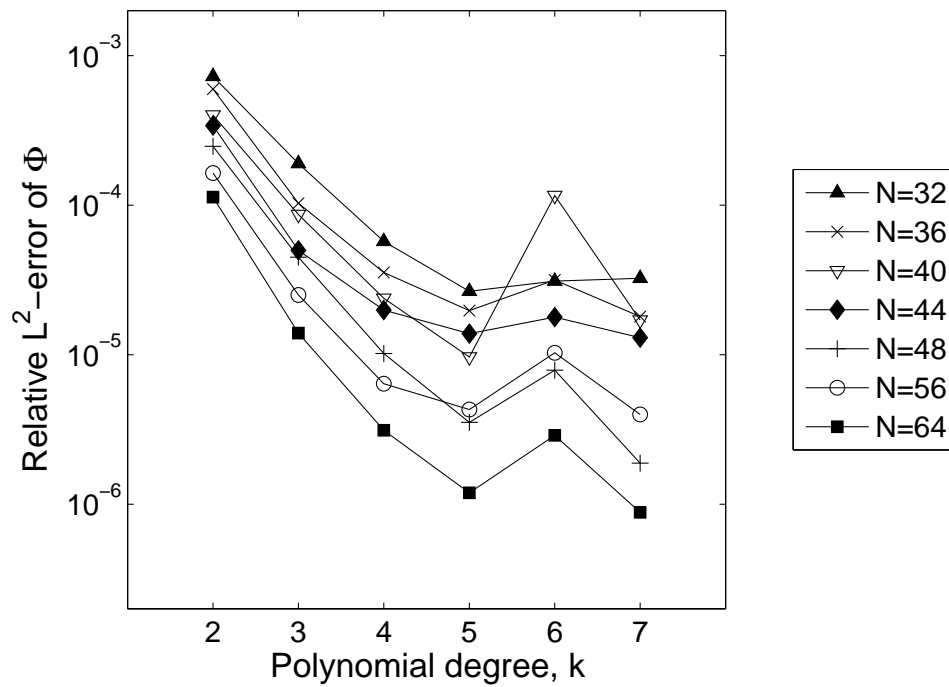
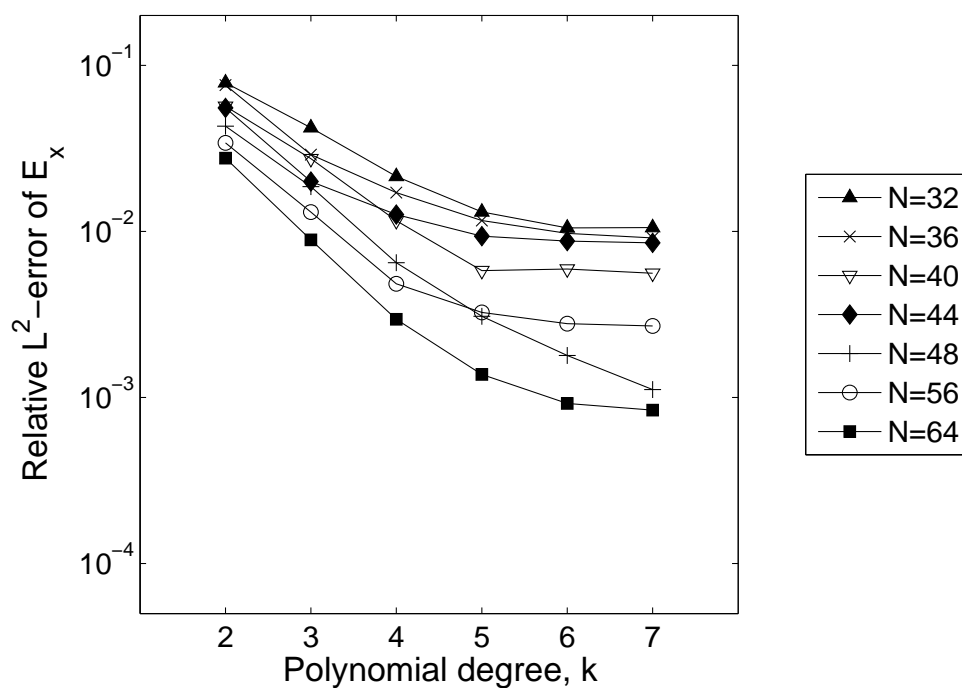
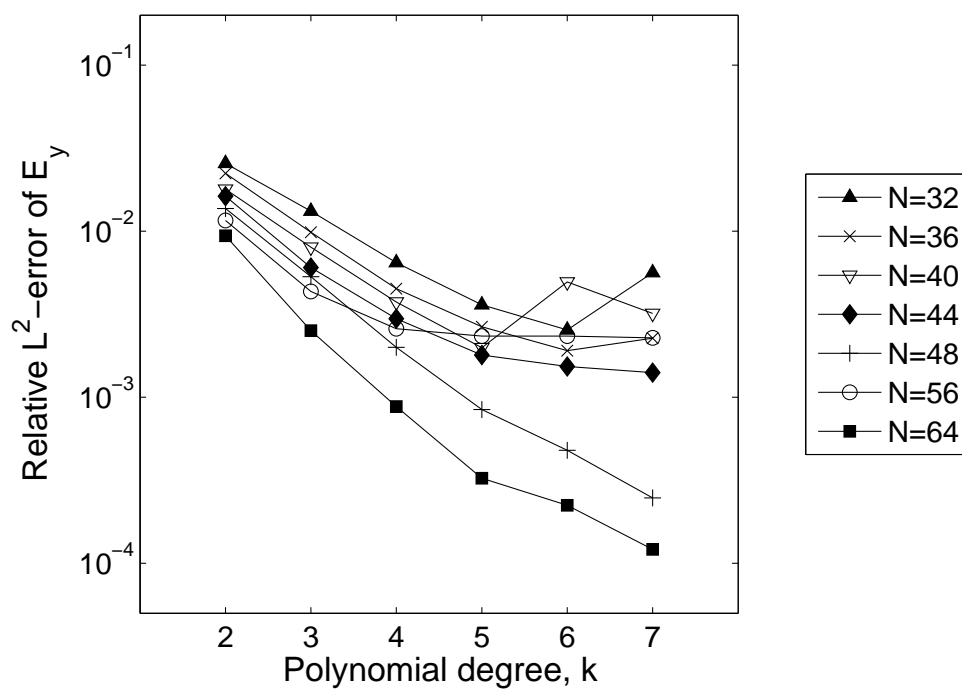


Figure 7.14: Convergence study for the test case with a jump of ratio 10 in the dielectric property at the interface. L^2 -norm errors of the electric potential are shown. The SIPG-ACP method with a penalty parameter coefficient of $\alpha_P = 10$ is used. The computational domain is a $[-2, 2] \times [-2, 2]$ square. Grids of $N \times N$ cells are employed.



(a)



(b)

Figure 7.15: Convergence study for the test case with a jump of ratio 10 in the dielectric property at the interface. L^2 -norm errors of the electric field are shown. The SIPG-ACP method with a penalty parameter coefficient of $\alpha_P = 10$ is used. The computational domain is a $[-2, 2] \times [-2, 2]$ square. Grids of $N \times N$ cells are employed. (a) Electric field in x -direction. (b) Electric field in y -direction.

7.4.2 Maximum coefficient for the penalty term

The results shown in section 7.4.1, which were obtained by modifying the penalty term, are promising. However, they show that there is still room for improvement. An idea to further improve the performance of the method is to interpret the $\mu_P a$ as a new penalty parameter. Following the general guide lines that are known for a penalty parameter, we know that the penalty parameter is a constant and that it does not affect the accuracy of the solution if it is higher than a certain limit, see for example (Hazra 2009). We replace the coefficient a by its maximum in the computational domain divided by the half-thickness of the diffuse interface. This is because of the definition of the coefficient a in the one-fluid approach using the regularized Heaviside function. The factor $\frac{1}{\epsilon}$ appears in the regularized Heaviside function, that can be seen directly from its formulation (see section 6.1). The modified form of the SIPG method with the maximum coefficient for the penalty term (SIPG-MCP) is the following

$$u^* = \{u\},$$

$$\boldsymbol{\sigma}^* = \{a \nabla u\} - \mu_P \frac{\max(a_1, a_2)}{\epsilon} [[u]]$$

The same test case as before with the permittivity ratio of 10 is repeated here. The elevated contours of the electric potential and electric field in x and y -directions are shown in figures 7.16, 7.17 and 7.18, respectively. Using the coarse grid, the results are quite smooth and look almost the same as the solution with the fine grid.

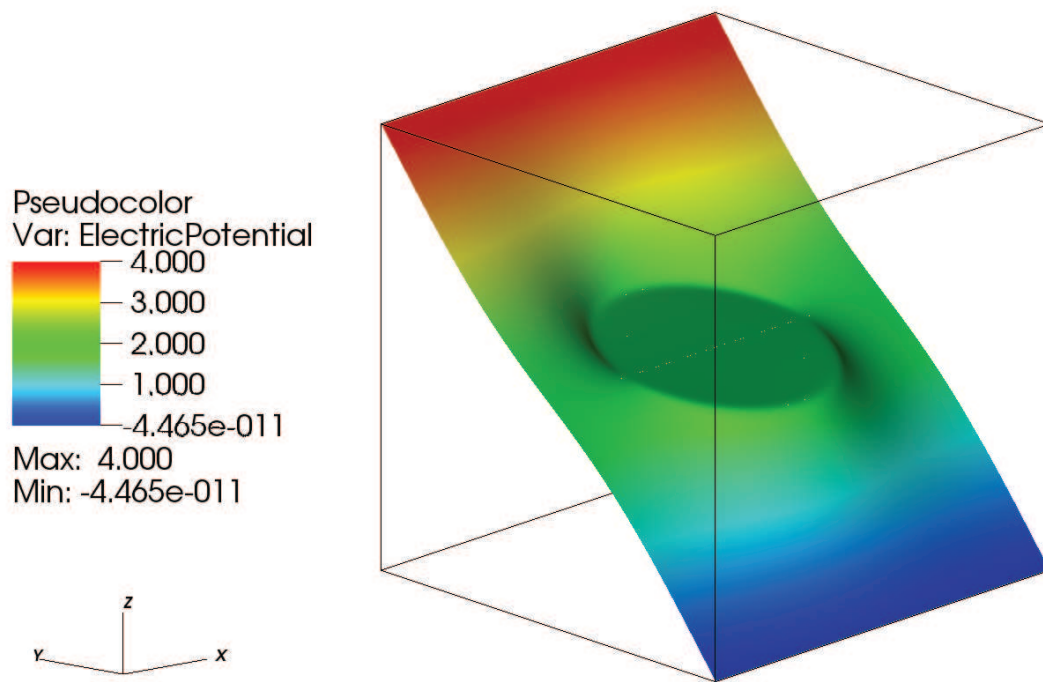
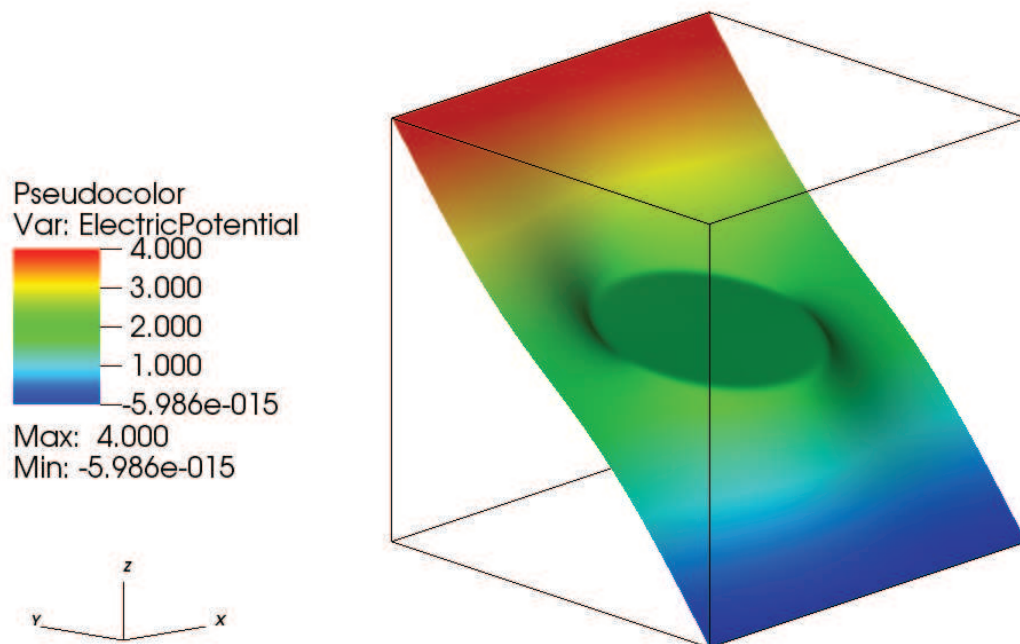
(a) $N = 32$ (b) $N = 64$

Figure 7.16: Effect of using the SIPG-MCP method for the test case with a jump of ratio 10 in the dielectric property at the interface. Contours of the electric potential are shown. A penalty parameter coefficient of $\alpha_P = 1$ is used. The computational domain is a $[-2, 2] \times [-2, 2]$ square. Grids of $N \times N$ cells and a polynomial degree of 8 are employed.

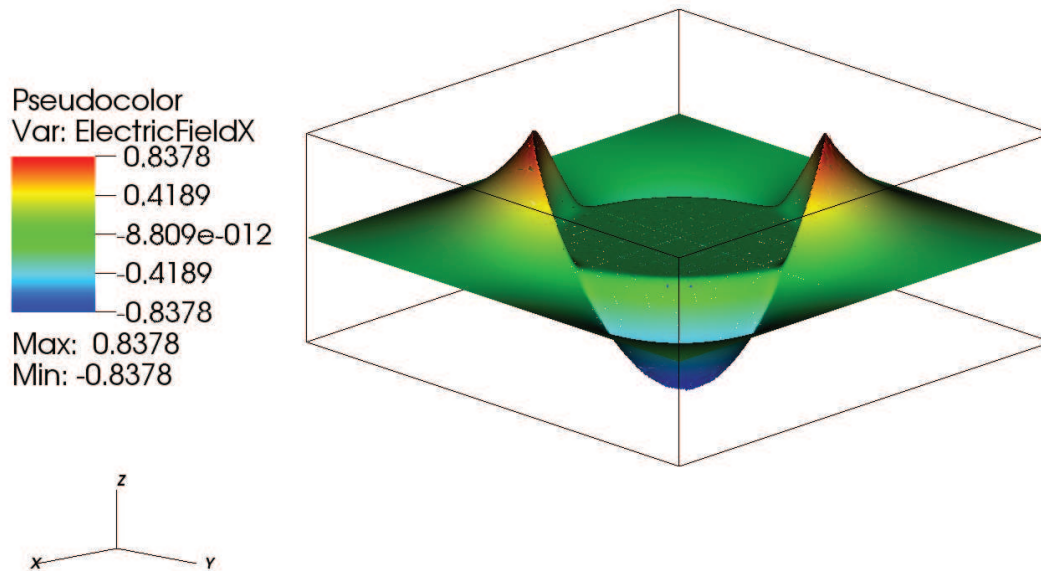
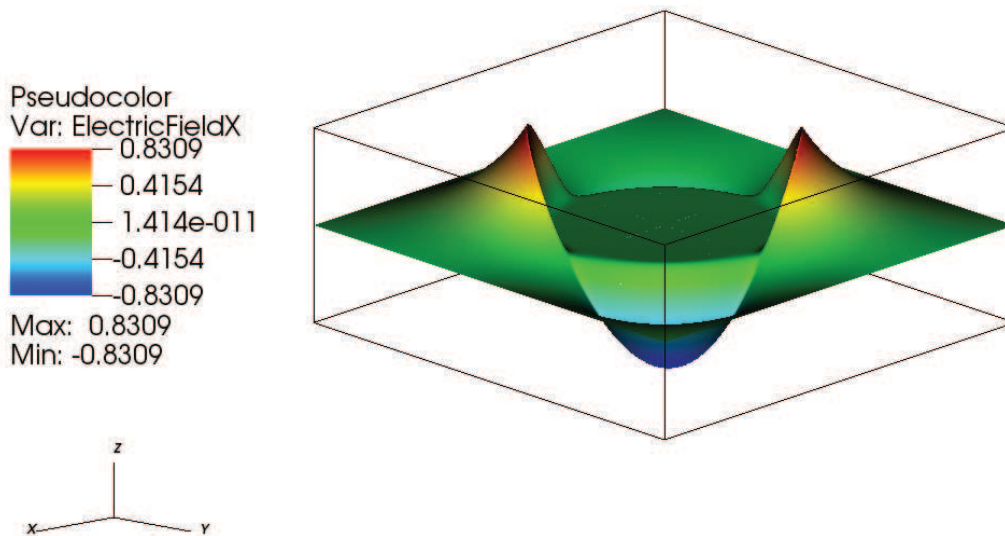
(a) $N = 32$ (b) $N = 64$

Figure 7.17: Effect of using the SIPG-MCP method for the test case with a jump of ratio 10 in the dielectric property at the interface. Contours of the electric field in x -direction are shown. A penalty parameter coefficient of $\alpha_P = 1$ is used. The computational domain is a $[-2, 2] \times [-2, 2]$ square. Grids of $N \times N$ cells are employed. Polynomial degrees of 8 and 7 are used for the electric potential and electric field, respectively.

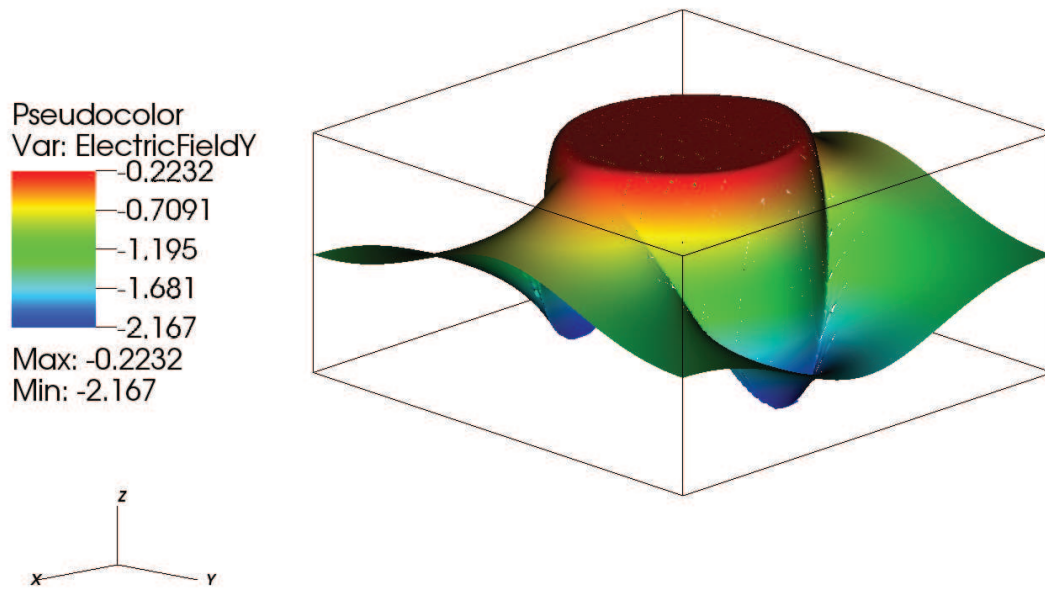
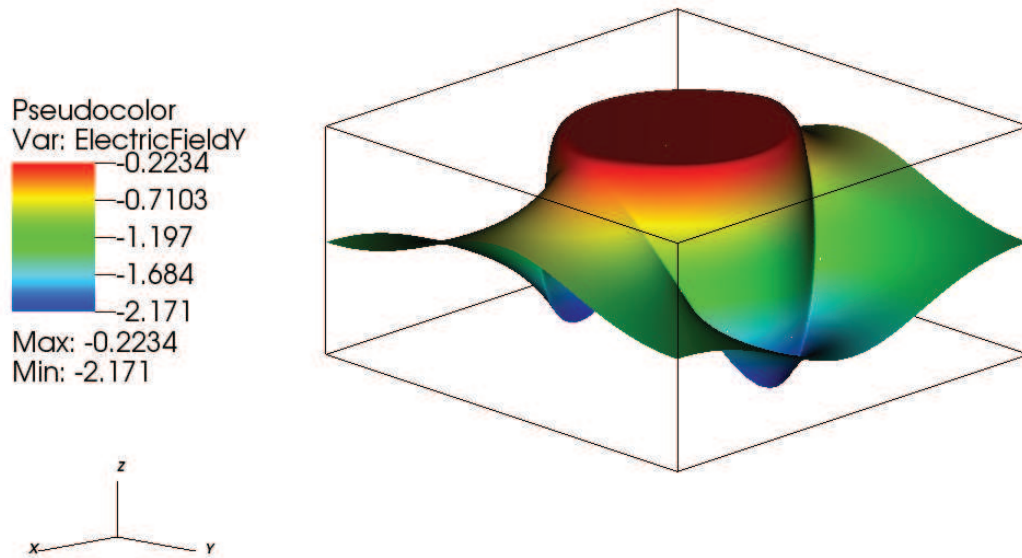
(a) $N = 32$ (b) $N = 64$

Figure 7.18: Effect of using the SIPG-MCP method for the test case with a jump of ratio 10 in the dielectric property at the interface. Contours of the electric field in y -direction are shown. A penalty parameter coefficient of $\alpha_P = 1$ is used. The computational domain is a $[-2, 2] \times [-2, 2]$ square. Grids of $N \times N$ cells are employed. Polynomial degrees of 8 and 7 are used for the electric potential and electric field, respectively.

The same convergence study of sections 7.3 and 7.4.1 is repeated here with the SIPG-MCP method. Two penalty parameter coefficients of $\alpha_P = 1$ and $\alpha_P = 10$ are used. Using $\alpha_P = 1$, the L^2 -norm errors for the electric potential and electric field are shown in figures 7.19 and 7.20. The results show the expected exponential convergence rate (neglecting the coarse grid with 32×32 cells). Using $\alpha_P = 10$, the results are shown in figures 7.21 and 7.22. The exponential convergence rate is achieved for the electric potential and electric field. The errors are slightly less than the corresponding errors using $\alpha_P = 1$, which is the expected effect of using a high penalty parameter coefficient. In figures 7.23 and 7.24, the three methods SIPG, SIPG-MCP and SIPG-ACP are compared with each other for $\alpha_P = 10$. As mentioned before, the results with the SIPG and SIPG-ACP are the same and do not show the exponential convergence rate by increasing the polynomial degree but with the SIPG-MCP method, the errors are reduced with an exponential convergence rate.

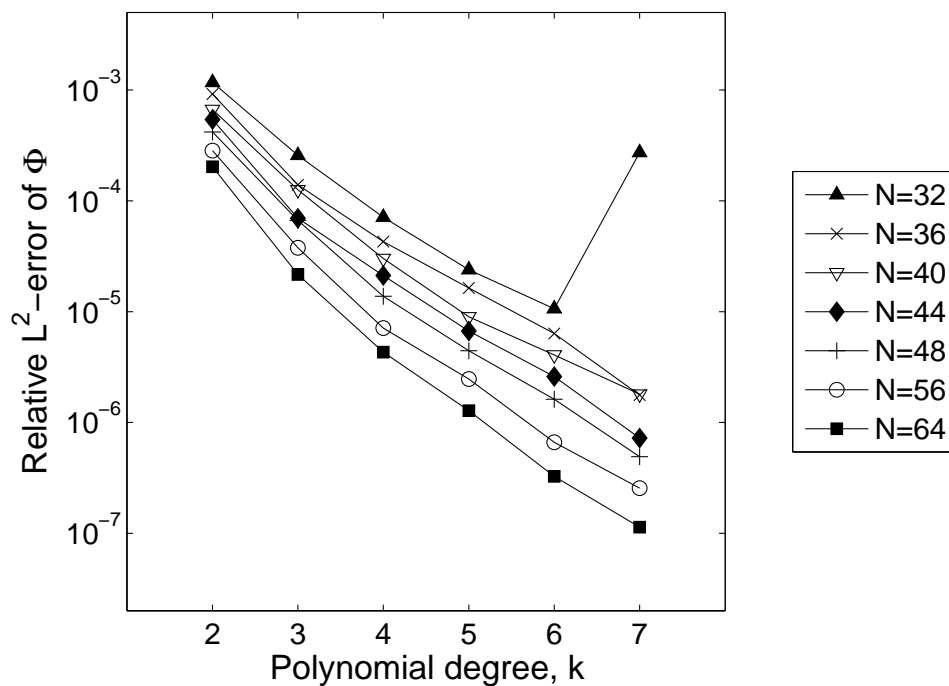
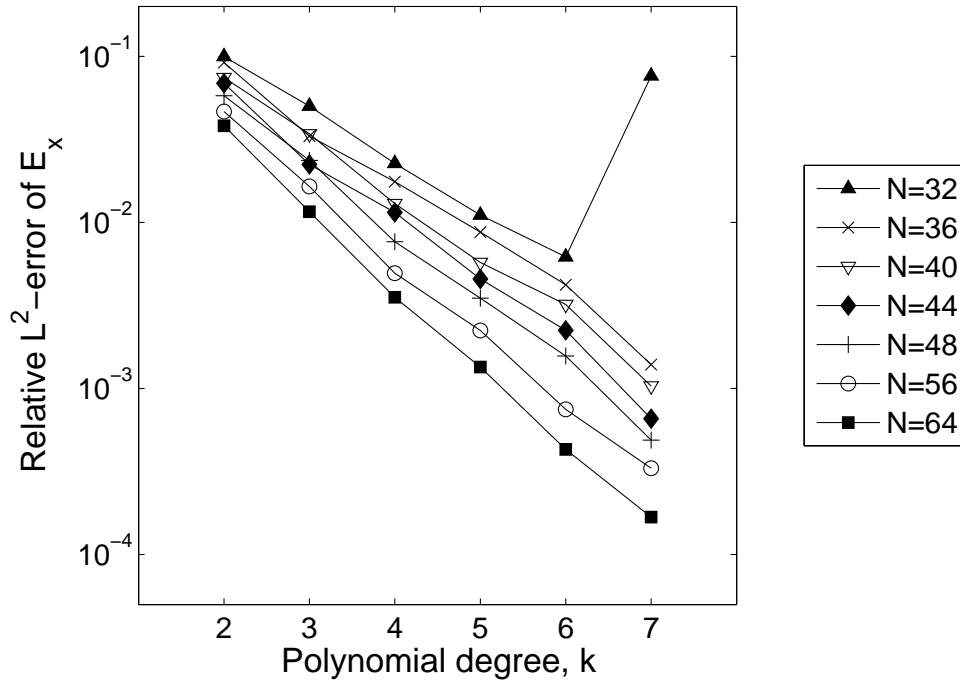
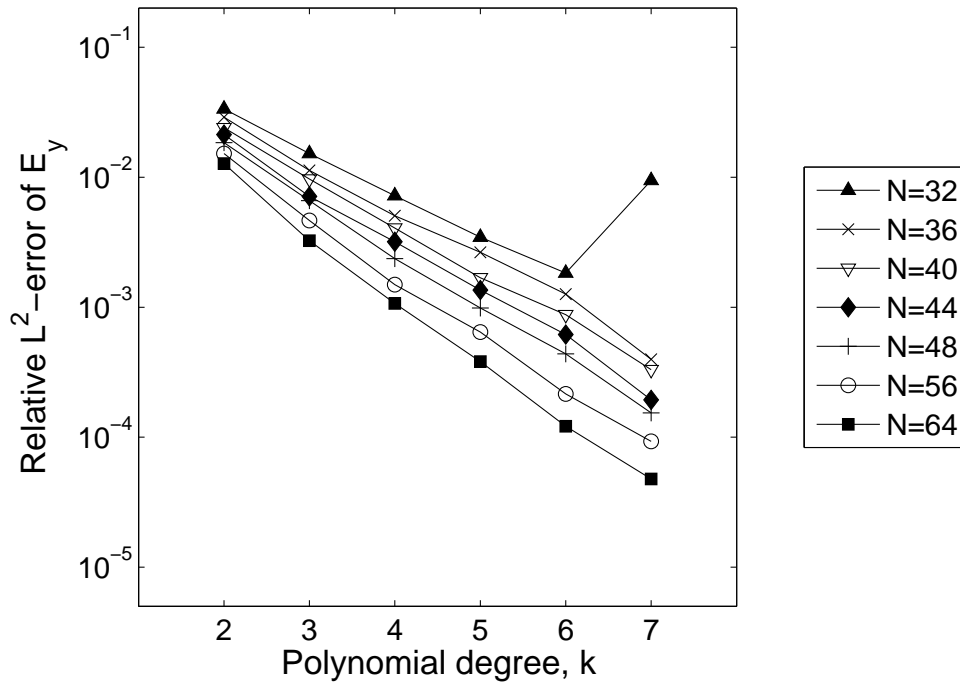


Figure 7.19: Convergence study for the test case with a jump of ratio 10 in the dielectric property at the interface. L^2 -norm errors of the electric potential are shown. The SIPG-MCP method with a penalty parameter coefficient of $\alpha_P = 1$ is used. The computational domain is a $[-2, 2] \times [-2, 2]$ square. Grids of $N \times N$ cells are employed.



(a)



(b)

Figure 7.20: Convergence study for the test case with a jump of ratio 10 in the dielectric property at the interface. L^2 -norm errors of the electric field are shown. The SIPG-MCP method with a penalty parameter coefficient of $\alpha_P = 1$ is used. The computational domain is a $[-2, 2] \times [-2, 2]$ square. Grids of $N \times N$ cells are employed. (a) Electric field in x -direction. (b) Electric field in y -direction.

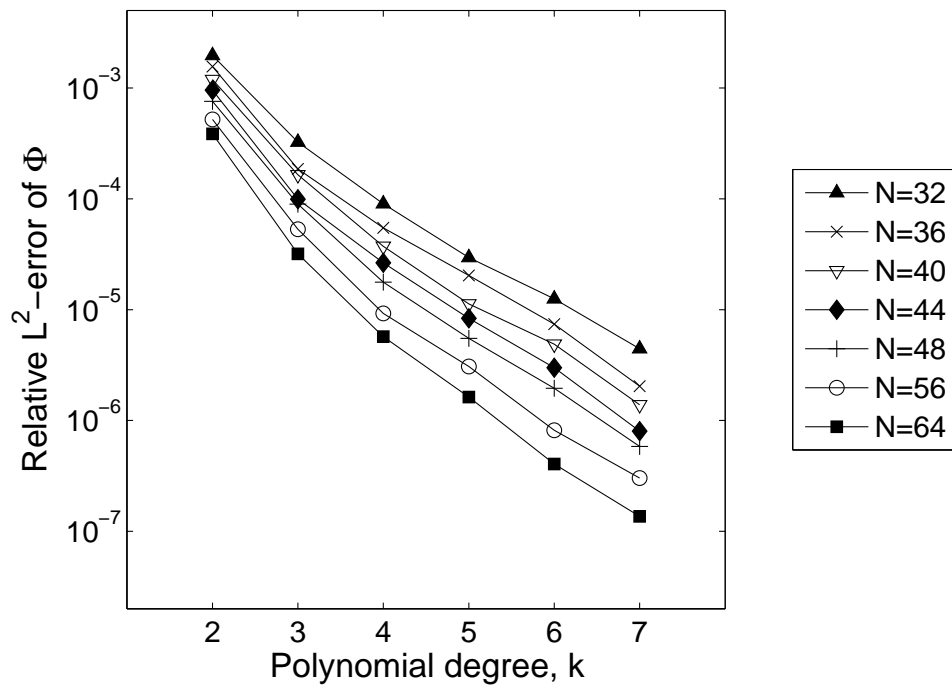
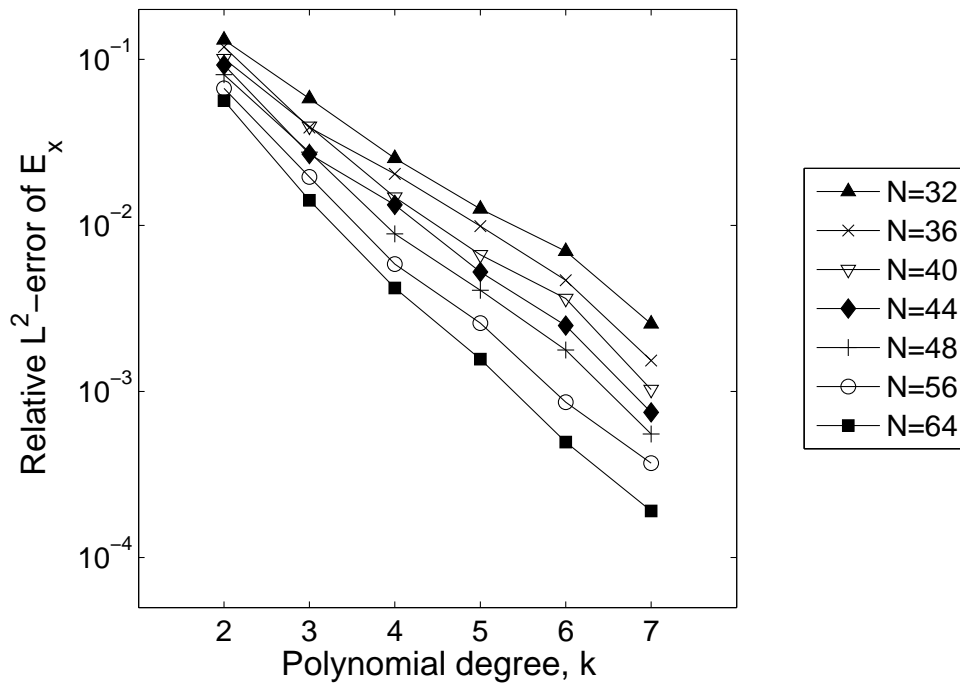
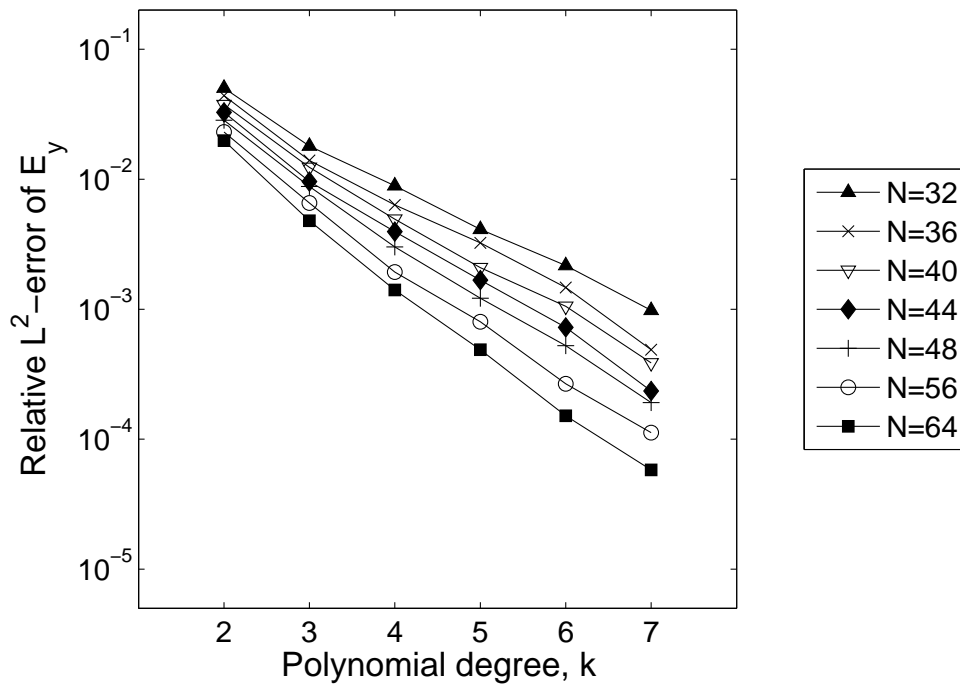


Figure 7.21: Convergence study for the test case with a jump of ratio 10 in the dielectric property at the interface. L^2 -norm errors of the electric potential are shown. The SIPG-MCP method with a penalty parameter coefficient of $\alpha_P = 10$ is used. The computational domain is a $[-2, 2] \times [-2, 2]$ square. Grids of $N \times N$ cells are employed.



(a)



(b)

Figure 7.22: Convergence study for the test case with a jump of ratio 10 in the dielectric property at the interface. L^2 -norm errors of the electric field are shown. The SIPG-MCP method with a penalty parameter coefficient of $\alpha_P = 10$ is used. The computational domain is a $[-2, 2] \times [-2, 2]$ square. Grids of $N \times N$ cells are employed. (a) Electric field in x -direction. (b) Electric field in y -direction.

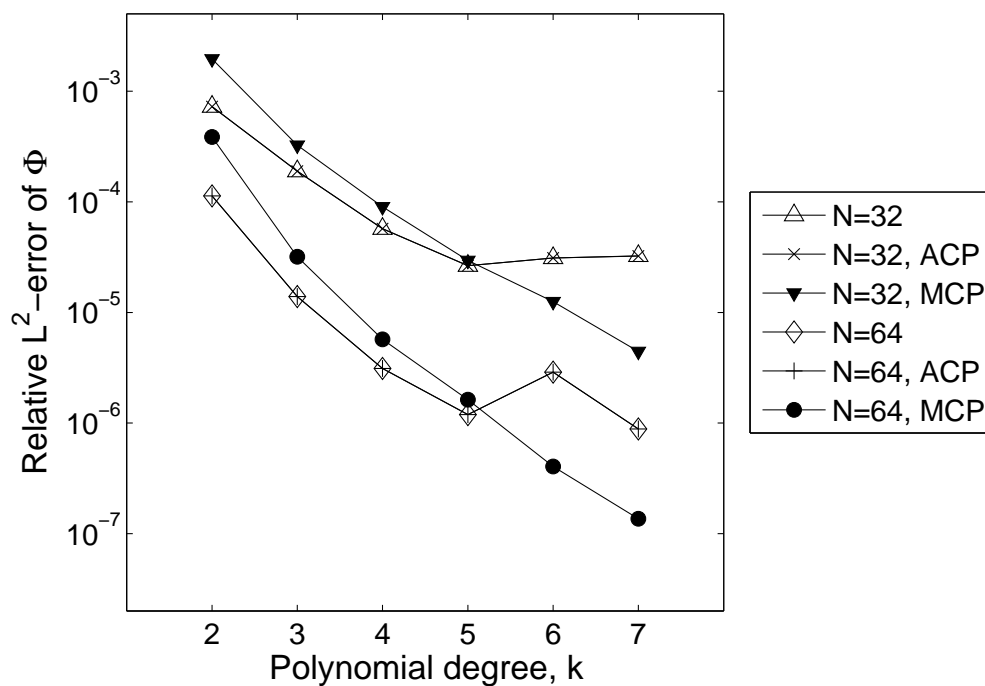
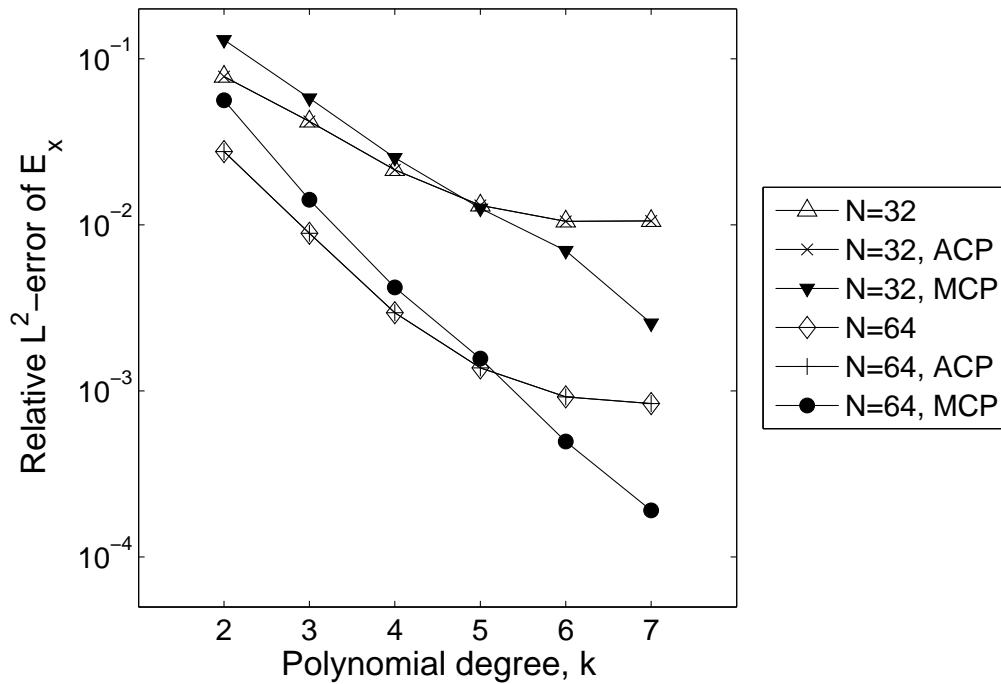
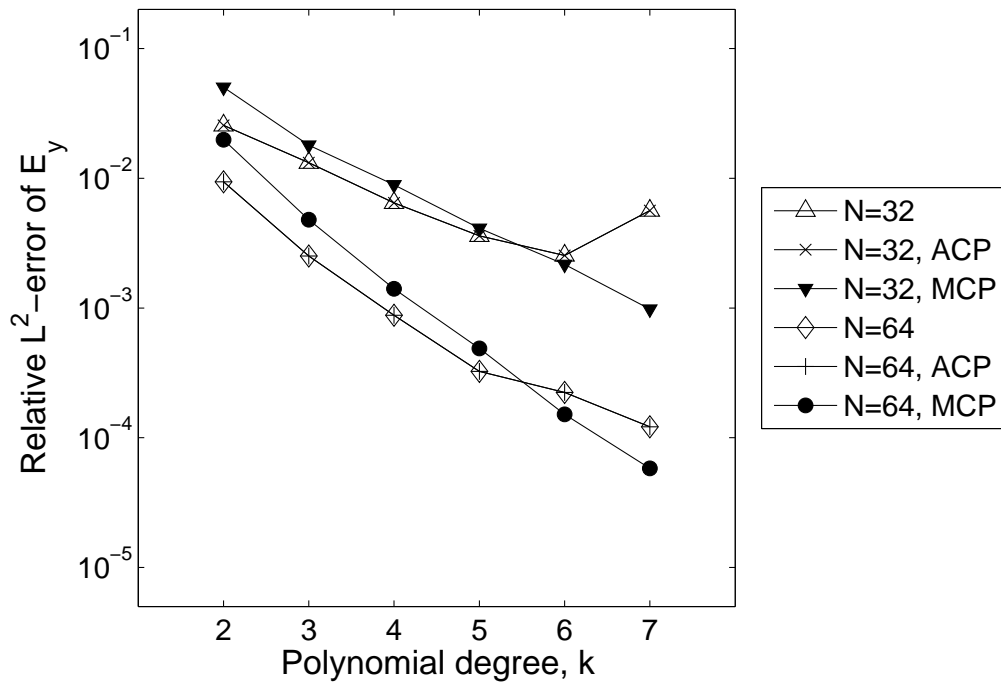


Figure 7.23: Effect of the stabilization method on the convergence rate for the test case with a jump of ratio 10 in the dielectric property at the interface. L^2 -norm errors of the electric potential are shown. The SIPG, SIPG-ACP and SIPG-MCP methods with a penalty parameter coefficient of $\alpha_P = 10$ are used. The computational domain is a $[-2, 2] \times [-2, 2]$ square. The errors for grids of 32×32 and 64×64 cells are shown.



(a)



(b)

Figure 7.24: Effect of the stabilization method on the convergence rate for the test case with a jump of ratio 10 in the dielectric property at the interface. L^2 -norm errors of the electric field are shown. The SIPG, SIPG-ACP and SIPG-MCP methods with a penalty parameter coefficient of $\alpha_P = 10$ are used. The computational domain is a $[-2, 2] \times [-2, 2]$ square. The errors for grids of 32×32 and 64×64 cells are shown. (a) Electric field in x -direction. (b) Electric field in y -direction.

As a final check, the satisfaction of the physical jump condition $\|D_n\| = \|\varepsilon E_n\| = 0$ at the interface (see section 3.1) is examined using the SIPG, SIPG-ACP and SIPG-MCP methods. The error is considered as $\text{err} = \text{abs}(\frac{\|\varepsilon E_y\|}{\{\varepsilon E_y\}})$ at the point $(0, 1)$ or $(0, -1)$ of the computational domain, where the direction of the electric field (y -direction) is normal to the interface. The jump and average operators are computed as

$$\|\varepsilon E_y\| = \varepsilon_2 E_{y_{\max}} - \varepsilon_1 E_{y_{\min}}, \quad (7.6a)$$

$$\{\varepsilon E_y\} = \varepsilon_2 E_{y_{\max}} + \varepsilon_1 E_{y_{\min}} \quad (7.6b)$$

The maximum and minimum values of the E_y are taken from the contours of the electric field in y -direction from figures 7.8b, 7.13a and 7.18a. The errors are shown in table 7.1. In tables 7.2 and 7.3 a grid refinement is applied using the SIPG/SIPG-ACP and SIPG-MCP methods, respectively. A penalty parameter of $\alpha_P = 10$ is applied, for which the SIPG and SIPG-ACP provide the same results (discussed before for figure 7.24b).

Table 7.1: Satisfaction of the physical jump condition $\|\varepsilon E_n\| = 0$ at the interface. The permittivity ratio is $\frac{\varepsilon_2}{\varepsilon_1} = 10$. The SIPG, SIPG-ACP and SIPG-MCP methods with a penalty parameter coefficient of $\alpha_P = 1$ are compared. The polynomial degree is 8. The relative error is computed as $\text{err} = \text{abs}(\frac{\|\varepsilon E_y\|}{\{\varepsilon E_y\}})$ at point $(0, 1)$ of the computational domain. $\|\cdot\|$ and $\{\cdot\}$ are the jump and average operators defined in equation 7.6. *DOF* is the degrees of freedom.

Method	No. of cells	DOF	$E_{y_{\max}}$	$E_{y_{\min}}$	$\{\varepsilon E_y\}$	$\ \varepsilon E_y\ $	err%
SIPG	64×64	184320	-0.2234	-2.171	-2.2025	-0.063	2.9
SIPG-ACP	32×32	46080	-0.1936	-2.184	-2.06	0.248	12
SIPG-MCP	32×32	46080	-0.2232	-2.167	-2.1995	-0.065	3

Table 7.2: Satisfaction of the physical jump condition $\|\varepsilon E_n\| = 0$ at the interface. The permittivity ratio is $\frac{\varepsilon_2}{\varepsilon_1} = 10$. The SIPG/SIPG-ACP method with a penalty parameter coefficient of $\alpha_P = 10$ is used. A grid refinement is applied. The polynomial degree is 8. The relative error is computed as $\text{err} = \text{abs}(\frac{\|\varepsilon E_y\|}{\{\varepsilon E_y\}})$ at point $(0, 1)$ of the computational domain. $\|\cdot\|$ and $\{\cdot\}$ are the jump and average operators defined in equation 7.6. *DOF* is the degrees of freedom.

No. of cells	DOF	$E_{y_{\max}}$	$E_{y_{\min}}$	$\{\varepsilon E_y\}$	$\ \varepsilon E_y\ $	err%
32×32	46080	-0.2162	-2.178	-2.17	0.016	0.7
36×36	58320	-0.2138	-2.183	-2.1605	0.045	2.1
40×40	72000	-0.2214	-2.166	-2.19	-0.048	2.2
44×44	87120	-0.2132	-2.169	-2.1505	0.037	1.7
48×48	103680	-0.2231	-2.169	-2.2	-0.062	2.8
56×56	141120	-0.2227	-2.171	-2.199	-0.056	2.5
64×64	184320	-0.2233	-2.171	-2.202	-0.062	2.8

Table 7.3: Satisfaction of the physical jump condition $||\varepsilon E_n|| = 0$ at the interface. The permittivity ratio is $\frac{\varepsilon_2}{\varepsilon_1} = 10$. The SIPG-MCP method with a penalty parameter coefficient of $\alpha_P = 10$ is used. A grid refinement is applied. The polynomial degree is 8. The relative error is computed as $\text{err} = \text{abs}(\frac{||\varepsilon E_y||}{\{\varepsilon E_y\}})$ at point $(0, 1)$ of the computational domain. $||\cdot||$ and $\{\cdot\}$ are the jump and average operators defined in equation 7.6. DOF is the degrees of freedom.

No. of cells	DOF	$E_{y_{\max}}$	$E_{y_{\min}}$	$\{\varepsilon E_y\}$	$ \varepsilon E_y $	err%
32×32	46080	-0.2234	-2.163	-2.1985	-0.071	3.2
36×36	58320	-0.2234	-2.164	-2.1990	-0.07	3.2
40×40	72000	-0.2234	-2.165	-2.1995	-0.069	3.1
44×44	87120	-0.2234	-2.167	-2.2005	-0.067	3
48×48	103680	-0.2234	-2.169	-2.2015	-0.065	3
56×56	141120	-0.2234	-2.171	-2.2025	-0.063	2.9
64×64	184320	-0.2234	-2.171	-2.2025	-0.063	2.9

7.5 High jumps in the dielectric property

A high permittivity ratio of 80 occurs in the electrowetting applications that corresponds to water-air systems. To be able to solve the problems with high ratios of the permittivity, we have chosen the SIPG-MCP method which has been introduced in the previous section. A series of permittivity ratios among 2 and 100 are chosen. A grid of 32×32 cells and a polynomial degree of 8 is used. The contours of the electric field in x - and y - directions are shown in figures 7.25 and 7.26, respectively. The high ratios of 50 and 100 are also well simulated using the SIPG-MCP method but some little disturbances appear in the solution that suggest using a finer grid.

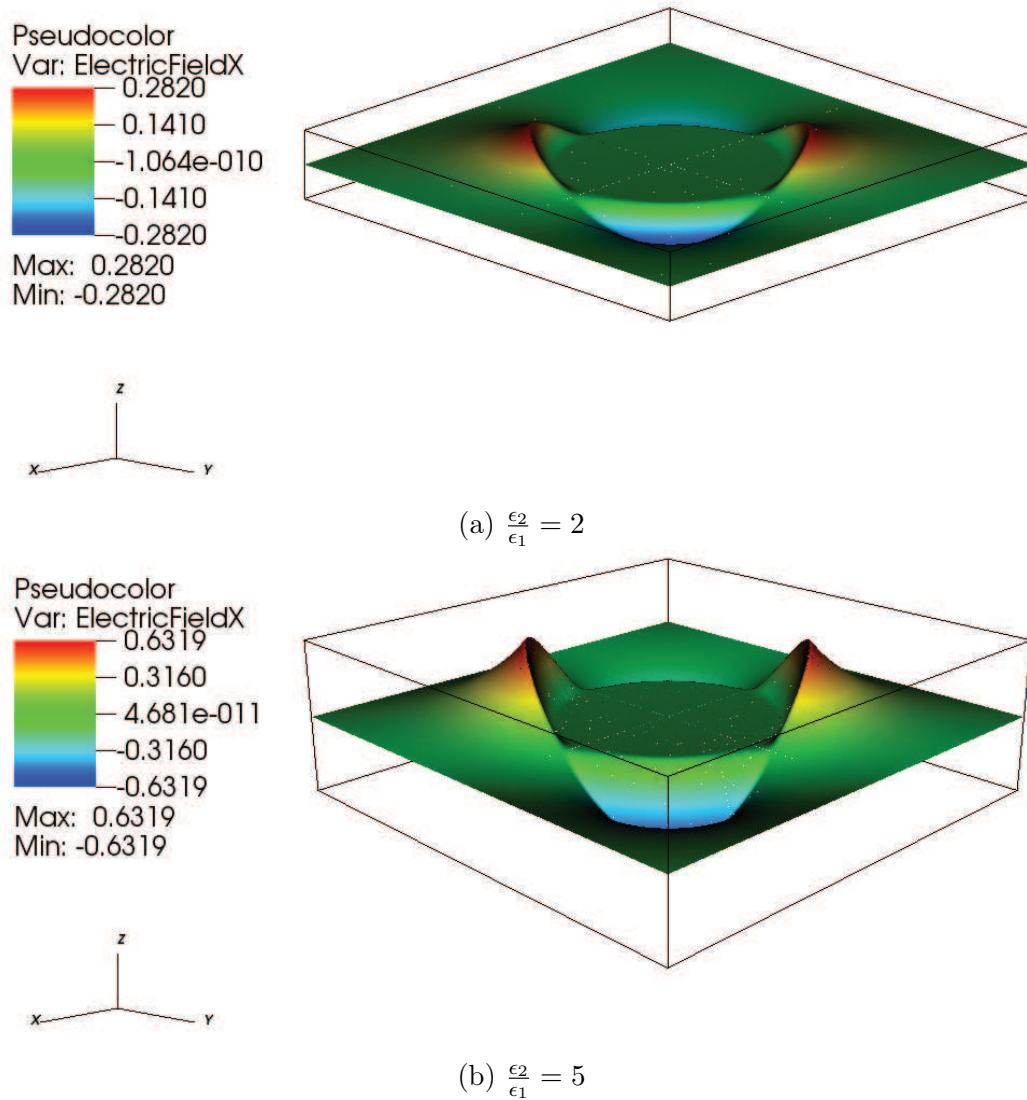
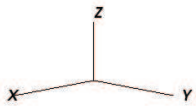
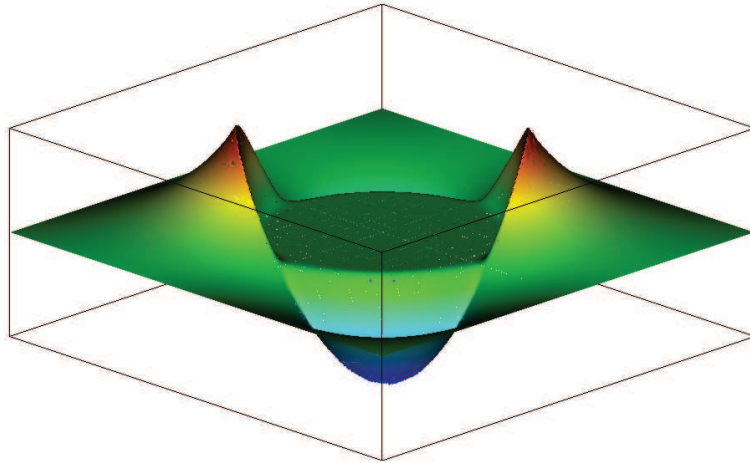


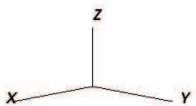
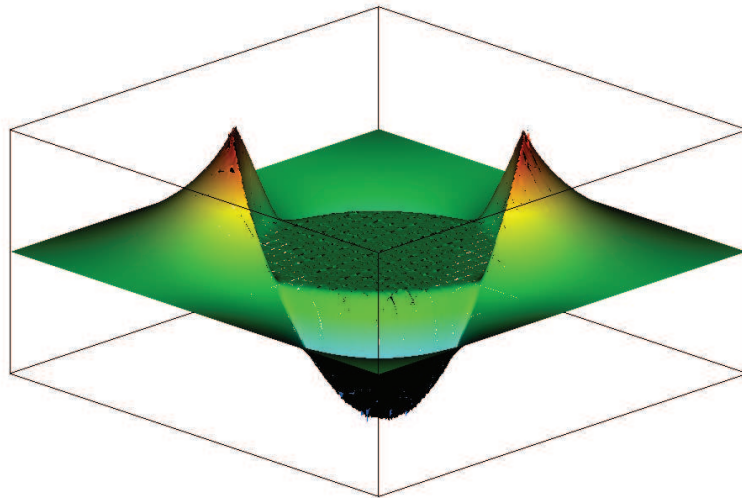
Figure 7.25: High permittivity ratios at the interface are simulated using the SIPG-MCP method with a penalty parameter coefficient of $\alpha_P = 1$. Contours of the electric field in x -direction are shown. The computational domain is a $[-2, 2] \times [-2, 2]$ square. A grid of 32×32 cells is employed. Polynomial degrees of 8 and 7 are used for the electric potential and electric field, respectively (to be continued on the next pages).

Pseudocolor
Var: ElectricFieldX
0.8378
0.4189
-8.809e-012
-0.4189
-0.8378
Max: 0.8378
Min: -0.8378



(c) $\frac{\epsilon_2}{\epsilon_1} = 10$

Pseudocolor
Var: ElectricFieldX
0.9907
0.4954
-4.085e-009
-0.4954
-0.9907
Max: 0.9907
Min: -0.9907



(d) $\frac{\epsilon_2}{\epsilon_1} = 20$

Figure 7.25: To be continued on the next page.

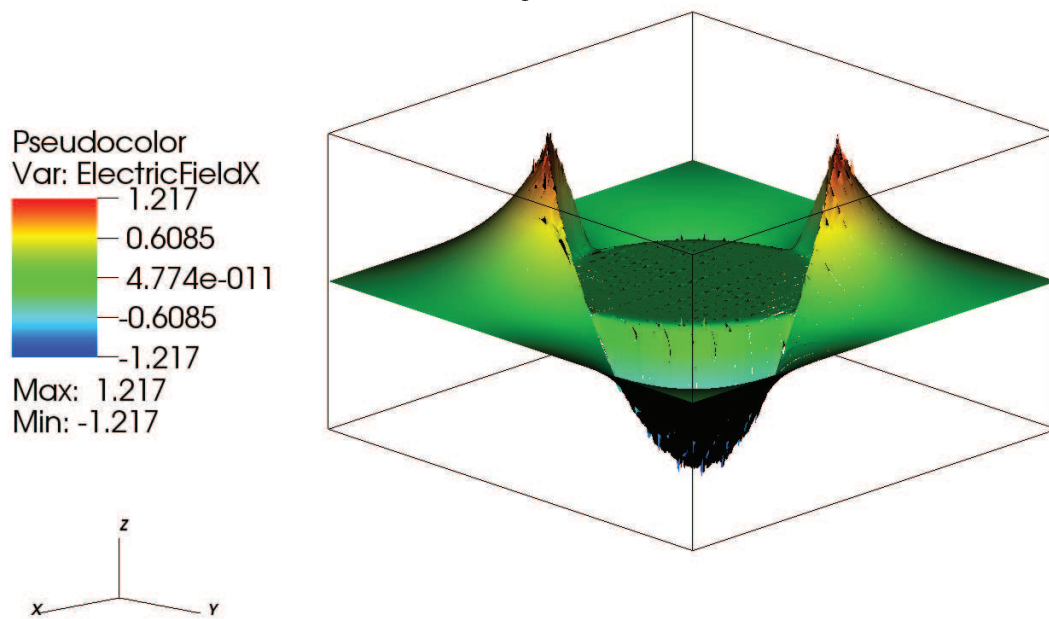
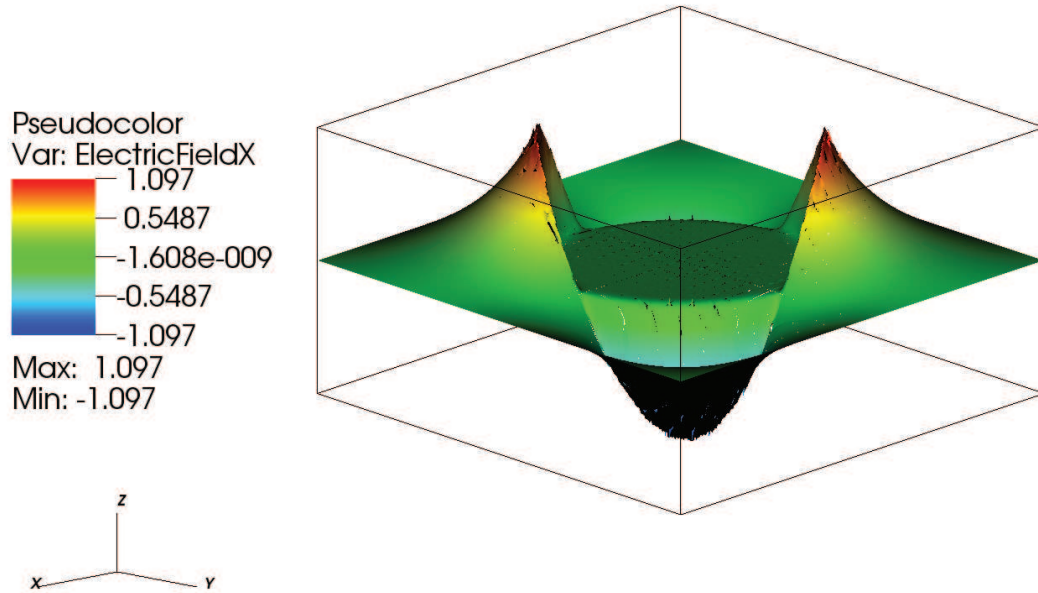


Figure 7.25: Continued.

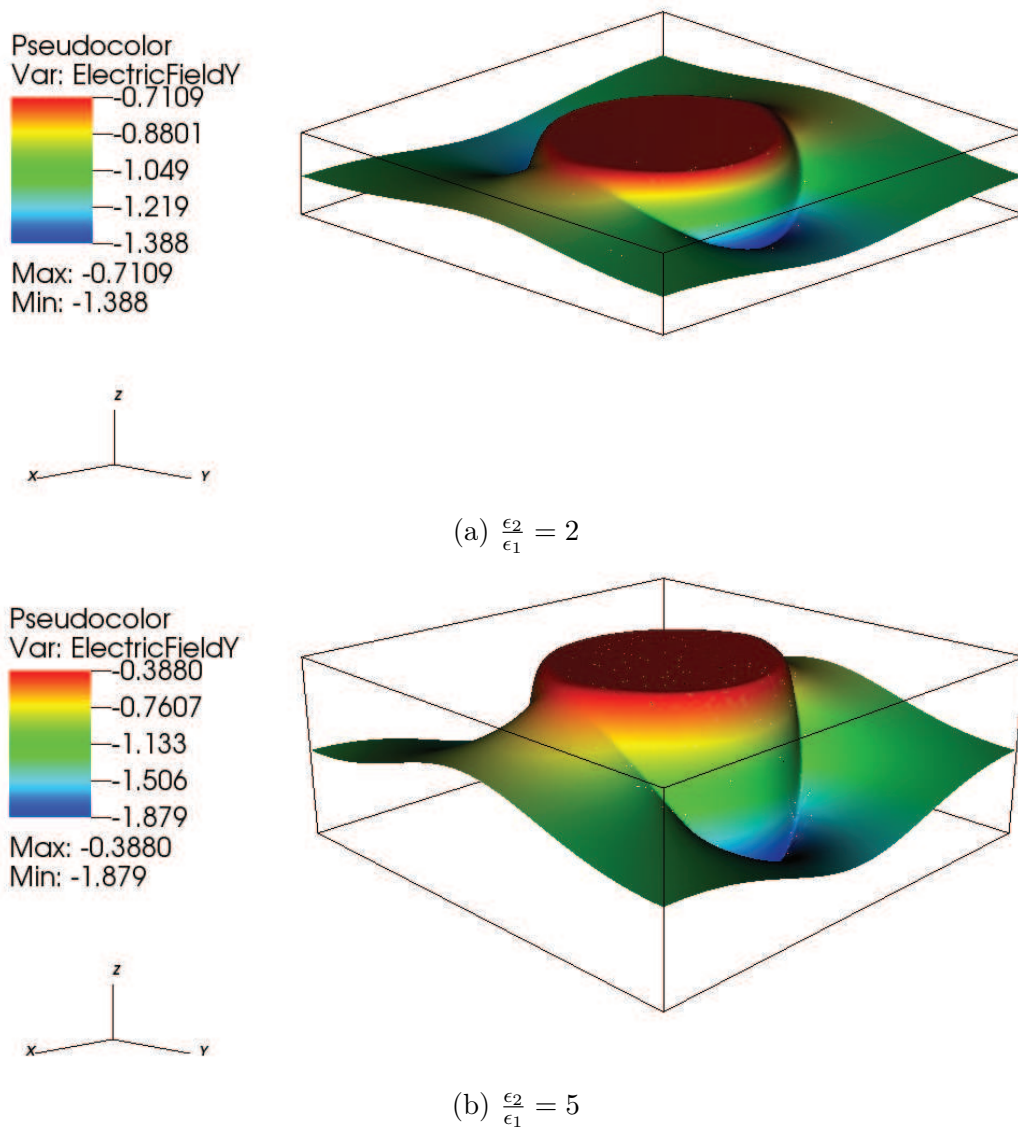
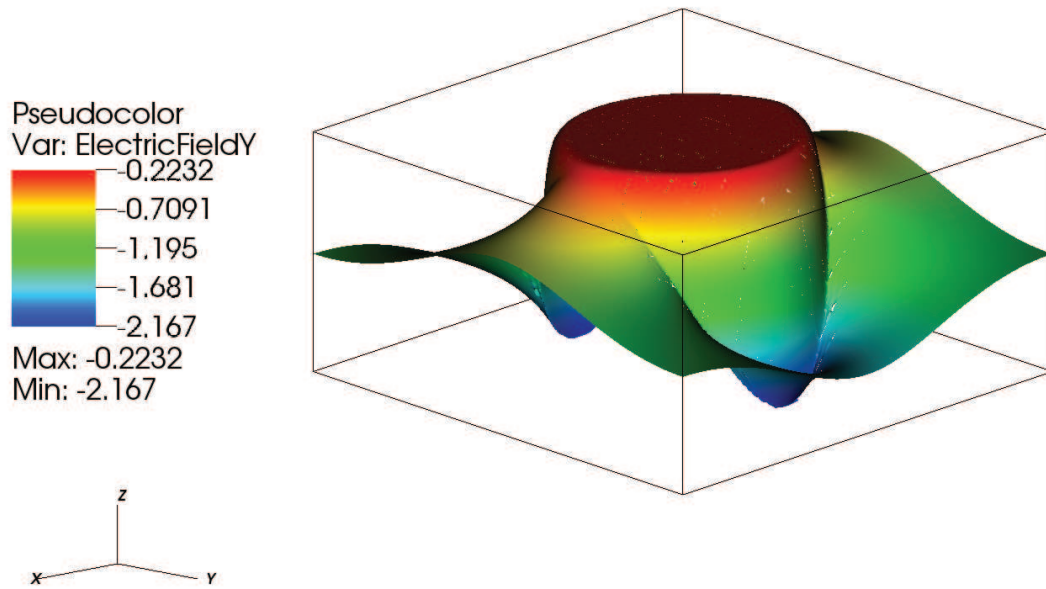
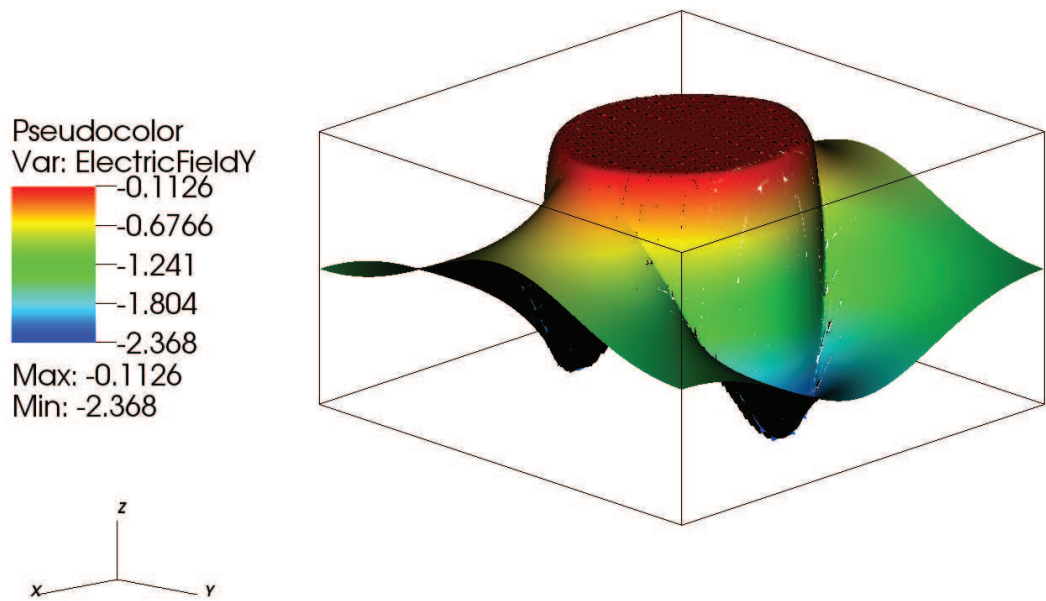


Figure 7.26: High permittivity ratios at the interface are simulated using the SIPG-MCP method with a penalty parameter coefficient of $\alpha_P = 1$. Contours of the electric field in y -direction are shown. The computational domain is a $[-2, 2] \times [-2, 2]$ square. A grid of 32×32 cells is employed. Polynomial degrees of 8 and 7 are used for the electric potential and electric field, respectively (to be continued on the next pages).



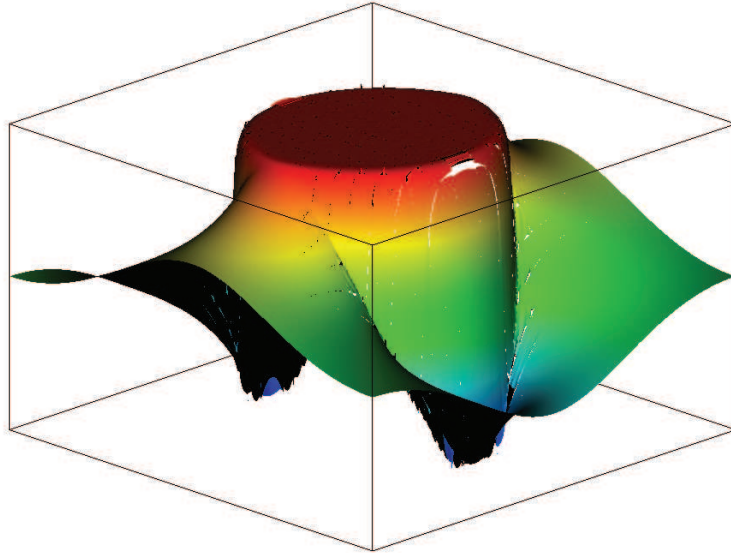
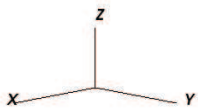
(c) $\frac{\epsilon_2}{\epsilon_1} = 10$



(d) $\frac{\epsilon_2}{\epsilon_1} = 20$

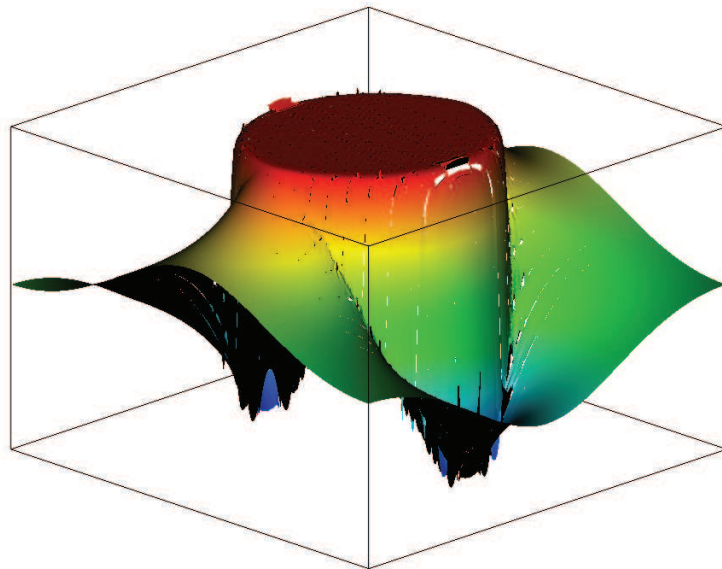
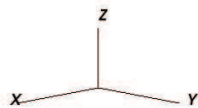
Figure 7.26: To be continued on the next page.

Pseudocolor
Var: ElectricFieldY
-0.02063
-0.6513
-1.282
-1.913
-2.543
Max: -0.02063
Min: -2.543



(e) $\frac{\epsilon_2}{\epsilon_1} = 50$

Pseudocolor
Var: ElectricFieldY
0.03112
-0.6445
-1.320
-1.996
-2.671
Max: 0.03112
Min: -2.671



(f) $\frac{\epsilon_2}{\epsilon_1} = 100$

Figure 7.26: Continued.

Satisfaction of the physical jump condition $\|D_n\| = \|\varepsilon E_n\| = 0$ at the interface is examined in the same manner as in section 7.4.2. The maximum and minimum values of the computed electric field in y -direction are taken from figure 7.26. The errors, which are shown in table 7.4 are computed as it has been described in section 7.4.2. The errors were not calculated for the ratios of 50 and 100; because of the above mentioned disturbances in the solution that affect the error calculation.

Table 7.4: Satisfaction of the physical jump condition $\|\varepsilon E_n\| = 0$ at the interface. The SIPG-MCP method with a penalty parameter coefficient of $\alpha_P = 1$ is applied. The relative error is computed as $\text{err} = \text{abs}(\frac{\|\varepsilon E_y\|}{\{\varepsilon E_y\}})$ at point $(0, 1)$ of the computational domain. $\|\cdot\|$ and $\{\cdot\}$ are the jump and average operators defined in equation 7.6. A 32×32 grid and a polynomial degree of 8 are used. The number of degrees of freedom, DOF, is 46080.

$\frac{\varepsilon_2}{\varepsilon_1}$	$E_{y_{\max}}$	$E_{y_{\min}}$	$\{\varepsilon E_y\}$	$\ \varepsilon E_y\ $	$\text{err} = \text{abs}(\frac{\ \varepsilon E_y\ }{\{\varepsilon E_y\}})\%$
2	-0.7109	-1.388	-1.4049	-0.0338	2.4
5	-0.388	-1.879	-1.9095	-0.061	3.2
10	-0.2232	-2.167	-2.1995	-0.065	3
20	-0.1126	-2.368	-2.31	0.116	5

8 Coupling the electric and fluid fields

In this chapter, the test case of a droplet suspended in another immiscible fluid with a jump in the dielectric property at the interface is considered (figure 8.1). The droplet and the surrounding medium are both perfect dielectrics. By applying a uniform stationary electric field, the dielectrophoretic force (see section 2.3) is exerted to the fluid, which induces a flow that moves the interface. By movement of the interface, the droplet deforms and the geometry for the computation of the electric field changes and the dielectrophoretic force must be computed again. This is the two-way coupling algorithm that was described in section 1.3. The droplet deforms until a force balance is reached between the electric force, pressure and surface tension. The equilibrium shape is a spheroid, for which the equilibrium deformation is given by an analytical relation in case of small deformations (see section 8.5).

The computation of the electric field was described before in chapter 7. Concerning the fluid flow, the same density and viscosities are considered for the droplet and the surrounding medium, therefore the non-dimensional density $\rho(\phi)$ and viscosity $\mu(\phi)$ are equal to 1 and the multiphase equations (3.8) are not different from the single-phase equations, except including the surface tension term. To capture the movement of the interface, a level set advection equation (3.11) is solved (Mousavi 2012).

In section 8.1, the electric force is considered. In section 8.2, the assumption of a creeping flow is made. In section 8.3, the electric force is added to the flow field (without considering the surface tension force) and the deformation of the droplet is studied. In section 8.4, the effect of the spurious currents are considered. Finally, in section 8.5, the surface tension force is added and the equilibrium shape of a droplet is achieved.

8.1 Numerical modeling of the electric force

The non-dimensional form of the dielectrophoretic force,

$$\begin{aligned}\mathbf{f}_\Omega &= -Eu \left(\frac{1}{2} |\mathbf{E}|^2 \nabla \varepsilon(\phi) \right), \\ \nabla \varepsilon(\phi) &= (\varepsilon_1 - \varepsilon_2) \nabla H(\phi), \\ \nabla H(\phi) &= \delta(\phi) \nabla \phi\end{aligned}$$

is added to the single-phase Navier-Stokes/Stokes equations (see section 3.3). As an external body force, this term is integrated with the unsteady term of the equation in the first step of the projection scheme (equation (5.6a)). A first order time integration scheme is applied. Concerning the DG discretization, this term is discretized as a source term (see section 4.2).

The delta function in the above equation is the regularized delta function that was

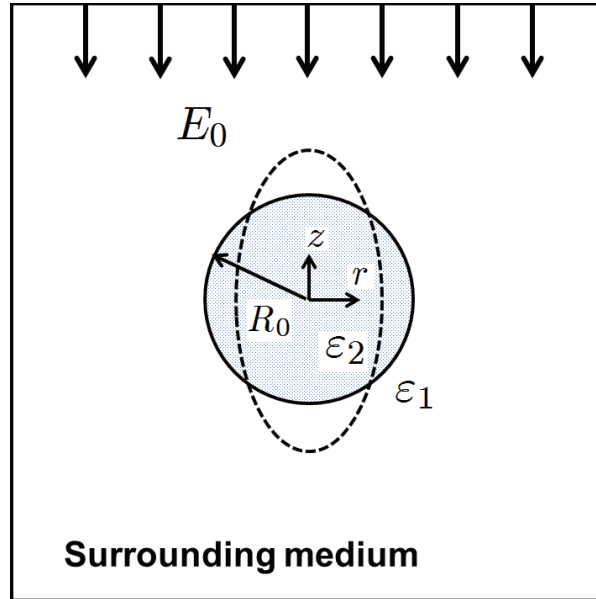


Figure 8.1: Test case of a droplet suspended in another immiscible fluid with a jump in the dielectric property at the interface.

defined in section 6.1. This means that for the numerical modeling, the force \mathbf{f}_Ω is distributed over a thickness 2ϵ around the interface and is not a concentrated force anymore. The actual concentrated dielectrophoretic force acts in the normal direction to the interface but distributing it over the interface results in some components in the tangential direction which produce recirculating spurious currents as a consequence (see section 8.4).

8.2 The creeping flow

Considering an example of a water droplet suspended in decyl alcohol, according to an experiment done by Lu (Lu 2002) for a droplet with the radius of millimeter scale and an applied electric field of order of hundreds of $\frac{kV}{m}$, the induced flow is a creeping flow ($Re \ll 1$). For creeping flows, the inertia of the fluid is negligible. Therefore the Navier-Stokes equations reduce to the Stokes equations by ignoring the convective terms with respect to the diffusive viscous terms. For the creeping flows, the Re is small enough and the spurious currents are smaller than the physical velocity field and do not affect the solution accuracy.

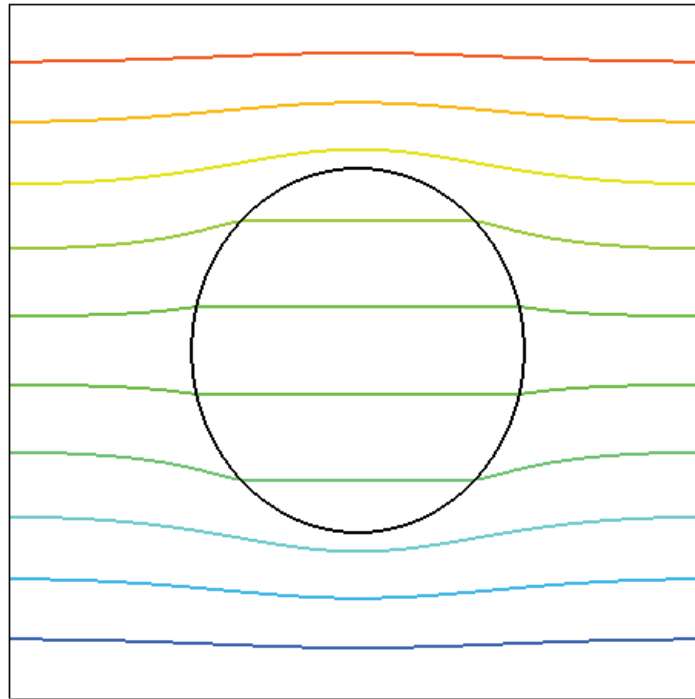
8.3 Deformation of a droplet in a stationary electric field

For the numerical solution of the above mentioned problem, the computational domain is considered as a $[-2, 2] \times [-2, 2]$ square. The droplet has a non-dimensional radius of 1. The numerical simulation is performed in 2D and the gravity is normal to the plane and therefore is not considered. A stationary and uniform electric field $E_0 = 1$ is applied

which is shown in figure 8.1. The permittivity ratio is 2 at the interface. There is no surface tension considered in this section, therefore the droplet continues to deform. A Reynolds number of 1 is considered and the Stokes equations are solved for this problem. A Cartesian grid of 24×24 cells is employed. A polynomial degree of 8 is used for the electric potential. Polynomial degrees of 5 are used for the flow field variables, see section 6.2.2. Half-thickness of the diffuse interface ϵ is equal to 0.125 which is $\frac{1}{8}$ of the radius of the droplet. The time step size is equal to $dt = 0.01$. Iso-lines of the electric potential are shown in figure 8.2. There is a change in the slope of iso-lines at the interface which implies the physical jump in the normal component of the electric field at the interface. Iso-lines of the electric field in x - and y - directions are shown in figures 8.3 and 8.4, respectively. The flow field is shown in figure 8.5. Considering the deformation of the droplet during the time (shown in figure 8.6), it preserves its spheroid shape almost until the end time of the simulation.

Results for higher permittivity ratios are not shown here because in the absence of the surface tension the simulations were not stable for a long time.

Pseudocolor
Var: ElectricPotential
4.000
3.000
2.000
1.000
-9.083e-010
Max: 4.000
Min: -9.083e-010

(a) $t = 2$

Pseudocolor
Var: ElectricPotential
4.000
3.000
2.000
1.000
-1.779e-009
Max: 4.000
Min: -1.779e-009

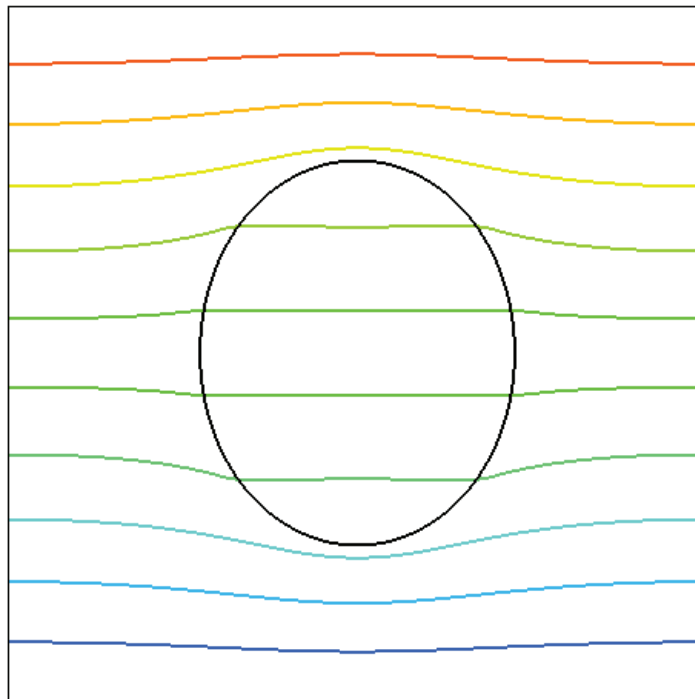
(b) $t = 4$

Figure 8.2: Iso-lines of the electric potential for the case of a droplet suspended in another immiscible fluid. A jump of ratio 2 in the dielectric property exists at the interface. The computational domain is a $[-2, 2] \times [-2, 2]$ square. The radius of the droplet is 1 and the half-thickness of the diffuse interface is $\frac{1}{8}$. A Cartesian grid of 24×24 cells is employed. A polynomial degree of 8 is used for the electric potential (to be continued on the next pages).

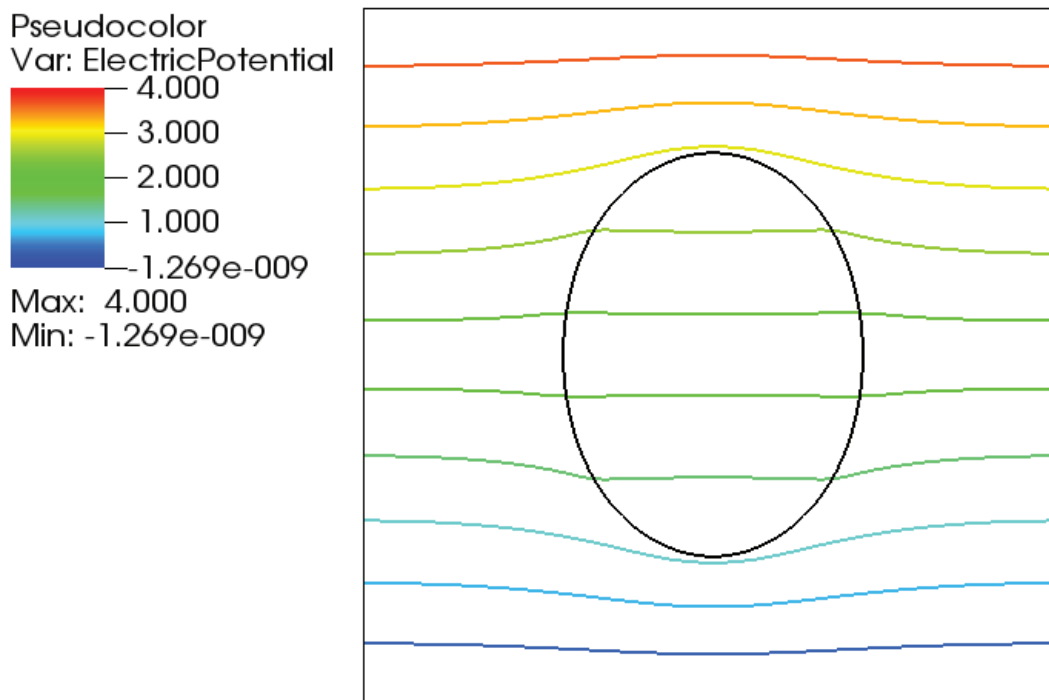
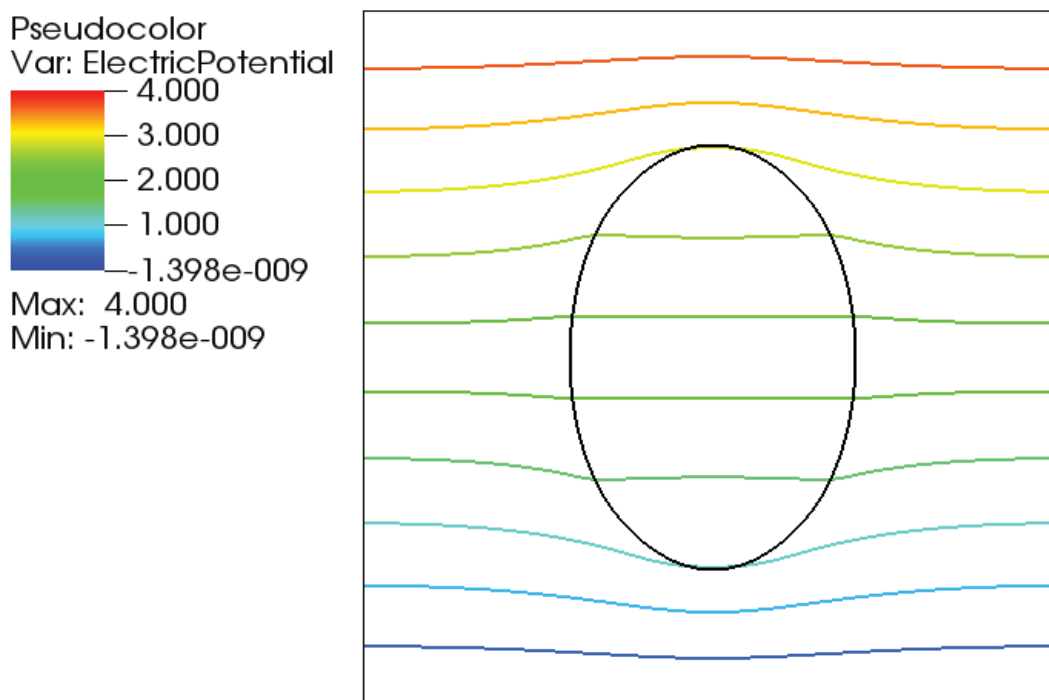
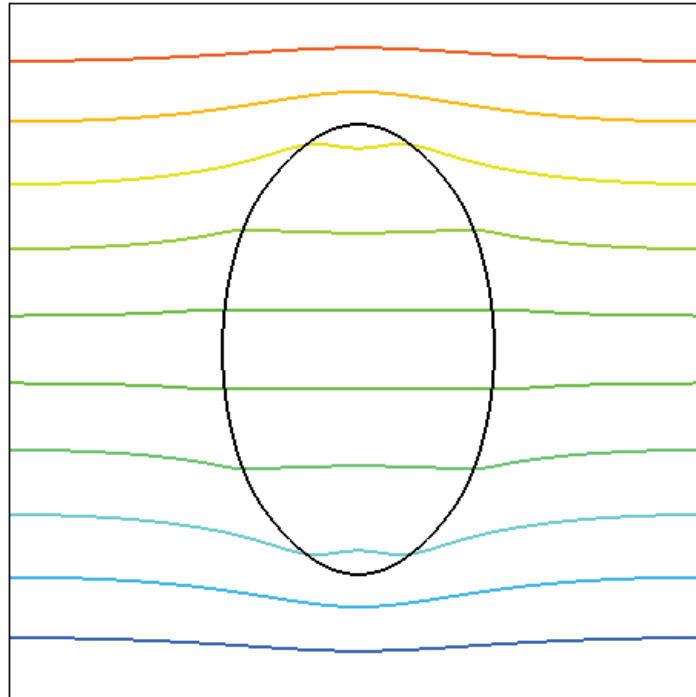
(c) $t = 6$ (d) $t = 8$

Figure 8.2: To be continued on the next pages.

Pseudocolor
Var: ElectricPotential
4.000
3.000
2.000
1.000
-4.549e-009
Max: 4.000
Min: -4.549e-009

(e) $t = 10$

Pseudocolor
Var: ElectricPotential
4.000
3.000
2.000
1.000
-4.472e-009
Max: 4.000
Min: -4.472e-009

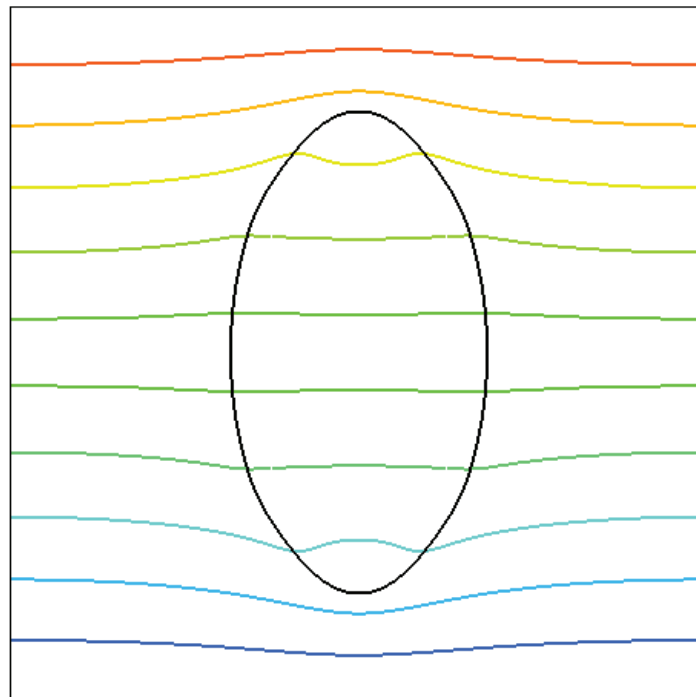
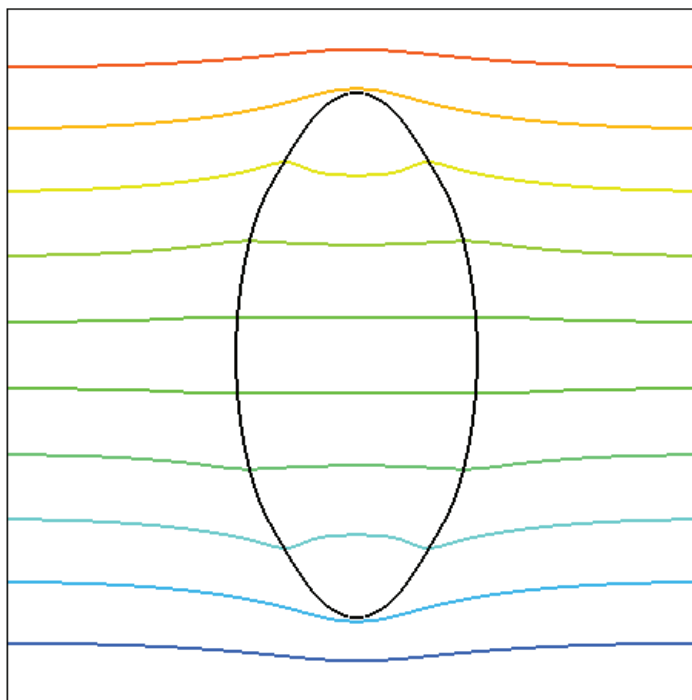
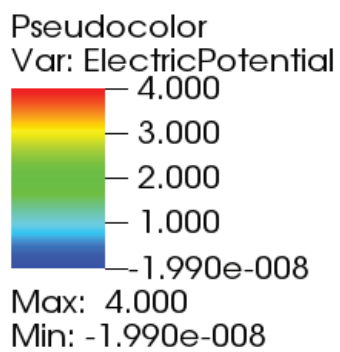
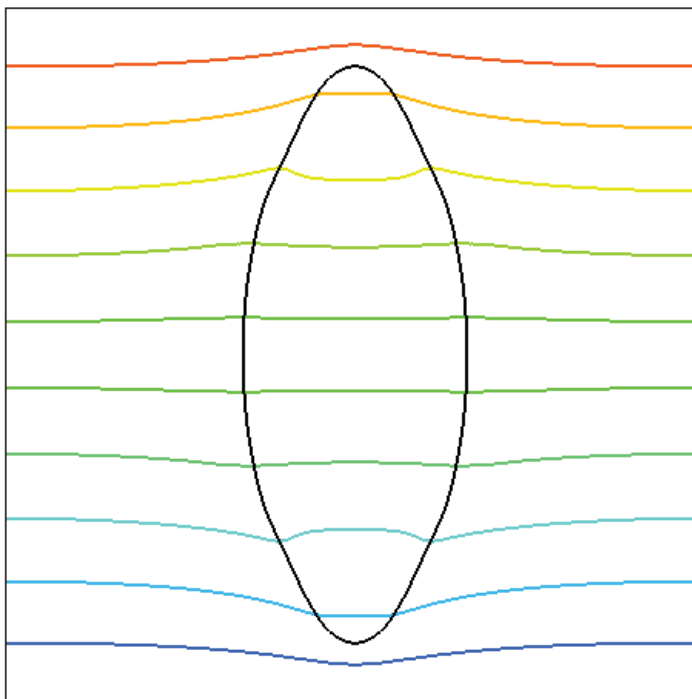
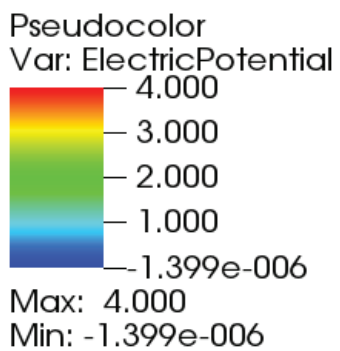
(f) $t = 12$

Figure 8.2: To be continued on the next page.




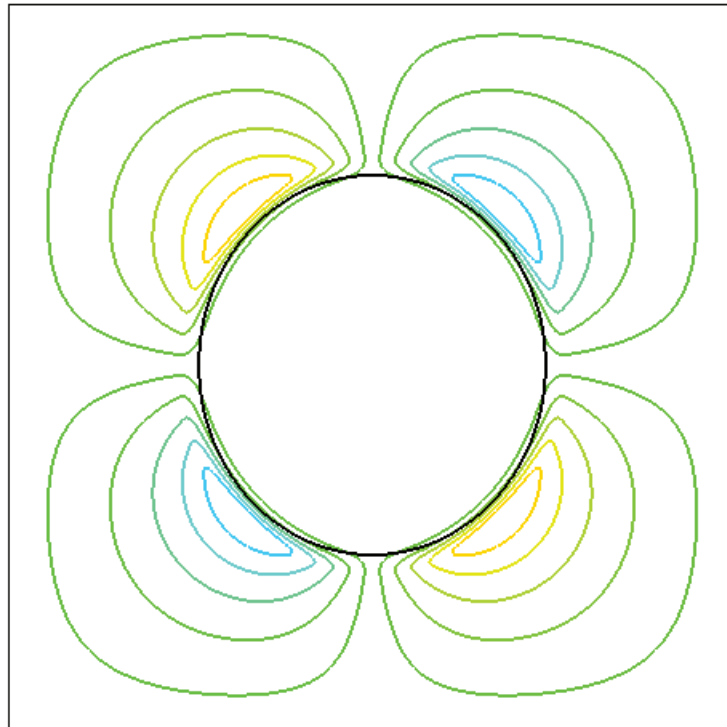
(g) $t = 14$




(h) $t = 16$

Figure 8.2: Continued.

Pseudocolor
 Var: ElectricFieldX

 0.4000
 0.2000
 0.0000
 -0.2000
 -0.4000
 Max: 0.2857
 Min: -0.2857

(a) $t = 2$

Pseudocolor
 Var: ElectricFieldX

 0.4000
 0.2000
 0.0000
 -0.2000
 -0.4000
 Max: 0.2991
 Min: -0.2991

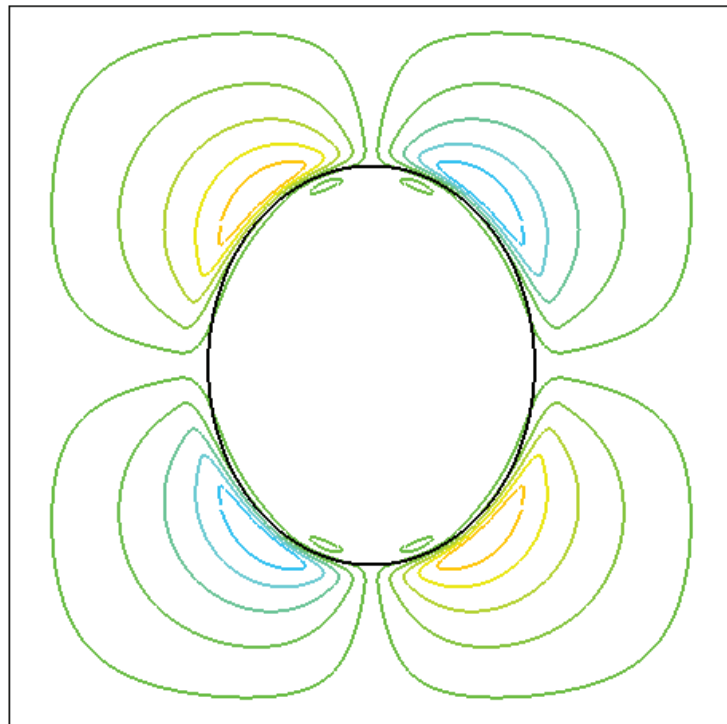
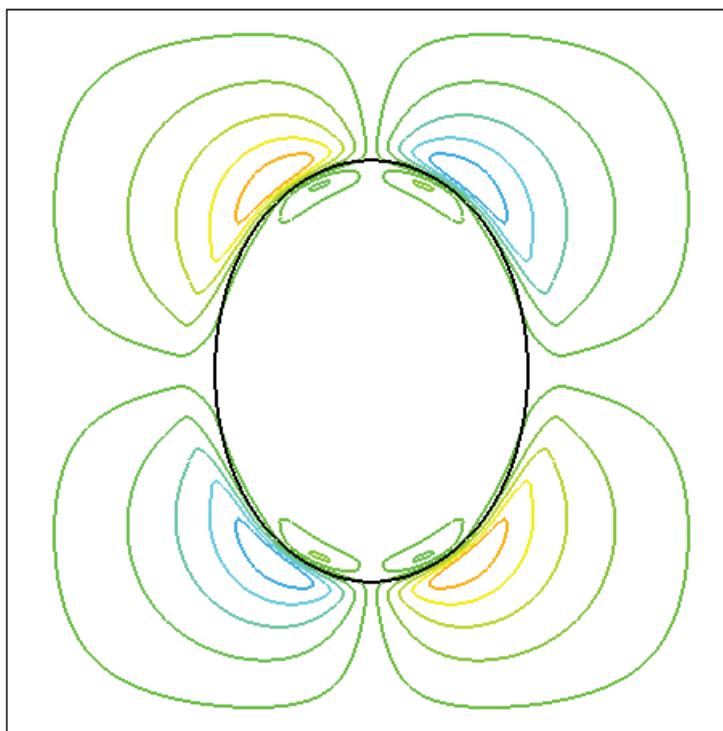
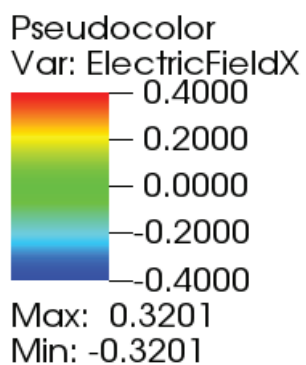
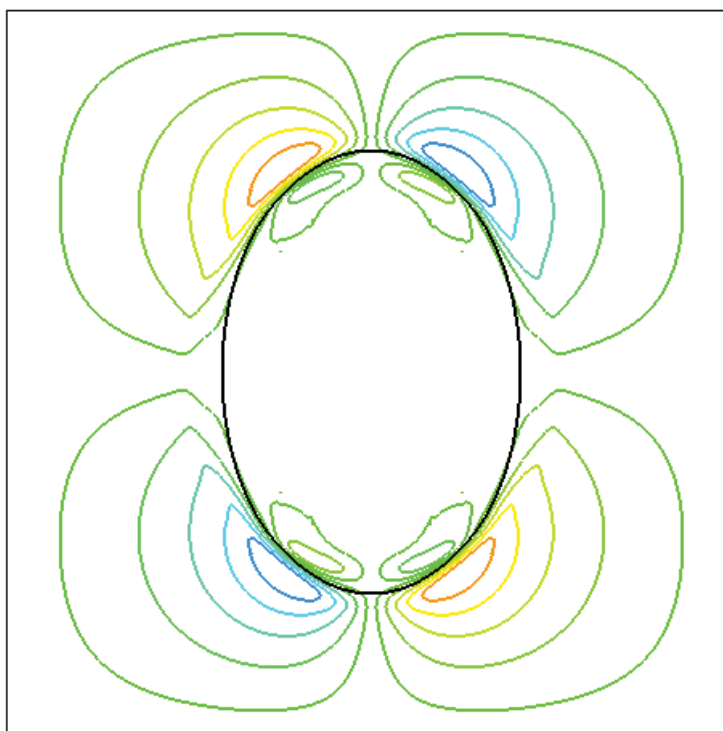
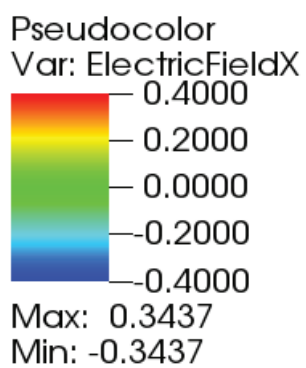
(b) $t = 4$

Figure 8.3: Iso-lines of the electric field in x -direction for the case of a droplet suspended in another immiscible fluid. A jump of ratio 2 in the dielectric property exists at the interface. The computational domain is a $[-2, 2] \times [-2, 2]$ square. The radius of the droplet is 1 and the half-thickness of the diffuse interface is $\frac{1}{8}$. A Cartesian grid of 24×24 cells is employed. Polynomial degrees of 8 and 7 are used for the electric potential and electric field, respectively (to be continued on the next pages).



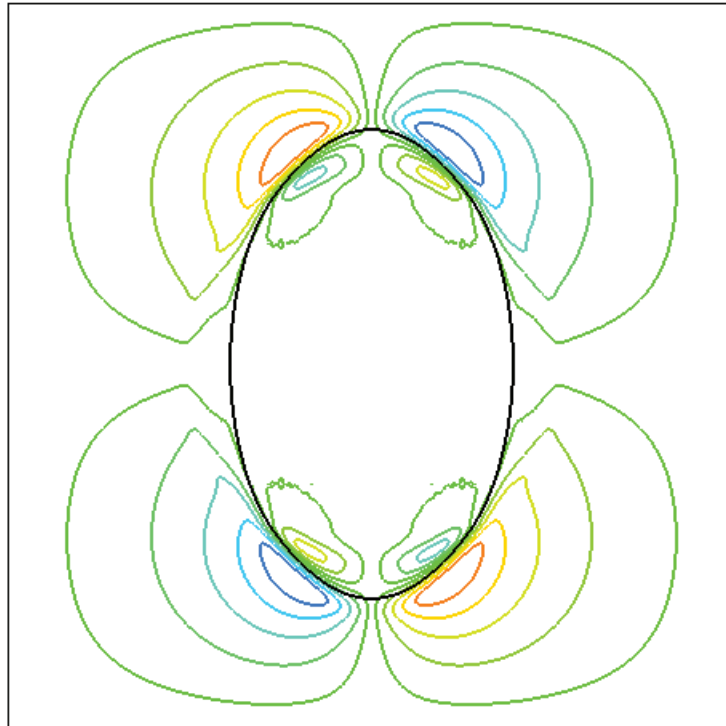
(c) $t = 6$



(d) $t = 8$

Figure 8.3: To be continued on the next pages.

Pseudocolor
Var: ElectricFieldX
0.4000
0.2000
0.0000
-0.2000
-0.4000
Max: 0.3651
Min: -0.3651

(e) $t = 10$

Pseudocolor
Var: ElectricFieldX
0.4000
0.2000
0.0000
-0.2000
-0.4000
Max: 0.3841
Min: -0.3841

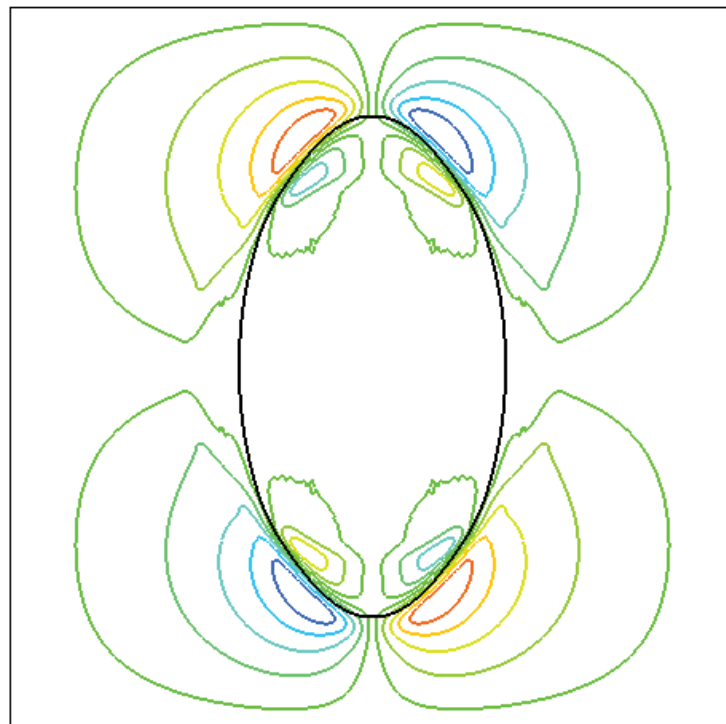
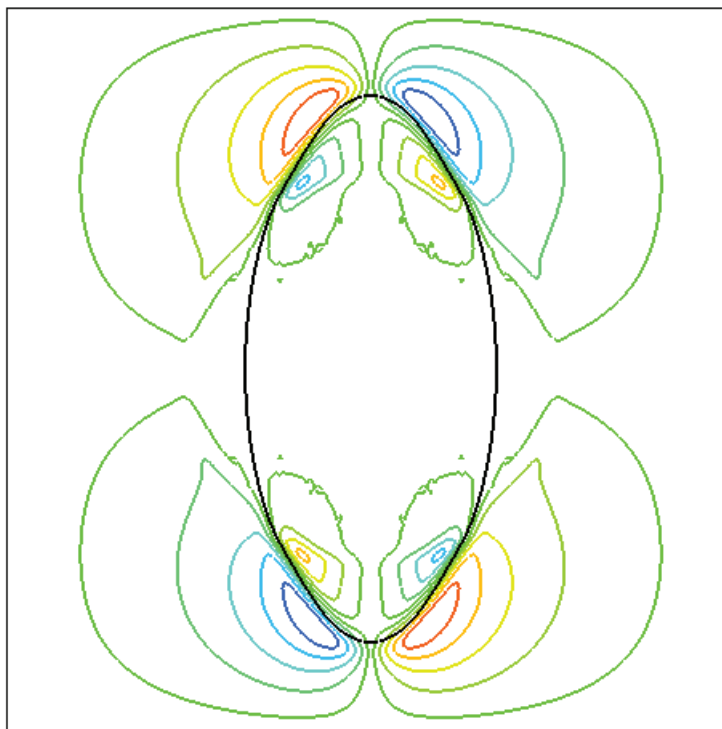
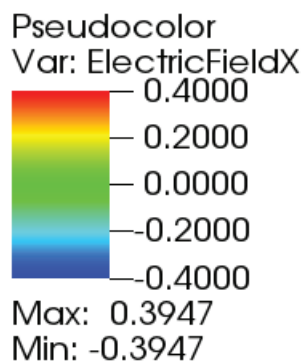
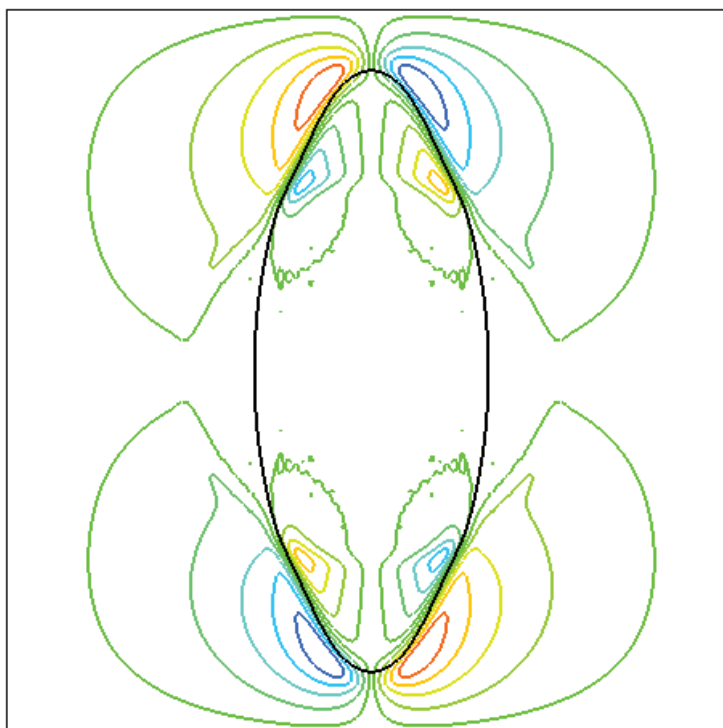
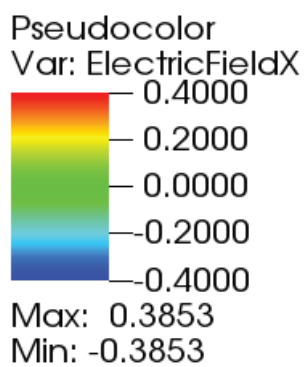
(f) $t = 12$

Figure 8.3: To be continued on the next page.



(g) $t = 14$



(h) $t = 16$

Figure 8.3: Continued.

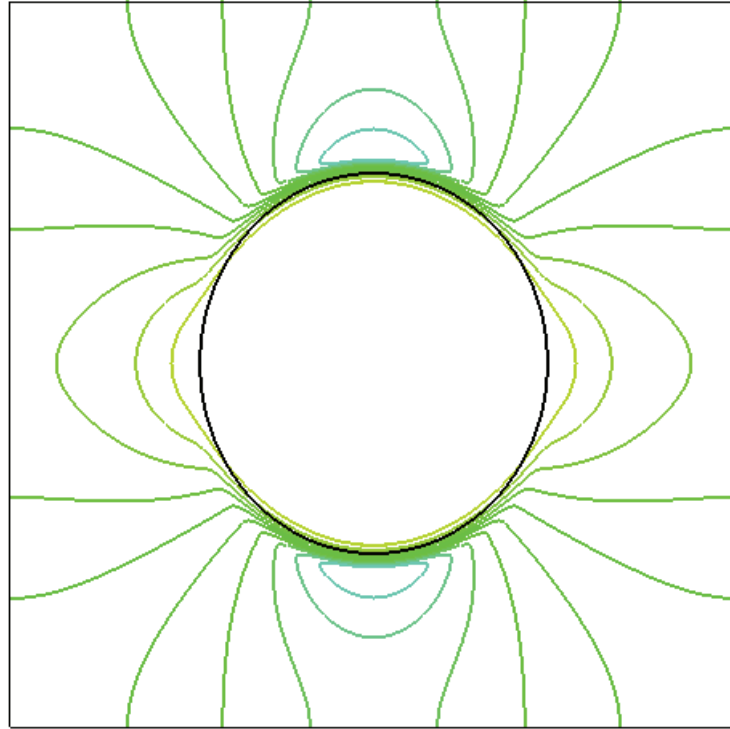
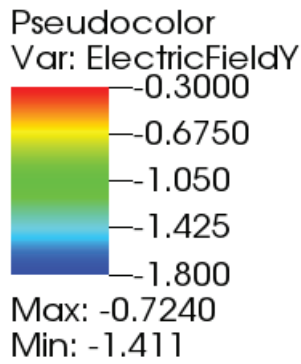
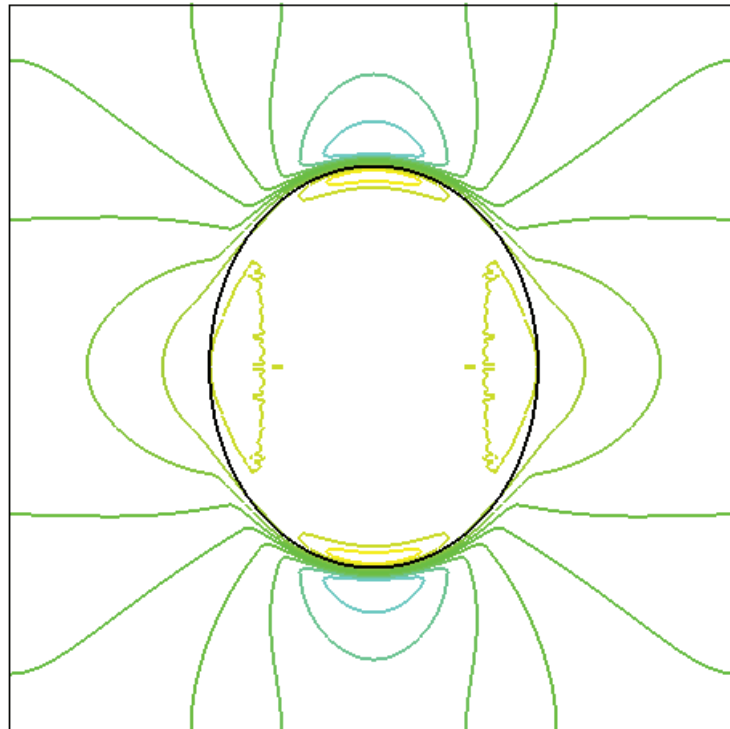
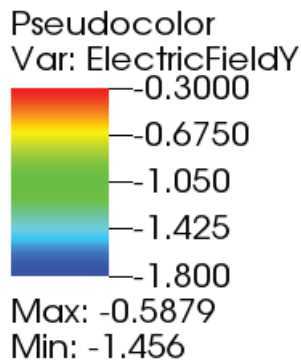
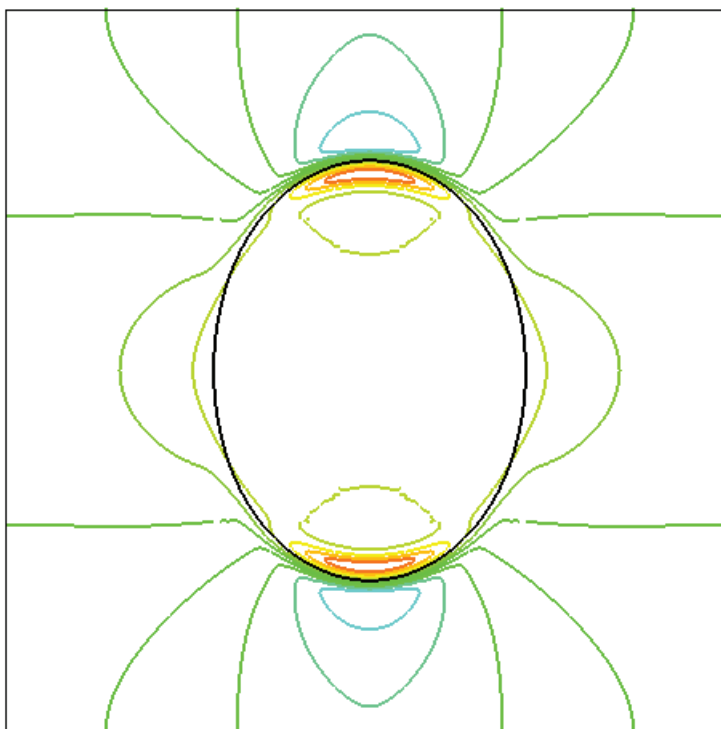
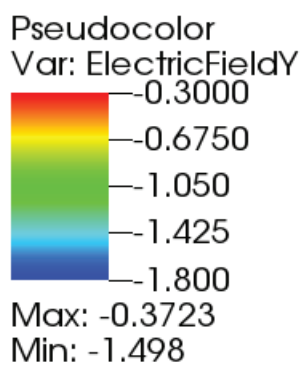
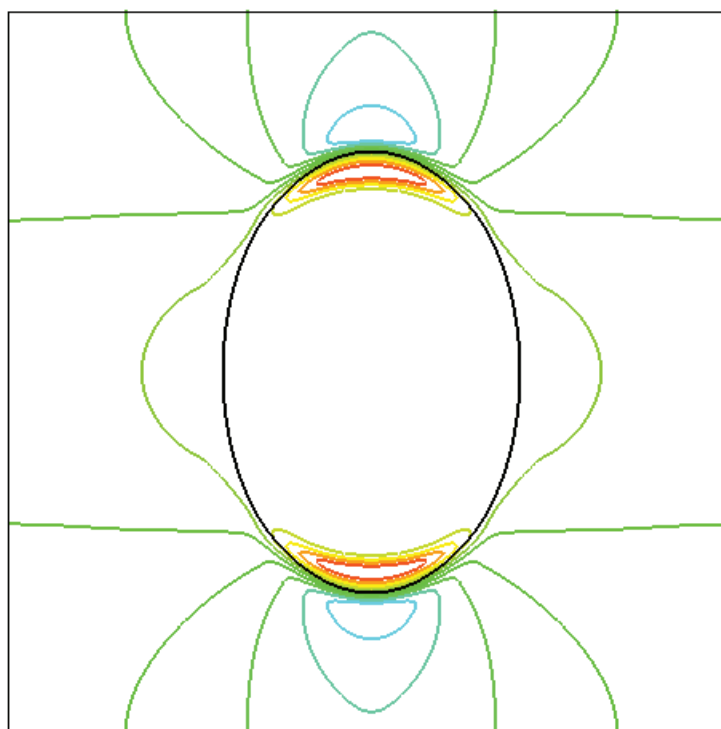
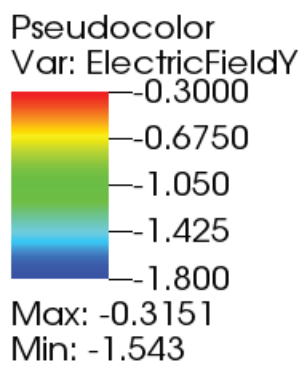
(a) $t = 2$ (b) $t = 4$

Figure 8.4: Iso-lines of the electric field in y -direction for the case of a droplet suspended in another immiscible fluid. A jump of ratio 2 in the dielectric property exists at the interface. The computational domain is a $[-2, 2] \times [-2, 2]$ square. The radius of the droplet is 1 and the half-thickness of the diffuse interface is $\frac{1}{8}$. A Cartesian grid of 24×24 cells is employed. Polynomial degrees of 8 and 7 are used for the electric potential and electric field, respectively (to be continued on the next pages).



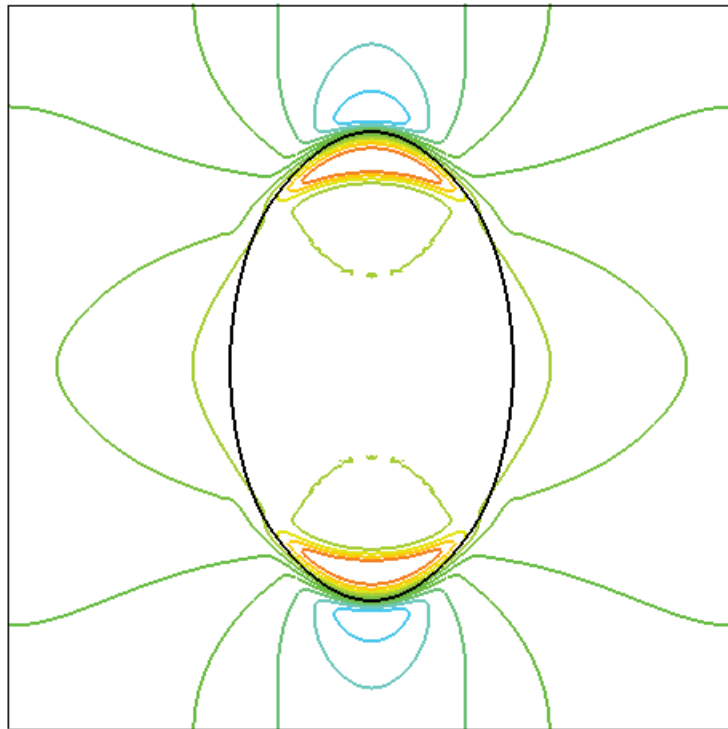
(c) $t = 6$



(d) $t = 8$

Figure 8.4: To be continued on the next pages.

Pseudocolor
Var: ElectricFieldY
-0.3000
-0.6750
-1.050
-1.425
-1.800
Max: -0.3773
Min: -1.592

(e) $t = 10$

Pseudocolor
Var: ElectricFieldY
-0.3000
-0.6750
-1.050
-1.425
-1.800
Max: -0.4519
Min: -1.644

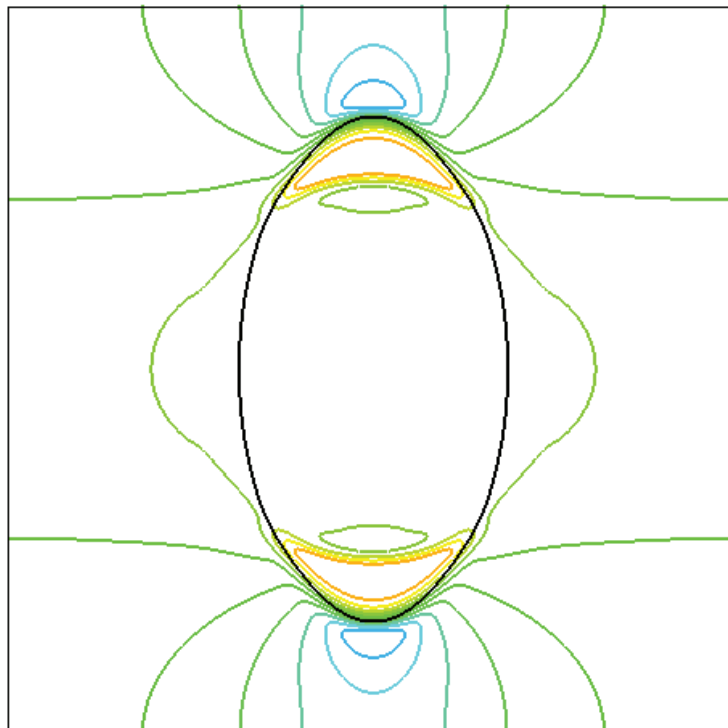
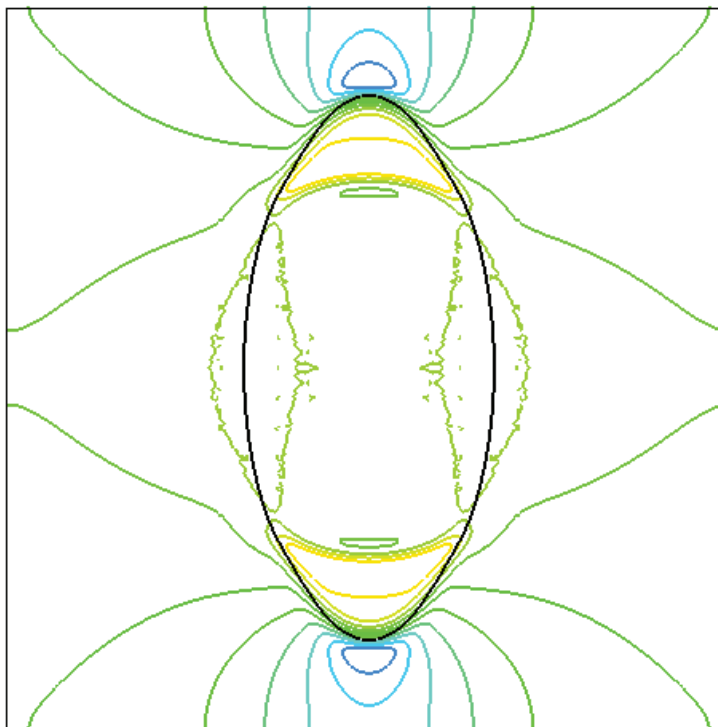
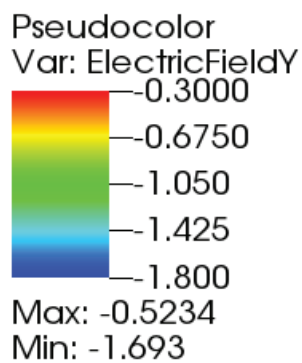
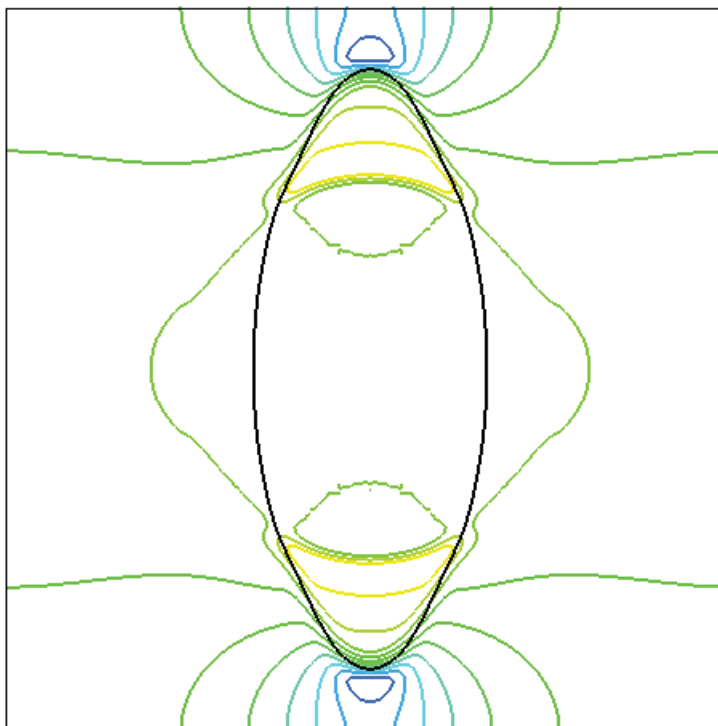
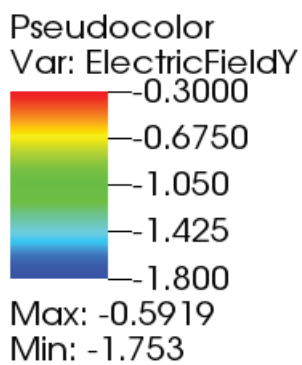
(f) $t = 12$

Figure 8.4: To be continued on the next page.



(g) $t = 14$

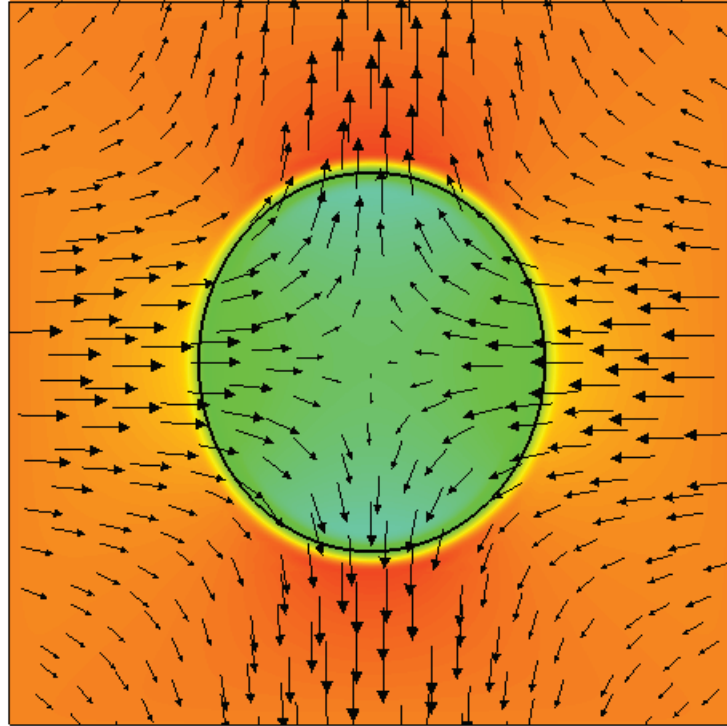


(h) $t = 16$

Figure 8.4: Continued.

Pseudocolor
Var: Phi
0.1000
0.09250
0.2850
0.4775
0.6700
Max: 0.04702
Min: -0.4270

Vector
Var: Velocity
Max: 0.03076
Min: 9.600e-006

(a) $t = 2$

Pseudocolor
Var: Phi
0.1000
0.09250
0.2850
0.4775
0.6700
Max: 0.04046
Min: -0.3973

Vector
Var: Velocity
Max: 0.03174
Min: 3.155e-006

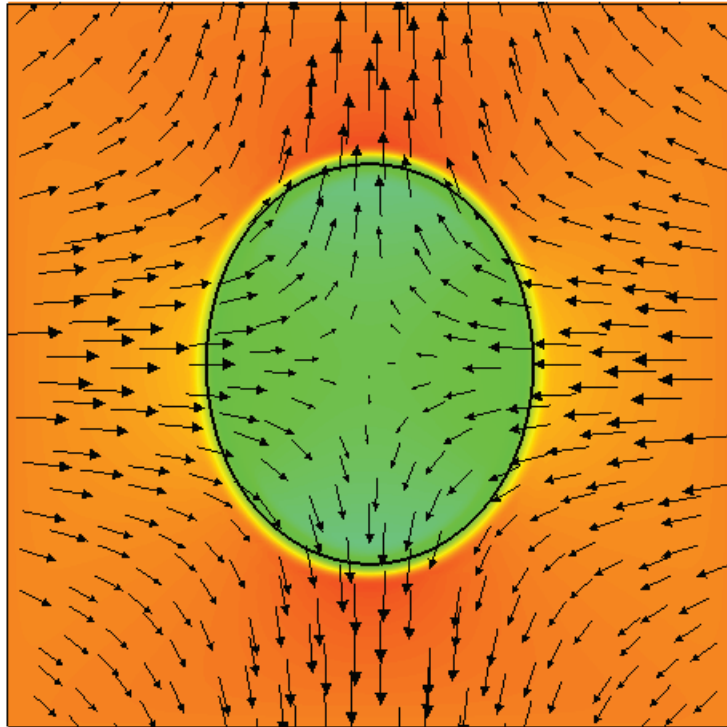
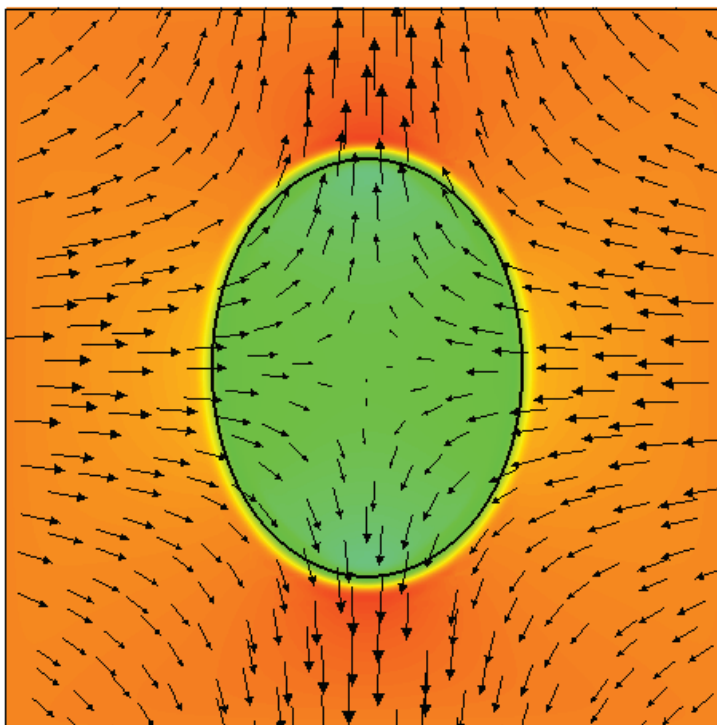
(b) $t = 4$

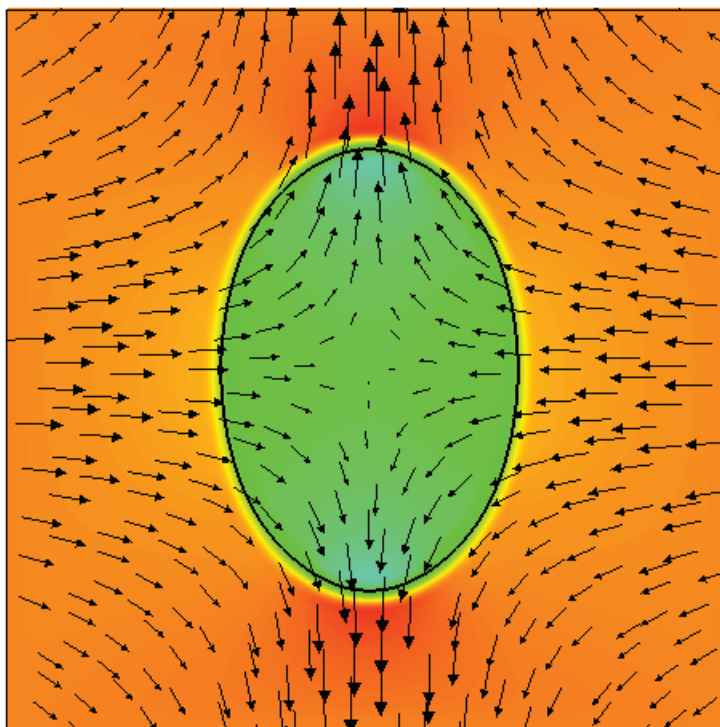
Figure 8.5: Flow field for the case of a droplet suspended in another immiscible fluid. A jump of ratio 2 in the dielectric property exists at the interface. No surface tension force is considered. The computational domain is a $[-2, 2] \times [-2, 2]$ square. The radius of the droplet is 1 and the half-thickness of the diffuse interface is $\frac{1}{8}$. A Cartesian grid of 24×24 cells is employed. A polynomial degree of 5 is used for the flow field variables (to be continued on the next pages).

Pseudocolor
 Var: Phi
 0.1000
 0.09250
 0.2850
 0.4775
 0.6700
 Max: 0.04867
 Min: -0.3977
 Vector
 Var: Velocity
 Max: 0.03023
 Min: 1.871e-006



(c) $t = 6$

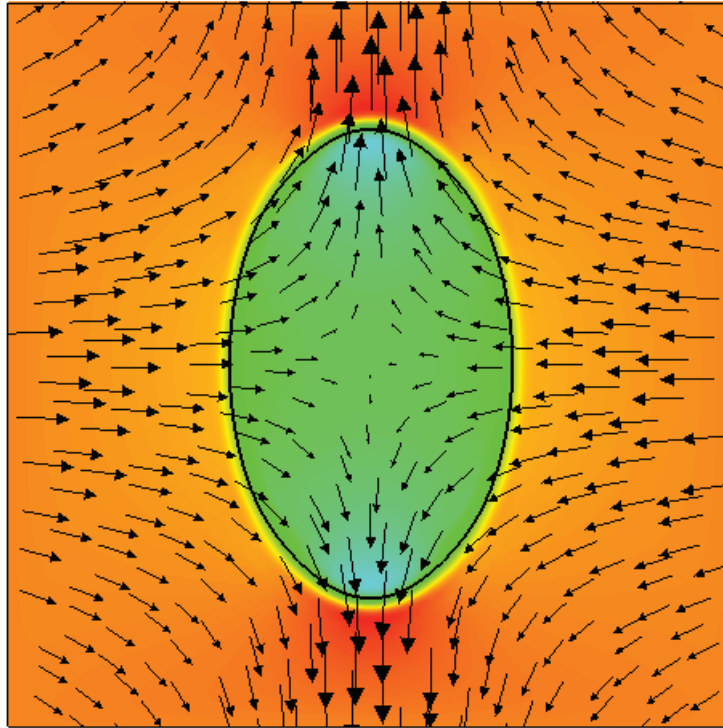
Pseudocolor
 Var: Phi
 0.1000
 0.09250
 0.2850
 0.4775
 0.6700
 Max: 0.06057
 Min: -0.4287
 Vector
 Var: Velocity
 Max: 0.03350
 Min: 3.704e-006



(d) $t = 8$

Figure 8.5: To be continued on the next pages.

Pseudocolor
Var: Phi
0.1000
-0.09250
-0.2850
-0.4775
-0.6700
Max: 0.07655
Min: -0.4696
Vector
Var: Velocity
Max: 0.04183
Min: 5.872e-006

(e) $t = 10$

Pseudocolor
Var: Phi
0.1000
-0.09250
-0.2850
-0.4775
-0.6700
Max: 0.08924
Min: -0.5195
Vector
Var: Velocity
Max: 0.05285
Min: 3.551e-006

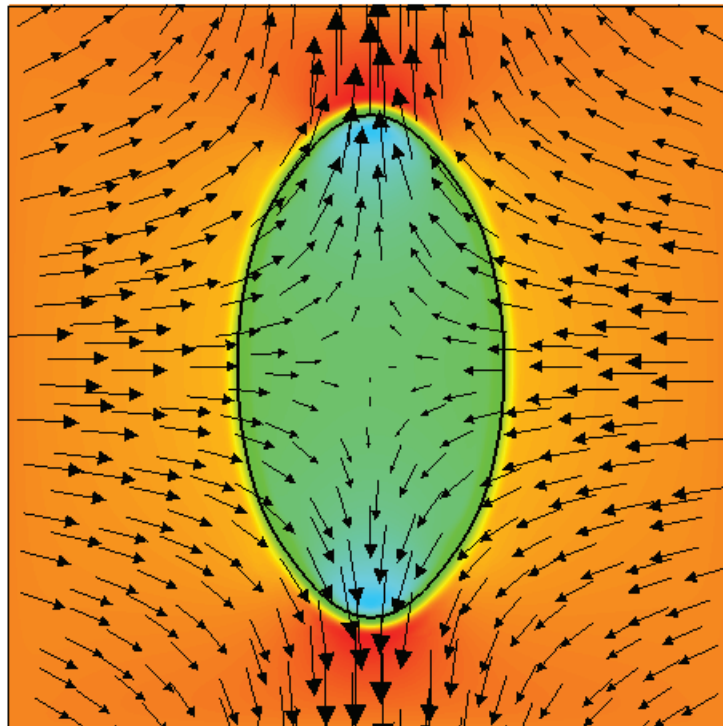
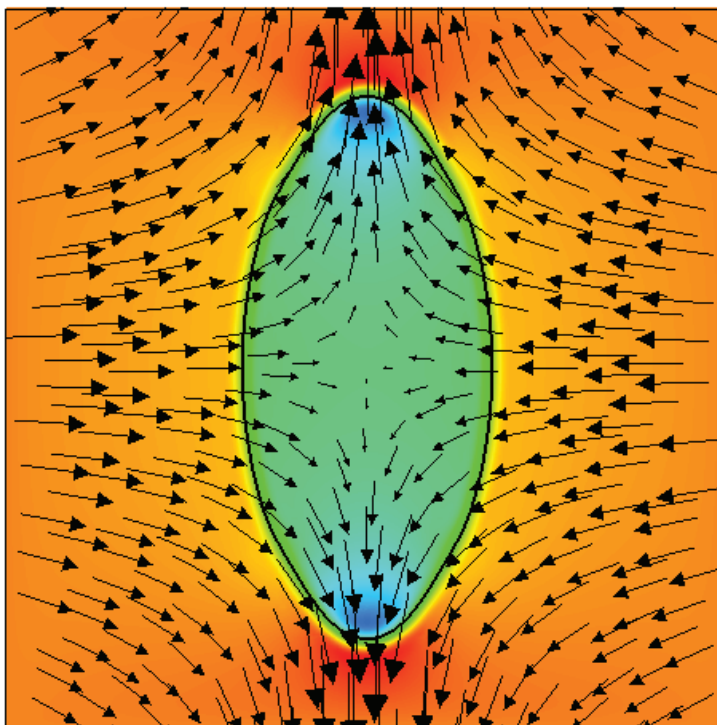
(f) $t = 12$

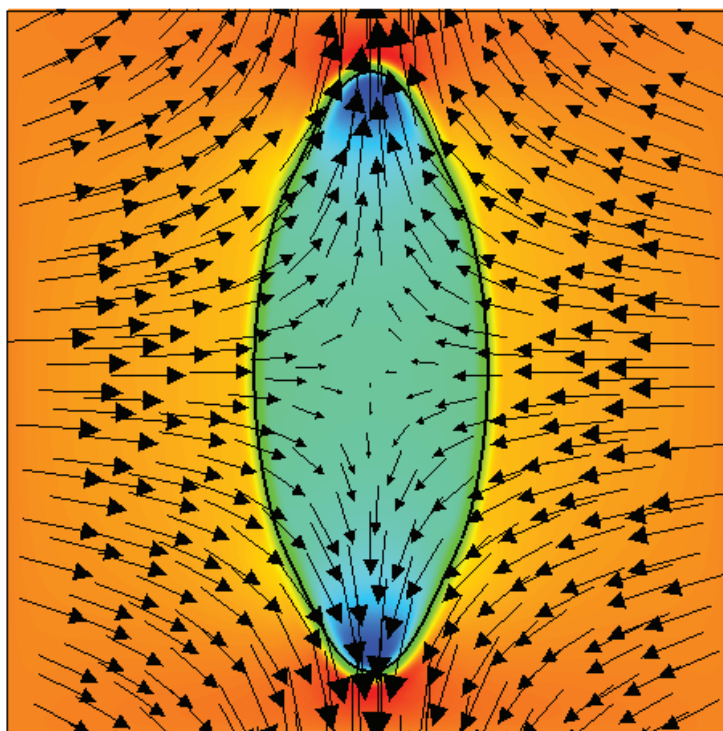
Figure 8.5: To be continued on the next page.

Pseudocolor
 Var: Phi
 0.1000
 -0.09250
 -0.2850
 -0.4775
 -0.6700
 Max: 0.09891
 Min: -0.5820
 Vector
 Var: Velocity
 Max: 0.06617
 Min: 5.134e-006



(g) $t = 14$

Pseudocolor
 Var: Phi
 0.1000
 -0.09250
 -0.2850
 -0.4775
 -0.6700
 Max: 0.09928
 Min: -0.6627
 Vector
 Var: Velocity
 Max: 0.08279
 Min: 1.039e-005



(h) $t = 16$

Figure 8.5: Continued.

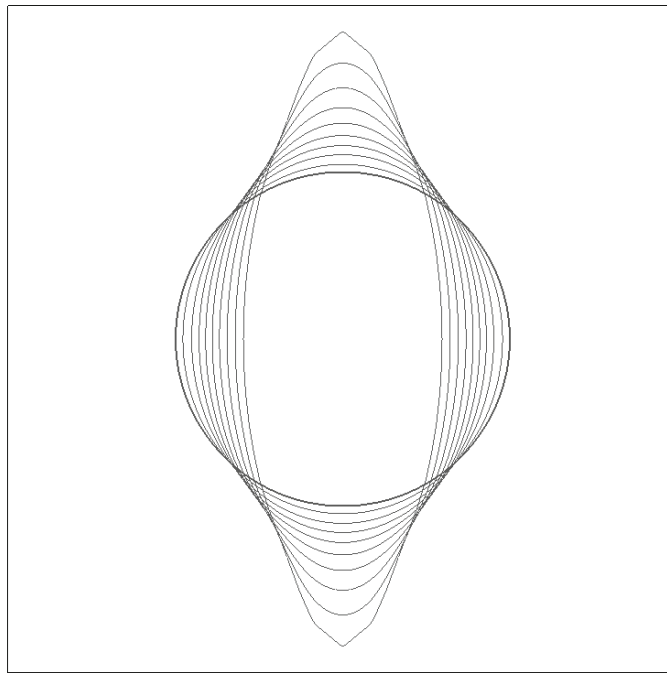


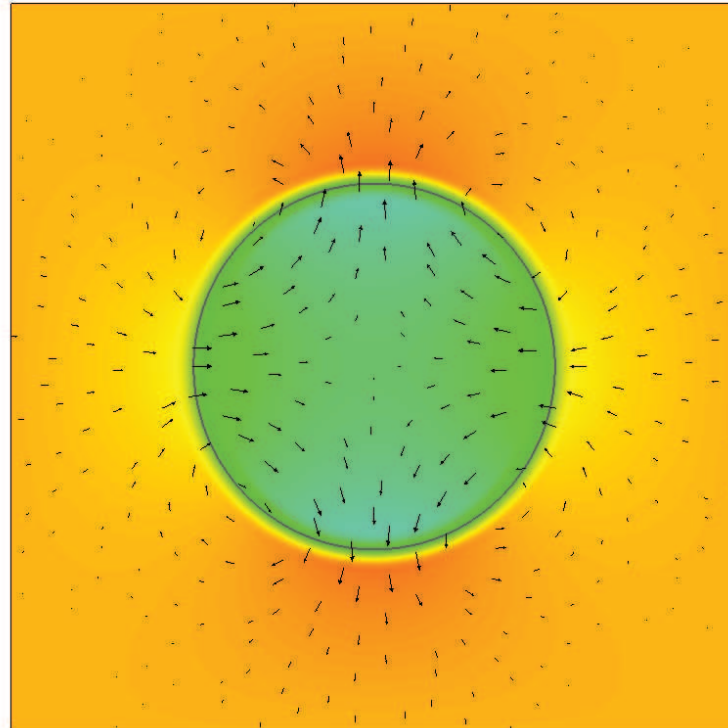
Figure 8.6: Deformation of a droplet suspended in another immiscible fluid during at the times $t = 2$ to $t = 16$. A jump of ratio 2 in the dielectric property exists at the interface. No surface tension force is considered. The computational domain is a $[-2, 2] \times [-2, 2]$ square. The radius of the droplet is 1 and the half-thickness of the diffuse interface is $\frac{1}{8}$. A Cartesian grid of 24×24 cells is employed. A polynomial degree of 8 is used for the electric potential and polynomial degrees of 5 are used for the flow field variables.

8.4 Spurious currents

The test case in section 8.3 is considered again. To show the effect of the Reynolds number in amplifying the spurious currents, we have chosen $Re = 1000$ and solved the Navier-Stokes equations. The flow field is shown in figure 8.7. Although the simulation is stable and the droplet continues to deform, the circulating regions in the flow are due to the spurious currents and are not physical.

Pseudocolor
 Var: Phi
 0.0001500
 -6.250e-005
 -0.0002750
 -0.0004875
 -0.0007000
 Max: 5.134e-005
 Min: -0.0004349

Vector
 Var: Velocity
 Max: 0.001199
 Min: 5.336e-008

(a) $t = 10$

Pseudocolor
 Var: Phi
 0.0001500
 -6.250e-005
 -0.0002750
 -0.0004875
 -0.0007000
 Max: 5.013e-005
 Min: -0.0004359

Vector
 Var: Velocity
 Max: 0.002249
 Min: 6.485e-008

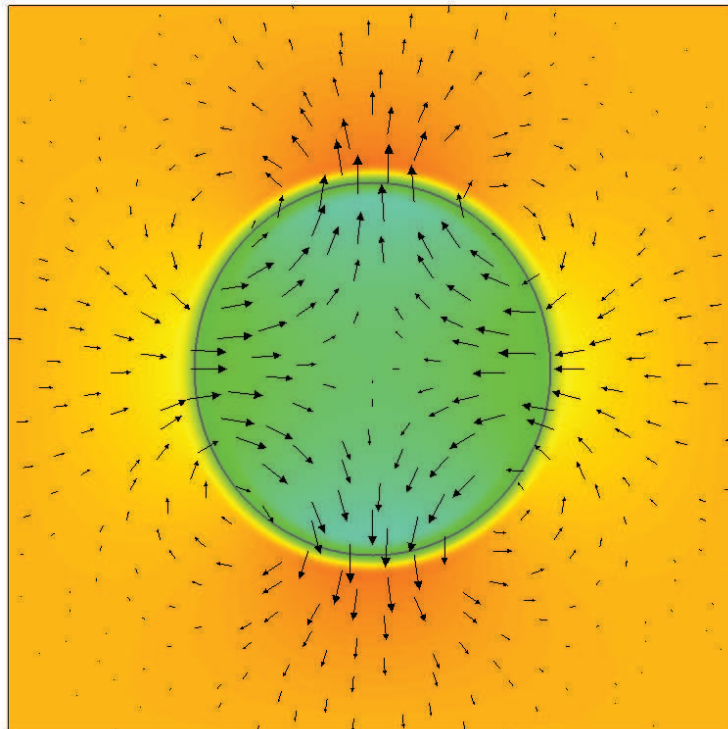
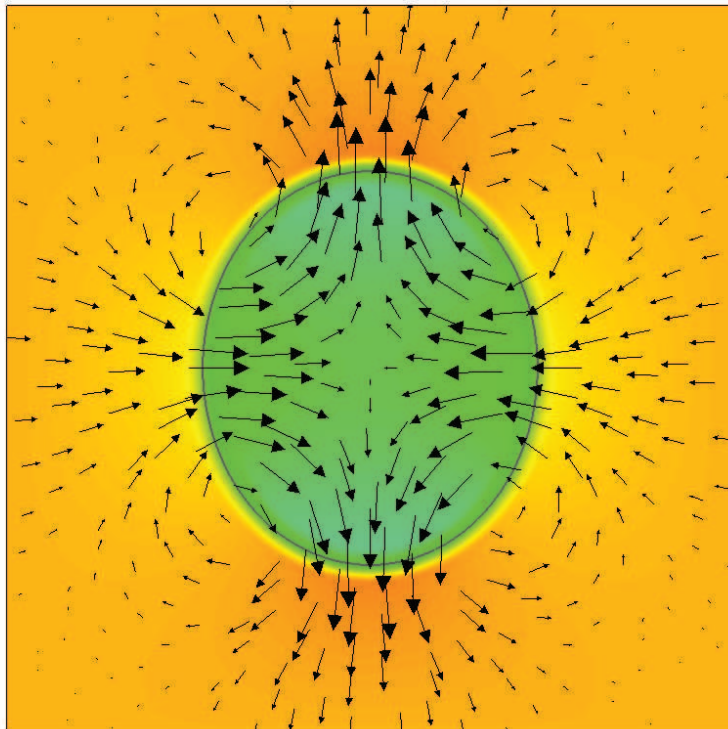
(b) $t = 20$

Figure 8.7: Effect of the Reynolds number in amplifying the spurious currents for the case of a droplet suspended in another immiscible fluid. A Reynolds number of 1000 is considered. A jump of ratio 2 in the dielectric property exists at the interface. No surface tension force is considered. The computational domain is a $[-2, 2] \times [-2, 2]$ square. The radius of the droplet is 1 and the half-thickness of the diffuse interface is $\frac{1}{8}$. A Cartesian grid of 24×24 cells is employed. Polynomial degrees of 5 are used for the flow field variables (to be continued on the next pages).

Pseudocolor
 Var: Phi
 0.0001500
 -6.250e-005
 -0.0002750
 -0.0004875
 -0.0007000
 Max: 3.733e-005
 Min: -0.0004114

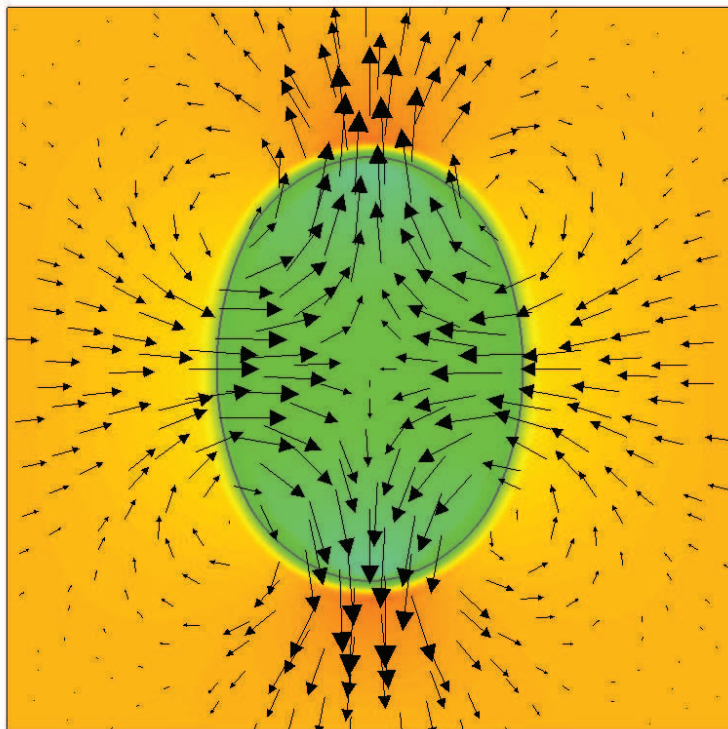
Vector
 Var: Velocity
 Max: 0.003759
 Min: 4.302e-007



(c) $t = 40$

Pseudocolor
 Var: Phi
 0.0001500
 -6.250e-005
 -0.0002750
 -0.0004875
 -0.0007000
 Max: 5.213e-005
 Min: -0.0004116

Vector
 Var: Velocity
 Max: 0.005231
 Min: 5.322e-008

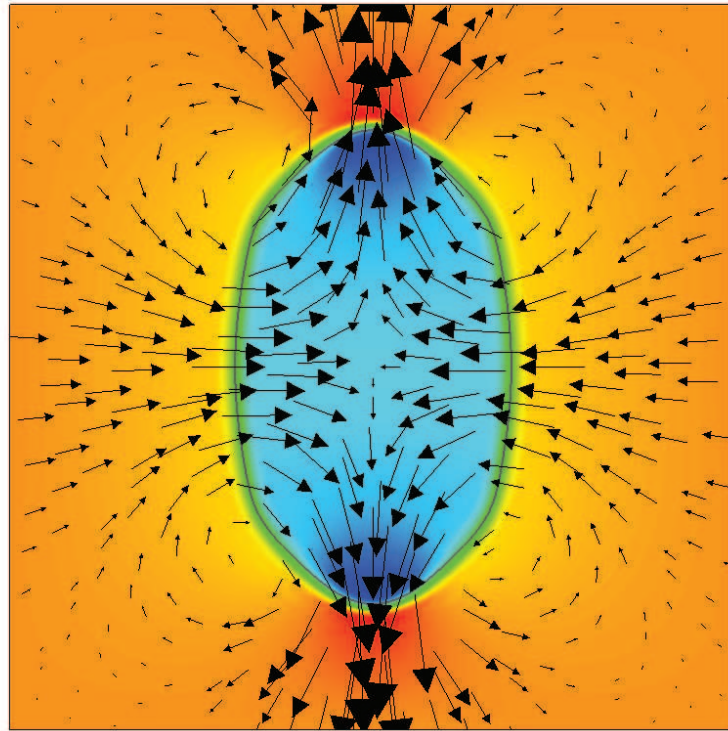


(d) $t = 60$

Figure 8.7: To be continued on the next page.

Pseudocolor
Var: Phi
8.555e-005
-6.109e-005
-0.0002077
-0.0003544
-0.0005010
Max: 8.555e-005
Min: -0.0005010

Vector
Var: Velocity
Max: 0.008808
Min: 1.513e-007

(e) $t = 80$

Pseudocolor
Var: Phi
0.0001500
-6.250e-005
-0.0002750
-0.0004875
-0.0007000
Max: 0.0001472
Min: -0.0006821

Vector
Var: Velocity
Max: 0.01466
Min: 1.950e-007

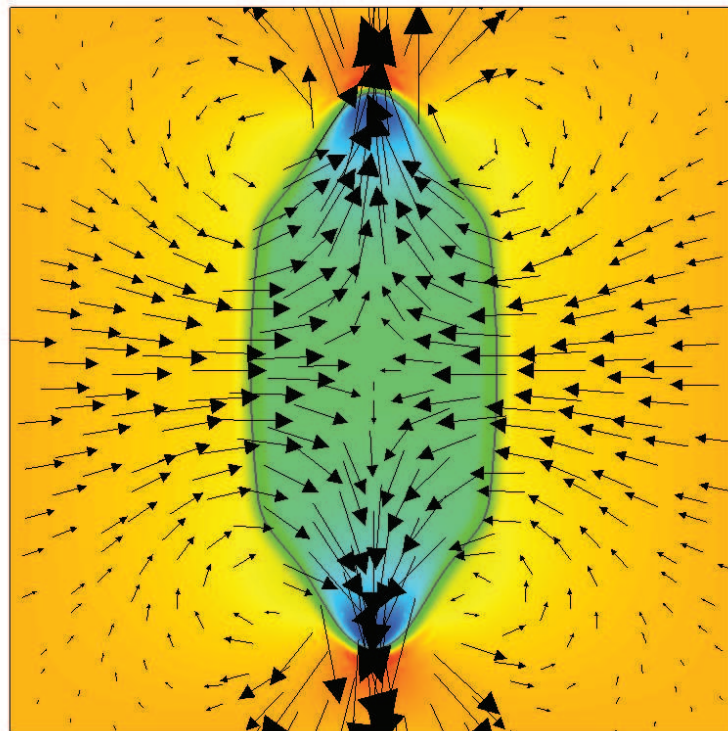
(f) $t = 100$

Figure 8.7: Continued.

8.5 Equilibrium shape of a droplet in a stationary electric field

The surface tension force is added here to find the equilibrium shape of the deformed droplet of the previous test case of section 8.3. The droplet is deformed until a force balance is reached at the interface. By adding the surface tension force, there are additional spurious currents induced in the flow field (see chapter 6). In order to make sure that the spurious currents do not become dominant, creeping flows (low Reynolds number) are considered.

8.5.1 The steady state deformation

The steady state deformation of the droplet is defined, according to figure 8.8, as

$$d_{\infty} = \frac{b - a}{b + a}, \quad (8.1)$$

where a is the equatorial radius and b is the polar semi-axis of the spheroid. The following analytical expression of (OTAM) (O’Konski & Thacher 1953) and (Allan & Mason 1962) is used to predict the steady state deformation of the droplet,

$$d_{\infty} = \frac{\varepsilon_0 \varepsilon_1 E_0^2 R_0}{\gamma} \frac{9(S - 1)^2}{16(S + 2)^2}, \quad (8.2)$$

where $S = \frac{\varepsilon_2}{\varepsilon_1}$ and R_0 is the initial radius of the droplet. The OTAM expression is valid for small deformations (Lu 2002) and (Supeene et al. 2008). Considering that the flow is a creeping flow, the Weber number is defined as

$$We = \frac{p_c l_c}{\gamma_c} = \frac{\varepsilon_0 \varepsilon_1 E_0^2 R_0}{\gamma} \quad (8.3)$$

Therefore, the deformation is defined as

$$d_{\infty} = We \frac{9(S - 1)^2}{16(S + 2)^2} \quad (8.4)$$

For large ratios of the permittivity, $S > 10$, the deformation does not depend on the permittivity ratio,

$$d_{\infty} = \frac{9}{16} We \quad (8.5)$$

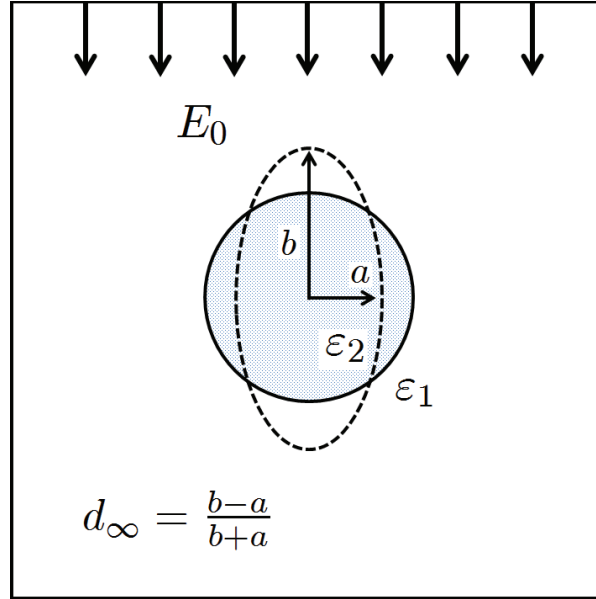


Figure 8.8: Deformation of a droplet suspended in another immiscible fluid with a jump in the dielectric property at the interface.

8.5.2 Numerical test case

For the numerical simulation, a We number of 0.2 and a permittivity ratio of $S = 10$ were considered. In order to make sure that the spurious currents do not become dominant, a Reynolds number of 0.01 is considered. The computational domain is a $[-2, 2] \times [-2, 2]$ square. The radius of the droplet is 1. The half-thickness of the diffuse interface is 0.1429 which is $\frac{1}{7}$ of the radius of the droplet. A grid of 40×40 cells is employed. A polynomial degree of 8 is used for the electric potential and polynomial degrees of 5 are used for the flow field variables, see section 6.2.2. The flow field is shown in figure 8.9. The deformation of the droplet to a spheroid is shown in figure 8.10. In figures 8.10b and 8.10c, for the visualization purpose, each cell is divided into 64 sub-cells. Therefore, the resolution is $\frac{h}{8} = 0.0125$. From figures 8.10b and 8.10c, the equatorial radius and polar semi-axis are found as $a = 0.9666$ and $b = 1.0335$. The computed deformation is $d_\infty = 0.033$ that is in a good agreement with the predicted deformation of 0.032 according to the OTAM expression. The relative error $\frac{d_\infty - d_{OTAM}}{d_{OTAM}}$ is 3%. The area of the spheroid is computed as $\pi ab = 3.135$ which, in comparison to the area of the droplet before applying the electric field, $\pi R_0^2 = \pi = 3.1416$, has a relative error of 0.2%. This implies that the mass is well conserved in our numerical simulation.

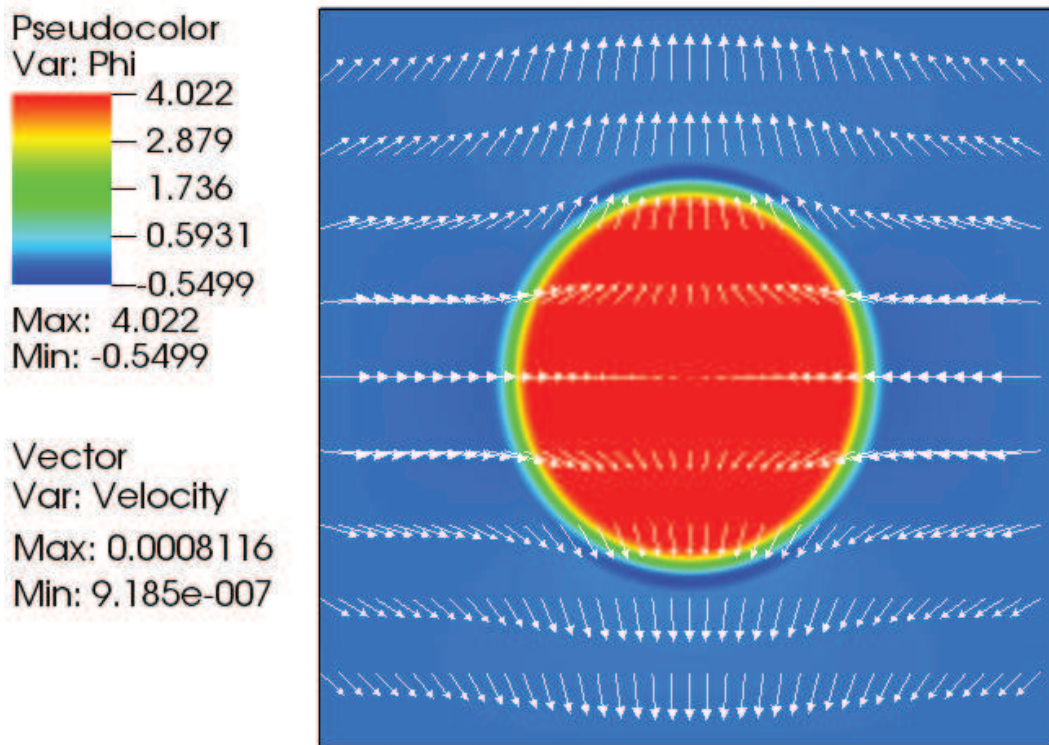
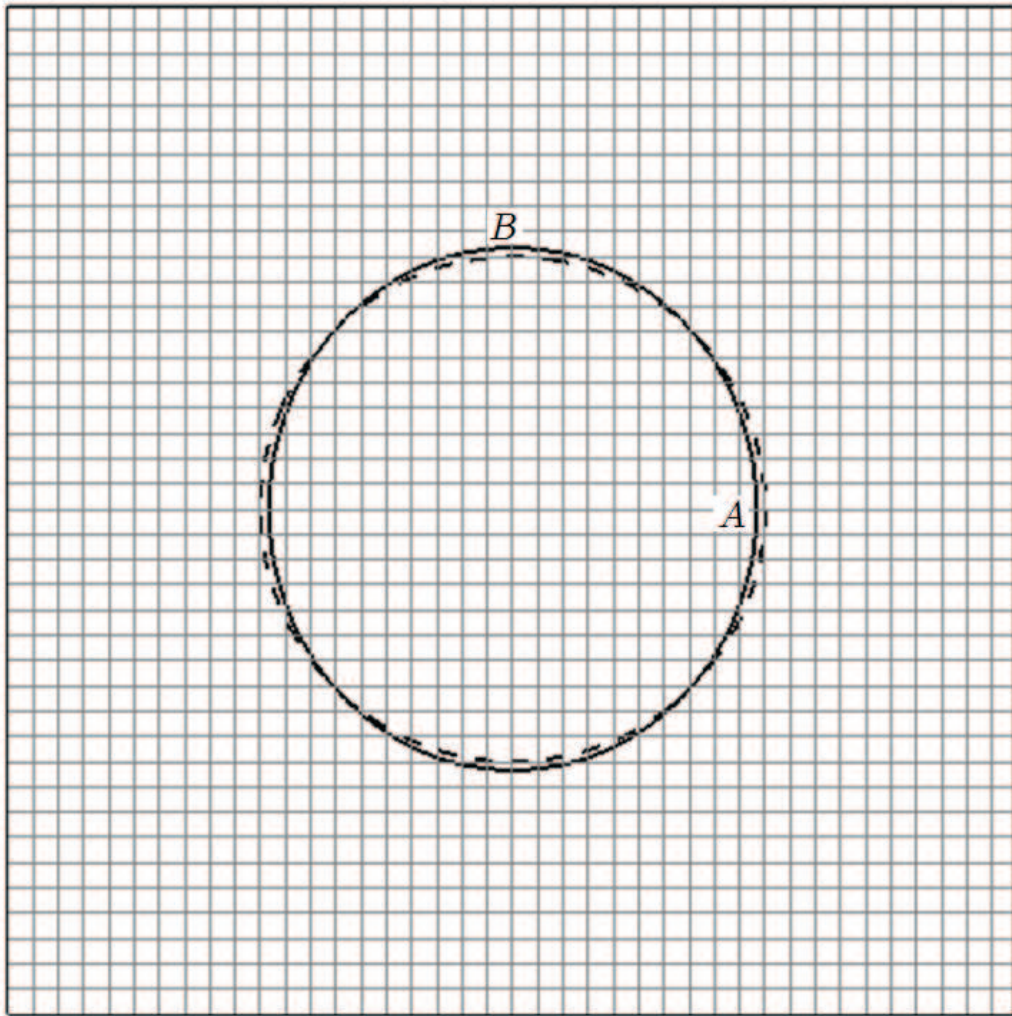
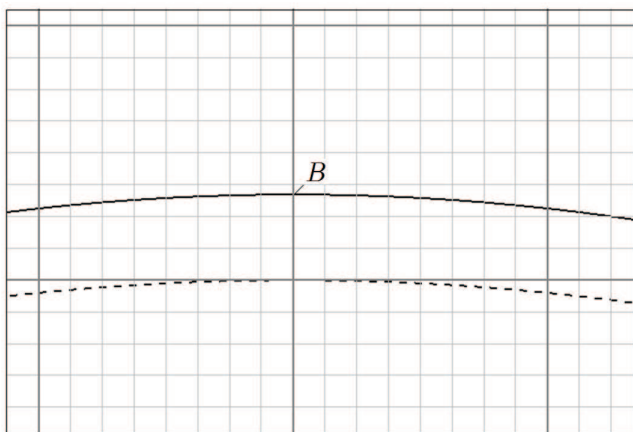


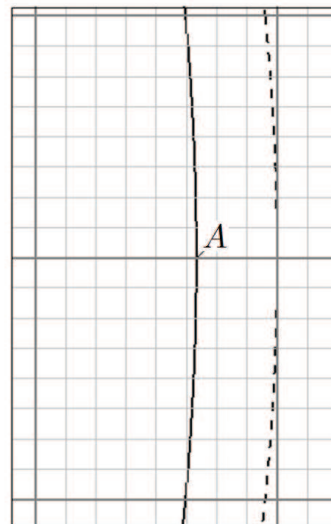
Figure 8.9: Flow field of the test case of a perfect dielectric droplet suspended in another perfect dielectric liquid. Contours of the pressure and vectors of the velocity are shown. A jump of ratio 10 in the dielectric property exists at the interface. A We number of 0.2 and a Reynolds number of 0.01 are considered. The computational domain is a $[-2, 2] \times [-2, 2]$ square. The radius of the droplet is 1 and the half-thickness of the diffuse interface is $\frac{1}{7}$. A grid of 40×40 cells is employed. A polynomial degree of 8 is used for the electric potential and polynomial degrees of 5 are used for the flow field variables.



(a)



(b)



(c)

Figure 8.10: Deformation a perfect dielectric droplet suspended in another perfect dielectric liquid. Interface of the droplet from figure 8.9 is shown. (a) The droplet (dashed line) is deformed to a spheroid (solid line). (b) zoomed view of the polar axis. (c) Zoomed view of the equatorial axis.

9 Summary, discussions and outlook

An electromechanical model for the numerical simulation of deformation of a droplet suspended in another immiscible liquid was successfully developed using the DG method. The physical phenomenon is that the droplet deforms in response to applying an external electric field. Due to the difference in the electrical properties of the droplet and the surrounding medium, there are electric forces exerted at the common interface of the droplet and the medium which deform the interface. The developed algorithm for the numerical simulation was based on a two-way coupling between the electric and fluid fields. First, the electric field was computed then the electric forces exerted to the fluid flow were found and the new shape of the interface was achieved. By deformation of the interface, the geometry for the computation of the electric field is changed. Therefore, the electric field must be computed again and the procedure continues. The external electric field was considered to be stationary. When a stationary electric field is applied, the droplet deforms until an equilibrium shape is reached. The equilibrium is the result of a force balance at the interface between the electric forces, pressure and surface tension.

For the numerical simulations, the droplet and the surrounding medium were considered as perfect dielectrics. When both materials are perfect dielectrics, the droplet deforms to a spheroid for which the polar axis is aligned to the direction of the applied electric field. Our numerical simulations showed the expected deformation of the droplet to a spheroid. Moreover, the results showed that the mass is well conserved through the deformation and the steady state deformation of the droplet was in a good agreement with the analytical OTAM formula.

For solving the electric problem, an electrostatic assumption was made. Considering that both materials were perfect dielectrics, a Laplace equation with a jump in the permittivity coefficient was solved to find the electric potential. To be able to define the permittivity coefficient for the whole computational domain, the one-fluid approach was applied. In this approach, the jump in the material properties is defined using a Heaviside function. Moreover, the diffuse interface model was adopted, which allowed us to regularize the heaviside function around the interface for integration. The heaviside function was a function of a signed-distance level set function which represented the interface as its zero iso-surface.

The above mentioned Laplace equation for the electric potential was discretized and solved using the symmetric interior penalty method, SIPG. The electric field was then computed as the gradient of the electric potential. The SIPG method, which is stabilized using a penalty parameter, failed to provide reasonable results for the electric field. The resultant electric field suffered from high oscillations. Therefore, a modification and stabilization of the SIPG method appeared to be necessary because the IP method is originally designed for discretizing the linear second order derivative terms with constant

coefficient. For our case with the coefficients ε_1 and ε_2 for the permittivities of the two materials, two methods were provided and tested which were based on modifying the penalty parameter. The first method, SIPG-ACP, uses the average of the coefficients ε_1 and ε_2 in the penalty term. The second method, SIPG-MCP, uses the maximum of the coefficients ε_1 and ε_2 and the half-thickness of the diffuse interface in the penalty term. Although the SIPG-ACP method showed to perform better than the SIPG method for low penalty parameter coefficients, it was not different from the SIPG method for high penalty parameter coefficients. The SIPG-MCP method showed to be quite effective in stabilizing the SIPG method. More over, in contrast to the SIPG and SIPG-ACP methods, the SIPG-MCP method provides the expected exponential convergence rate in error reduction. Therefore, the SIPG-MCP method was adopted and was tested up to a ratio of 100 for the permittivity which is satisfactory considering the permittivity ratio of 80 for the water-air systems, in the electrowetting applications. The modification of the penalty term may increase the number of iterations of the iterative solvers, which we did not study.

The exerted force from the electric field to the fluid flow is the dielectrophoretic force in case of two perfect dielectric materials. This force, which depends on the magnitude of the electric field and the gradient of the permittivity, was computed from the Kortweg-Helmholz formula. To be able to compute the magnitude of the electric field accurately using DG, high polynomial degrees were employed. The dielectrophoretic force, which acts in the normal direction to the interface, was added (considering the one-fluid approach) to the fluid flow as a body force. Due to the use of the diffuse interface model for regularizing the jump in the permittivity, the electrophoretic force is not concentrated at the interface but is distributed over a distance around the interface. Because of this distribution, some artificial components of the body force were produced in the tangential direction to the interface which gave rise to circulating spurious velocities. However, the spurious velocities, which are intrinsic to the use of the diffuse interface model, did not affect the numerical simulations because the simulations were performed for creeping flows. In the range of creeping flows which have low Reynolds numbers, the spurious currents are numerically suppressed. Creeping flows are reported in some experiments performed for the deformation of droplets in response to applied electric fields.

The fluid flow was simulated by solving the incompressible Navier-stokes equations. The droplet and the surrounding medium were assumed to have the same density and viscosity. Therefore, a single-phase version of the Navier-Stokes equations were employed which included the surface tension force as a body force. The surface tension force which acts in the normal direction to the interface was computed using the continuous surface force (CSF) model. Using this model, the surface tension force was distributed over a distance around the interface. Therefore, like in the case of the electric body force, some spurious velocities were produced. An accurate regularization of the dirac delta function, which appears in the CSF model, can be effective in reducing the spurious velocities. For the regularization of the delta function a cosine formulation was used. A suggestion for future investigations is to employ a function from the DG polynomial space.

To compute the surface tension force accurately, precise computations of the normal vector (to the interface) and mean curvature of the interface are essential. Therefore, we proposed the ideas of p-enrichment of the normal vector and using a non signed-distance

level set functions, ϕ_{NS} . The normal vector is the gradient of the level set function divided by its magnitude, therefore, $\mathbf{n} = \frac{\nabla\phi_{NS}}{|\nabla\phi_{NS}|}$. The p-enrichment was done by using a high polynomial degree (equal or greater than 5) for the normal vector while keeping a low polynomial degree (2 or 3) for the level set function. Having low polynomial degrees for the level set function is advantageous because an advection (and perhaps a reinitialization equation) must be solved for the level set function. As the curvature is the divergence of the normal vector, the polynomial degree for the curvature was one degree less than the polynomial degree of the normal vector. The idea of using a non signed-distance level set function was due to the fact that analytically both the sign-distance and non signed-distance level set functions define the same normal vector and curvature but numerically the signed-distance one involves the computation of the distance (the square root function), which can not be computed precisely with low polynomial degrees. Although a non sign-distance level set function does not exist for any arbitrary shape of the interface, it exists for a circle or a sphere which define a droplet in 2D or 3D. The p-enrichment of the normal vector together with using a non signed-distance level set function could minimize the errors related to the computation of the normal vector and curvature. However, the dominant error showed to be related to the regularized delta function. This suggests to investigate better regularization techniques.

For solving the single phase Navier-Stokes equations, a projection scheme with the consistent Neumann pressure boundary condition was used to decouple between the pressure and velocity fields. The time integration was performed using a stiffly stable scheme for the first and second orders. Using the consistent Neumann pressure boundary condition, a convergence rate of $k + 1$ was observed for both the velocity and pressure. The DG implementation was performed using different options regarding to the computation of derivatives of the flow variables. The first option, which uses the derivatives of the DG polynomials, showed not to be stable when coarse grids and low polynomial degrees were used. This can be explained as the inter-cell discontinuity of the DG solutions may not be negligible in case of coarse grids and low polynomial degrees. To handle the inter-cell discontinuity, a flux option was employed to compute the derivatives of the flow variables. The flux option appeared to be both stable and more accurate rather than the first option, which uses the derivatives of DG polynomials. The flux option was used also for computing the normal vector and curvature, which resulted in one order of magnitude reduction in the spurious velocities. Based on these experiences, the flux option was used for the calculation of the electric field from the electric potential.

10 Bibliography

- ALLAN, R. S., MASON, S. G. (1962): Particle Behaviour in Shear and Electric Fields. I. Deformation and Burst of Fluid Drops *267*, 1328, 45–61.
- ARNOLD, D., BREZZI, F., COCKBURN, B., MARINI, L. (2002): Unified Analysis of Discontinuous Galerkin Methods for Elliptic Problems. *SIAM Journal on Numerical Analysis* *39*, 5, 1749–1779.
- BOBBIO, S. (2000): *Electrodynamics of materials: forces, stresses, and energies in solids and fluids*. Automatic Computation, Academic Press.
- BRACKBILL, J. U., KOTHE, D. B., ZEMACH, C. (1992): A continuum method for modeling surface tension. *J. Comput. Phys.* *100*, 335–354.
- COCKBURN, B., KANSCHAT, G., SCHÖTZAU, D. (2005): A locally conservative LDG method for the incompressible Navier-Stokes equations. *Math. Comput.* *74*, 251, 1067–1095.
- COCKBURN, B., KANSCHAT, G., SCHÖTZAU, D. (2007): A Note on Discontinuous Galerkin Divergence-free Solutions of the Navier-Stokes Equations. *J. Sci. Comput.* *31*, 61–73.
- COCKBURN, B., KANSCHAT, G., SCHÖTZAU, D., SCHWAB, C. (2002): Local Discontinuous Galerkin Methods for the Stokes System. *SIAM J. Numerical Analysis* *40*, 1, 319–343.
- COCKBURN, B., SHU, C. (2001): Runge-Kutta Discontinuous Galerkin Methods for Convection-Dominated Problems. *J. Sci. Comput.* *16*, 3, 173–261.
- DEVILLE, K. L., M., MONTIGNY-RANNOU, F. (1984): Pressure and time treatment for Chebyshev spectral solution of a Stokes problem. *International Journal for Numerical Methods in Fluids* *4*, 1149–1163.
- DEVILLE, M. O., FISCHER, P. F., MUND, E. H. (2002): *High order methods for incompressible fluid flow*. Cambridge university press.
- DI PIETRO, D. A., ERN, A. (2012): *Mathematical Aspects of Discontinuous Galerkin Methods*. Mathématiques et Applications, Vol. 69, Springer.
- DRYJA, M. (2003): On discontinuous Galerkin methods for elliptic problems with discontinuous coefficients. *Computational Methods in Applied Mathematics* *3*, 1, 76–85.
- DULIKRAVICH, G. S., LYNN, S. R. (1997): Unified electro-magneto-fluid dynamics (EMFD): A survey of mathematical models. *International Journal of Non-Linear Mechanics* *32*, 5, 923–932.

- E, W., LIU, J.-G. (1995): Projection Method I: Convergence and Numerical Boundary Layers. *SIAM Journal on Numerical Analysis* 32, 1017–1091.
- EMAMY, N. (2010): *BoSSS For Solving Conservation Laws*. Fachgebiet für Strömungsdynamik des Fachbereichs Maschinenbau an der Technischen Universität Darmstadt.
- FERRER, E., WILLDEN, R. (2011): A high order Discontinuous Galerkin Finite Element solver for the incompressible Navier-Stokes equations. *Computers & Fluids* 46, 1, 224 – 230. 10th ICFD Conference Series on Numerical Methods for Fluid Dynamics (ICFD 2010).
- FRÖHLCKE, A. (2013): *A boundary conformal discontinuous Galerkin method for electromagnetic field problems on Cartesian grids*. Dissertation, TU Darmstadt Fachgebiet für Theorie Elektromagnetischer Felder.
- GEAR, C. W. (1971): *Numerical Initial Value Problems in Ordinary Differential Equations*. Automatic Computation, Prentice-Hall, Englewood Cliffs, NJ.
- GUERMOND, J. L., MINEV, P., SHEN, J. (2006): An overview of projection methods for incompressible flows. *Computer Methods in Applied Mechanics and Engineering* 195, 6011–6045.
- HARTMANN, R. (2008): Numerical Analysis of Higher Order Discontinuous Galerkin Finite Element Methods. In: *VKI LS 2008-08: CFD - ADIGMA course on very high order discretization methods, Oct. 13-17, 2008*, H. Deconinck, Hrsg., Von Karman Institute for Fluid Dynamics, Rhode Saint Genèse, Belgium.
- HAZRA, S. B. (2009): *Status of the linear solvers in the discontinuous Galerkin simulation tool BoSSS*. Fachgebiet für Strömungsdynamik des Fachbereichs Maschinenbau an der Technischen Universität Darmstadt.
- HESTHAVEN, J. S. (2008): *Nodal Discontinuous Galerkin Methods: Algorithms, Analysis, and Applications*. Texts in Applied Mathematics , Vol. 54, Springer-Verlag.
- HULSEN, M. A. (1996): *Stability of the implicit/explicit extension of the stiffly-stable schemes of Gear*. Laboratory for Aero and Hydrodynamics Faculty of Mechanical Engineering and Marine Technology Delft University of Technology.
- KARAKASHIAN, O., KATSAOUNIS, T. (2000): A discontinuous Galerkin method for the incompressible Navier-Stokes equations. In: *Discontinuous Galerkin methods: theory, computation, and applications*, B. Cockburn, G. Karniadakis, C.-W. Shu, Herausgeber, Springer Verlag, Bd. 11 von *Lecture notes in computational science and engineering*, 157–166.
- KARAKASHIAN, O., KATSAOUNIS, T. (2006): Numerical simulation of incompressible fluid flow using locally solenoidal elements. *Computers & Mathematics with Applications* 51, 9-10, 1551–1570.

- KARAKASHIAN, O. A., JUREIDINI, W. N. (1998): A Nonconforming Finite Element Method for the Stationary Navier-Stokes Equations. *SIAM J. Numer. Anal.* 35, 93–120.
- KARNIADAKIS, G. E., ISRAELI, M., ORSZAG, S. A. (1991): High-order splitting methods for the incompressible Navier-Stokes equations. *Journal of Computational Physics* 97, 2, 414–443.
- KEIM, S. (2004): *Optische Diagnose an singulären Tropfen auf polymeren Isolierstoffoberflächen im elektrischen Feld*. Dissertation, TU Darmstadt.
- KO, H.-J., DULIKRAVICH, G. S. (2000): A fully non-linear theory of electro-magneto-hydrodynamics. *International Journal of Non-Linear Mechanics* 35, 4, 709 – 719.
- KUMMER, F. (2012): *The BoSSS Discontinuous Galerkin solver for incompressible fluid dynamics and an extension to singular equations*. Dissertation, TU Darmstadt Fachgebiet für Strömungsdynamik.
- KUMMER, F., EMAMY, N., MOUSAVI B. T., R., OBERLACK, M. (2009): Report on the development of a generic discontinuous Galerkin framework in .NET. Parallel Computational Fluid Dynamics (ParCFD) 2009, Moffett Field, California, USA.
- LU (2002): *Electrohydrodynamic Deformation of Water Drops in Oil with an Electric Field*. University of Alberta.
- MADAY, Y., PATERA, A. T., RØNQUIST, E. M. (1990): An Operator-integration-factor splitting method for time-dependent problems: Application to incompressible fluid flow. *Journal of Scientific Computing* 5, 263–292.
- MELCHER, J. R., TAYLOR, G. I. (1969): Electrohydrodynamics: A review of the role of interfacial shear stresses. *Annual Review of Fluid Mechanics* 1, 111–146.
- MOUSAVI, R. (2012): *Solving the level set advection and re-initialization equations applying a discontinuous Galerkin method*. Fachgebiet für Strömungsdynamik des Fachbereichs Maschinenbau an der Technischen Universität Darmstadt.
- MUGELE, F., BARET, J. (2005): Electrowetting: from basics to applications. *Journal of Physics: Condensed Matter* 17, R705–R774.
- MUGELE, F., BUEHRLE, J. (2007): Equilibrium drop surface profiles in electric fields. *Journal of Physics: Condensed Matter* 19, 375112.
- NGUYEN, N. C., PERAIRE, J., COCKBURN, B. (2011): An implicit high-order hybridizable discontinuous Galerkin method for the incompressible Navier-Stokes equations. *Journal of Computational Physics* 230, 4, 1147–1170.
- O’KONSKI, C. T., THACHER, H. C. (1953): The Distortion of Aerosol Droplets by an Electric Field. *The Journal of Physical Chemistry* 57, 9, 955–958.
- ORSZAG, S. A., ISRAELI, M., DEVILLE, M. O. (1986): Boundary conditions for incompressible flows. *Journal of Scientific Computing* 1, 75–111.

- QUILLIET, C., BERGE, B. (2001): Electrowetting: a recent outbreak. *Current Opinion in Colloid & Interface Science* 6, 1, 34–39.
- SAVILLE, D. A. (1997): ELECTROHYDRODYNAMICS: The Taylor-Melcher Leaky Dielectric Model. *Annual Review of Fluid Mechanics* 29, 27–64.
- SCHLICHTING, H. (1950): *Boundary Layer Theory*. McGraw-Hill, New York.
- SHAHBAZI, K. (2005): An explicit expression for the penalty parameter of the interior penalty method. *Journal of Computational Physics* 205, 2, 401–407.
- SHAHBAZI, K., FISCHER, P. F., ETHIER, C. R. (2007): A high-order discontinuous Galerkin method for the unsteady incompressible Navier-Stokes equations. *J. Comput. Phys.* 222, 1, 391–407.
- SUPEENE, G., KOCH, C. R., BHATTACHARJEE, S. (2008): Deformation of a droplet in an electric field: Nonlinear transient response in perfect and leaky dielectric media. *Journal of Colloid and Interface Science* 318, 2, 463–476.
- TAYLOR, G. (1966): Studies in Electrohydrodynamics. I. The Circulation Produced in a Drop by Electrical Field. *Proceedings of the Royal Society of London. Series A, Mathematical and Physical Sciences* 291, 1425, 159–166.
- TSORI, Y., STEINER, U. (2009): *Polymers, liquids and colloids in electric fields: interfacial instabilities, orientation and phase transitions*. World Scientific.
- WANG, Y., OBERLACK, M. (2011): A thermodynamic model of multiphase flows with moving interfaces and contact line. *Continuum Mechanics and Thermodynamics* 23, 409–433.
- WEILAND, T. (1977): Eine Methode zur Lösung der Maxwellschen Gleichungen für sechskomponentige Felder auf diskreter Basis. *International Journal of Electronics and Communication (AEÜ)* 31, 3, 116–120.

11 Curriculum Vitae

Der Lebenslauf ist aufgrund von Datenschutzgründen in der Online Version nicht enthalten.